CONVERGENT FIELD ELASTOGRAPHY

A Dissertation
Presented to
The Academic Faculty

by

Michael D. Gray

In Partial Fulfillment
of the Requirements for the Degree
Doctor of Philosophy in Mechanical Engineering

Georgia Institute of Technology
May 2015

CONVERGENT FIELD ELASTOGRAPHY

Approved by:

Dr. Peter Rogers, Chair
School of Mechanical Engineering
Georgia Institute of Technology

Dr. Mark Prausnitz
School of Chemical and Biomolecular Engineering
Georgia Institute of Technology

Dr. David Ku
School of Mechanical Engineering
Georgia Institute of Technology

Dr. Darlene Ketten
Woods Hole Oceanographic Institution

Dr. Mardi Hastings
School of Mechanical Engineering
Georgia Institute of Technology

Date Approved: January 30, 2015

ACKNOWLEDGEMENTS

I wish to thank Peter Rogers - advisor, mentor, and long-time friend - for always putting me in a position to succeed. The confidence that he and Gary Caille expressed in my abilities was an early enabling force as I evolved from technical writer to research group leader.

I received valuable technical advice and a wellspring of common sense from James Martin, and received vital technical support from Van Biesel, Jayme Caspall, and Peter Cameron. Drs. Mardi Hastings and Karim Sabra provided critical test equipment, and the ME machine shop manufactured high quality parts for use in the thesis experiments.

Funding for this work was provided by Code 322 of the Office of Naval Research, and the Neely Chair in Mechanical Engineering.

Most importantly, I thank my wife Lee and father Peter, who supported this effort from beginning to end. I could not and would not have done this without them.

TABLE OF CONTENTS

LIST OF TABLES

LIST OF FIGURES

LIST OF ABBREVIATIONS

CFE	Convergent Field Elastography
FT	Force generation transducer
ICP	Intracranial pressure
RMS	Root mean square
ROI	Region of interest
SNR	Signal to noise ratio
TBI	Traumatic brain injury
VT	Vibrometer transducer

SUMMARY

A new approach to soft tissue elastography is presented. The work was motivated by the need to understand and mitigate the effects of anthropogenic sound on marine mammals. These efforts have been hampered by a lack of knowledge of *in vivo* tissue viscoelastic moduli. To address this problem, a measurement system concept was developed to non-invasively determine shear viscoelastic properties at tissue depths of over 12 cm – well beyond the capabilities of existing systems.

The central design feature of the measurement system is a focused, sectored, annular ultrasonic source that generates a ring-like pressure field. This in turn produces a ring-like radiation force distribution in soft tissue, the response of which is primarily observable as a shear wave field that converges to the center of the force pattern. A second confocal transducer nested inside the shear wave generation source is used to measure the component of the shear wave motion along the beam axis. Propagation speed is estimated from displacement phase changes resulting from drive frequency induced dilation of the forcing radius. Forcing beams are modulated in order to establish shear speed frequency dependence, allowing quantification of shear speed dispersion. This concept for convergent field elastography (CFE) is intended to significantly improve the overall ability to estimate soft tissue shear speeds in thick, complex tissues while keeping within FDA-mandated ultrasound exposure limits.

A prototype system was developed and tested in tissue mimicking materials for which properties were independently determined. Experiments were first carried out in a

homogeneous material, and subsequently in a material containing elastic contrast inclusions. Transmission experiments with re-hydrated samples of bottlenose dolphin skull and mandibular bone samples were conducted to quantify ultrasonic beam attenuation and distortion effects, and their cumulative impact on CFE shear estimation performance. In addition to supporting marine mammal studies, the techniques developed in this thesis may enable or extend a wide range of human medical diagnostics.

CHAPTER 1

INTRODUCTION

"Everything is related to everything." – Wilfred Mueller, 2011

1.1 Motivation

Whales, dolphins and porpoises belong to the biological order Cetacea, and are marine mammals ranging in size from 1 to 33 meters in body length (Ballance, 2009). In recent years, as concerns arose over the possible relationship between human generated sound, including naval activity, and cetacean mass stranding events (Evans & England, 2001), a broad range of research activities has sought to improve the understanding of cetacean biology and behavior, both under "normal" conditions and in the response to anthropogenic sound (Cox, et al., 2006). To understand mechanical responses of tissues and biological systems to incident sound, basic knowledge of constituent tissue elasticity is required. These properties may be used along with anatomical information to construct acoustic response models (Aroyan 2001, Krysl, et al. 2006, Tubelli et al., 2012). Amongst the difficulties encountered in building such models is the lack of *in vivo* elastic property information for cetaceans.

1.2 Soft Biological Tissue Properties

Studies of soft biological tissue elastic properties in cetaceans have been limited to samples extracted from deceased animals (Soldevilla, et al. 2005). The difficulty in use or interpretation of *ex vivo* data, whether for cetaceans or any other animal, stems

from evidence that these data are not representative of *in vivo* values, accompanied by the apparent sensitivity of *ex vivo* or *post mortem* results to time elapsed between harvesting and testing, and how the samples were handled over that time. This issue has been studied in detail for brain shear modulus (Chatelin, et al. 2010), with a variety of studies describing the impact of loading history (Garo, et al. 2007), post mortem time (Gefen & Margulies 2004, Vappou, et al. 2008), and handling temperature (Hrapko, et al. 2008, Nicolle, et al. 2005, Zhang, et al. 2011). Related work has indicated differences in pre- and post-mortem properties for pilot whale blubber (Fitzgerald & Fitzgerald, 1995), fish (M. Cox, 1987), and bovine and canine tissues (Fitzgerald, 1975). A study of bottlenose dolphin postmortem changes (McKenna, et al. 2007) concluded that on the basis of CT (computed tomography) images, gross tissue structure and density did not change significantly, but the study did not include any *in vivo* elasticity measurements.

Noteworthy in the above studies were the *post mortem* changes in shear modulus and/or modulus loss factors, the latter being especially critical in assessing resonance effects, and in the context of anthropogenic noise, the potential for acoustically – induced tissue damage (Cox, et al., 2006). In mammalian tissues, the shear modulus may be five to six orders of magnitude lower than bulk modulus (Sarvazyan et al. 1998, Frizzell 1976, Goss et al. 1980). Mechanically, this illustrates the relative ease of soft tissue deformation without volume change (as in shear) relative to deformation with volume change (as in compression). Even when exposed to zero-wavenumber excitations, large shear displacements can be generated due to mode conversion at tissue boundaries (Baryshnikova, 1986). In reaction to an arbitrary applied stress distribution, soft tissues are expected to respond by the mechanism of least resistance – shear deformation.

Several reports and papers have documented *post mortem* pathologies in stranded cetaceans (Ketten 2005, Jepson, et al. 2003). Necropsies on stranded cetaceans found blood present intracranially and in mandibular fat bodies (Figure 1.1) which motivated the interest in examining tissue volumes obscured by bone. More generally, if the sound paths through the heads of cetaceans are to be understood for either damage risk assessments or hearing studies, the properties of all head tissues should be characterized.

Illustration reprinted with permission, Copyright Jon Baldur Hlidberg, www.fauna.is

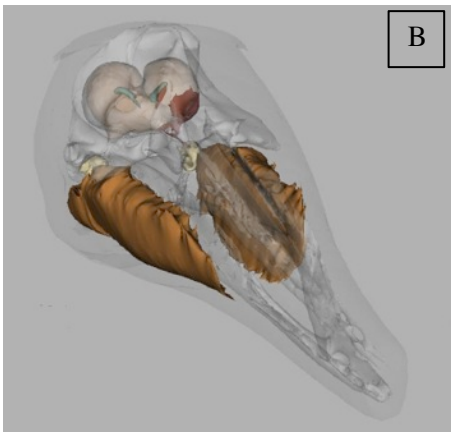

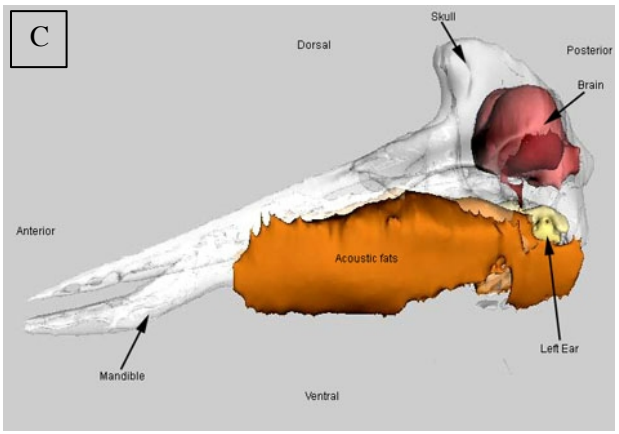

Images reprinted with permission, Copyright D. R. Ketten, WHOI

Figure 1.1. Blainville's Beaked Whale (*Mesoplodon densirostris*). (A): illustration of free-swimming animal. (B,C): annotated scans of head tissues in a stranded animal.

1.3 Elastography

The term "elastography" describes a class of techniques in which some aspect of a material's elasticity is determined through mechanical excitation and response measurement. Early work in this area with animal tissues was performed exclusively with *ex vivo* samples, such as with fish swimbladder (Alexander, 1961), fish muscle and skin (Lebedeva, 1965) and cow muscle (Fitzgerald, et al. 1957) placed in special mechanical rigs. Pioneering *in situ* soft tissue elastography studies employed static (Ophir, et al. 1991) and dynamic externally applied forces (Krouskop, et al. 1987, Lerner, et al. 1990). Ultrasound was used to measure the tissue strain along the loading direction, leading to calculation of relative local stiffness and facilitating identification of pathologies (Krouskop, et al. 1999). It was shown (Yamakoshi, et al. 1990) that viscoelastic properties could be estimated from frequency-dependent data by fitting to a simple model for the tissue that included complex moduli (Oestreicher, 1951). While these methods are relatively straightforward to implement, they do have some drawbacks. Specifically, when a force is applied at an external tissue surface (e.g. epidermis), the stress distribution on an internal region of interest is dependent on intervening tissues, and is not generally known, complicating the analysis and estimation of absolute material properties. This is especially problematic for examination of tissues obscured by bone. In addition, surface mechanical force elastography methods can be somewhat unwieldy, in that they require both an actuator (which tends to be massive) and an imaging probe, and the results may be sensitive to actuator orientation and pre-stressing of the tissue.

A considerably more sophisticated methodology has been developed by coupling elastic inversion methods with magnetic resonance imaging (Muthupillai, et al. 1996), in

a class of techniques called magnetic resonance elastography (MRE). Dynamic excitation of the test subject is typically provided by a table or head actuator, and the MRI scan data are inverted from wave equations with second (Manduca, et al., 2001) or third (Green, et al. 2008) order spatial derivatives to yield shear moduli tissue maps. The successful use of such calculations demonstrates the high signal to noise ratios in the raw displacement data. These methods have been used to calculate complex valued shear moduli in human brains, showing low frequency shear speeds in the 1.5 m/s range, with loss tangents near unity (Sack, et al. 2008). The MRE methods provide highly detailed viscoelasticity maps of scanned tissues, but there are clear drawbacks in cost and availability. The extent to which the imaging system and subject animal could be brought together is highly constrained, and cost, size, and weight factors make MRE impractical for use in cetacean stranding response diagnostics, or in cases where the weight and/or size of the animal exceeds the capacity of the imaging system.

1.4 Radiation Force Elastography

A somewhat intermediate solution, offering high spatial resolution shear modulus estimation in relatively affordable and portable configurations has been developed in recent years in the form of "radiation force elastography" methods, which use ultrasound to generate highly localized internal tissue loads. Sound generates a force as it propagates through tissue due to transfer of momentum from the sound wave to the tissue as a result of absorption and scattering (Sarvazyan, et al. 2010). This force per unit volume, referred to as radiation force, is given by $F_V = 2\alpha I/c = 2\alpha(I_0 e^{-2\alpha z})/c$ for an absorbing medium (Starritt, et al. 1991) where α is the absorption coefficient, I is the

time average intensity, c is the speed of sound, I_0 is the intensity in the absence of absorption, and z is the propagation distance. This is the Langevin form of radiation force, differentiated from the Rayleigh form in that the beam of sound is not laterally confined (Chu & Apfel, 1982). The force magnitude is proportional to intensity, or under plane wave or farfield conditions, the square of the pressure. The forcing volume created by a beam of sound is then strongly correlated to the shape of the beam in space, and the nominal shape and location of a force inside a tissue volume can therefore be controlled through design of the transducer and/or through beamforming of a multi-element transducer. Although the force described above is related to ultrasonic absorption, it has been shown that there was no significant difference between absorption and total attenuation (which includes scattering effects) for certain tissue types (Parker, 1983, Campbell & Waag, 1984). The practical significance of this result lies in the relative ease of *in vivo* determination of effective attenuation. Scattering, and more generally, reflection, can produce large changes in incident field momentum and therefore create large radiation pressures. However, in soft tissues, the scatterers are small compared to typical ultrasonic wavelengths. In this case the scattered field is extremely broad in angular extent, so that the net generated force is negligible (Nightingale, Palmeri, Nightingale, & Trahey, 2001).

When a line-like force is dynamically applied inside an isotropic solid, cylindrical waves are radiated from the forcing region in the form of shear and longitudinal waves, in addition to non-propagating components (Bercoff, et al. 2004). For soft tissues, the shear modulus is much smaller than the bulk modulus, so shear displacements dominate close to the force. Shear waves in soft tissues attenuate rapidly away from the force region due

to their short wavelength and high intrinsic attenuation, so the displacement field produced by a concentrated radiation force excitation is highly localized. This is a desirable situation for estimating properties within a tissue volume without influence from neighboring tissues or other boundary conditions (Melodelima, et al. 2007).

For a harmonic line force inside a homogeneous infinite elastic medium, the shear wave displacement in the direction parallel to the force, as observed at a large distance from the force *($k_s r > 1$)*, is proportional to $(k_s r)^{-1/2} e^{(ik_s r - \psi)}$ where k_s is the shear wavenumber, r is the radial distance from the force, and ψ is a phase term unrelated to material properties or position (Chen, et al. 2004). If displacement is measured at two successive radial points, and the excitation frequency is known, the shear wave speed c_s can be estimated simply from the phase change $\Delta\phi$ with respect to distance Δr: $c_s = 2\pi f_L \left(\Delta r / \Delta\phi\right)$ (Chen, et al. 2004). In reality, the applied force has a finite extent, and diffraction effects complicate the analysis (Calle, et al. 2005) at short radial distances. Alternately, wave equation inversion methods have been used when scanning array systems provided displacement fields with high signal to noise ratios over extended regions (Nightingale, et al. 2003, Bercoff, et al. 2004).

1.5 Tissue Motion Measurement

Ultrasound is a commonly used mechanism for remote measurement of vibrations within soft tissues, offering lower attenuation rates than light-based methods and reduced cost and logistical challenges relative to magnetic resonance imaging methods. Ultrasonic methods for tissue motion measurement generally fall into two classes – pulse echo and Doppler (Martin, et al. 2011). Pulse echo methods involve correlation of

backscatter echoes from specific tissue sites as a function of time (Lubinski, et al. 1999). Tissue motion causes a perturbation in the time at which the backscatter from a particular location in space occurs. Calculation of this perturbation provides an estimate of displacement using a known or estimated sound speed. These methods have been shown to provide minimum detectible displacements on the order of 10^{-6} meters (Pinton, et al. 2006).

Doppler methods estimate tissue displacement from the size of side bands of the drive frequency observed in ultrasound backscatter. When an acoustic field with fundamental carrier frequency ω_h is incident upon a scatterer vibrating with periodic motion $d = d_o \cos(\omega_L/c)$, the change in path length between source and scatterer introduces additional frequency components at $\omega_h \pm n\omega_L$ (Cox & Rogers, 1987), where n is an integer. If the scatterer motion is ultrasonically small, the amplitude of the motion d_o can be determined directly from the amplitude ratio of the $n=1$ sidebands to the primary carrier tone provided that the speed of sound in the medium is known. More generally, the high frequency transmitted signal does not have to be sinusoidal, and the scatterer motion signal is obtained from a demodulation process performed on the high frequency received signal. Regardless of methodology used, ultrasonic observation of tissue motion yields an estimate of the component of the displacement vector along the direction of the interrogating ultrasound beam(s). For the typical case of parallel forcing and motion tracking beams, the directional nature of the motion measurements should favor observation of shear waves (which have displacements primarily parallel to the ultrasound beam) over compressional waves (with displacements primarily orthogonal to the beam.)

1.6 Radiation Force Elastography Systems

Ultrasound radiation force elastography systems based on the above principles have been widely studied over the last two decades. Most of these methods employ the basic physical processes illustrated in Figure 1.2, illustrated with a time domain simulation of the forced response of a viscoelastic solid. A burst of ultrasound is used to generate a line-like radiation force in a region of interest. At the time and location of force application (on the order of 0.1-1 mN), a relatively large local soft tissue deformation (on the order of 1-10 μm) is observed. This disturbance, primarily consisting of shear motion, attenuates as it propagates as a result of geometric and absorptive mechanisms. The diverging wave field displacements are measured at multiple locations outside of the force application region, and the results are used to estimate material properties using a wave propagation model.

Early development of all-ultrasonic radiation force systems was pioneered by Sugimoto (Sugimoto, Ueha, & Itoh, 1990). Significant theoretical development followed in Sarvazyan (Sarvazyan, et al. 1998), which laid the groundwork for much of the system development that followed. The Mayo Clinic demonstrated generation of tissue motion at specific locations in space with specific modulation frequencies (Fatemi & Greenleaf, 1999), with subsequent work demonstrating the relative merits of different transduction and signal production schemes (Chen, et al. 2004). The modulated force method allowed for direct observation of shear speed dispersion and estimation of shear loss tangent.

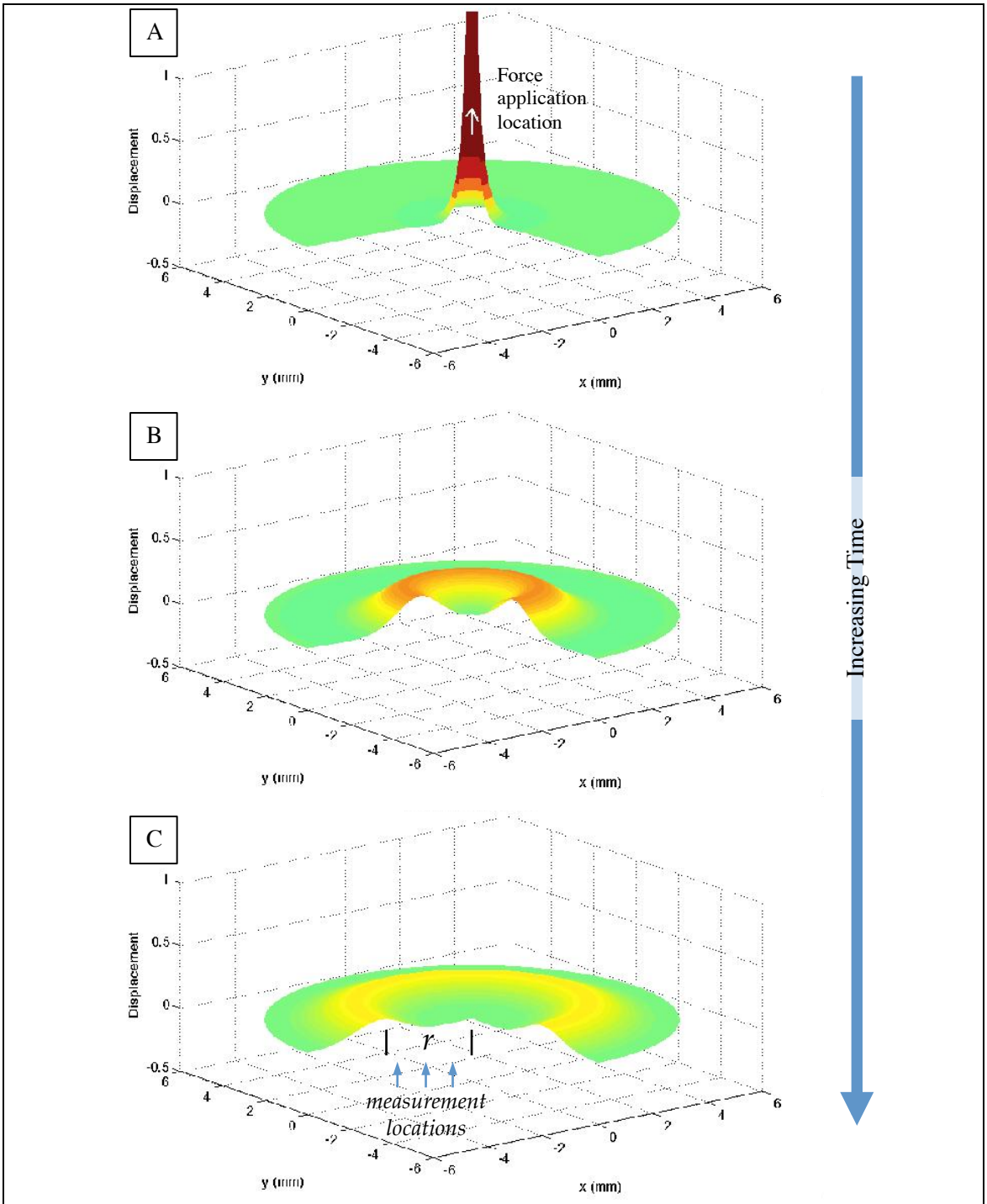

Figure 1.2. Illustration of the general principles of ultrasonic radiation force elastography. Application of a line-like conventional beam of ultrasound produces a line-like force (white arrow) and local tissue displacement (A). The resulting shear wave propagates away from the drive point, where its displacement is measured at several points (B, C) and used with a propagation model to estimate shear properties.

This approach was later modified to use pulsed drive signals whose repetition rate was used to impose a temporal step function force profile which generated displacements at a primary modulation frequency as well as several harmonics, allowing dispersion within a prescribed frequency band from a single measurement (Chen, et al., 2009).

Methods such as those by Sarvazyan and Chen required mechanical scanning of either the forcing or motion tracking transducers in order to evaluate phase change due to radial shear wave propagation. Mechanical scanning was obviated by a team at Duke University, which implemented radiation force generation of shear waves and pulse echo displacement tracking in a single commercially available medical array system (Nightingale, et al. 2001). Bercoff and colleagues (Bercoff, et al. 2004) also used an array-based system, wherein the forcing location was progressively steered away from the transducer, allowing shear speed estimation by ultrasonically observing the angle of the shear wave propagation Mach cone.

All of these methods estimate shear properties with wave models of regions excluding the region that contains the force. An exception to this approach was developed by Konofagou (Konofagou & Hynynen, 2003), where the forcing and motion assessments occurred at the same location in space. While this method did not require mechanical scanning of the system transducers to determine elastic properties in a region of interest, specific knowledge or assumption of the beam intensity distribution inside the tissue was required for modulus estimation. In later work, the method was used with the aim of characterizing changes in living tissues due to thermal effects through assessment of displacement magnitude changes, but stopping short of estimating absolute properties (Maleke, et al. 2006). Even when the radiation force distribution is not known, it was

shown that relative measures of viscoelastic behavior could still be extracted for *in vivo* diagnostic purposes (Walker et al. 2000, Viola et al. 2004). At present, ultrasonic radiation force elastography methods have been transitioned to commercially available diagnostic array systems offered by GE, Siemens, and Toshiba.

1.7 Ultrasound Safety

All the methods described above are subject to federally mandated limitations on living tissue ultrasound exposure for diagnostic systems (US Dept. of Health and Human Services, 2008). There are two types of ultrasound bioeffects addressed in the federal regulations – mechanical and thermal, and each has been assigned an index to facilitate safety assessment (Abbott, 1999). Mechanical effects are associated with cavitation due to large negative pressures in the rarefaction cycles of incident ultrasound. The Mechanical Index (MI) is defined as $MI = \frac{p_{max,neg}}{K\sqrt{f}}$, where f is the acoustic "working" frequency (MHz), K is a units correction constant, and $p_{max,neg}$ is the maximum negative pressure (MPa), diminished by an assumed *in vivo* attenuation of 0.3 dB/cm/MHz relative to a measurement made in water. This derating factor is relatively conservative compared to known values for most mammalian tissues (Goss, et al. 1980, Kremkau, et al. 1981, Strowitzki, et al. 2007). Diagnostic ultrasound systems are required to have a mechanical index less than or equal to 1.9.

Thermal effects are associated with tissue heating as a result of absorption of ultrasonic energy (Filipczynski, 1986). Thermal safety indices have been defined for different types of tissues and interfaces, and are proportional to incident power, rather than pressure. The thermal index (TI) indicates the output power of the ultrasound device

at the region of interest (e.g. at the focus) relative to the power required to raise tissue temperature by 1° C (Abbott, 1999), assuming steady-state conditions (Bigelow, et al. 2001). A temperature rise of 6° C is allowable without further justification or approval from the FDA (Nightingale, Palmeri, Nightingale, & Trahey, 2001).

A candidate system design is often limited by either MI or TI, but not both simultaneously. However, the formal federal guidance is not listed specifically as a combination of indices, but rather that for non-ophthalmologic applications, the global maximum derated spatial peak time averaged intensity (I_{spta}, which is integrated over a signal repetition period) must not exceed 720 mW/cm^2, and either MI<1.9 or the maximum derated spatial peak pulse average intensity (I_{sppa}, which is integrated over a single pulse, assuming use of a transient) must not exceed 190 W/cm^2. The values listed are thought to represent those up to which no adverse bioeffects have been observed. The thermal index is not specifically called out, and it has been pointed out that existing TI formulations do not properly account for the high amplitude, long duration, low duty cycle pulses employed in existing elastography systems (Palmeri & Nightingale, 2004) (Bigelow, et al., 2001).

1.8 Limitations of Existing Elastography Systems

In the systems described above, federal diagnostic ultrasound exposure safety regulations ultimately constrain the strength of radiation force that can be applied, and may also impact the size of incident signal that can be used for displacement tracking. This in turn limits the tissue depth at which measurements can be made and the range of distances from the force over which displacement can be measured. The net result is that

ultrasonic elastography systems tend to be limited to use at shallow depths in relatively simple tissues. Nonetheless, the diagnostic effectiveness of these types of systems has been clinically demonstrated in humans for tissues un-obscured by bone (Palmeri, et al. 2007, Tanter, et al. 2007). The employed systems operated at frequencies between 3 and 9 MHz, and were limited to tissue depths on the order of 1-5 cm. All operated at or near the limits of ultrasound exposure safety.

The challenges involved in application of existing systems to the cetacean measurement problem (or to thick tissues in general) are exemplified with the Cuvier's beaked whale CT image (Cranford, et al., 2008) in Figure 1.3. The soft tissues in many locations extend 10 cm or more from the water-skin interface before any bony tissue is encountered. Such distances, whether in the head of a cetacean or any part of any other animal, represent a prohibiting technical hurdle for existing elastography systems as a consequence of ultrasonic signal losses due to soft tissue attenuation. For example, assuming a 1 dB/MHz/cm tissue average attenuation value, a 5 MHz beam transmitted to a tissue depth of 10 cm instead of 5 cm results in an additional one way intensity loss (as relevant to force generation) of 50 dB, which would reduce the radiation force induced displacements commensurately. The two-way loss in backscatter would be the same as the displacement reduction if the forcing and motion tracking transducers operated at identical frequencies, so that the measurement signal to noise ratio (SNR) would be enormously degraded. It would not be possible to compensate for these signal losses purely by increasing drive power of the system, as doing so would exceed ultrasound safety limits.

A

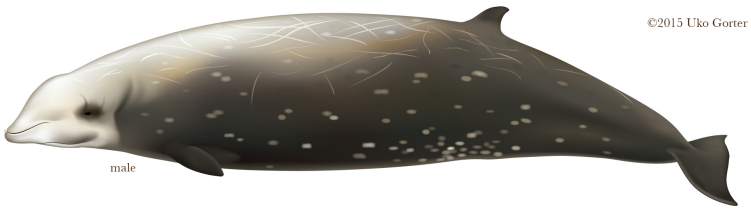

Reprinted with permission, Copyright 2015 Uko Gorter

B

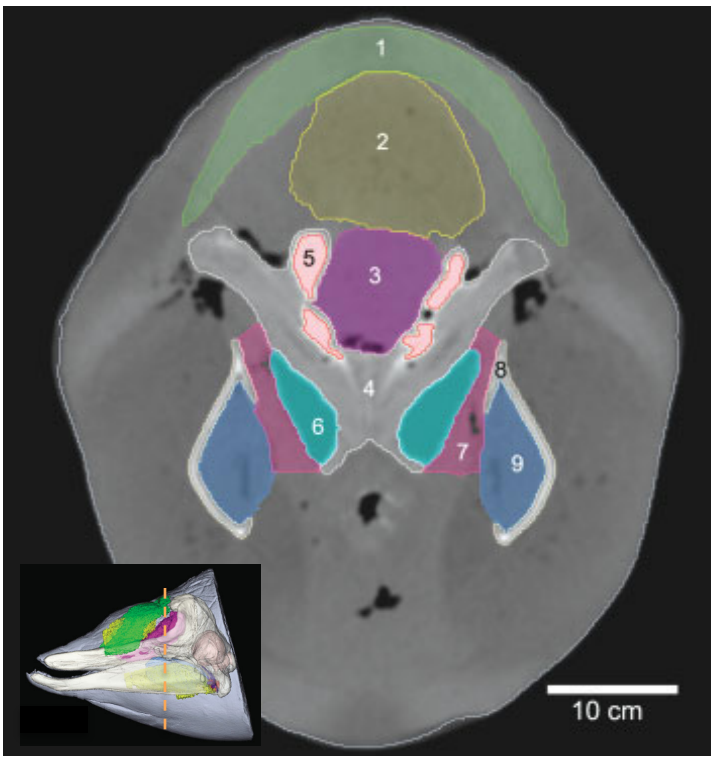

Image from Cranford et al., The Anatomical Record, 291:353–378 (2008)
Copyright 2008 Wiley-Liss, Inc.

Legend: 1: connective tissue; 2: melon; 3:anterior melon; 4: skull; 5: high density components of the skull; 6: pterygoid sinuses; 7: fibrous venous plexus; 8: mandibles; 9: mandibular fat bodies.

Figure 1.3. Cuvier's beaked whale illustration (A) and CT scan (B).

It is reasonable to ask how existing systems may perform if simply modified to operate at lower frequencies. Lowering the frequency decreases path propagation losses, but comes with some downsides, namely, decrease in allowable mechanical index

(limiting drive pressure at focus), a decrease in absorption (to which radiation force is proportional), and a decrease (with frequency-squared) of the strength of speckle-scattered pressure that is used to determine displacement. Since the methods operate in the extreme nearfield of the ultrasound transducers, scaling to lower frequencies would require a significant increase in transducer size to maintain the lateral resolution of the system. For example, consider the array transducer used by Bercoff (Bercoff, Tanter, & Fink, 2004), with a 4.2 cm aperture, operating at a center frequency of 4.3 MHz, and a maximum tissue depth of 4 cm. If the desired tissue depth were raised to 12 cm:

- The transducer would need to have an active aperture of 71 cm and operate at approximately 1 MHz to produce radiation force within 8 dB of that which was produced by the original array.
- The original force level could not be replicated due to (pressure) safety limits;
- The best frequency for backscatter strength, accounting for Rayleigh scattering frequency dependence and propagation losses, would be approximately 1.5 MHz. Operating at this reduced frequency would still yield a backscatter strength 19 dB below that of the original system;
- The total SNR deficit relative to the original system would be about 27 dB, which would need to be made up through an increase in motion tracking field strength. However, the deficit cannot be fully abated without incurring a safety limit on incident intensity. Moreover, at high enough power levels, the strength of the motion-tracking field could complicate the analysis due to non-linear effects.

1.9 Bone Transmission

The situation described above would be even direr if the excess transmission loss associated with propagation through skull bone was included. As demonstrated with samples from *Tursiops truncatus* (Gray, et al. 2006), even the thinnest bones in the mandible induce total attenuations per unit thickness that are much greater than soft tissues, and may also distort or refract the incident beam. Moreover, since modulus estimation calculations rely on precise knowledge of relative beam locations (for evaluating phase change with respect to distance from the source, for example), existing high frequency methods may further fail due to propagation-induced uncertainties.

The skulls of cetaceans exhibit considerable inter-species variability (Rommel, et al. 2009), asymmetry (Beharse 1971) and complexity (Oelshlager 1990). Much of the braincase consists of thick trabecular (porous) and geometrically complex bone, which diminishes the likelihood of a bony transmission path to the brain for ultrasound. A potentially favorable path may be via the parietal section of the temporal fossa, indicated in Figure 1.4. The temporal fossa is comprised of the parietal and squamosal bones (Mead & Fordyce, 2009), and is relatively thin and low-porosity in many cetaceans, so that geometric lensing effects on ultrasound incident upon this region should be minimized.

Odontocete (toothed whale) mandibles, examples of which are shown in Figure 1.5, are characterized by their hollow structure which houses an arrangement of fatty tissues thought to be involved in channeling received sound to the ear (Ketten, 2000; Koopman, et al. 2006; Zahorodny-Duggan, et al. 2009), and for the thin, flat proximal region referred to as the pan bone (Norris, 1968). The role of the mandible and its

associated tissue structures in hearing has been studied extensively (Norris and Harvey 1974; Mohl, et al. 1999; Ridgway 1999; Au 2000), although little appears to be known about the elastic properties of the bone or proximate *in vivo* soft tissues.

A

B

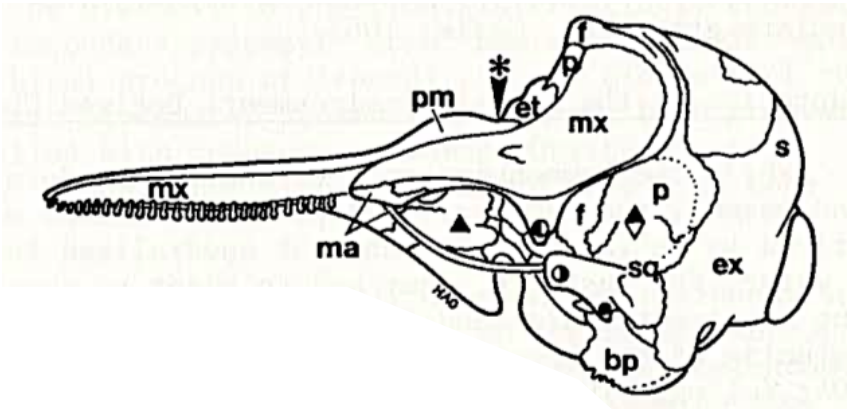

from: Oelshlager, H., Evolutionary morphology and acoustics in the dolphin skull, In: Sensory abilities of cetaceans, Thomas, J., Kastelein, R. Eds., Copyright 1990 Plenum Press

bp: lateral process of basioccipital, et: ethmoid, ex: exoccipital, f: frontal, ma: malar, mx: maxillary, p: parietal, pm: premaxillary, s: supraoccipital, sq: squamosal , ⧫ : temporal fossa

Figure 1.4. Photo (A) and labelled illustration (B) of an atlantic bottlenose dolphin skull.

Images from http://vertebrates.si.edu/mammals/beaked_whales/pages/zca/, Smithsonian Beaked Whale Identification Guide, Copyright 2007 Smithsonian Institution

Figure 1.5. Mandibles of a male Cuvier's beaked whale (*Ziphius cavirostris*): left lateral (A) and (B) posterior views.

Transmission of ultrasound through human skull bone has been studied extensively, with particular attention paid to methods for overcoming bone-induced beam distortion. Skull bone consists of high porosity ('trabecular') tissue bounded by layers of relatively compact ('cortical'), low-porosity tissue, all with individual layer thicknesses that may be highly variable (Fry 1978; Pichardo, et al. 2011). The small and large-scale complexities cause refraction, absorption and scattering that is difficult to predict and overcome. A further complication is that incident compressional waves may strongly couple to at least two elastic wave types in bone (White, et al. 2006), each with different speeds and attenuation rates. Thermal safety concerns also arise due to local ultrasonic

intensity increases brought about by the impedance mismatch between bone and soft tissue, and the high absorption rate of bone (Carstensen, et al. 1990).

Several corrective methods for focusing ultrasound through human skull bone have been developed, including iterative focusing with the assistance of an implanted hydrophone (Aubry, et al. 2001, Vignon, et al. 2007) and CT-assisted focusing (Aubry, et al. 2003, Clement & Hynynen, 2002).

1.10 Alternative System Concept

It is hypothesized that a novel form of ultrasound-based elastography can overcome limitations of existing systems while providing a unique capability to characterize the complex valued shear speed in relatively thick and complex soft tissues, including those obscured by certain types of bone. It was pointed out earlier that most ultrasound elastography systems determine shear speed through observation of the wave fronts diverging from a concentrated forcing location (as in Figure 1.2). An alternative is proposed wherein the forcing field is distributed in space, as shown in Figure 1.6. The ring-like force configuration can be thought of as a set of individual line-like forces distributed on a common radius. The response to this force distribution is primarily observable as an inwardly propagating shear wave field that grows in amplitude as it converges to the center of the force pattern. In other words, focused ultrasound is used to create a focused low frequency shear wave field. The resulting tissue motion at the force pattern center can be measured with a stationary, non-scanning vibrometer.

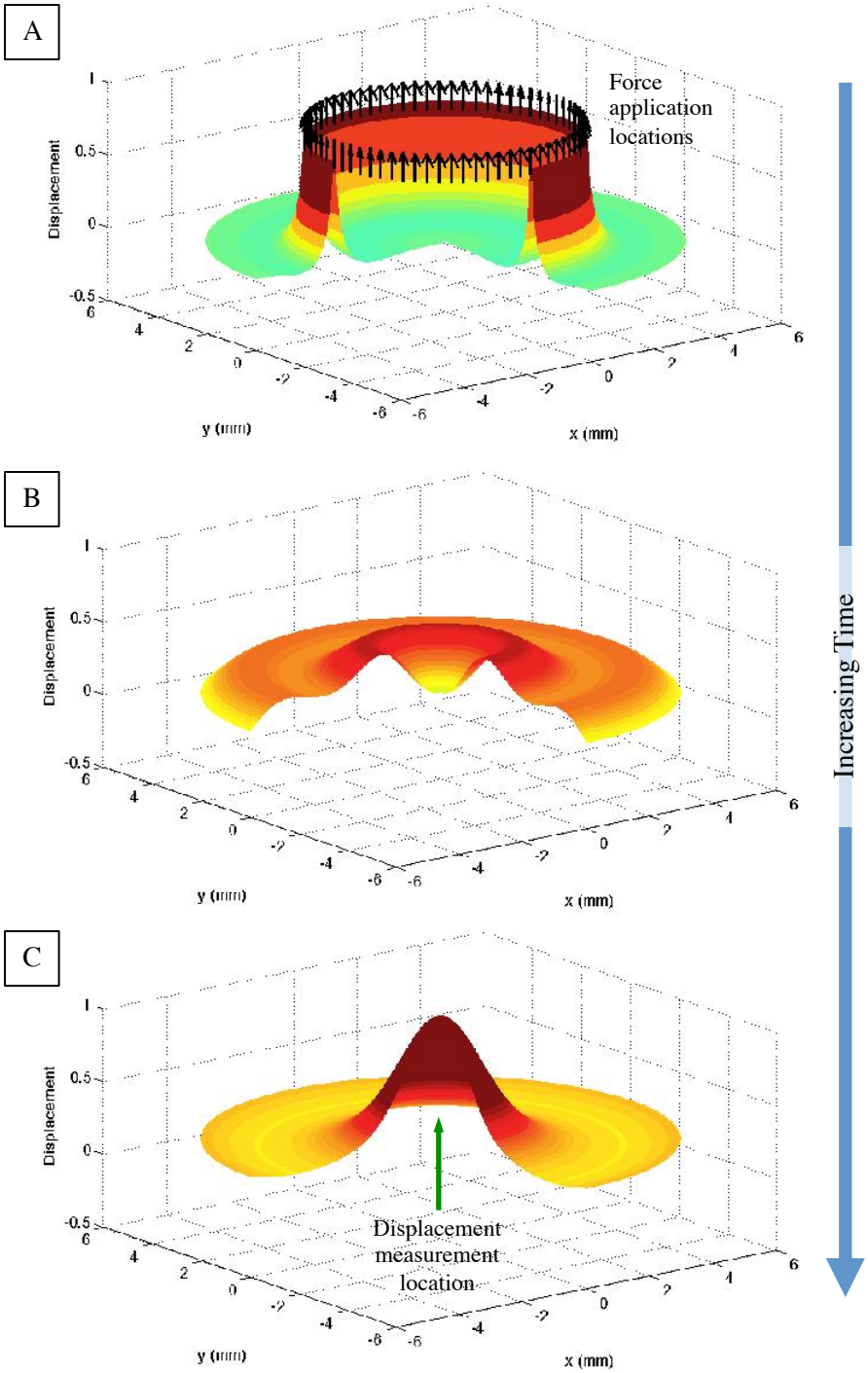

Figure 1.6. Illustration of the general principles of convergent field elastography (CFE). Application of a ring-shaped beam of pulsed ultrasound produces an annular force distribution (black arrows) (A). A portion of the resulting shear wave field focuses as it propagates inward (B), ultimately creating a maximum displacement at the force pattern center (C), where the motion is measured.

To facilitate estimation of shear speed, a phase change (delay) in the tissue response is induced by changing the mean radius of the forcing pattern. To determine shear speed as a function of frequency, the ultrasound beam(s) producing the forcing field are modulated at a controlled rate. Since the proposed technique measures the displacements formed by converging shear waves, the concept has been named convergent field elastography (CFE).

Distribution of the force application volume amongst several locations overcomes limits on displacement signal size imposed by ultrasonic safety restrictions. This can be illustrated qualitatively by considering a single ultrasonic forcing beam with intensity I_0 that satisfies all safety requirements while producing a tissue displacement amplitude X_0 at a distance R from the center of the beam.

- If N of these beams are arranged along a ring of radius R, the displacement at the center of the ring may be as large as $N \bullet X_0$.
- Thermal safety is unchanged provided that the spacing of the beams is such that tissue heating is locally dominated by heat generated by an individual beam.
- Mechanical safety (cavitation risk) with the ring distribution is unchanged relative to the individual beam because the peak negative pressure at any location is unchanged.
- Finally, the maximum intensity restriction is met because, while the tissue volume is exposed to N times the total incident power of an individual beam, the exposure area is N times larger, so that the net exposure intensity is still I_0.

With the ability to safely produce a larger displacement at a given tissue depth, it should be possible to probe deeper into tissues (or through heavily attenuating tissues)

without SNR problems. Another advantage to the proposed field shaping is that the region over which the displacement is maximized is on the order of a shear wavelength, making it relatively broad at low frequencies. This region is also characterized by a near constant phase, relative to the field outside the forcing region, which has a phase varying as $k_s r$. These features relax the requirements for the width and placement accuracy of the vibrometry beam.

The use of constructively interfering elastic wave fields has some precedent in elastography applications. The Mach cone imaging technique (Bercoff, et al. 2004) measures diverging wave field displacements caused by forces applied successively in time and space. A near-simultaneous multi-beam approach (McAleavey, et al. 2007) uses a presumed driving spatial wavenumber in one dimension (resembling a spatial comb), measures the displacements outside the forcing region, and then estimates the "dominant frequency" of vibration and deduces shear speed. In both cases, the frequency content of the shear wave field is broadly distributed and is not known in advance, the measured displacements are not maximized due to the forcing and receiving geometries, and a scanning vibrometer array is needed to determine the displacements. In the CFE concept, the forcing frequency content is prescribed through forcing beam modulation, and the displacements are maximized in a central location in space so that the vibrometer can be stationary. All these features are intended to simplify and enhance the robustness of the elastography system.

1.11 Hypothesis and Scope of Work

While motivated by the study of the impact of human-generated sound on cetaceans, the focus of this thesis is on the development of techniques for deep tissue elastography. The fundamental hypothesis of this dissertation is that the convergent field elastography technique can be used to determine low frequency, dynamic shear properties of soft biological tissues at depths of 10 cm or more - at least doubling the measurement range of existing systems - while staying within safety limits for diagnostic ultrasound exposure. The scope of work performed in order to test the hypothesis consisted of:

(i) System simulation. A combined ultrasonic-viscoelastic response model was developed for assessment of transducer design options, quantification of generated displacement fields, shear speed estimation performance and robustness, and prediction of tissue thermal exposure.

(ii) Prototype transducer design and calibration. Simulation results were used to specify designs for force generation and vibrometer transducers. Ultrasonic fields produced by the manufactured prototypes were quantified in detail, compared with predictions, and assessed for implementation of the CFE concept.

(iii) Experimental evaluation. The prototype CFE system, consisting of transducers, instrumentation, and data collection and processing methods, was developed and evaluated on materials designed to approximate properties of live mammalian tissues. Material samples were built in homogenous form and with spherical inclusions having shear properties contrast with the bulk

medium. The cumulative impact of bone on the performance of the CFE prototype was assessed using samples of re-hydrated bottlenose dolphin mandibular and cranial bone samples obtained from an authorized stranding network.

CHAPTER 2

SIMULATION METHODS

"Math is what people use when they do not know how to describe anything without math." – Armen Sarvazyan, 2011

2.1 Objectives

A simulation capability was developed to support the CFE development effort, from assessment of candidate transducer designs through prototype system experiment analyses. The specific objectives of the simulation effort were to predict:

(i) three-dimensional beam patterns of candidate ultrasonic transducer designs;

(ii) generation and measurement of motion in viscoelastic materials, using the predicted ultrasonic transducer patterns; and

(iii) temperature rise in natural biological tissues and tissue-like materials.

The methods employed to address these objectives are described in the following sections.

2.2 Ultrasound Field Simulation

In the present work, the pressure distributions produced by ultrasonic transducers within a homogeneous propagation medium are sought. Ultrasonic field predictions for notional radiator geometries are commonly carried out through discretization of the Rayleigh integral (Fjield, Fan, & Hynynen, 1996; Jensen & Svendsen, 1992). When used

for a curved, un-baffled surface, this approach is an approximation that may be expected to yield valid results if the radius of curvature and lateral dimensions are large with respect to an acoustic wavelength (Penttinen & Luukkala, 1976; Coulouvrat, 1993). A variety of closed form solutions have been developed for on-axis and focal plane field calculations for circular aperture radiators with uniform surface velocity distributions (Chen et al., 1993; Goldstein, 2006). More advanced methods are available as stand-alone simulation packages for 3-D field computation with flexibility to handle a variety of transducer geometries (Zeng & McGough, 2008; Treeby & Cox, 2010). Despite the sophistication of these codes, there are certain geometries that are not supported – most notably sectored transducers, the elements of which have weights or polarities which vary circumferentially.

In the interest of simulating the performance of a large number of candidate designs with a simple but flexible code, a variant of the discretized Rayleigh integral approach was employed for the prediction of ultrasonic fields radiated by transducers with axisymmetric geometries. Transducer apertures were represented in discretized form as segmented rings, with the segment angular and radial dimensions chosen to be no greater than one quarter of an ultrasonic wavelength. The field produced at the observation location *(x, y, z)* by the m^{th} source element geometrically centered at location *(x', y', z')* and driven at frequency *f* was found from:

$$p_m(x, y, z, f) = w_m \frac{e^{-ikR_m}}{R_m} \Delta S$$

where, w_m is a weighting factor, k is the acoustic wavenumber, R_m is the slant range between source element and observation point: $R_m = ((x' - x)^2 + (y' - y)^2 +$

$(z' - z)^2)^{1/2}$, and ΔS is the area of the ring segment: $\Delta S = \bar{r}\Delta\theta\Delta r$, where $\bar{r}$, $\Delta\theta$, Δr are the mean radius, angular span and radial thickness of the ring segment, respectively (Figure 2.1). If formally evaluating the Rayleigh integral, the weighting factor would include the absolute radiator normal velocity, which may be determined by piezoelectric properties and geometry of the transduction element under study. However, since only the field patterns were of primary interest, and not absolute levels, the weighting factor was typically only used to indicate relative velocity, including phase, of each radiating element. Propagation path attenuation (α) was accounted for by adding an imaginary component to the wavenumber: $k = k_0 - i\alpha$, where $k_0 = {}^{2\pi f}/_{c}$, and c is the real part of the sound speed. Values for attenuation were taken from the literature on soft tissue ultrasonic soft tissue properties.

The field $p_n(x, y, z, f)$ from all m elements in the n[th] ring was found from

$$p_n(x, y, z, f) = \sum_m p_m(x, y, z, f) = \Delta S \sum_m w_m \frac{e^{-ikR_m}}{R_m}$$

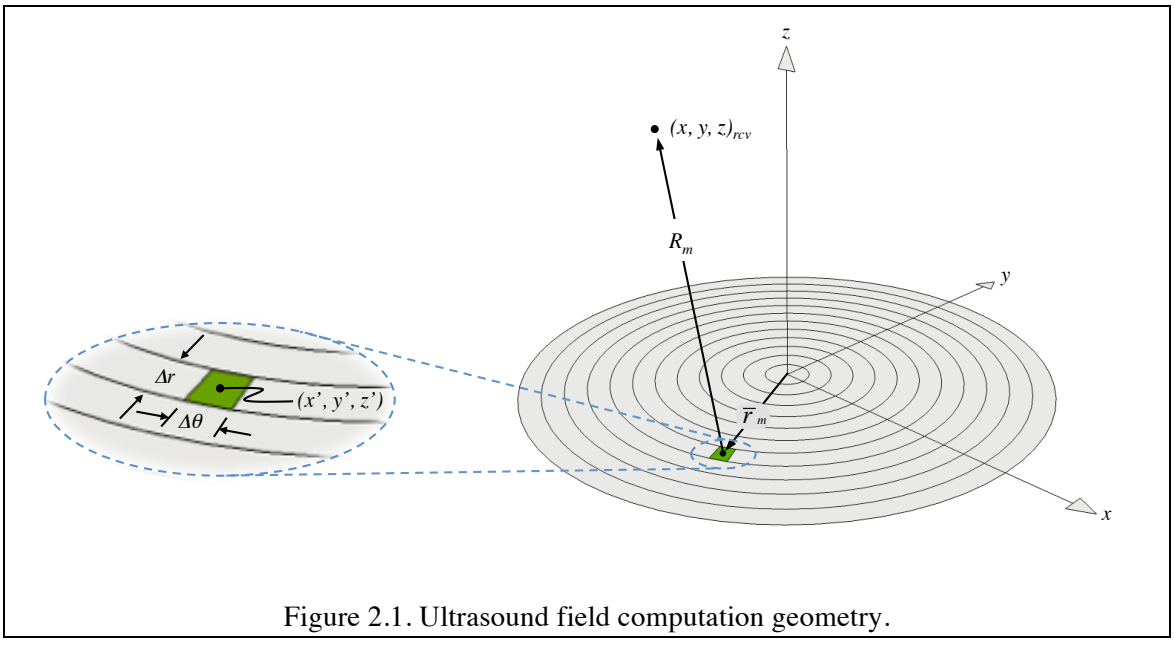

Figure 2.1. Ultrasound field computation geometry.

A typical code execution sequence was run upon defining:

- minimum and maximum ring radii;
- circumferential weighting functions, if any;
- drive frequencies; and
- the set of field observation points to be evaluated.

When run for a set of multiple ring radii, the compiled computations defined the emitted field from a finite aperture planar radiator. Simulation of a transducer with a fixed spherical radius of curvature (R_c) was carried out by applying a time lead to each ring of the form $\tau_n = \delta_n/c = R_c\left[\left(1+\left(\frac{\bar{r}_n}{R_c}\right)^2\right)^{1/2} - 1\right]/c$. One set of ring field calculations could then be used to examine a variety of geometric shapes by defining the desired radius of curvature, and a range of aperture effects by selecting which rings to sum ($n=a:b$) , as illustrated in Figure 2.2:

$$p_{total}(x,y,z,f) = \sum_{n=a}^{b} p_n\, e^{-i\omega\tau_n}$$

What this approach lacked in elegance it exponentially compounded through inefficiency of implementation in software - shortcomings that were nonetheless easily overcome with contemporary computing power, as predicted (McCall, 1994). The coarseness of the radial steps shown in Figure 2.2 was for clarity of illustration. The actual radial step sizes used in the simulations were quite fine – for example, 0.13 mm for calculations up to 2.5 MHz.

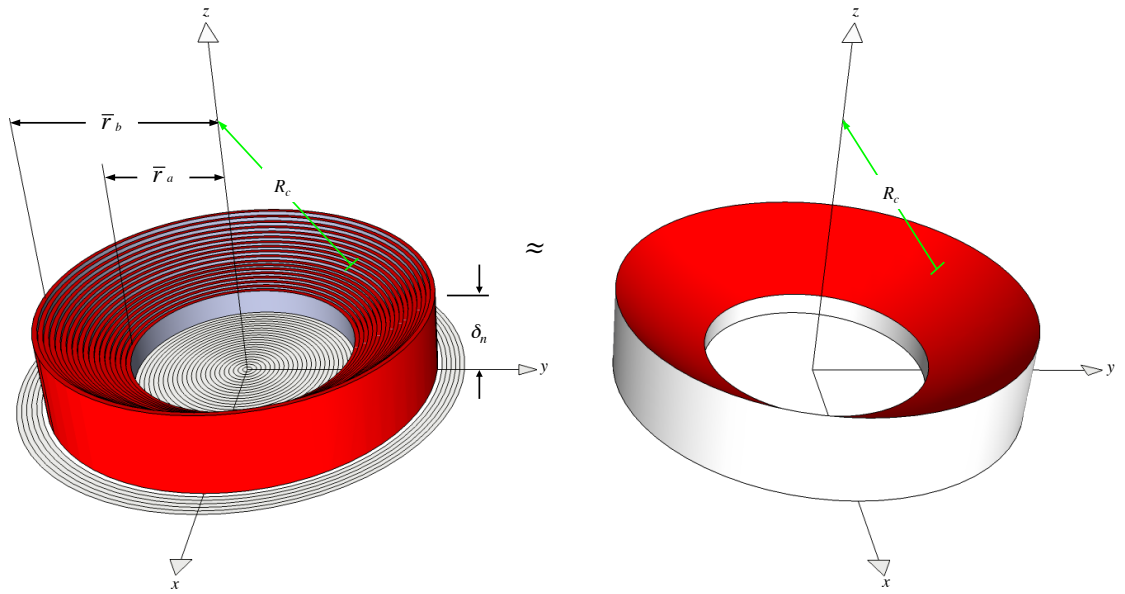

Figure 2.2. Illustration of ring array-based simulation of finite aperture focused transducer.

Example calculations are shown in Figure 2.3 for a spherical cap with a radius and radius of curvature of 25 and 140mm, respectively. The on-axis and focal plane lateral beam patterns show good agreement between the steered ring calculation and a closed form solution based on the Rayleigh integral (Chen et al., 1993). Discrepancies in the on-axis field in the pre-focal region are likely due to the coarseness of the radial step size, but this is of no consequence to the fields within +/-50mm of the focal length, which are most relevant to the present work. An example of the full radial-axial pattern for this transducer, as calculated with the steered ring method, is shown at the bottom of Figure 2.3. The ability to predict intensity variations near the focal plane will be important for design of both the force generation and vibrometer transducers.

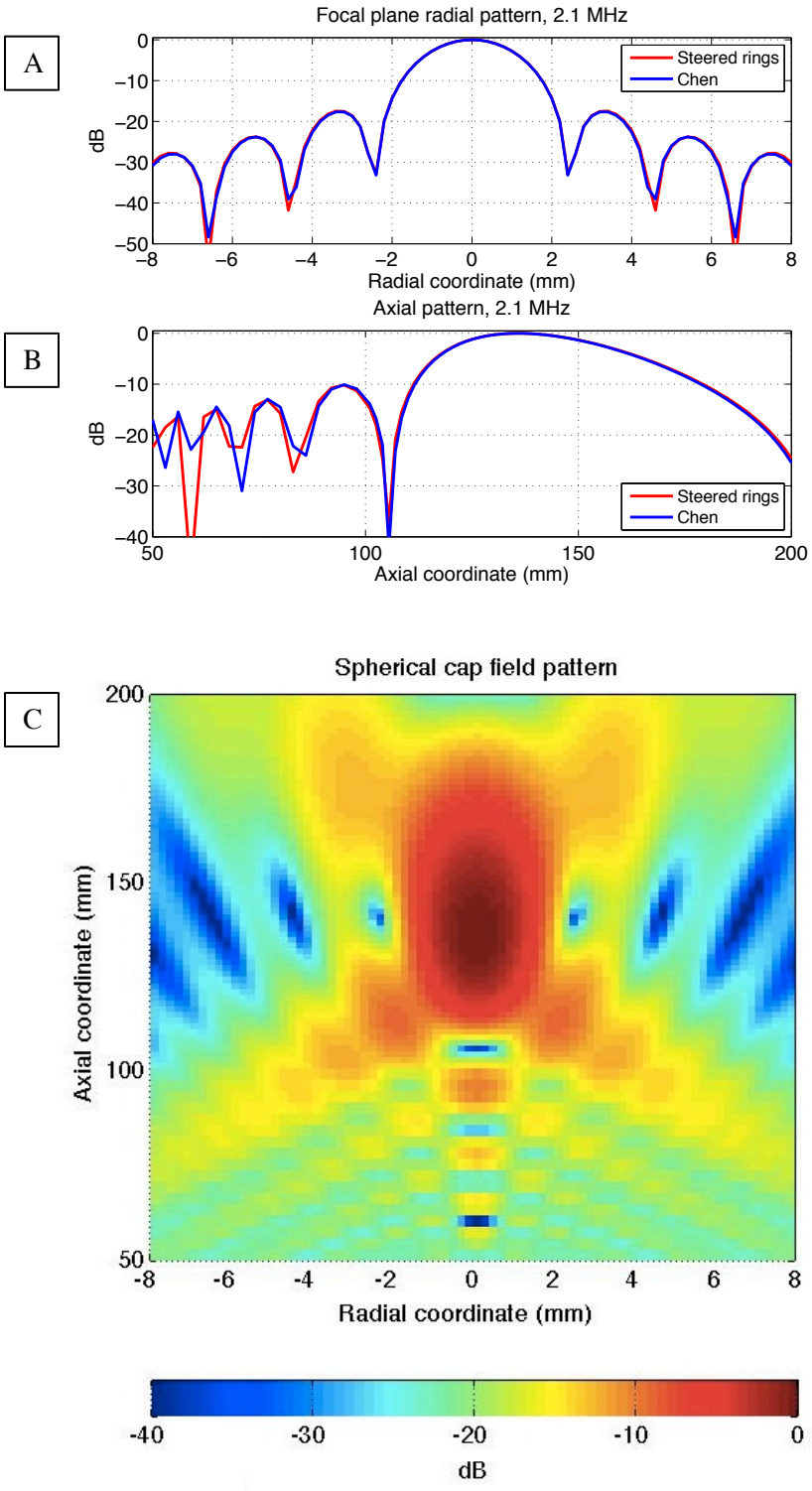

Figure 2.3. Beam pattern predictions for the (A) focal plane radial, (B) axial, and (C) radial-axial full fields of a spherical cap radiator at 2.1MHz.

2.3 Forced Motion Simulation

The preceding ultrasonic field predictions were intended for use with a viscoelastic response model to predict how candidate transducer designs would create and detect motion in tissue-like materials. The prediction framework was as follows:

1) Calculate the ultrasonic intensity distribution $I_F(x,y,z)$ for a candidate force generation transducer design;

2) Calculate the Langevin radiation force acting at each grid point from $dF = 2\alpha I_F(x,y,z)/c \bullet dV$, where dV is the volume of a grid element;

3) Determine the displacement field $H(x_d,y_d,z_d \mid x,y,z)$ due to a point force acting on a viscoelastic solid ;

4) Determine the total axial displacement field $u(x_d,y_d,z_d)$, created by the absorbed ultrasound by integrating the product of the force and forced-response functions over the grid: $u(x_d, y_d, z_d) = \int_V HdF$;

Displacements were predicted using an analytical solution for an axially directed point force F_z acting within an infinite solid (Rahman, 1995) subject to the axisymmetric equations of motion:

$$\mu(\nabla^2 u_r - r^{-2}u_r) + (\lambda + \mu)\partial_r e = \rho\partial_t^2 u_r$$

$$\mu\nabla^2 u_z + (\lambda + \mu)\partial_z e + F_z = \rho\partial_t^2 u_z$$

where λ and μ are the *Lamé* constants, ρ is density, u_r and u_z are the displacements in the radial and axial directions, $e = r^{-1}\partial_r(ru_r) + \partial_z u_z$, and $\partial_r, \partial_z, \partial_t$ indicate radial, axial and temporal partial derivatives. As with ultrasonic field predictions, alternatives

for displacement prediction were available in several forms, but the chosen approach allowed for flexible implementation in software and rapid incorporation into the overall simulation code. While both axial and radial displacement components are available in the analysis, the axial component was of primary interest, since the induced motion should be strongest along the forcing beam propagation axis, and ultrasonic vibrometers are only capable of detecting motion along their beam propagation axes. Multiple vibrometers inclined relative to the forcing axis could be used to resolve both in-plane and axial (out-of-plane) displacements, but there was no perceived benefit to offset the increased complexity of doing so in the present work.

Validation of the analytical solution[*] implementation was performed through comparison with an axisymmetric point force response computation in COMSOL, a commercially available finite element package[†]. Sample results obtained from both solution approaches are shown in Figure 2.4 at a force modulation frequency of 800 Hz, for a material having a bulk modulus $K = 2.3(1+0.01i)$ GPa, shear modulus $G = 1.6(1+0.20i)$ kPa, and density $\rho = 1000$ kg/m^3. The analytical solutions are singular (not valid for estimation of motion at the force location) - a problem circumvented by interleaving the evaluation grids for force application and displacement observation. The phase response plot in the right of Figure 2.4 includes a linear phase formed by the product of shear wavenumber and radial distance from the force ($k_s r$), representative of the shear "far field" when $k_s r >> 1$ (Graff, 1991). Both models converged to this

[*] One could equally argue that this process served to validate the finite element model.
[†] COMSOL Multiphysics, Burlington, MA. Models for this study were developed by Van Biesel, Georgia Institute of Technology.

condition at approximately r = 5mm ($k_s r \sim 2\pi$). Agreement between the two methods is very good in both magnitude and phase except within 0.1 mm ($k_s r$ <<1) of the force application point. This was of little consequence for the methods in the present study, since the force application and motion measurement regions would not be co-located.

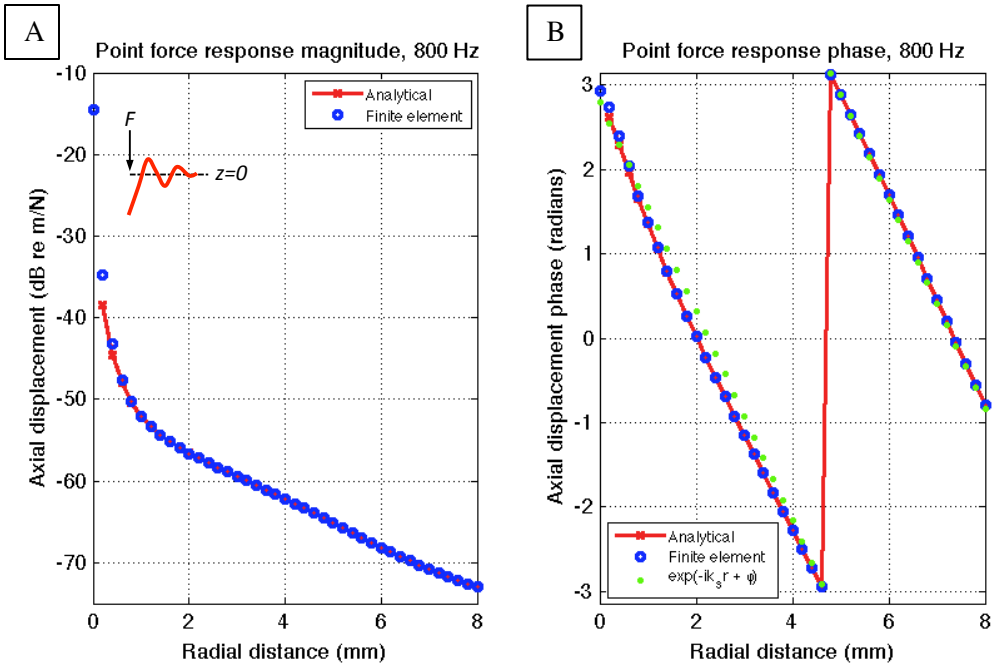

Figure 2.4. Predicted magnitude (A) and phase (B) of axial displacements in the drive plane for an axial point force applied at the origin.

An example of the cumulative process of combining ultrasonic and shear response functions to predict axial shear displacements is shown in Figure 2.5. The ultrasonic field illustrated in Figure 2.3C was used to specify a forcing field, with the absorption taken to be α = 0.115 np/cm (equivalent to 1 dB/cm). To estimate axial displacements in the ultrasound transducer's focal plane, the forcing field was convolved with point force model transfer function data calculated for a material with the same properties as used to

generate the results shown in Figure 2.4. The displacement magnitude scaling assumed a continuous (non-pulsed) incident ultrasonic pressure amplitude defined by diagnostic safety limits (US Dept. of Health and Human Services, 2008).

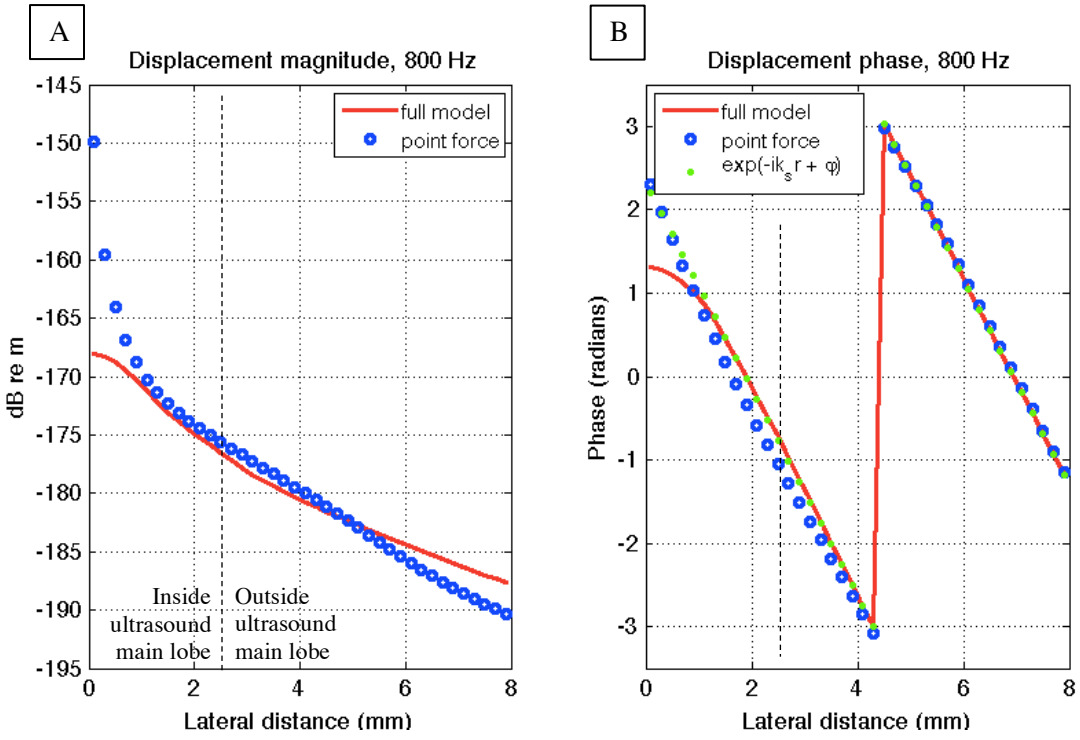

Figure 2.5. Calculated ultrasound-generated displacement magnitude (A) and phase (B) in the ultrasound transducer focal plane.

In Figure 2.5, full model results are compared with the result for a single point force at the focal plane origin (Figure 2.4). The single point force magnitudes were scaled to the full model value at r = 5mm for convenience of display. The full field results show a suppressed response peak near the origin as a consequence of finite extent of the ultrasonic intensity / forcing field. The ultrasonic field extent creates a distributed force that acts as a low pass (spatial smoothing) wavenumber filter. The full field phase response converges to the "shear far field" result, but deviates significantly for $r < 2.2$

mm, within the main lobe of the ultrasonic field. This result illustrates one of the reasons that motion measurements in the forcing region are not useful for elastography analysis. Despite the induced displacement being a maximum, the response phase is not indicative of a propagating shear wave.

When pulsed, rather than continuous ultrasound signals are used, it is of interest to observe the time domain displacement of the viscoelastic material. The process for finding this response was as follows:

1) Define an ultrasonic pressure signal $s(t)$ with non-zero transmission duration T_{pulse} and total duration T_s;

2) Form the signal intensity spectrum $I(f) = FFT(s(t)^2)/\rho c$, retaining only the frequency components < $1/T_{pulse}$;

3) Calculate the steady state response of the forced solid at modulation frequencies $f_L = 0: 1/T_s: 1/T_{pulse}$, and form a Hermetian-symmetric response spectrum $H(f)$;

4) Determine the time domain displacement at each location (x_d,y_d,z_d): $u(t) = real(IFFT(I(f) H(f)));$

An example calculation is shown in Figure 2.6 using the ultrasonic and solid forced response data described earlier. The ultrasonic drive pulse for this example consisted of a 500 μs transmission within a window of 20 ms total duration. Focal plane displacements are shown at distances of 2 and 4 mm from the beam axis, along with a scaled version of the drive pulse. The convention in this calculation is that displacement directed away from the driving ultrasonic transducer is negative. The signals are

displayed for a single response cycle. The results were calculated without a DC component (equivalent to the vibrometer processing described in Chapter 5), resulting responses biased relative to zero displacement.

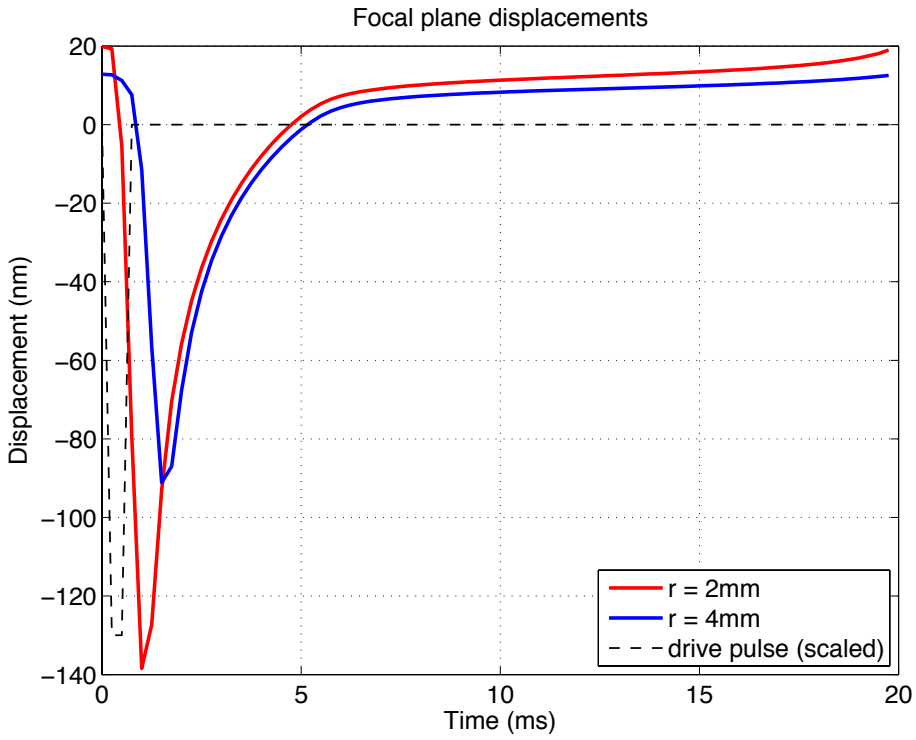

Figure 2.6. Time domain focal plane displacements 2 and 4mm from the ultrasonic beam axis.

The waveforms calculated at two distances from the force application point show response delays corresponding to the respective shear wave propagation times ($t=r/c_s$). Upon arrival at an observation point, wave displacements initially increase rapidly, with rise times that are associated with both the material properties and rise time of the drive pulse intensity. The force exerted by an ultrasonic beam has the same vector orientation as the beam intensity, so its effect is that of a pure "push" in the direction of ultrasound

propagation, and the force terminates when the ultrasound signal ends. After the drive pulse ends, the recovery phase of the material's displacement response is purely indicative of the shear properties of the material. Recovery duration increases in materials with lower shear elasticity and/or higher shear loss. The time between signal peaks at 2 and 4 mm is approximately 0.5 ms, corresponding to the expected delay time at the shear speed of 4 m/s. This example illustrates how relative signal delay (or phase) can be used to estimate shear speed.

2.4 Temperature Elevation Simulation

Thermal exposure estimates were developed in a manner similar to that which was used for tissue displacement calculations, with the objective of evaluating temperature elevations for planned ultrasonic exposures (pulse durations, rates, and amplitudes) relative to thermal safety regulations (US Dept. of Health and Human Services, 2008). The framework for making these predictions was as follows:

1) Calculate the ultrasonic intensity distribution $I_F(x,y,z)$ for a candidate force generation transducer design;

2) Calculate the rate of heat generation at each grid point, associated with the ultrasonic intensity distribution;

3) Determine the temperature field $N(x',y',z' \mid x,y,z)$ due to a point heat source in a homogeneous material;

4) Determine the total temperature field created by the absorbed ultrasound by integrating over all heat sources: $T(x', y', z') = \int_V NdV$;

As it was with the generation of force with ultrasound, the thermal source term is also intensity-driven. The rate of heat generation per unit volume resulting from absorption of ultrasound is $q_v = 2\alpha I$ (NCRP, 1992)[‡]. While this expression is equal in magnitude to the numerator of the Langevin force per unit volume (Section 2.3), ultrasonic heat generation is not a vector quantity, and the emitted thermal field from an individual source is spatially uniform in a homogenous environment.

The field equation describing biological tissue temperature change produced by a heat source is referred to as the bio-heat transfer equation (Pennes, 1948):

$$\dot{T} = \kappa \nabla^2 T - \frac{T}{\tau} + \frac{q_v}{c_v}$$

where T is the temperature rise above ambient, κ is the thermal diffusivity, τ is the perfusion time, and c_v is the tissue specific heat at constant volume. The solution forms vary depending on assumptions made about the relative importance of the conduction (first term on the right) and perfusion (transport via blood flow, second term on the right) heat transfer mechanisms. For the present study, an upper bound for ultrasound-induced heating can be found by neglecting perfusion effects. This approach is at times a necessity when perfusion rates for various marine mammal tissues are not known.

Solutions for the bio-heat transfer equation have been developed for the case of a point heat source (Nyborg, 1988). Total temperature rise can be estimated using these solutions by summing the contributions at each observation point from the grid of ultrasound-generated heat sources. Examples of ultrasound-generated temperature rise

[‡] Although q_v is a heat generation rate, the convention for this source term in the literature is to omit the "over-dot" notation indicating a time derivative.

calculations are shown in Figure 2.7 using the intensity pattern data displayed in Figure 2.3c, applied to a homogeneous solid with thermal properties of human brain tissue (NCRP, 1992). The incident intensities were scaled after assuming a continuous (non-pulsed) incident ultrasonic pressure amplitude defined by diagnostic safety limits (US Dept. of Health and Human Services, 2008). Temperature elevations are shown in the transducer focal plane for exposure times of 1, 10 and 100 seconds.

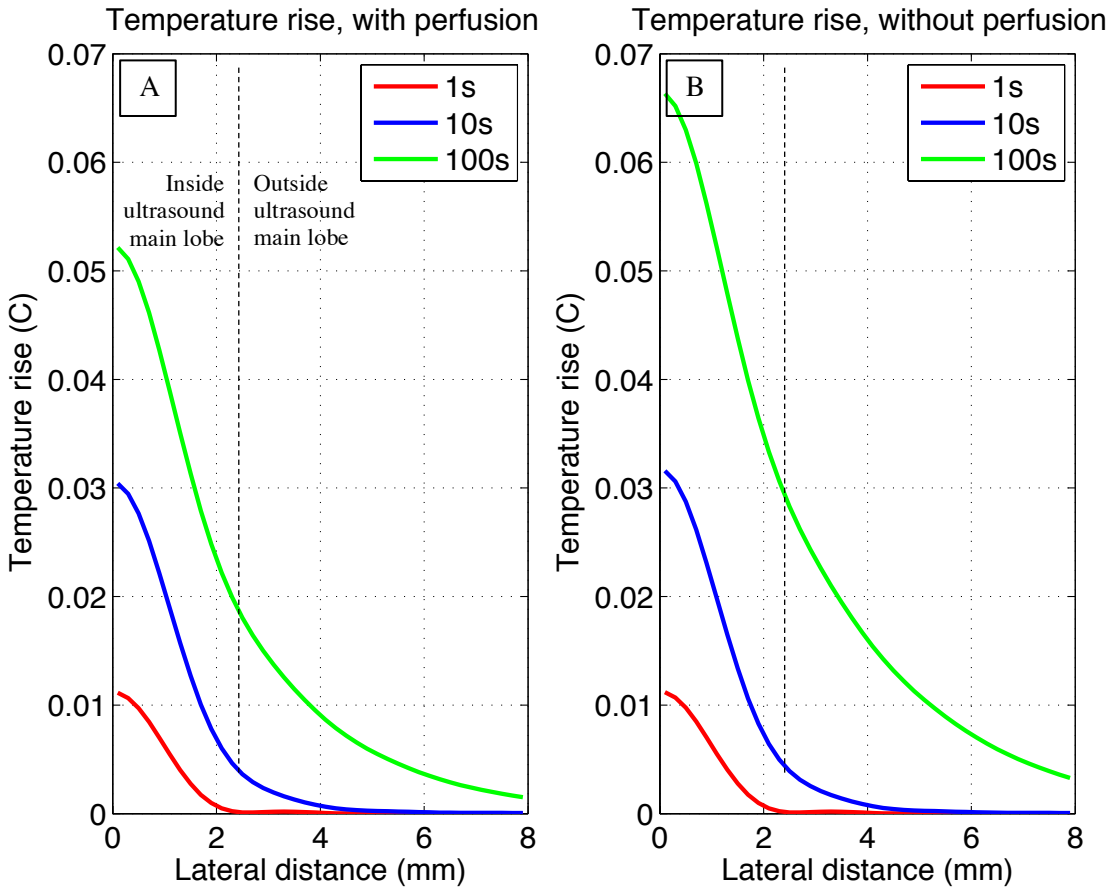

Figure 2.7. Calculated ultrasound-generated temperature elevations in the focal plane of a spherical cap transducer, using human brain tissue thermal properties including (A) and excluding (B) perfusion effects.

The field shapes resemble smoothed versions of the ultrasonic intensity. At short exposure times, a local temperature elevation is visible near r = 3.5mm, corresponding to a beam sidelobe. At longer exposure times, such local effects are overtaken by heat diffusion out of the main lobe region. The effect of perfusion for this particular set of tissues is seen to be minor. For the longest exposure time evaluated, the maximum temperature elevation was less than one-tenth of a degree – small with respect to the 6 °C safety threshold. This finding is generally consistent with other studies done in support of ultrasonic elastography systems (Palmeri & Nightingale, 2004), and has been used to justify significantly elevated incident intensities relative to those limited by intensity alone.

2.5 Simulation Summary

Methods were developed for simulating the ultrasonic fields produced by candidate transducer configurations, and for subsequent prediction of ultrasonically generated mechanical wave motion and thermal fields in absorbing solids. The field simulation capabilities described in this chapter were next used to numerically evaluate CFE prototype system designs.

CHAPTER 3

TRANSDUCER DESIGN

3.1 Force Generation Transducer Design Goals and Constraints

The development of a proof-of-concept CFE prototype was guided by the objective to operate at tissue depths of at least 12 cm, permitting measurements to be made mid-brain (mid-sagittal at the ventricles) in an adult bottlenose dolphin[§], as illustrated in Figure 3.1. The depth goal was subject to the primary constraint to minimize the cost and complexity of system instrumentation for the force generation (FT) and vibrometer (VT) transducers.

The measurement depth goal was used to determine the optimal operating frequency range for ultrasound-based force generation by calculating the amplitude of force per unit volume that could be created when the pressure amplitude was set to the Mechanical Index ultrasound exposure safety limit ($p_{MI,0.3}$):

$$F_v = \frac{2\alpha}{\rho c^2} p_{MI,0.3}^2 e^{-2(\alpha-\alpha_{0.3})z}$$

with $p_{MI,0.3} = 1.9\sqrt{f}$ (MPa/MHz), α is the actual attenuation in the tissue, $\alpha_{0.3}$ is the presumed for the Mechanical Index computation (0.3 dB/cm/MHz), and z is the axial path length (cm).

[§] The supporting grant for this research included provision for testing on bottlenose dolphins within the Navy's marine mammal program.

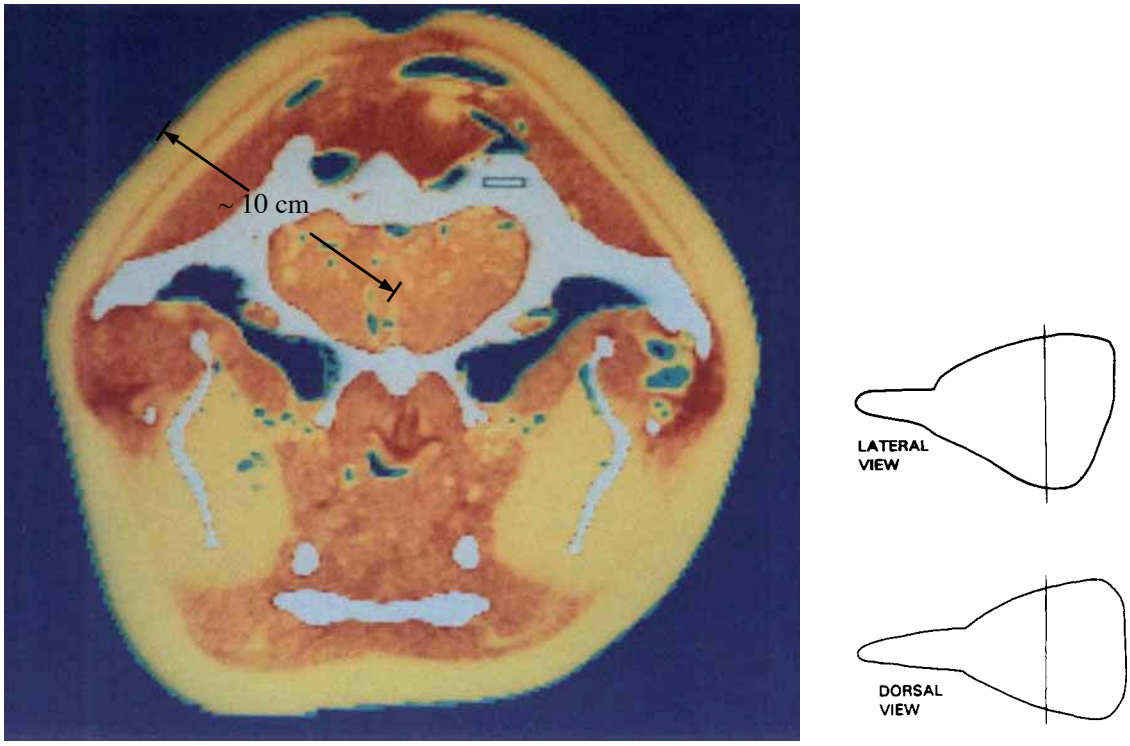

Images from Cranford, Amundin & Norris (1996), Copyright 1996 Wiley-Liss Inc.

Figure 3.1. Transverse CT image of the head of a bottlenose dolphin, with depth scale.

Figure 3.2 shows force calculations presuming a soft tissue attenuation of 0.115 np/cm, evaluated at tissue depths of 3, 6 and 12 cm. All values were normalized to the maximum for 3 cm depth. The results show dramatic losses in force generation when using high frequencies at large depths – for example, 50 dB force loss with a 4 MHz drive signal used at 12 cm instead of 3 cm. For a depth of 12 cm, the optimum frequency is approximately 1 MHz, with no more than a 1 dB penalty between 0.7 and 1.4 MHz. There is also a significant net loss of force generation capability (equating to a reduction in achievable displacement amplitude) relative to what is achievable at shallower depths with higher frequencies. Offsetting this loss with a distributed forcing beam was one of the goals of the CFE concept development.

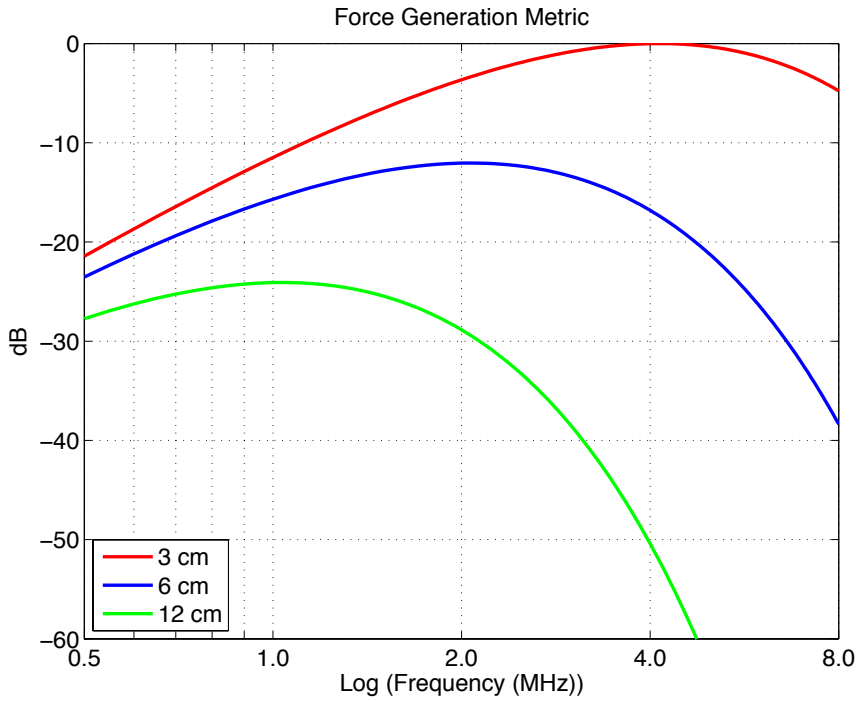

Figure 3.2. Normalized force generation levels for Mechanical Index limited incident beams.

An additional constraint on FT design arose through consideration of ultrasonic beamwidth relative to a shear wavelength in materials of interest. The effect of beamwidth on force generation was simulated by calculating the shear displacement (u_w) produced by a circular beam with radial Gaussian weighting (W):

$$u_w = \iint_{x,y} \frac{e^{-ik_s r}}{\sqrt{k_s r}} W^2 dA$$

where $k_s$is the shear wavenumber, r is the distance from a point in the beam to the observation point $(x_0,0)$, and the form $(\frac{e^{-ik_s r}}{\sqrt{k_s r}})$ is the displacement of a shear wave in the direction parallel to the applied point force, as illustrated in Figure 3.3.

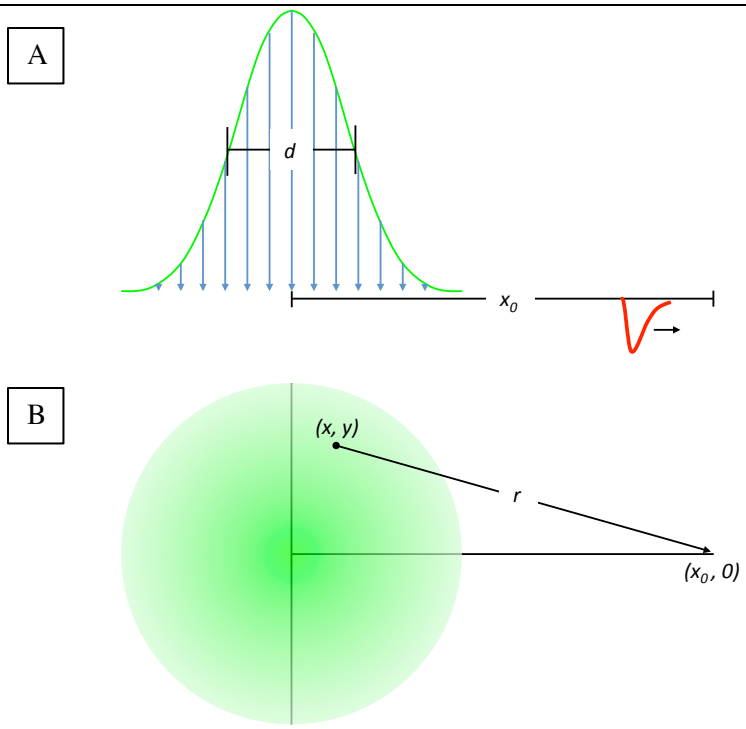

Figure 3.3. Illustration of beam width impact calculation geometry. (A) Gaussian beam profile as a weighting factor for force amplitude (blue arrows). (B) Beam cross-section and problem geometry in the x-y plane.

Figure 3.4 shows example results for 1, 2 and 4mm full width, quarter power forcing beamwidths (*d*). A shear speed of 1.6 m/s, corresponding to *in vivo* human brain tissues (Green, Bilston, & and Sinkus, 2008), was used in these calculations. This shear speed is the lowest *in vivo* value found in the literature, and is intended to give a conservative estimate of beam integration effects. The upper two plots show displacements in a material with a purely real-valued shear modulus, while the lower plots employ a shear modulus with a loss tangent of 0.5. The left side plot curves were normalized by the result obtained with a 0.5 mm beam, which gave a frequency-independent result for the analysis band shown.

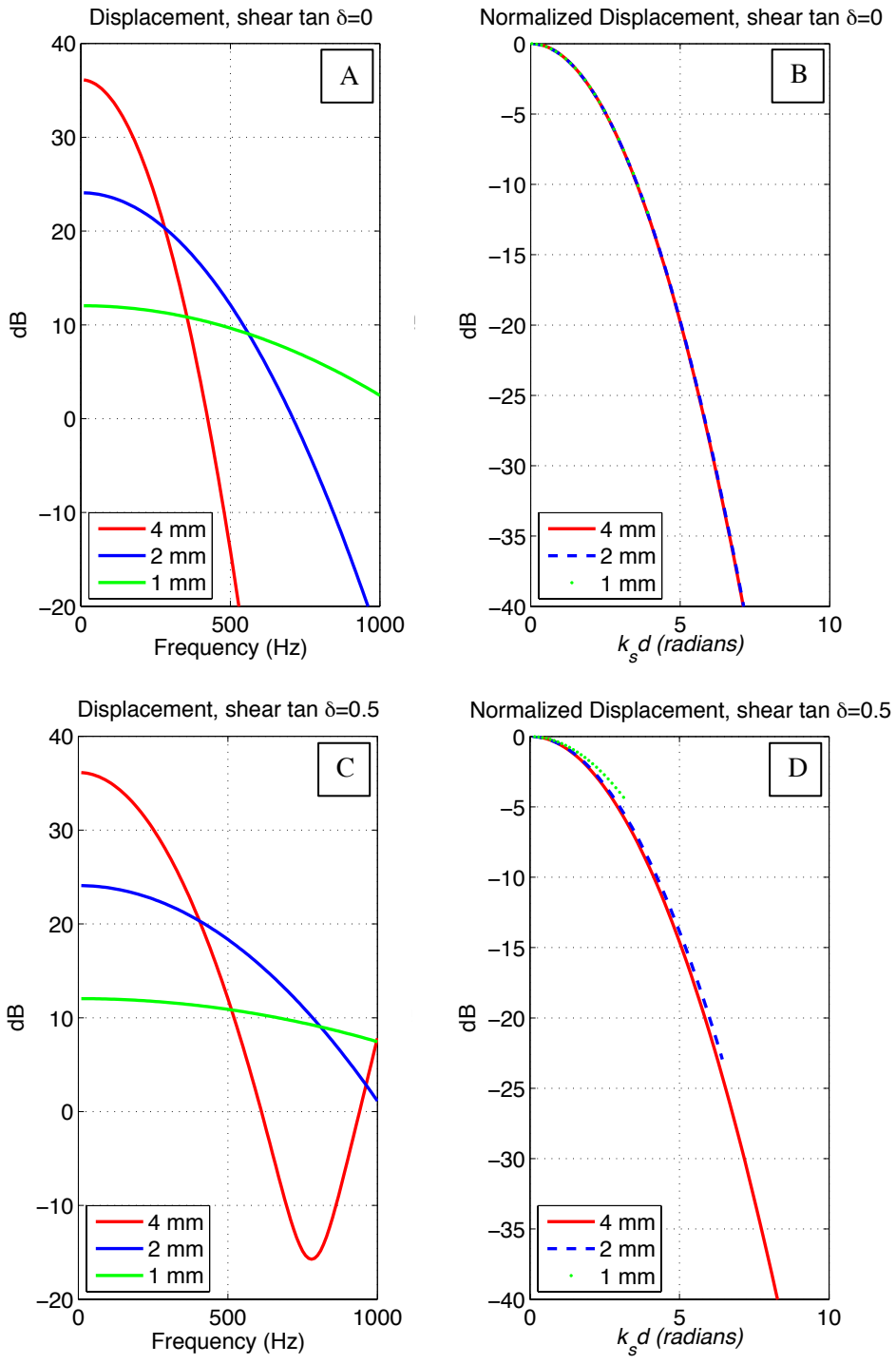

Figure 3.4. Simulated impact of forcing beam width on displacement generation. (A) Displacements in a lossless material, (B) Normalized lossless data plotted in terms of the beam size relative to shear wavenumber. (C) Displacement in a material with a loss tangent of 0.5, and corresponding normalized response (D).

As seen in the upper left plot in Figure 3.4, the expansion of the forcing beam preferentially enhances generation of low frequency displacement, the maximum of which scales directly with beam area – 12 dB per doubling of beamwidth. When these curves are amplitude-normalized and re-plotted in terms of the wavenumber-beamwidth product (upper right), all curves collapse to a single low pass filter function. When the beam diameter is equal to a shear wavelength ($k_s d = 2\pi$), the level is approximately -30 dB. The value is not zero because of how d is defined in this calculation (quarter power width, not full width), and because the Gaussian beam shading has the effect of reducing the effective beam diameter.

In the lower row of plots, the addition of shear loss widens the bandwidth of filter curves. This is because the attenuation essentially narrows the beam by deemphasizing the contributions from the parts of the beam furthest from the observation point. Still, there is a clear signal level advantage to expanded beamwidth. From these results, a full width, quarter power beam of 2 mm appears to represent an acceptable tradeoff between low frequency signal gain and high frequency rolloff. For reference, the forcing beam widths implemented in many 2D array-based elastography systems one millimeter or less (Nightingale, Soo, Nightingale, & Trahey, 2002), although good performance has been obtained with broad, unfocused beams (Zhao et al., 2012).

3.2 Candidate Force Generation Concepts

Four candidate FT design concepts were considered for the CFE prototype, as illustrated in Figure 3.5 and described below. All concepts were evaluated under the

assumption that the radiating faces could be built using conventional piezoelectric materials and manufacturing techniques.

Radially Phased Ring Array. A variety of beamforming approaches could be used form a ring or ring-like field using a two-dimensional phased array. Preliminary estimates indicated that an array of thin concentric ring elements (such as those illustrated in Chapter 2, Figure 2.1) could produce the desired field when driven with appropriate weighting functions, but the number of elements needed to provide the required focusing without production of unwanted grating lobes was on the order of 100, assuming a 1MHz operating frequency. Such an approach was well within the capability of commercially available electronic drive systems, but was well beyond the resources available for the proof of concept study.

Confocal Ring Transducer. In this considerably simpler approach, a spherically focused transducer was envisioned, consisting of a pair of coaxial ring elements. The elements would both produce a focus at a desired tissue depth, while the beams from each element would have slightly different lateral widths. Subtraction of one beam from the other could produce a ring-like pressure field. While the simplicity of this approach was attractive, there were concerns over lateral sidelobes (multiple, large amplitude), which would greatly complicate analysis of the shear field produced by ultrasound emitted from this type of transducer.

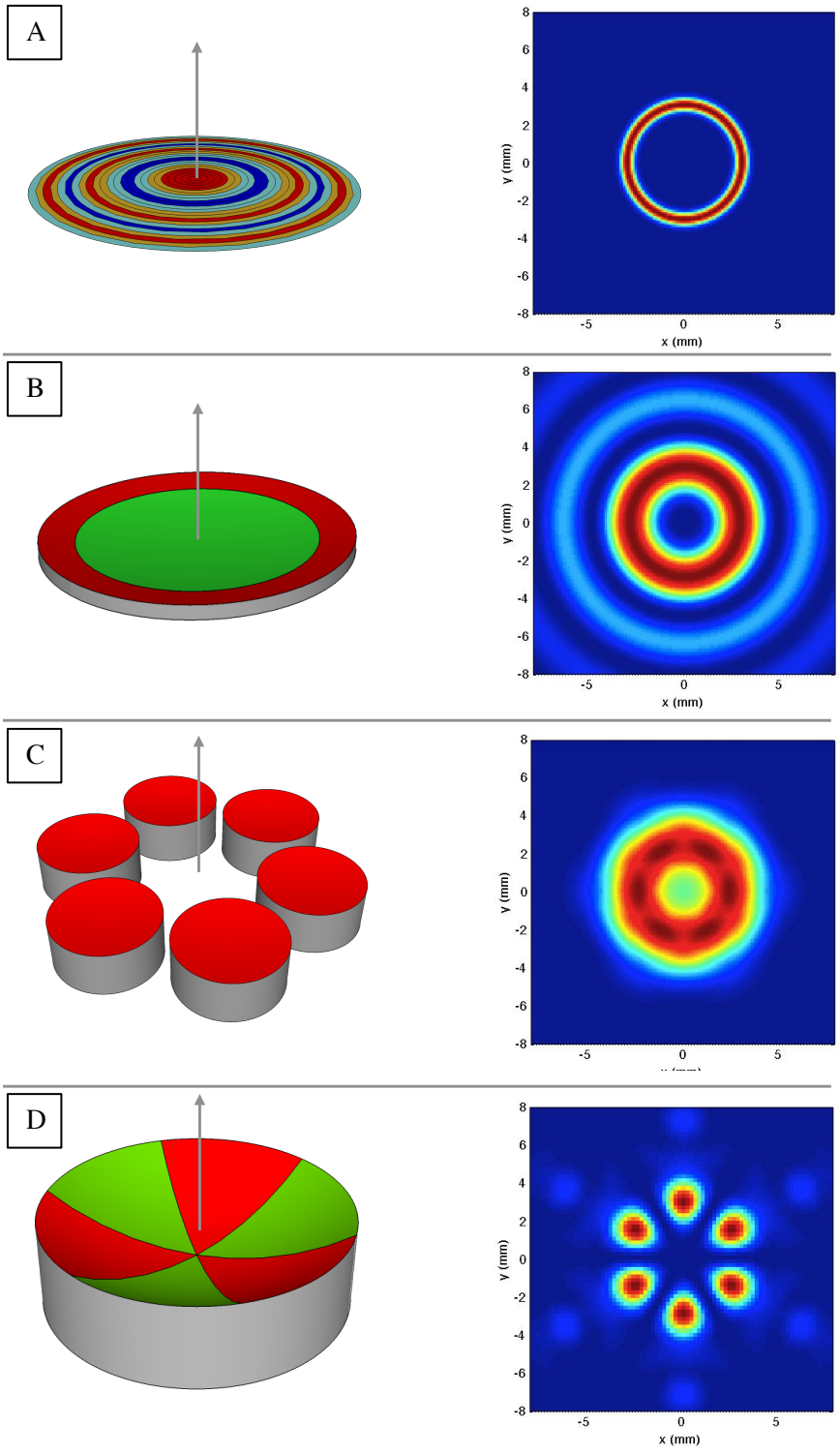

Figure 3.5. Candidate transducer configurations (left column) and example focal plane intensities (right column): (A) Radially phased ring array, (B) Fixed focus confocal rings, (C) Fixed focus transducer group, (D) Fixed focus sectored transducer.

Fixed Focus Transducer Group. This approach formed a ring-like field through arrangement of several fixed-focus transducers, each of which formed a conventional beam with a unique location in the focal plane. The primary drawback with this approach was in the difficulty of radial dilation of the forcing pattern – a high-precision mechanical actuator would be required to control the lateral position and/or tilt angle of each transducer.

Fixed Focus Sectored Transducer. This approach employed a spherically focused transducer whose surface was subdivided circumferentially into an even number of equal area sectors. Driving the sectors with alternating polarity produces a focal plane field with all beam lobes lying on a common radius, the size of which could be controlled by varying the number of alternate-polarity drive sectors (Fjield & Hynynen, 1997). This was a well-known property of sectored transducers (Umemura & Cain, 1989), but their application in the present work for force generation in an elastography scheme was novel. The fixed focus sectored transducer required fairly simple drive instrumentation (as few as two channels), while seemingly allowing simple control of focal plane beam radius. This approach was chosen for further analysis.

3.3 Sectored Force Generation Transducer Design

The ultrasonic field simulation code described in Chapter 2 was exercised in order to better understand the parameters that control sectored transducer behavior. In order to represent the alternating drive polarity of a sectored design, the simulation ring elements were given circumferential polarity weights $w_\theta = sign(sin(M\theta))$, where m is the mode number (0, 1, 2, …), $2M$ is the number of transducer sectors, and θ is circumferential

angle around the transducer (0 : 2π). For example, a design with *M=3* would have six sectors with an angular width of 60 degrees, as illustrated in Figure 3.5D. A distinction is drawn here between the "mode number" terminology and a single circumferential mode, as is common in structural analysis. A transducer that abruptly changes polarity from sector to sector, as investigated here, has a surface velocity distribution containing several modes for a specified single value of "M", in the same way that the spectrum of a square wave contains harmonics of its fundamental period.

FT design parameters that were varied for this study are listed below and illustrated in Figure 3.6:

- *M:* mode number
- f_c: drive frequency
- a_o: outer radius;
- a_i: inner radius; and
- R_c: radius of curvature;

The inclusion of an inner radius parameter allows for an annular FT geometry that can accommodate nested placement of a vibrometer transducer for shear wave motion measurement (Chapter 4). Although the target depth of operation was fixed at 12 cm, the R_c was allowed to vary as compensation for the transducer's curvature, which had the effect of recessing the radiator farther away from the target depth. The propagation medium was given a sound speed (c) of 1500 m/s and an attenuation of 1 dB/cm/MHz.

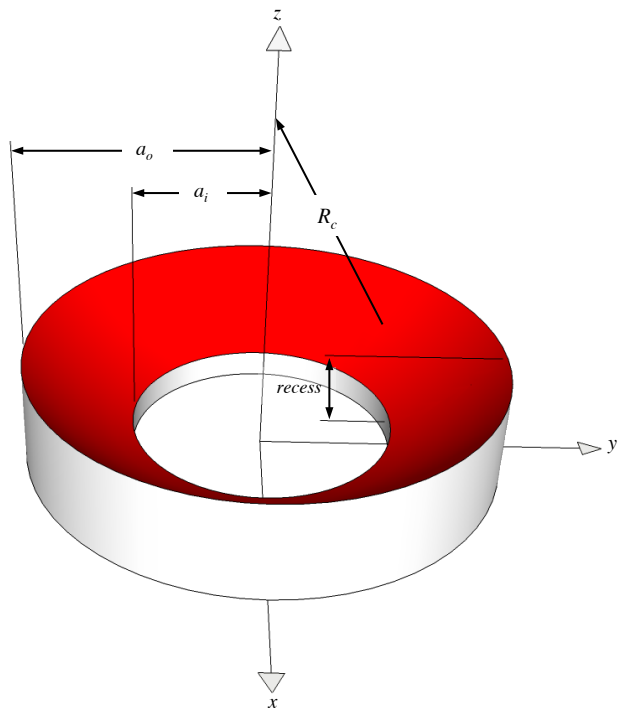

Figure 3.6. Annular sectored array transducer geometry.

Figure 3.7 shows how drive mode (M = 3, 4, 6) and frequency (f = 700, 800, 900 kHz) influence the intensity patterns of a radiator with a_i = 0 and a_o = 76mm. Intensities are shown as -3dB focal plane contours for clarity of primary lobe visualization. In 3.6A, the number of lobes and their radius (from the origin) are seen to both increase with M. In 3.6B, an increase in frequency for fixed mode, aperture and radius of curvature reduces the radius of the lobe pattern. These trends are captured by the expression for axial wavenumber $k_z = \sqrt{k_0^2 - k_{surf}^2}$, where k_0 is the fluid wavenumber (ω/c), $k_{surf} = \sqrt{k_r^2 + k_\theta^2}$, and k_r, k_θ are the radial and circumferential wavenumbers on the transducer surface, respectively.

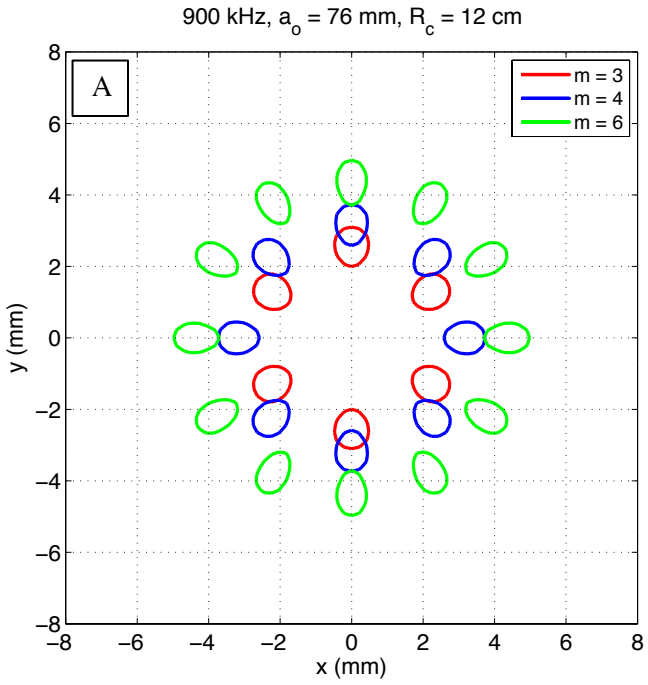

Figure 3.7. Focal plane -3dB intensity contours illustrating ultrasonic field relationship to mode number (A) and frequency (B).

The wavenumbers k_r and k_θ are distributions, not single values, but for first order assessment of radiation behavior, the smallest (non-trivial) radial and circumferential wavenumbers are approximated as $k_r \sim \pi/a_{cent}$ and $k_\theta \sim M/a_{cent}$, respectively, where a_{cent} is the radius to the lateral centroid of the radiating area. For typical values in these simulations, a_{cent} was approximately 60mm, f = 900kHz, k_0 ~3800 rad/m, and k_{surf} ~ 140, and therefore $k_z \sim k_0$. The radiated lobe pattern radius in the focal plane was then estimated from $r_{est} = R_c\ atan(k_{surf}/k_0)$. From this relation, it is seen that an increase in surface wavenumber (as with increasing M), or a decrease in acoustic wavenumber (with decreasing frequency), both increase the lobe pattern radius. This matches the trend in Figure 3.7.

The fact that both frequency and mode number can be used for lobe radius control provides flexibility in designing for the elastography application. As a practical matter, real time modal control would require more complex driving electronics than would frequency control. For example, switching from M=3 to M=6 would require driving twelve sectors individually or having a switch box designed for high frequency power handling. By contrast, for a fixed M, frequency control of the lobe pattern radius could be accomplished with as few as two drive lines (one for each drive polarity), with frequency changed through software control. So, while modal control would provide a greater range of pattern radii, frequency control appeared to be much simpler to implement for the prototype. Transducer bandwidth and mode number therefore would determine the possible range of lobe pattern radii.

Figure 3.8 shows how the focal plane and radial-vertical plane fields are impacted when the inner transducer radius is increased, while fixing the outer radius (76 mm), frequency (800kHz) and mode number (3). An increase in the inner radius increases the lateral centroid of the radiator, decreasing the surface wavenumber and lobe pattern radius. The effect is relatively weak for the 0-to-38mm inner radius step because the innermost portion of the surface has a very small contribution to the radiating surface area. The impact of the step to an inner radius of 57mm is more pronounced, particularly in the radial-vertical pattern. Here, the inner radius change removed half the radiating arc length and nearly half the radiating area, weakening the ability of the aperture to concentrate energy in the axial direction.

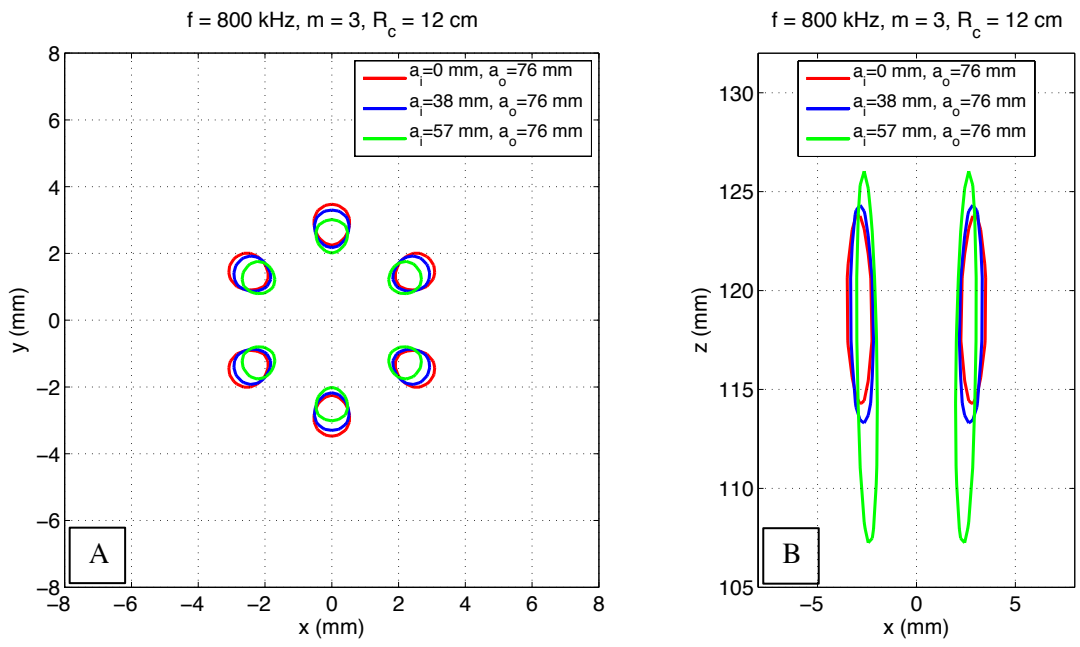

Figure 3.8. Focal plane -3dB intensity contours illustrating focal plane (A) and radial-vertical plane (B) ultrasonic field relationship to inner radius.

In principle, a longer axial focal region could be useful for the elastography problem, especially in a fixed focus prototype design, because it would allow interrogation of a greater range of tissue depths without having to axially translate the transducer. A concern with using aperture reduction to increase focal volume was that the transducer drive voltages would have to be elevated in order to offset the loss of radiating area. This was relevant both to transducer and power amplifier specification: the former in terms of piezoelectric element damage risk when used at higher drive powers, and the latter in terms of cost of higher capacity amplifiers.

Figure 3.9 shows the focal and radial-axial plane fields for varying radii of curvature, for fixed frequency (800 kHz), mode number (3), and aperture ($a_i = 0$, $a_o =$ 76mm). An increased radius of curvature slightly "flattens" the transducer, so that it focuses less tightly and exhibits a dilated focal volume. The interest in larger radius of curvature was motivated by the interest in setting the focal plane of the transducer 12cm or more into tissue. For a transducer with a_o = 76mm and R_c = 120mm, the center of the transducer was recessed by 27 mm relative to the leading edge of the transducer, which would be pressed to the test subject (e.g. skin surface). This placed the transducer's focal plane only 93mm into the tissue. It was found that values of a_o = 73mm and R_c = 140mm would meet the in-situ focal plane depth goal of 12 cm.

Selection of the inner transducer radius – the last major geometric constraint for the force generation transducer – required knowledge of the design for the nested vibrometer transducer. This subject is discussed in the next section.

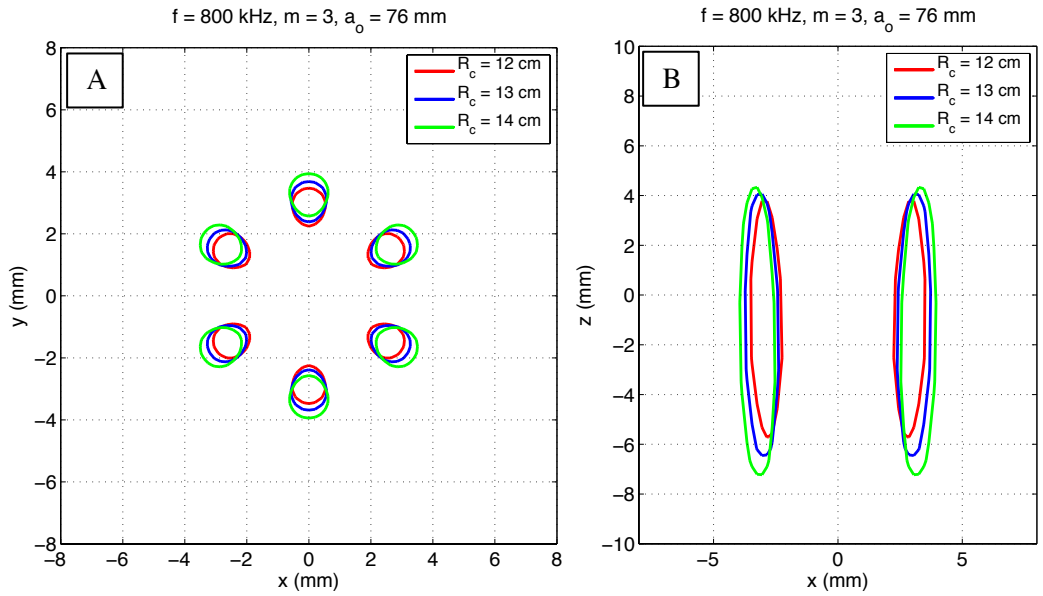

Figure 3.9. Focal plane (A) and radial-axial plane (B) intensity contours showing the impact of radiator radius of curvature.

3.4 Vibrometer Transducer Design Goals and Constraints

The CFE prototype was intended to have a simple vibrometer transducer (VT) for use in measuring shear displacements at the center of the ultrasonically generated force pattern. Regardless of signal processing method employed, ultrasonic vibrometers require at least one drive channel to produce a tissue interrogation signal, and one receive channel for collection of internal tissue backscatter. A single element could be used for both purposes if the appropriate transmit/receive switching equipment were available. However, based on our laboratory's past experiences with these devices, and concerns of electronic noise, a design with independent drive and receive channels was pursued.

In addition to the primary goal of operating at tissue depths of at least 12 cm, additional design goals were to fit within the force generation transducer, to minimize

drive and receive instrumentation and complexity, and to maximize bandwidth. The goal of fitting the VT within the annular FT coupled their radial dimensions. The goal to maximize bandwidth came from its relationship to range resolution. The ability to resolve targets a distance Δz apart is related to the signal bandwidth BW and the propagation speed c: $\Delta z \geq \frac{c}{2BW}$ (Taylor, 1995). In the present system, range resolution is of interest for describing tissue properties as a function of depth along the ultrasound beam.

As a first design step, the preferred operating frequency range of the VT was defined in terms of a backscattered ultrasonic intensity metric, subject to the constraint that the drive channel pressure amplitude was set to the Mechanical Index safety limit ($p_{MI,0.3}$):

$$B = (f^4)\left(\frac{p_{MI,0.3}^2}{\rho c}\right)e^{-4(\alpha-\alpha_{0.3})z}\,(f) \;=\; (f^5)\left(\frac{p_{MI,0.3}^2}{\rho c}\right)e^{-4(\alpha-\alpha_{0.3})z}$$

with the Rayleigh scattered intensity represented by the leading f^4 term, $p_{MI,0.3} = 1.9\sqrt{f}$ (MPa/MHz), α is the actual attenuation in the tissue, $\alpha_{0.3}$ is the presumed for the Mechanical Index computation (0.3 dB/cm/MHz), and z is the axial path length (cm). The final frequency term accounts for vibrometer processing performance. A conventional delay-correlation processor is more noise-immune when a fixed displacement (d) produces a larger phase shift ($kd = \frac{2\pi f}{c}d$) as a consequence of operating at a higher frequency. In a Doppler based system, displacement sensitivity scales directly with kd. Therefore the performance benefit of increased frequency is included in the backscatter metric.

Figure 3.10 shows the ultrasonic intensity metric for tissue depths of 3, 6 and 12 cm, assuming a path attenuation of 1 dB/cm/MHz. The best frequency range for 3-6 cm is 3-7 MHz, which is consistent with the literature on vibrometer usage in elastography systems. The best frequency for operation at 12 cm is 1.55MHz, with a penalty of no more than 3 dB up to 2.5 MHz. In practice, vibrometry transmission levels are well below safety limits, so the relative depth-dependent signal losses in Figure 3.10 do not represent insurmountable bounds on vibrometer operation.

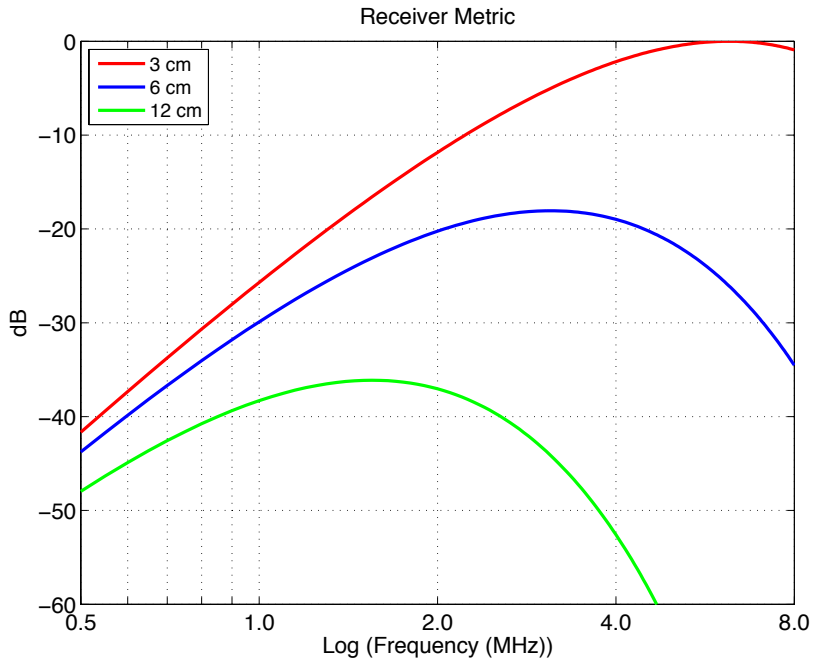

Figure 3.10. Vibrometer response metrics for tissue depths of 3, 6 and 12 cm.

A coaxial, spherically confocal arrangement was pursued for the vibrometer element design, based on its simplicity. Prior vibrometer developments at Georgia Tech utilized angled spherically focused elements that required careful alignment of their foci (Cox & Rogers, 1987). The coaxial design was intended to eliminate the need for

alignment, while ensuring that the transmitter and receiver beams would share a common axial path regardless of any refraction that may occur in complex tissues. The critical parameters in the VT design study were the inner and outer element radii, subject to the constraint of fitting within the force generation transducer. It was of interest to further minimize:

- the vibrometer main lobe width, so that the bandwidth of incoming shear waves would be preserved; and

- the vibrometer sidelobe response in the range of radii of the force generation transducer primary lobes.

The first goal could be met by using the largest possible outer radius. The second goal was addressed by manipulating the inner and outer element dimensions in order to minimize the magnitude of the transmit-receive product pattern in the range of 2.5-3.5mm off axis. Figure 3.11 shows the lateral and axial transmit-receive product beam patterns for transducers defined to have outer to inner element area ratio S_o/S_i values of 2, 1, and 0.5. The patterns are frequency-weighted sums over the 1.7 - 2.5 MHz band, calculated for fixed values of R_c (140 mm) and a_o (32 mm). The use of the geometry with a smaller outer element ($S_o/S_i = 0.5$) significantly suppresses sidelobes in the 1.5 and 3.5 mm lateral range. Main lobe width and overall axial beam characteristics were only slightly impacted by area ratio.

The quarter power full width of the radial pattern in the example shown in Figure 3.11 was approximately 2mm. However, main lobe width turned out not to be as critical a factor for the vibrometer as it was for force generation. The reason for this is illustrated in Figure 3.12, which shows the phase of the displacement field generated by a CFE force

field with 3mm radius. The red curve is the phase of the displacement field in a material having a shear speed of 2 m/s, driven continuously at a frequency of 200 Hz.

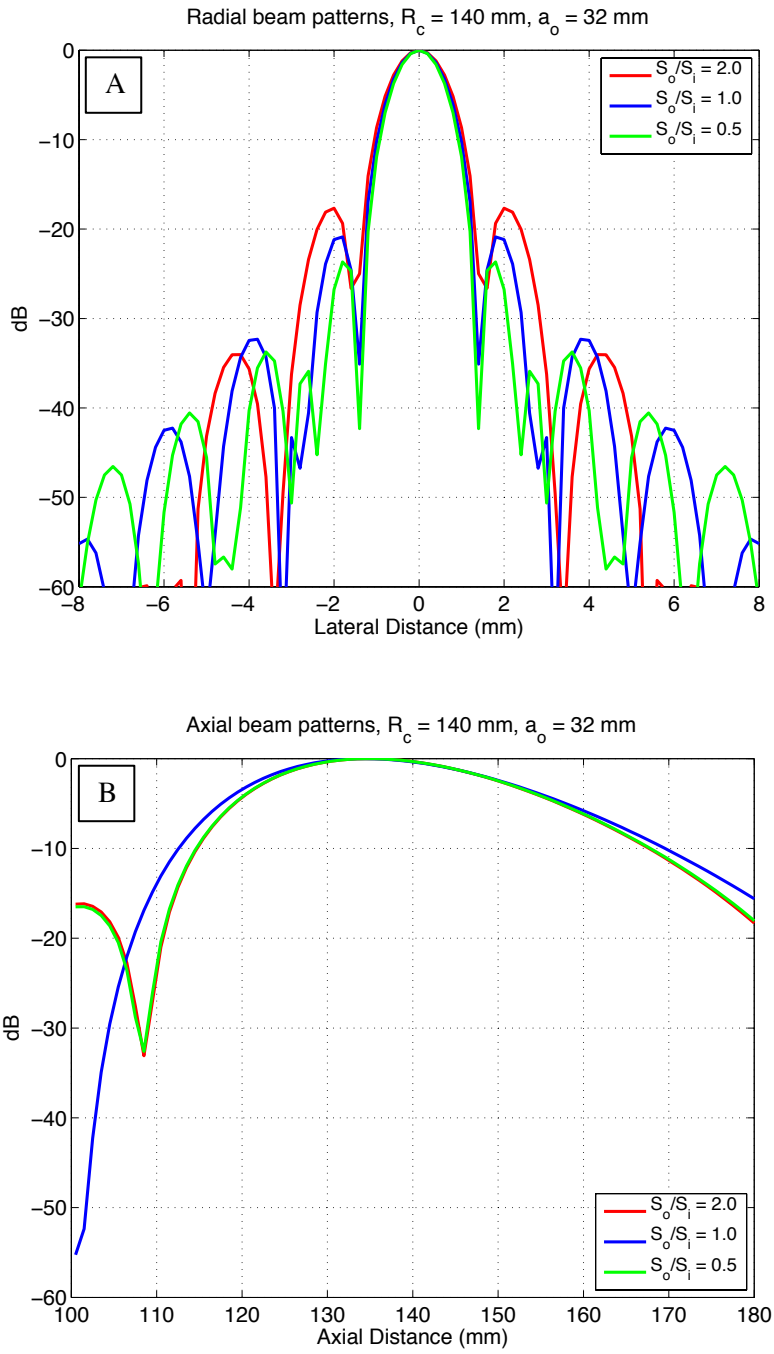

Figure 3.11. Lateral (A) and axial (B) transmit-receive beam patterns for vibrometer designs with different coaxial element area ratios.

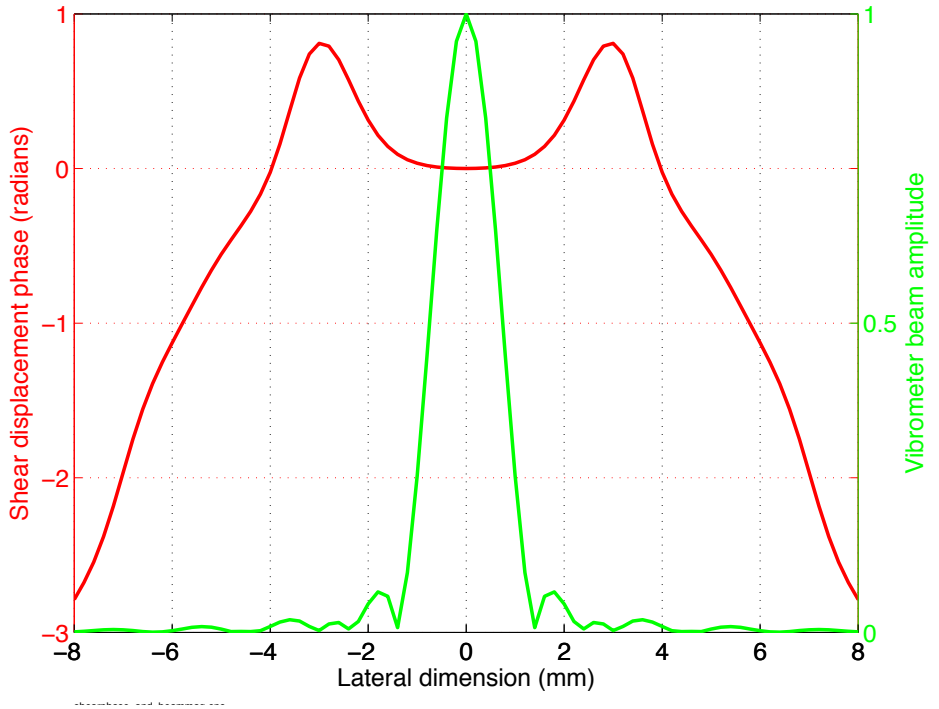

Figure 3.12. Example of shear field displacement phase generated by CFE (red), and vibrometer beam intensity (green).

Near the pattern center (+/- 1mm), the displacement phase is nearly uniform, so that when the response is integrated by the vibrometer beam width (green), low pass effects are nearly non-existent. By contrast, a vibrometer interrogating tissue outside the forcing radius (>3mm) would integrate over the rapidly changing phase associated with a diverging shear wave, and spatial integration filtering effects would be significant. This is consistent with the literature on ultrasonic vibrometers used in shear elastography, where beam widths are on the order of 0.2mm (Nightingale et al., 2002, for example) in order to preserve shear wave bandwidth.

3.5 Final Design Tradeoffs

Arrival at final transducer designs involved evaluation of a series of performance, construction, and electronics tradeoffs. The individual issues and their resolution are discussed below.

3.5.1 Force lobe positioning

The method for controlling the locations of the force lobes was discussed earlier, where it was proposed that the simplest control method would be to vary transducer drive frequency for a fixed driving mode number *M*. The optimal frequency range for operation at a tissue depth of 12cm had been identified, so the remaining question centered on the range of force lobe pattern radii of interest for the prototype evaluation. From there, the combination of transducer aperture and M could be specified.

Having a large pattern radius allows the incident intensity to be applied over a greater tissue volume, increasing the displacements that may be generated. This benefit may be offset by larger shear wave path length attenuation in extremely lossy tissues. Allowing the pattern radius to be large also raises concerns about spatial integration over varying tissue types or structures. For example, the gyri on the surface of the brain of a beluga whale had characteristic widths on the order of 1 cm (Marino, et al., 2001), and the layering of the chemical content of jaw fats in bottlenose dolphins (thought to be correlated to acoustic function) was seen to vary on a similar scale (Zahorodny-Duggan, Koopman, & Budge, 2009).

At the other extreme, concentrating the force pattern in a tight radius limits the benefit of a distributed force configuration. At the limit of zero radius, the ring pattern

condenses to a line-distribution. A small radius also increases the likelihood of spatial overlap and unwanted interactions between the forcing and vibrometry beams. From all the above considerations, a range of 2.5 – 3.5 mm was selected for the force pattern radii.

3.5.2 Transducer dimensions

The radial distance between the outer diameter of the vibrometer active element and the inner active diameter of the force generator sector elements were determined with input from a transducer manufacturer with respect to casing thicknesses. A total of 6 mm was allowed for casing walls, with an additional 1 mm added for space between the transducer cases to allow for beam alignment. The physical offset between transducers could have been reduced if one transducer body had been built which contained both transducers. However, the flexibility to independently work with the devices was desired.

The FT outer radius was set after consideration of several factors. In addition to its relationship to lobe placement (a larger diameter moves the force lobes closer to the beam axis) and ultrasonic source strength (scales with diameter-squared), the size of the force generation transducer was bounded with consideration to the physical size of the device and its handling. A broader transducer also adds performance risk in terms of the diversity of possible tissue paths between the system and the focal plane in tissue. The FT outer radius was capped at 82mm, including casing thickness.

3.5.3 Force Generation Mode Number

Given the constraints of operating frequency, lobe pattern radius and transducer size, the FT mode number was set to M=3 (six total sectors). An added benefit of this

modest number of sectors was in light of weighting corrections. If it was determined that individual sectors needed some degree of in situ correction of magnitude and/or phase in order maintain beam pattern integrity, finding instrumentation to do so was thought to be feasible. It was also found through discussion with candidate manufacturers that transducer cost increased considerably with number of sectors. The chosen value for M set the drive bandwidth between 800 and 900 kHz.

3.5.4 Vibrometer Operating Band

To reduce the likelihood that FT transmissions would adversely impact the performance of the vibrometer, the operating frequency band of the VT was centered between FT harmonics. At issue was scattering or directly path coupling from the FT that would contaminate VT signals. A center frequency of 2.1MHz was therefore chosen, between the 2nd harmonic of 900 kHz (1.8 MHz), and the 3rd harmonic of 800 kHz (2.4 MHz). A band centered between lower FT transmissions (0.9 – 1.6 MHz) would have worked just as well on the basis of the combined effects of backscatter and vibrometer sensitivity (Section 3.4). However, the higher end of the frequency range was used in order to take advantage of expected higher frequency attenuation in reducing FT harmonic levels.

3.6 Final Design Specifications and Predictions

The final design specifications for the prototype CFE transducers are listed in Table 3.1 and illustrated in Figures 3.13-15. The specification for internal thermocouples was added at the suggestion of candidate manufacturers to monitor active element temperatures as a safeguard against excessive heating. The specifications for drive

conditions were intended to ensure that the transducers could operate without damage when providing focal plane intensity levels exceeding soft tissue safety limits. In other words, the transducers should operate normally up to the highest of any actual biological safety-limited drive conditions. The vertical extent of the transducer casings and the rear threaded hole patterns were specified to allow multiple options for transducer mounting and beam alignment.

Table 3.1. Specifications for Force Generation (FT) and Vibrometer (VT) Transducers

Design Feature	**FT**	**VT**
Focusing	Spherical	Spherical
Radius of curvature	140 mm	140 mm
Elements	6 equal area sectors (60 deg.)	2 concentric
Active element radius	40 mm inner 73 mm outer	25 mm disk 33 mm ring
Casing radius	37 mm inner, 82 mm outer	36 mm outer
Operating band	0.7 – 1.0 MHz	1.7 – 2.5 MHz
Cabling	One for each sector	One for each element
Thermocouples	Two internal	Two internal
Drive intensity	2100 W/cm^2 pulsed	500 W/cm^2 pulsed

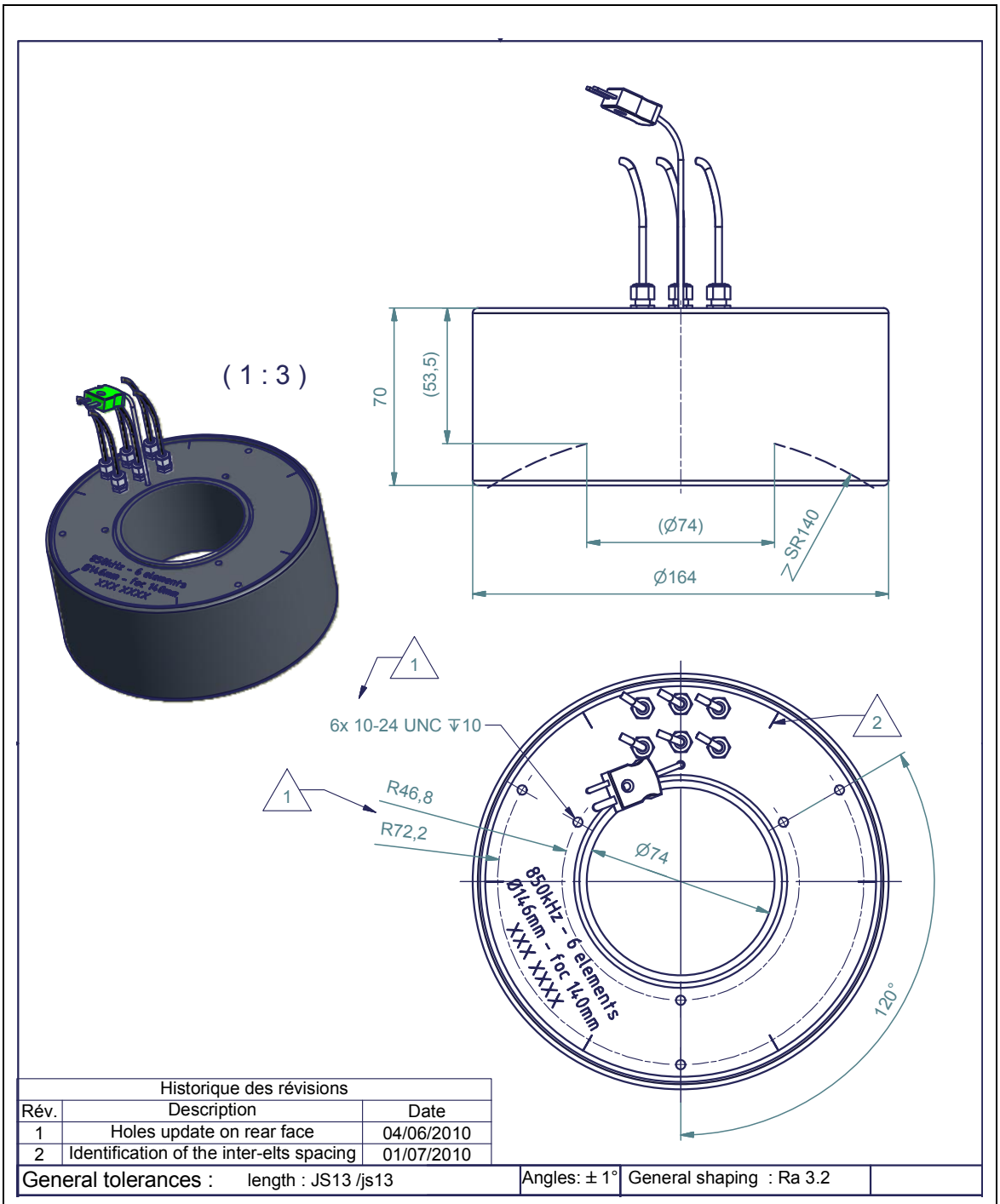

Figure 3.13. FT transducer as-built drawings from manufacturer.

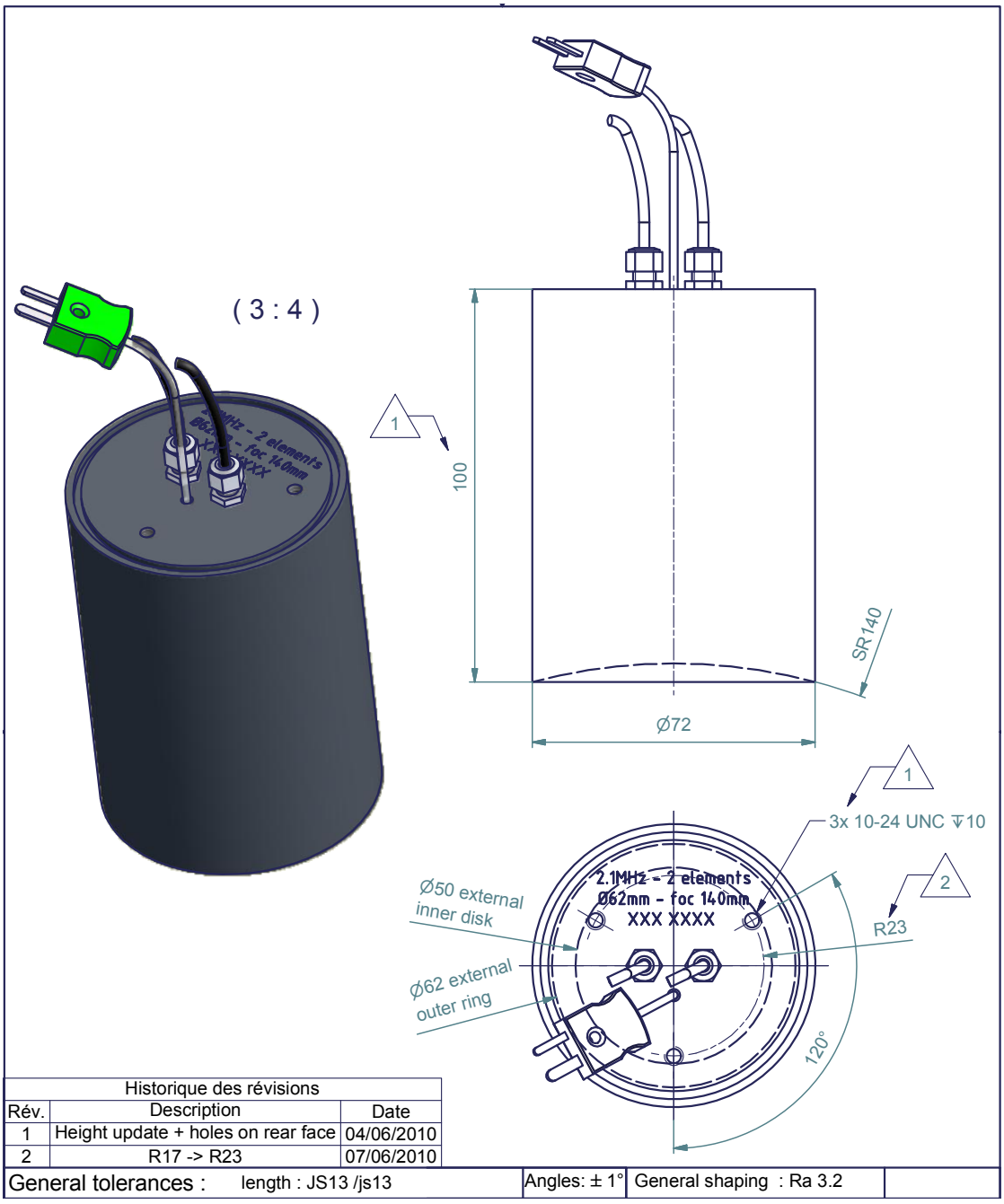

Figure 3.14. VT as-built drawings from the manufacturer.

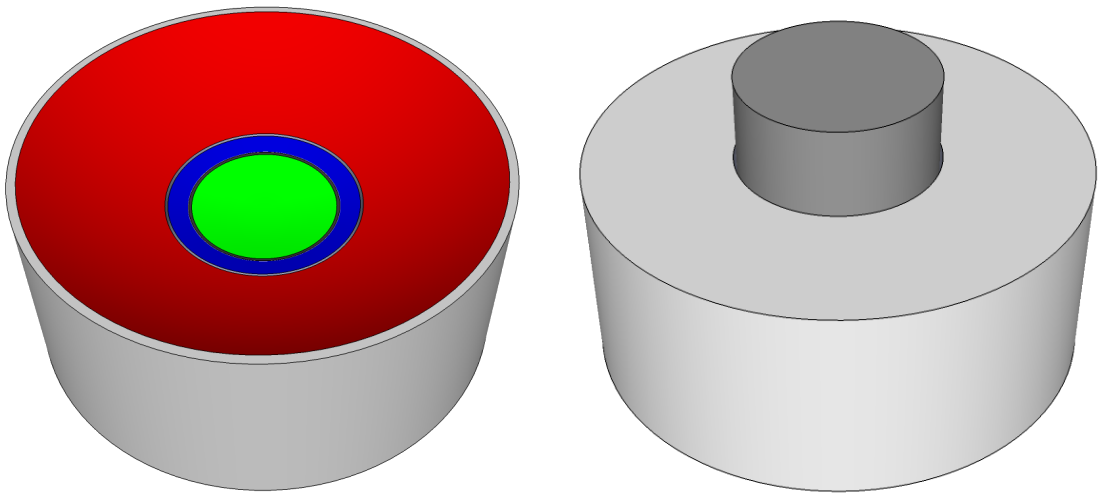

Radiating Faces Back Faces

Figure 3.15. Nested CFE prototype transducers. Red: FT radiating face, Green: VT radiating face, Blue: VT receiver face.

Figure 3.16 shows the predicted normalized lateral-axial plane intensities for the final FT and VT prototype designs. The FT lobes have a half intensity full axial width of approximately 20mm, indicating the range over which material characterization is likely to have the highest signal to noise ratio. Figure 3.16C shows focal plane overlays of -3 dB intensity contours of the FT at 800 and 900 kHz, and for the VT averaged over the 1.7 – 2.5MHz band. This illustrates the general principles of CFE operation – the FT produces a set of distributed forces on a common radius, generating shear wave field that focuses to the center of the force pattern, where it is measured using a central vibrometer beam.

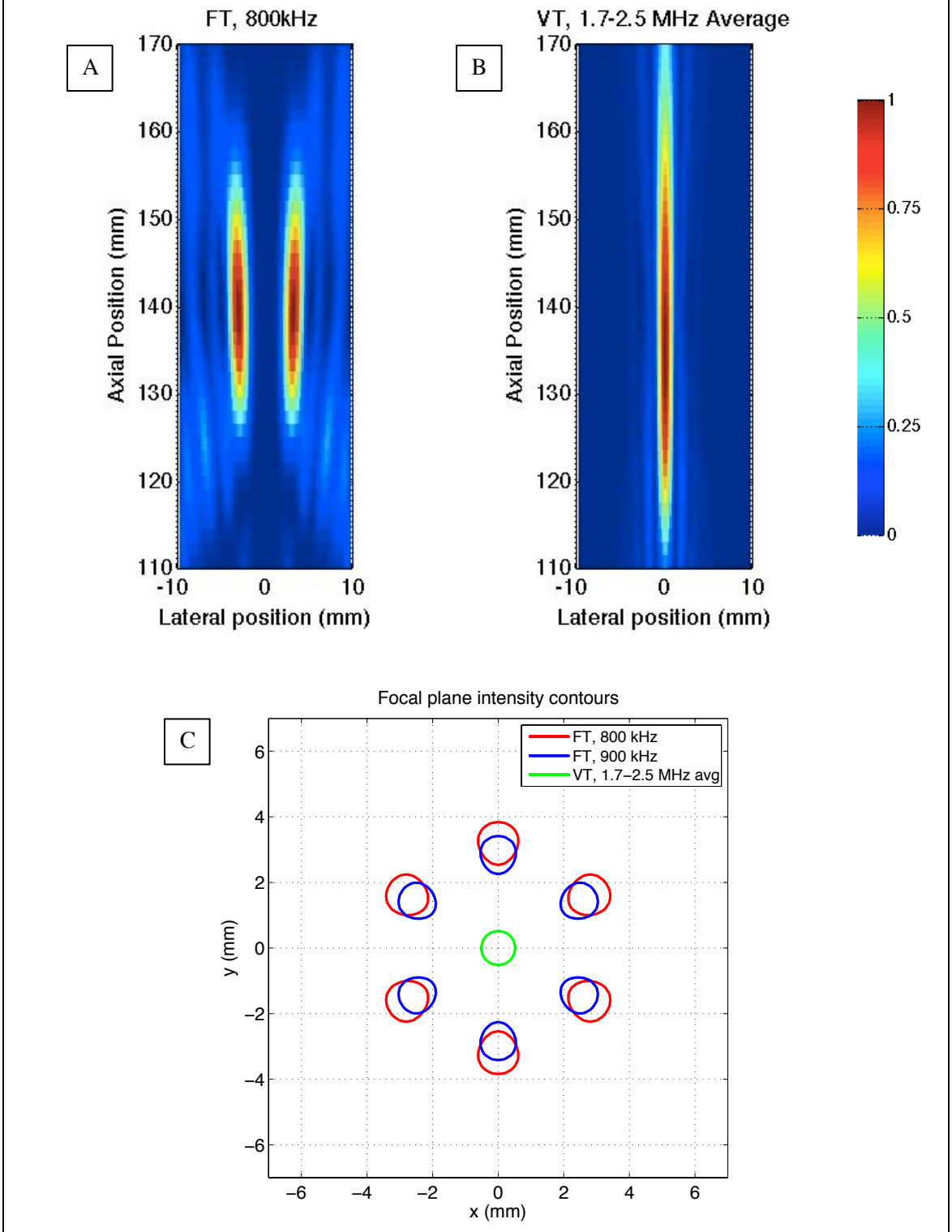

Figure 3.16. Predicted lateral-vertical plane intensity patterns for (A) FT at 800 kHz, (B) VT averaged over the 1.7 – 2.5 MHz band, and (C) focal plane -3dB intensity contours.

Figure 3.17 shows the predicted shear speed estimation performance of the CFE system, using the ultrasonic fields shown in Figure 3.16 in a material with a shear speed of 3 m/s. Calculations were made using FT carriers of 800 and 900 kHz, and shear speed was calculated using the phase change induced by the predicted RT radial beam position shift. The estimated shear speed was within 10% of the actual value for vibration frequencies up to 800 Hz. In this frequency range, the varying degree of error was related to displacement contributions from secondary FT lobes, and that the forcing beams generated at the two carrier frequencies are not identical in size. Above 900 Hz, the diameter of the forcing beam degraded the estimate. These results indicated that the proposed transducer designs should be effective, and that the full CFE system concept would work as intended.

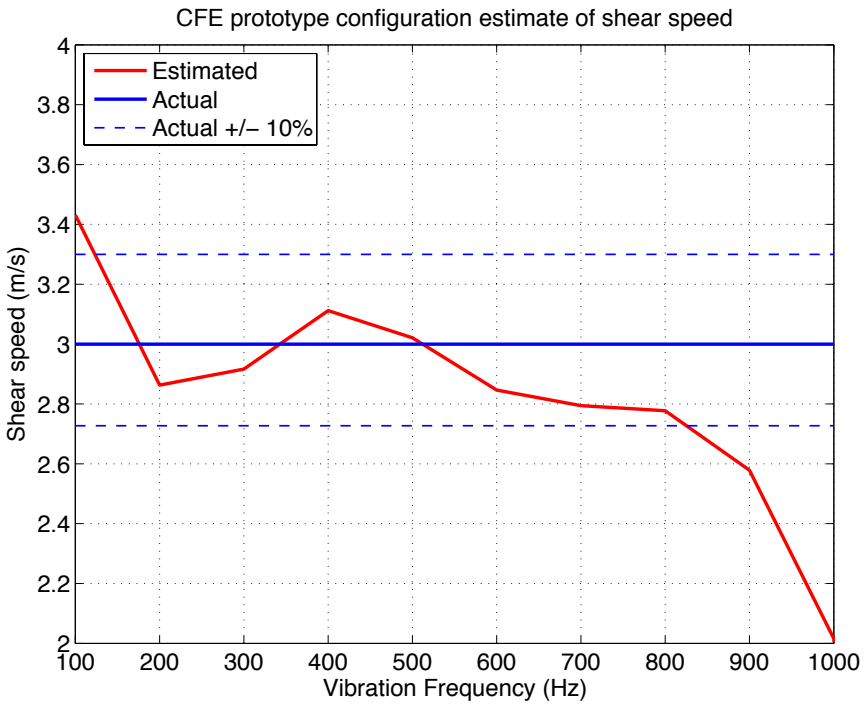

Figure 3.17. Simulated shear speed estimation performance of the prototype CFE system in a material with 3 m/s shear speed.

3.7 Summary

In this section, prototype CFE transducer designs were formulated for an imaging depth goal of 12 cm. A six-sector annular design was chosen for force generation, using drive frequency to control the radius of the forcing lobe pattern. A dual confocal element design was chosen for the vibrometer, which nests within the force generation transducer. Simulations made for a tissue-like material demonstrated the shear speed estimation capability of the prototype designs.

CHAPTER 4

TRANSDUCER TESTING

4.1 Transducer Manufacturing

The specifications developed in Chapter 3 were used to competitively bid the manufacture of the CFE prototypes. Figure 4.1 shows the transducers in their nested configuration. The VT was centered within the FT inner casing using a 1mm diameter O-ring, and held in place using adjustable clamps on the back face. The mounting arrangement allowed for fine-scale alignment of the VT and FT beams using spring-loaded thumbscrews, and provided a means for attachment to an external positioning system for performing acoustic field scans.

4.2 Transducer Calibration

Broadband pressure field calibrations were performed using the instrumentation shown in Figure 4.2. The nested transducers were suspended in a 50-gallon water tank, and were mounted on a translating sled for gross positioning. Pressure signals were measured using a needle hydrophone (ONDA HNC-0400) attached to a three-axis positioning system (not shown), and data was collected using a LabView[**] routine. The wall of the tank facing the transducers was covered with ultrasound absorbing material.

[**] Labview code for positioner and data acquisition control during volume scans was written by Jayme Caspall, Georgia Institute of Technology.

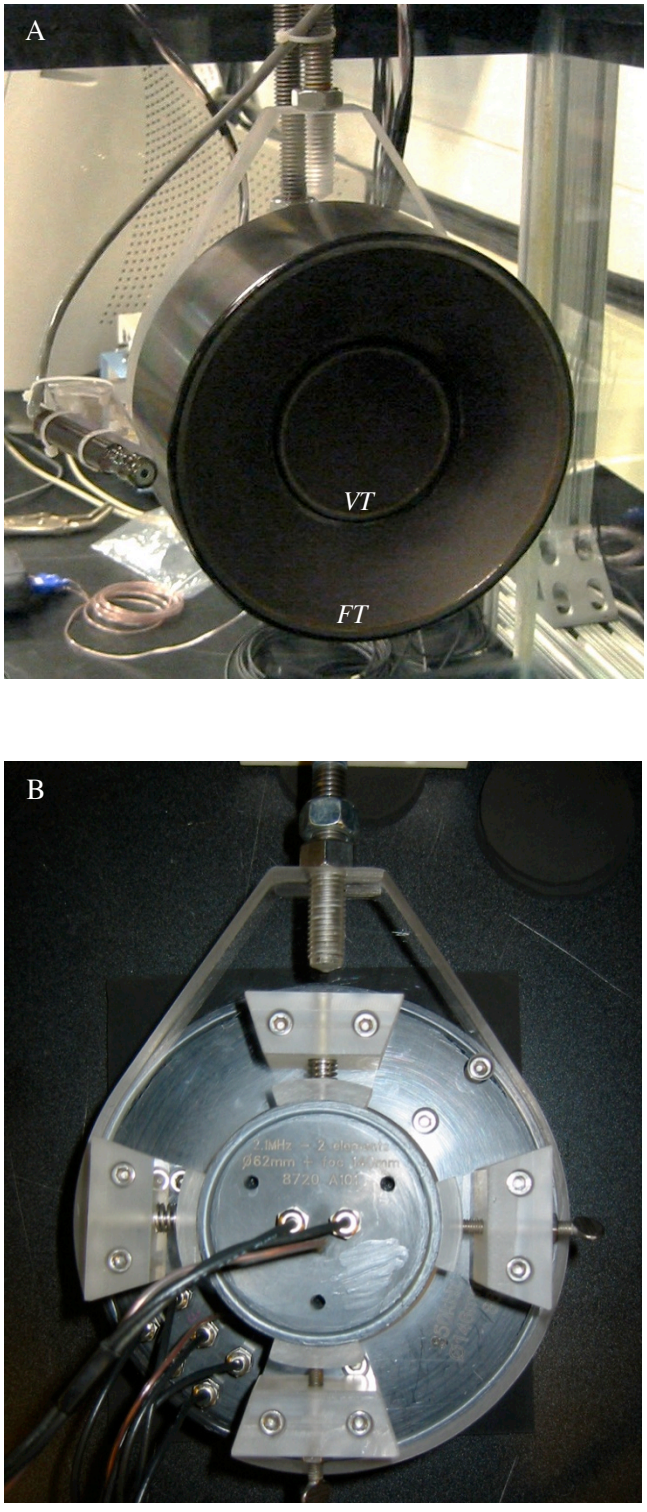

Figure 4.1. Active face (A) and back face (B) views of nested CFE prototype transducers.

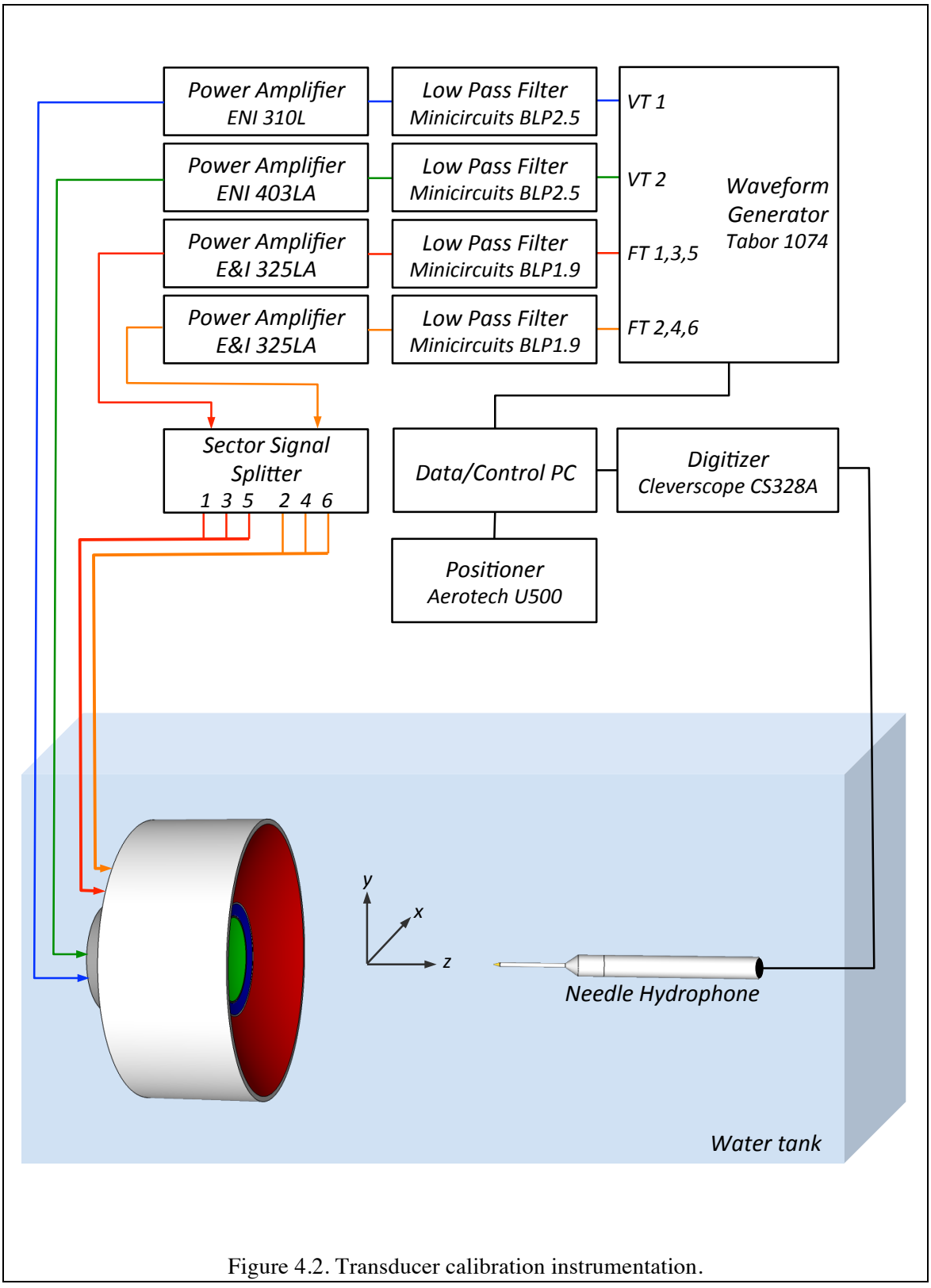

Figure 4.2. Transducer calibration instrumentation.

Pressure field scans typically employed x-y step sizes of 0.2mm and z-steps of 1.5mm, taking approximately 3.5 hours per x-y plane as a consequence of the total plane width (16x16 mm) and ensemble averaging of multiple transmissions at each point. The longer axial step sizes were found to be acceptable for field sampling based on ultrasonic field predictions discussed previously. Position verification data was collected using two 5.0 MHz transducers (not shown) oriented towards the tank side and bottom and driven with a pulser-receiver (Panametrics 5072PR) in order to verify alignment of start and end positions between successive scans. Water temperature was measured at the beginning and end of each scan using a T-type thermocouple, and used to estimate sound speed (Chen & Millero, 1976), which was in turn used in hydrophone position estimates as a complement to positioner controller readings.

Linear chirp pulses for all transducer drive signals were defined in MATLAB and synthesized using a four-channel arbitrary waveform generator. Output filters were placed on all waveform generator channels as a noise reduction and anti-aliasing measure. The six sectors of the FT transducer were driven in two groups of three, and amplified using matching power amplifiers. To create the M=3 drive condition, the two waveforms were opposite in polarity but otherwise identical. The two channels of the VT were driven separately for the purposes of time-efficient calibration. Although only one of the elements would be used as a vibrometer transmitter, the beam patterns of reversible transducers are the same whether used for transmission or signal reception (Pierce, 1989). Signals for the FT and VT transducers were sequenced in time so that the tank was free of reverberation during all direct path arrivals. Power amplifier output signals were acquired at the start and end of each scan for use in hydrophone signal normalization.

Hydrophone scan data were processed in MATLAB to yield frequency domain transmitting voltage responses for the FT and the individual VT elements:

$$TVR(x,y,z,f) = \frac{V_H(x,y,z,f)}{M_H(f)\,V_{PA,avg}(f)}$$

where $V_H(x,y,z,f)$ is the Fourier spectrum of the hydrophone data, $M_H(f)$ is the hydrophone sensitivity, and $V_{PA,avg}(f)$ is the start/end average Fourier spectrum of the power amplifier output voltages.

4.3 FT Calibration Results

Figure 4.3 shows the predicted and measured focal plane FT intensity patterns at 800 kHz, M = 3. All values were normalized to the respective focal plane maxima. The measurement exhibited the expected six-lobe pattern with well-defined nulls at the center and along sector boundary planes. The pattern sidelobes in the range of r = 6 mm were slightly lower than predicted[††], which was somewhat surprising since no individual sector weights were applied for this experiment. Upon closer examination, the entire measured focal plane pattern appeared slightly condensed relative to the prediction. Review of the spectrum data between 700 and 900 kHz showed that the measured patterns behaved as if upshifted in frequency by approximately 10%. This is illustrated in Figure 4.4, where the measurement at 725kHz is seen to be a good match to the prediction at 800 kHz. Similar agreement occurred in the lateral-axial plane data, although the measurements showed a shorter axial width and increased incline angle relative to the prediction.

[††] This is an event of such improbability as to draw comparison with a Yeti sighting.

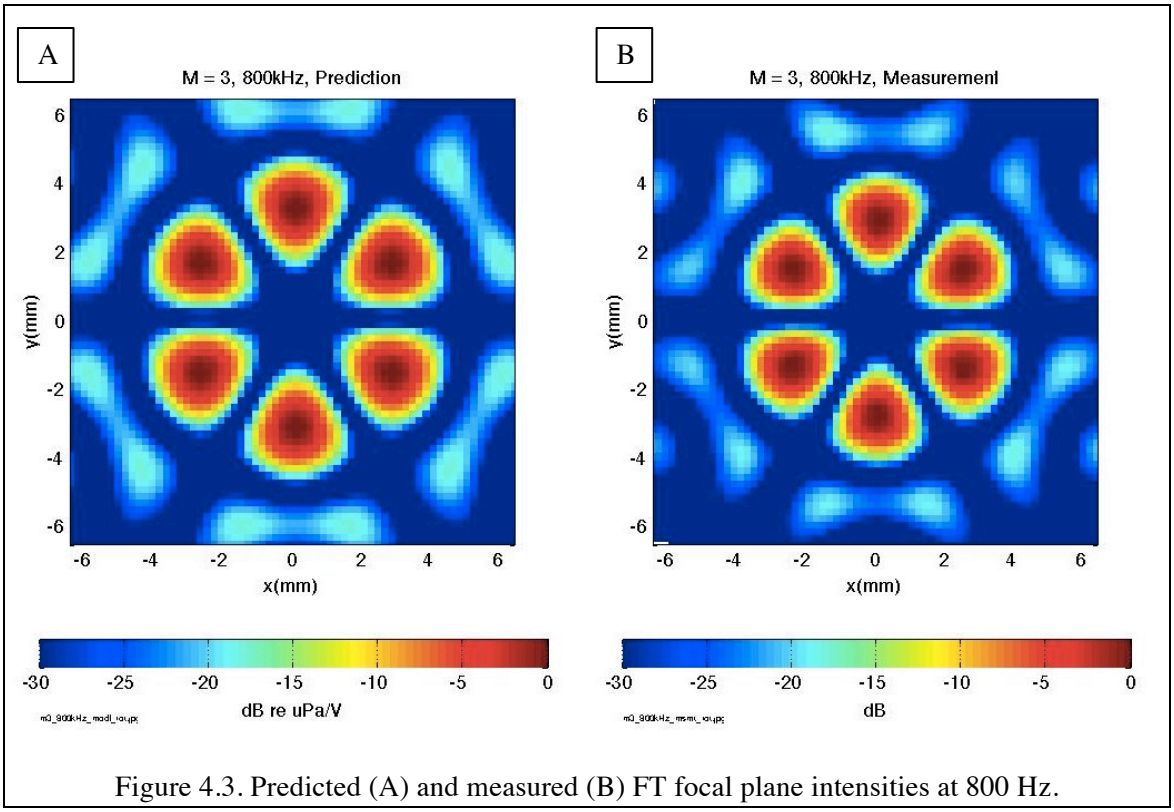

Figure 4.3. Predicted (A) and measured (B) FT focal plane intensities at 800 Hz.

Ultimately, the observed differences between measurements and predictions were of little consequence to the intended operation of the CFE system. Most importantly, the FT as manufactured had sufficient bandwidth to support a downshift in order to keep the force lobes in the desired range of locations. However, it was of interest to attempt to understand the origin of the discrepancies. Figure 4.5 shows the predicted and measured focal plane intensities at 800 kHz for the FT operating with M = 0, so that the transducer ideally would behave like a conventional spherically focused device. Measurement beam patterns are displayed through two orthogonal axes (x, y). The predicted and measured beam widths were in good agreement, without any frequency shift. This suggests that the transducer dimensions and curvature were very close their specified values.

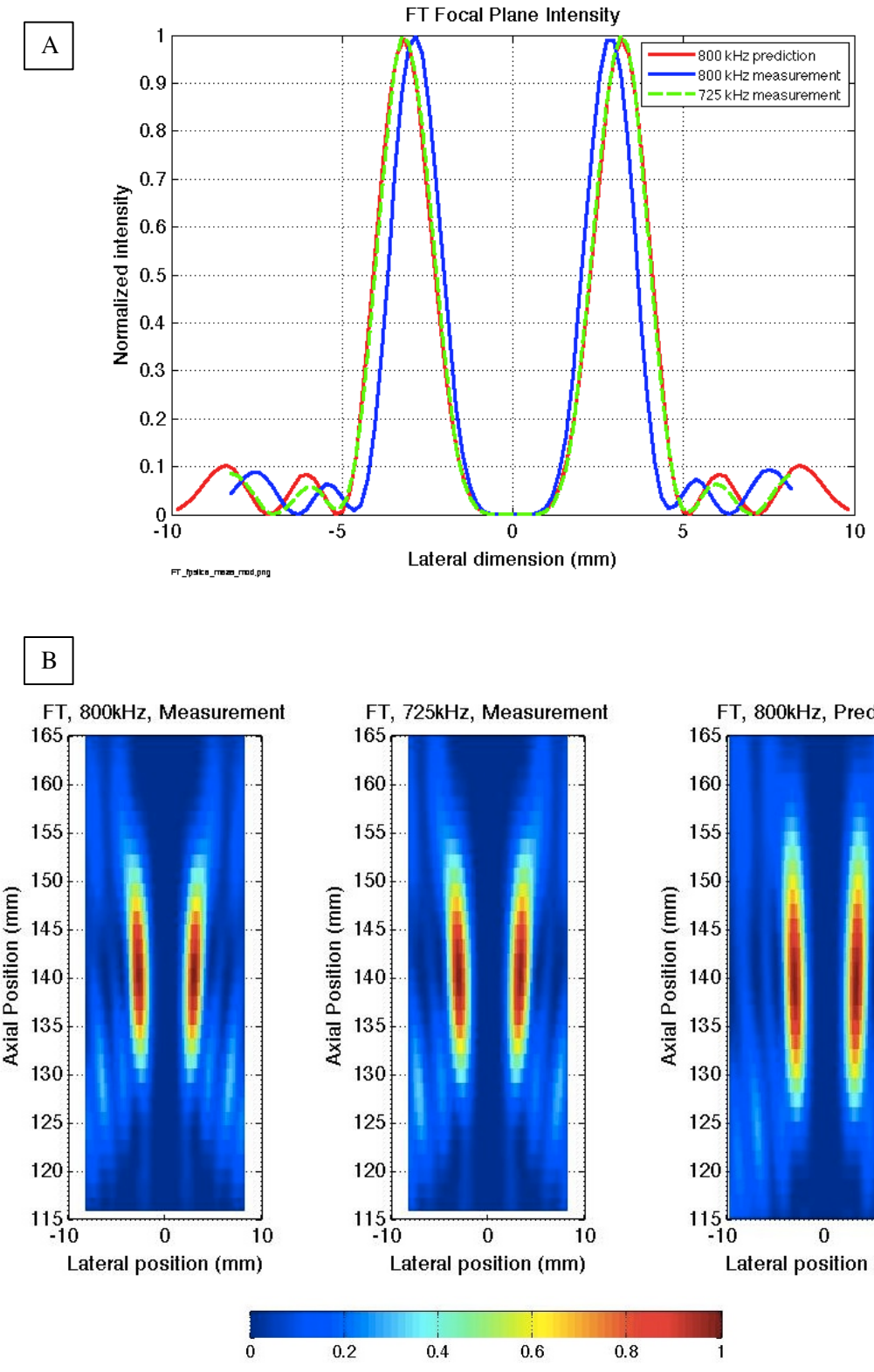

Figure 4.4. FT focal plane intensity cross-section (A) and lateral-axial field maps (B).

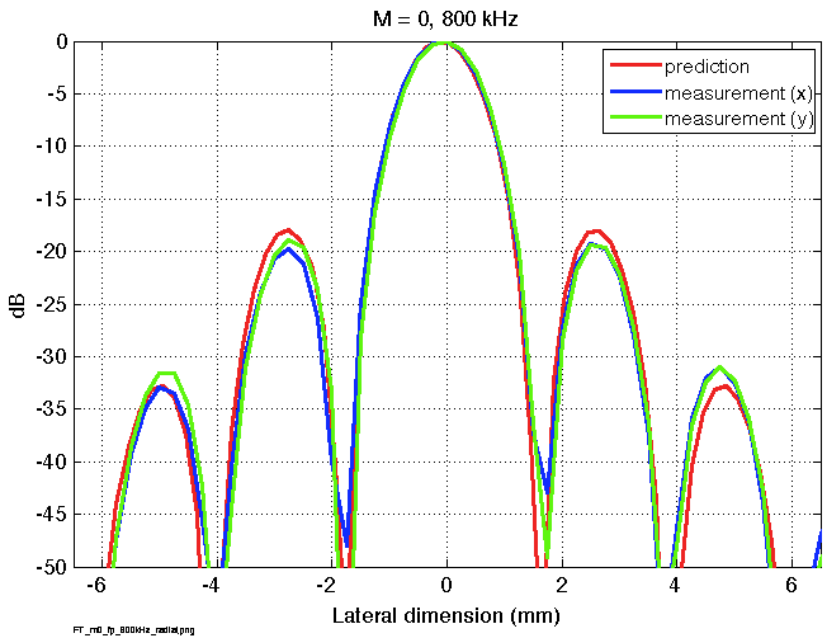

Figure 4.5. FT focal plane normalized intensity cross-sections, M=0, 800 kHz.

One possible explanation is that the active element backing structure of the as-built transducer may have been influencing the strength of the modes activated by the alternate-sector drive weights. The model assumed all modes (harmonics of M=3) could be produced exactly as dictated by the sector-weighting scheme. Investigation of this question could be pursued by measuring the transducer surface motion with a high frequency laser vibrometer, or by scanning over the transducer face in parallel planes so that local motion gradients could be calculated.

Another possibility is that the model did not properly account for radiation loading of the modes of the transducer surface velocity. Testing this issue would require formulation of a solution explicitly on a spherical surface, rather than using steered co-planar rings.

Before moving on to the VT calibration results, a few additional notes are made regarding features of the FT acoustic field. Figure 4.6 shows the M=0 and M=3 focal plane transmitting voltage responses. The M=3 pattern is rotated relative to prior plots in this chapter, as this data set was taken with the FT installed at a slightly different angle. The lobes of the M=3 drive have peak values approximately half that of the M=0 main lobe. The summed square of pressure over the full scan region yielded a value of 92% for the M=3 drive relative to the M=0 drive. Although this is not a formal accounting of system energy, it nonetheless indicates that the sectored drive condition did not induce any significant loss in acoustic output efficiency. This is presumably because the characteristic length scales of the transducer elements were all much larger than a wavelength. So, for example, unloading effects between neighboring sectors of alternate polarity should be highly localized. This is in contrast to how such an arrangement would work at low frequencies, where the zero volume velocity of the radiator would produce a very small acoustic field.

Figure 4.6C shows the measured M=3 focal plane phase response at 800 kHz, demonstrating that the six main pressure lobes have alternating polarity, matching the transducer surface drive condition. This might at first glance appear to be a complication or problem, but since the ultrasound-generated force is proportional to intensity, all forcing polarities are positive and directed along the direction of propagation. In soft tissue this is expected to always be the case, although there are specific combinations of material interfaces that can lead to a "radiation pull" towards the radiating transducer (Hertz & Mende, 1939).

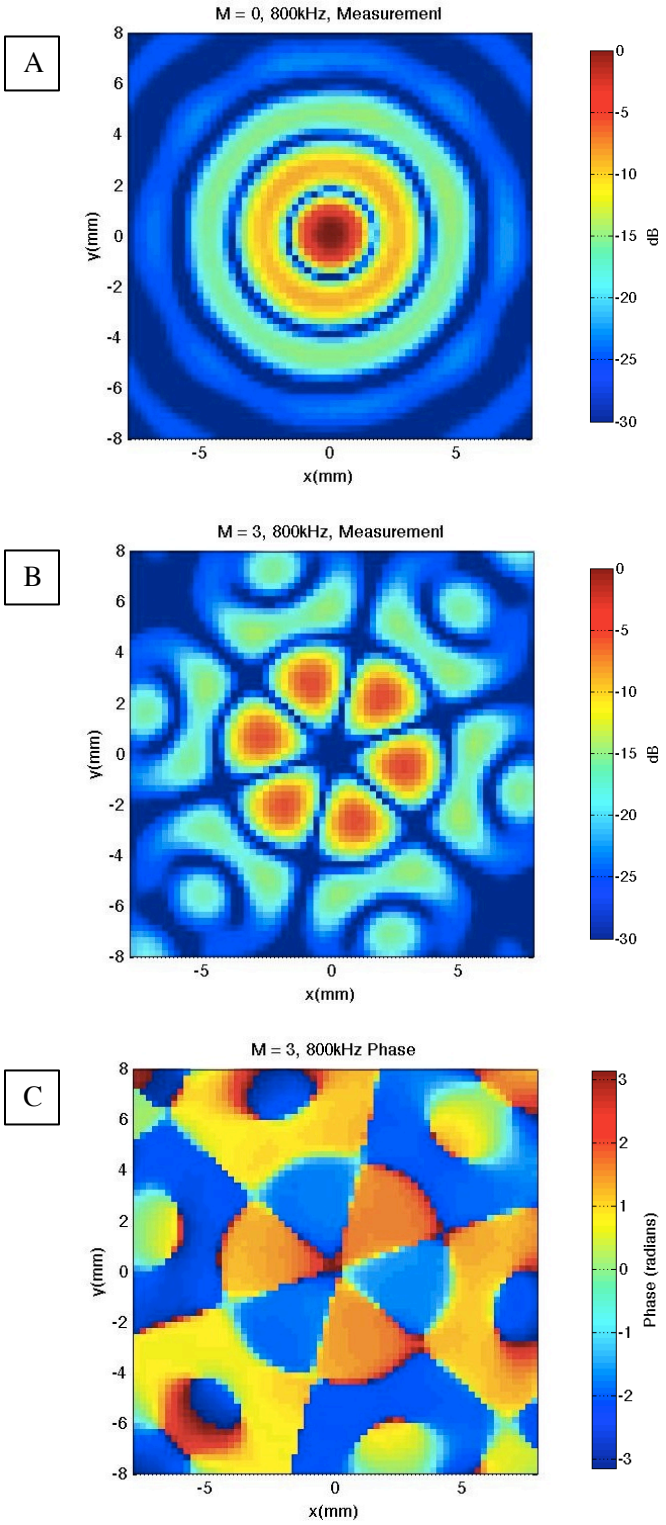

Figure 4.6. FT focal plane transmitting voltage responses, 800 kHz: M=0 magnitude (A), M=3 magnitude (B), and M=3 phase (C).

4.4 VT Calibration Results

Measured and predicted inner disk and outer ring element product beam patterns of the VT are shown in Figure 4.7. The measured pattern sidelobes appear elevated and the overall pattern is asymmetric. Concern that this might have been related to nested configuration with the FT was alleviated through un-nested testing, which revealed no changes in field behavior. After consultation with the manufacturer, the degraded field characteristics were confirmed to be a consequence of slight warping of the elements during transducer construction. The impact of the defect is more clearly quantified with the focal plane cross-sections in Figure 4.8. Predicted and measured main lobe widths and first sidelobe levels are in good agreement. The major discrepancy was in the 3-4 mm lateral range, where measured values were typically 6 dB larger than predicted.

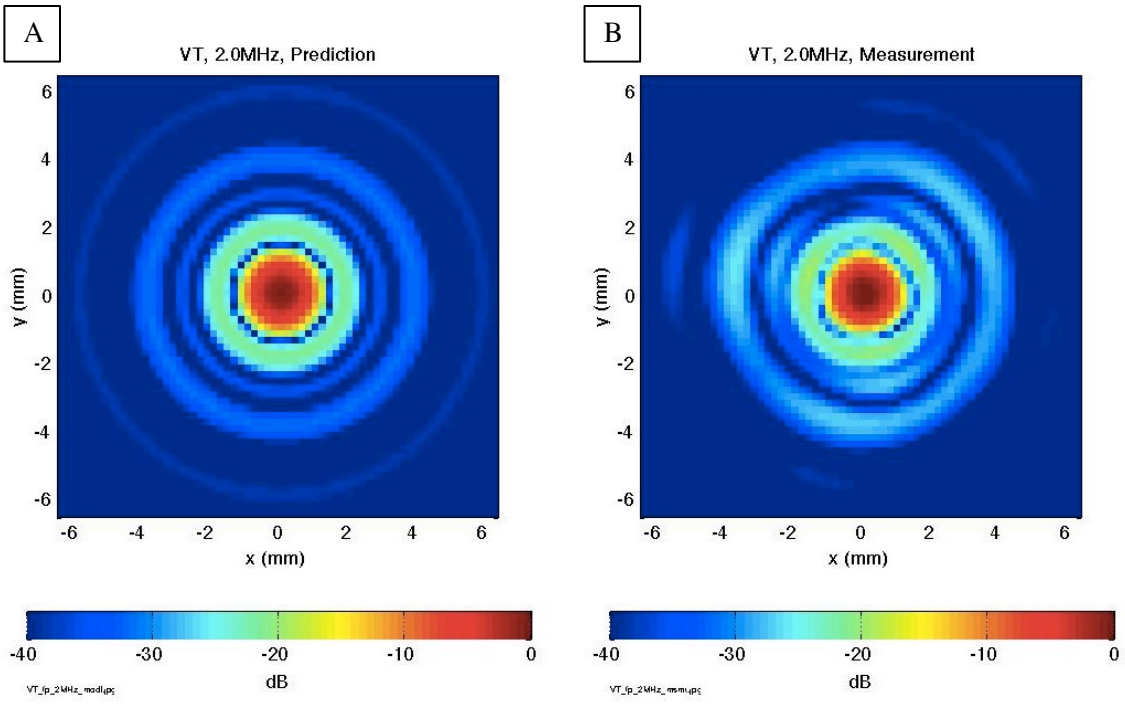

Figure 4.7. VT focal plane product predicted (A) and measured (B) intensities at 2.0 MHz.

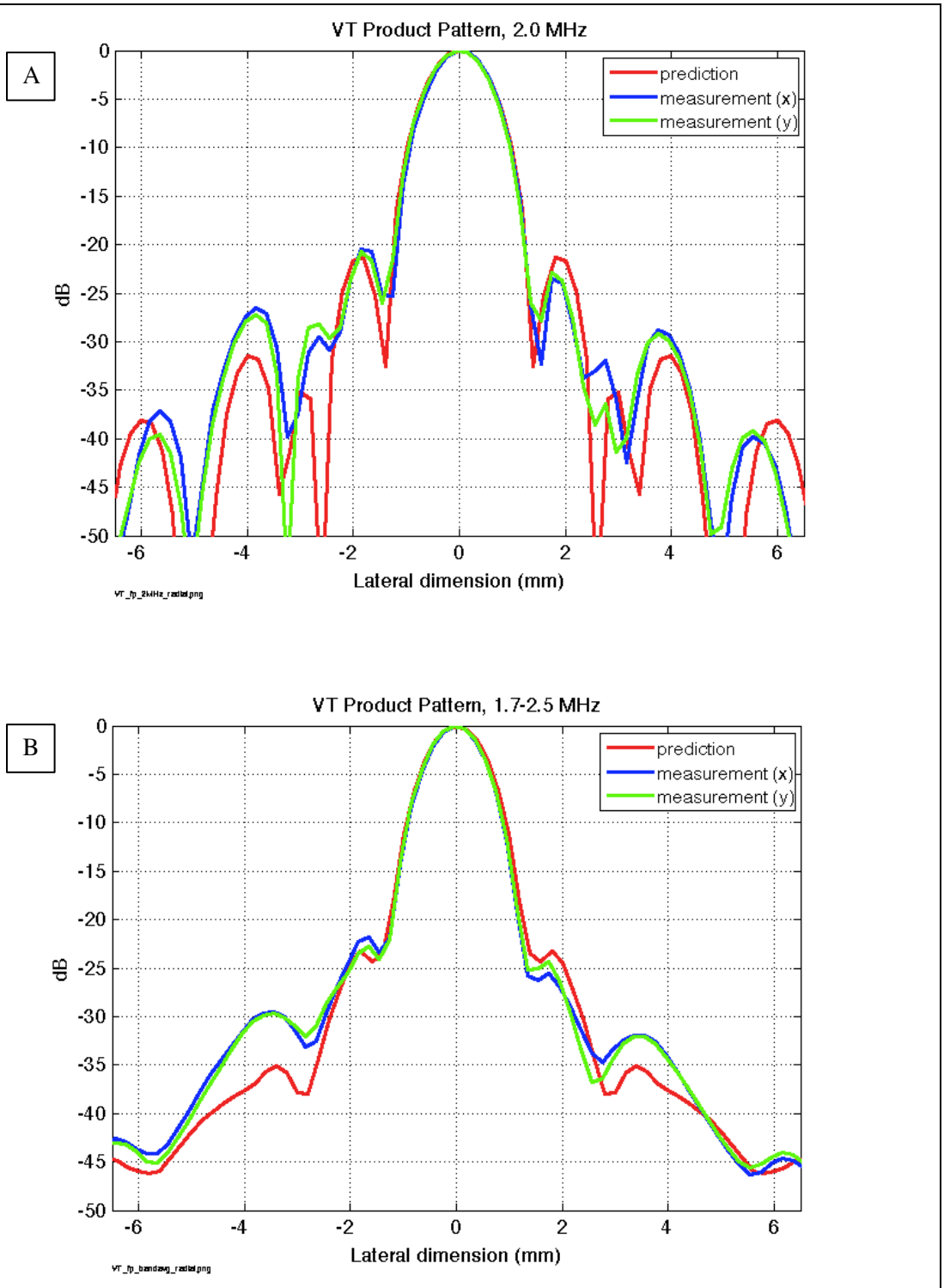

Figure 4.8. VT element product focal plane cross-section patterns at 2.0 MHz (A) and averaged over 1.7-2.5 MHz (B).

Figure 4.9 shows the lateral-axial plane product intensities. The VT axial beam width is considerably larger than that of the FT, as predicted. The degraded sidelobe levels in the 3-4mm radial range were a concern for continuous or long duration pulse FT transmissions, during which the tissue is moving at the forcing locations when the VT interrogates. However, if the FT was driven with a pulse short enough such the generated shear wave had propagated away from the drive region by the time the VT interrogated, the sidelobe degradation would be of no consequence. This approach is described in Chapters 5 and 6.

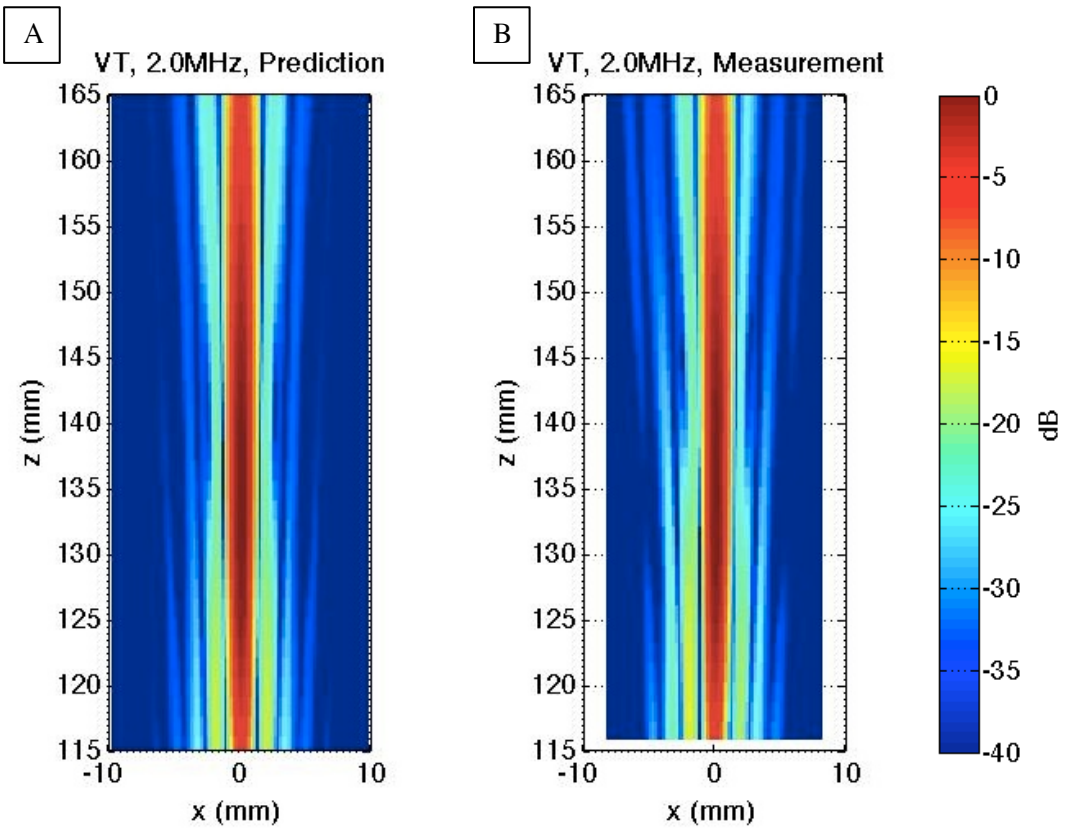

Figure 4.9. VT lateral-axial plane product pattern intensities at 2.0 MHz, predicted (A) and measured (B).

Figure 4.10 shows the on-axis focal plane transmitting voltage responses of the two VT elements. These responses were quite broad in frequency, and easily cover the 1.7-2.5 MHz design band. However, since the FT drive frequencies would be lowered to position the forcing lobes in a target range, the VT transmission band should be lowered as well, and the VT elements clearly had sufficient bandwidth to do so.

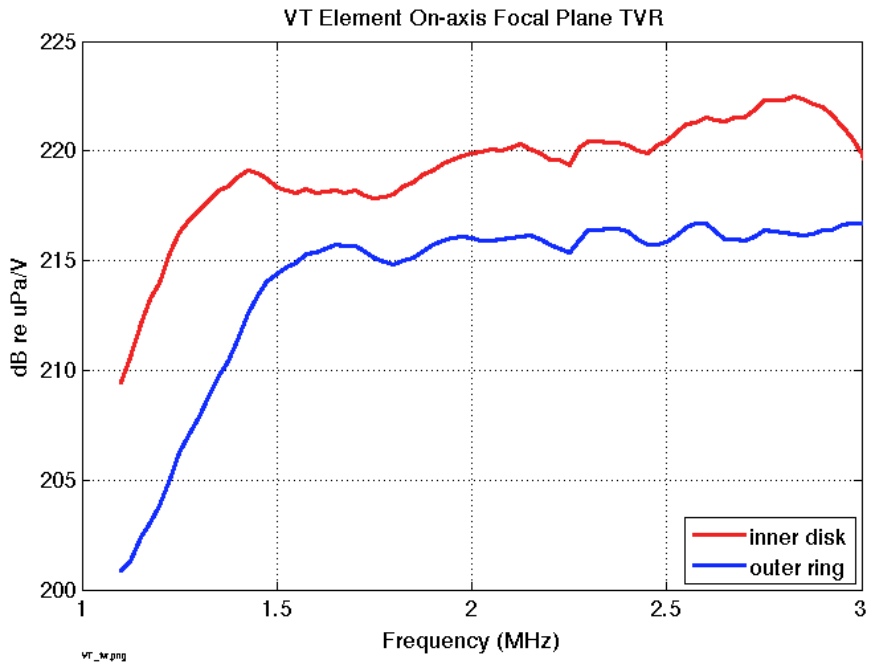

Figure 4.10. VT on-axis focal plane transmitting voltage response.

4.5 Beam Alignment

The intended and measured alignment of FT and VT beams in the focal plane are illustrated with -3dB focal plane intensity contours in Figure 4.11. Despite some discrepancies between the designed and manufactured transducers, the essential features of the CFE concept were seen to be intact. The FT produced a well-defined peripheral

lobe pattern whose radius could be controlled by carrier frequency, and the VT could be aligned to the center of the FT pattern.

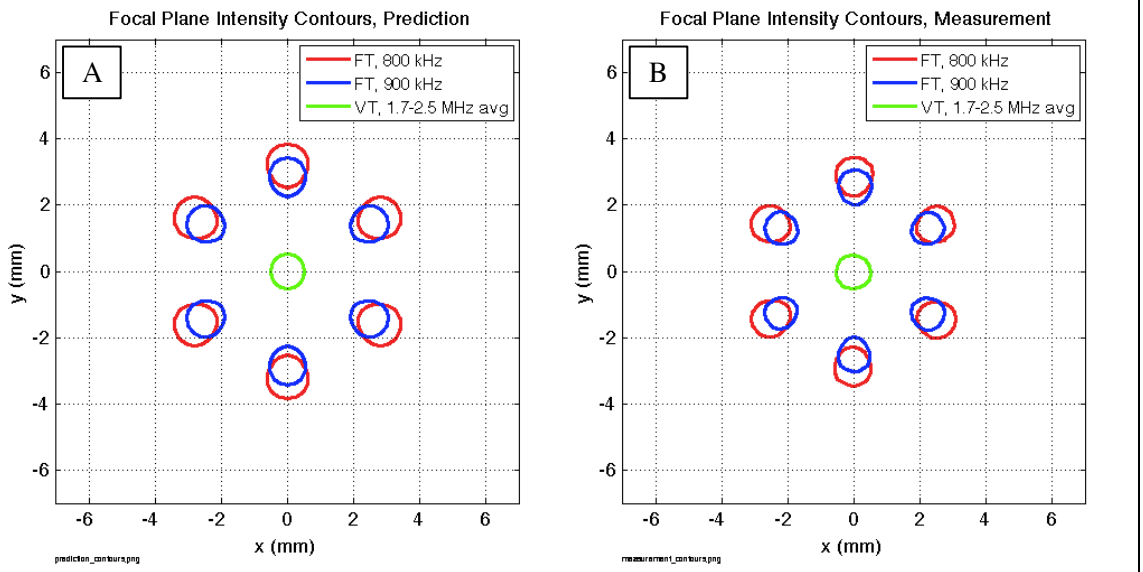

Figure 4.11. Predicted (A) and measured (B) CFE system focal plane intensity contours.

4.6 FT Harmonic Generation

It was noticed during FT calibration that significant harmonic levels were present in the hydrophone data. Since the calibration drive levels were fairly low, it was of interest to examine harmonic generation for drive levels in the range of those envisioned for CFE system testing. The subset of the calibration scans were therefore repeated using a chirp drive signal spanning 700-900 kHz, with measured power amplifier output amplitudes of 2.9, 5.8, 9.3, and 19.7V. The measured focal plane field pressures are shown in Figure 4.12 at the "primary" frequency of 850kHz, as well as at 1.7MHz ("second harmonic") and 2.55 MHz ("third harmonic").

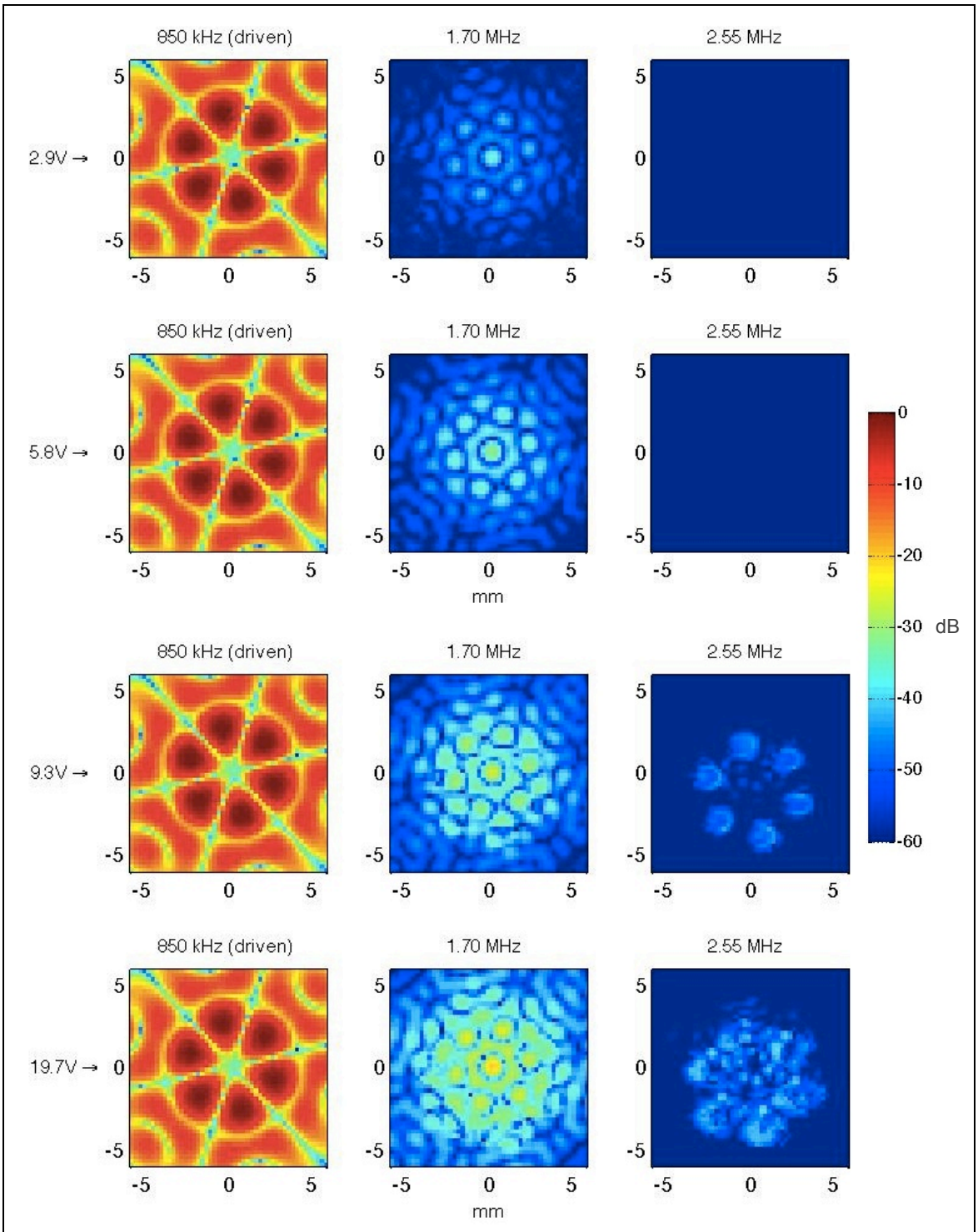

Figure 4.12. Focal plane pressures for four FT drive voltages (rows) evaluated at three frequencies (columns). Levels (dB) are normalized in each row to the peak at 850kHz.

While the field patterns at 850kHz did not change meaningfully with drive level, the harmonic levels clearly grew with increasing drive. Specifically, the second harmonic amplitude grew with the square of the primary drive level, while the second harmonic trend was difficult to judge due to the low overall levels relative to the noise floor of the measurement. The second harmonic pattern contained significant on-axis and near-axis responses, which were of some concern in their potential to produce unwanted displacements in the region the VT observes. The second harmonic pattern was considerably lower in amplitude and was vertically offset, suggesting the involvement of a scattering mechanism, perhaps related to a slight tilt of the hydrophone relative to the FT beam axis.

The magnitude of second harmonic contributions to force generation was estimated first by noting that at the highest drive level, the maximum on-axis second harmonic pressure was 22 dB lower than the peak pressure in any of the six lobes of the primary pattern. Recalling that force generation in an absorbing medium is proportional to intensity and attenuation: $F_v = 2\alpha I_0 e^{-2\alpha z}$, and noting that in a tissue-like material, the attenuation at the second harmonic would typically be twice as high as that of the fundamental, the combined intensity and attenuation differences would make the second harmonic on-axis force approximately two orders of magnitude smaller than any of the primary frequency peripheral pattern force levels. Simulations of total displacement generation in a soft tissue-like material by primary and second harmonic patterns as measured for the highest drive level showed that total on-axis motion from the second harmonic would be 40-50 dB smaller than from the converging shear field motion

produced by the primary drive frequency. So, concern over displacement field contamination by drive harmonics was alleviated.

The origin of the harmonics was initially investigated within the drive instrumentation. The waveform generator, with a 1.9MHz passive low pass filter at its output, had first and second harmonics that were below the fundamental by approximately 60 and 80 dB, respectively. At the output of the power amplifiers driving the FT, the harmonic levels were 50 and 60 dB, respectively, when operating with the highest input voltage tested. Addition of a high power capacity low pass filter at the amplifier output lowered the harmonics by approximately 10 dB each. By comparison with the observed field pressures, the bulk of the harmonic generation must have occurred in the transducer or in the propagation path.

The signal received by the VT outer ring element during the focal plane scans was also processed, and is shown in Figure 4.13. The signals correspond to scattering from the needle hydrophone tip as it traversed the focal plane. Measurements were made with a band pass filter in place, so frequencies below 1.4 MHz and above 3.4MHz were heavily attenuated. The second harmonic was the largest contributor to the VT response. This raised a concern that FT harmonic scattering from within tissue would contaminate the vibrometer processing band.

For the transducer generation mechanism, the second harmonic may be formed by a simple quadratic non-linearity in the transducer. This would rectify all the drive polarities so that the transducer would feature an M=0 output mode characterized by an on-axis main lobe. If generated in the propagation path, harmonics would be produced in the focal regions produced by the fundamental. That is, the six lobes produced by the

fundamental M=3 drive would each act as sources of the second harmonic. Directivity calculations for such a distributed volumetric source showed a weak on-axis field.

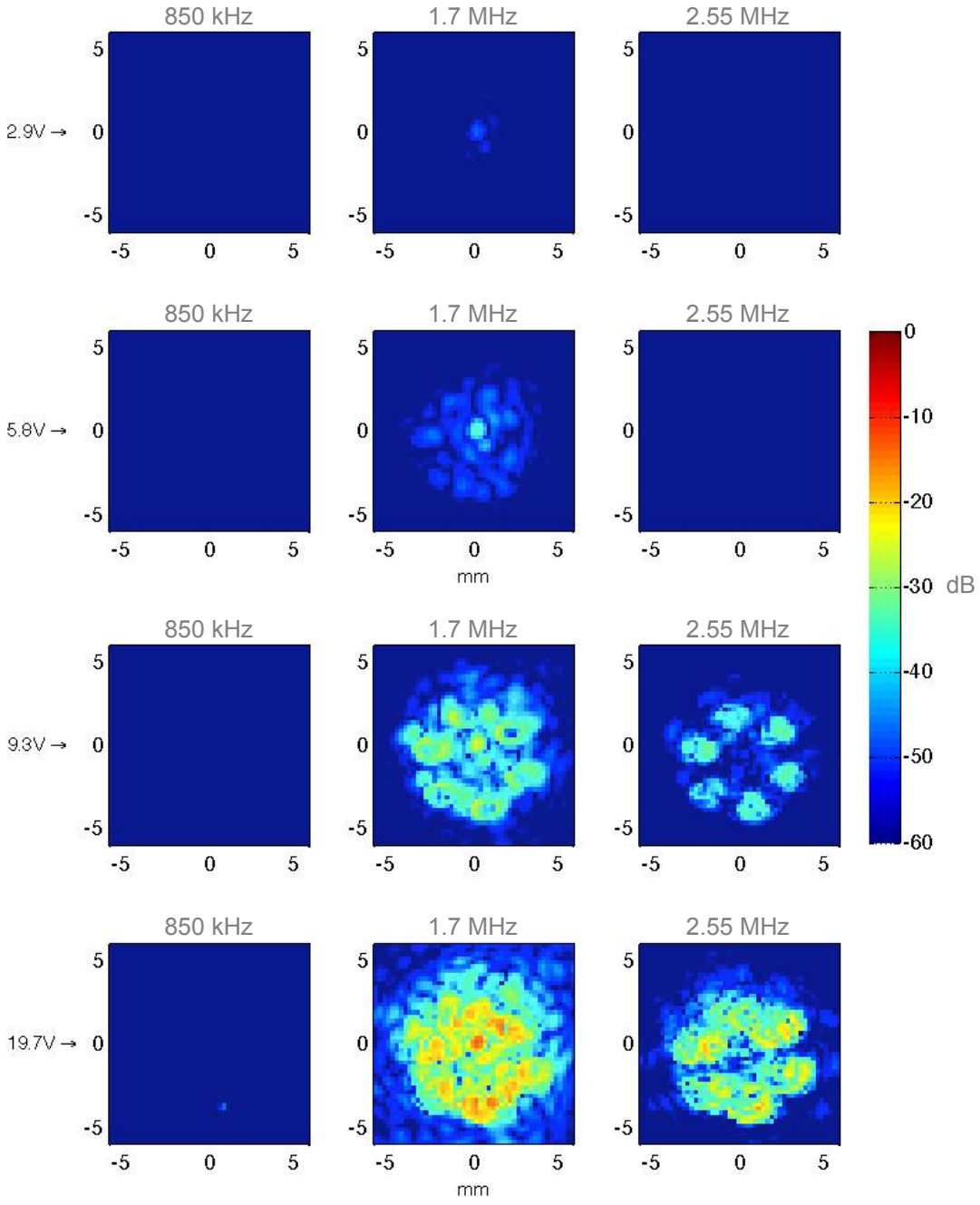

Figure 4.13. VT receiver levels as a function of FT primary drive level. Levels (dB) are normalized in each row to the peak at 850kHz.

However, path-generated harmonics may enhance force generation in the primary (peripheral) lobe regions because higher frequencies have higher attenuation rates, and therefore produce higher force per unit volume. This type of non-linear contribution to force generation has been studied for "conventional" ultrasonic elastography systems (Sarvazyan et al., 1998; Nightingale et al., 2001).

An additional calibration experiment was performed in order to ultimately enable suppression of second harmonic generation by the transducer. Such "predistortion" methods have been investigated for medical ultrasound applications (Krishnan, Hamilton, & O'Donnell, 1998). The FT was driven in the primary frequency band with M=3, and subsequently in the second harmonic band with M=0. A frequency domain transfer function for second harmonic generation was formed:

$X(f) = \frac{H_0/D_0^2}{H_1/D_1}$, where H_0 and H_1 are the pressure spectra resulting from driving the transducer at the fundamental (D_0) and second harmonic D_1, respectively. The fundamental drive term is squared to capture quadratic nonlinear generation of the second harmonic. The transfer function was applied to a typical 700-900 kHz calibration waveform $w_0(t)$ in order to produce a pre-distorted waveform $w_1(t)$ with a suppressed second harmonic: $w_1(t) = real(\, ifft(\, [\, fft(w_0(t)) \, - fft(w_0^2(t)) * X]))$.

Figure 4.14 shows focal plane pressures resulting from a test of the above approach to second harmonic suppression. The upper pair of plots shows the spectrum levels at 800 kHz using the baseline (normal) and harmonic suppressed waveforms. No meaningful changes were observed, as expected. The lower pair of plots shows the spectrum levels at 1.6 MHz for the same waveform sets. The average second harmonic

suppression within a 1.5mm radius spot (where the VT would image) was 16.5 dB. The residual pattern appeared to consist of higher order modal contributions, with highest amplitudes in twelve lobes approximately at the same radius as the 800kHz fundamental pattern. From a subsequent axial field scan, the harmonic suppression within a 1.5mm radius spot was found to be at least 10 dB within +/5 mm axially of the focal plane.

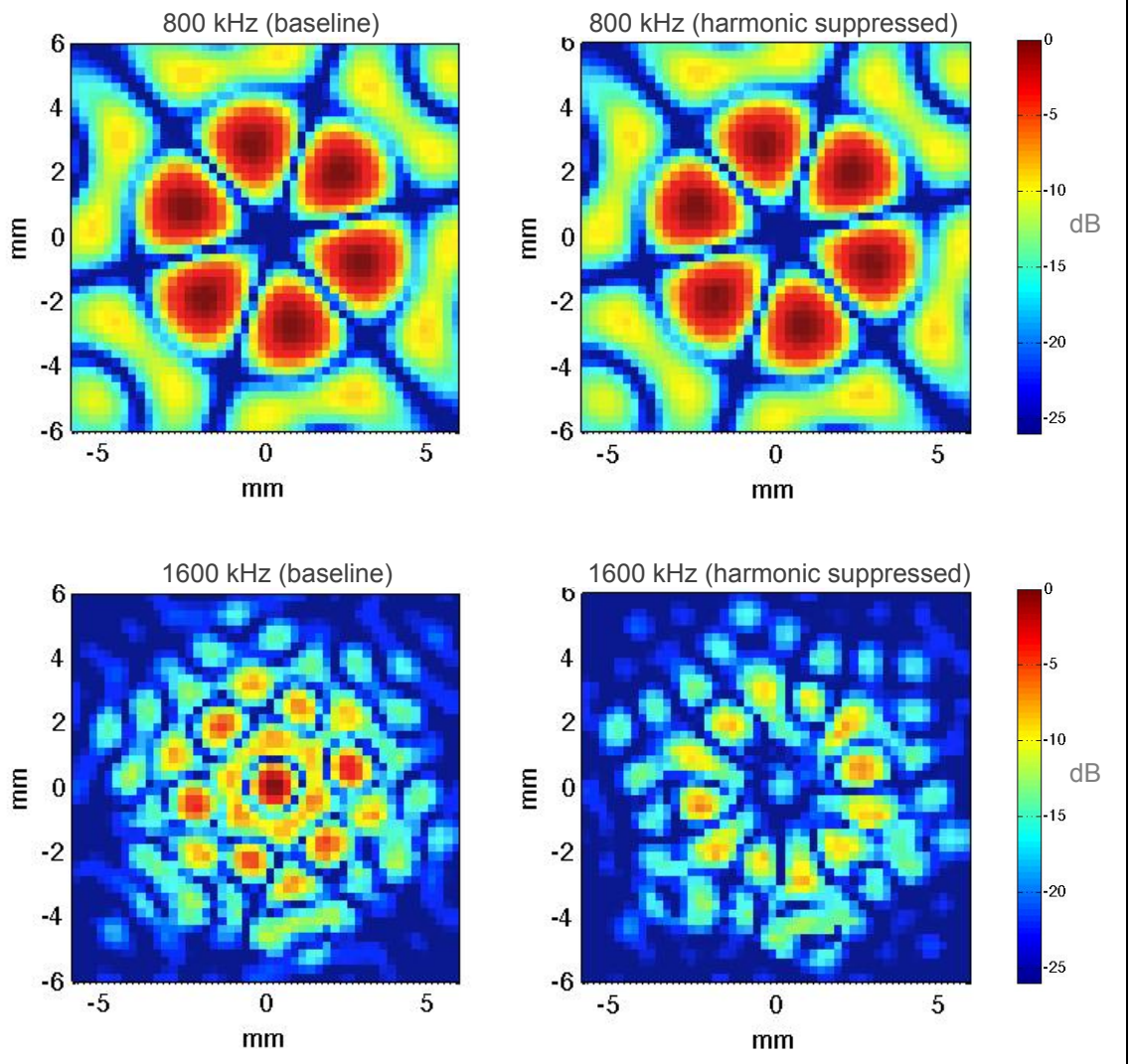

Figure 4.14. Second harmonic suppression results in the FT focal plane, 800 kHz (upper row), and 1.6 MHz (lower row).

These results suggest that the observed second harmonic was being primarily generated by the transducer. This may not necessarily be the case when testing in tissues or tissue-like materials, which have been reported to have higher parameters of non-linearity than water (Duck, 2002)

4.7 FT Field Robustness

In addition to running the field scans described above, a focal plane pressure field measurement was made for each of the individual FT sector elements. The primary objective of this work was to support simulation of field formation robustness with respect to sector magnitude and phase errors, whether produced by the actual variations in the elements, or through drive signal errors. Since the six FT sector elements are required to produce an intensity field with well defined peripheral lobes around a center null, it was of interest to see how tolerant the as-built prototype system was to uncorrected element-level errors.

Baseline field pressures were calculated by summing all elements (M=0) or subtracting alternating elements (M=3). Subsequent simulations were carried out by applying zero-mean magnitude and phase errors of a specified RMS value to each of the elements before field formation. These error weights were of the form $w_n = (1 + \varepsilon_n)e^{-i\gamma_n}$, where ε_n and γ_n were arrays of six random numbers with rms value of n, with n varying from 0.1 to 0.4. For these simulations 200 realizations of each error level (n) were run.

Figure 4.15 shows focal plane intensity patterns at 825 kHz for four RMS sector weight levels. All values were normalized by the maximum of the baseline (no error) pattern. The blue curves are the magnitude averages of the random error ensembles, and the green curves span ±1 standard deviation. Over the range of values tested, the random weighting errors do little to impact the field shape.

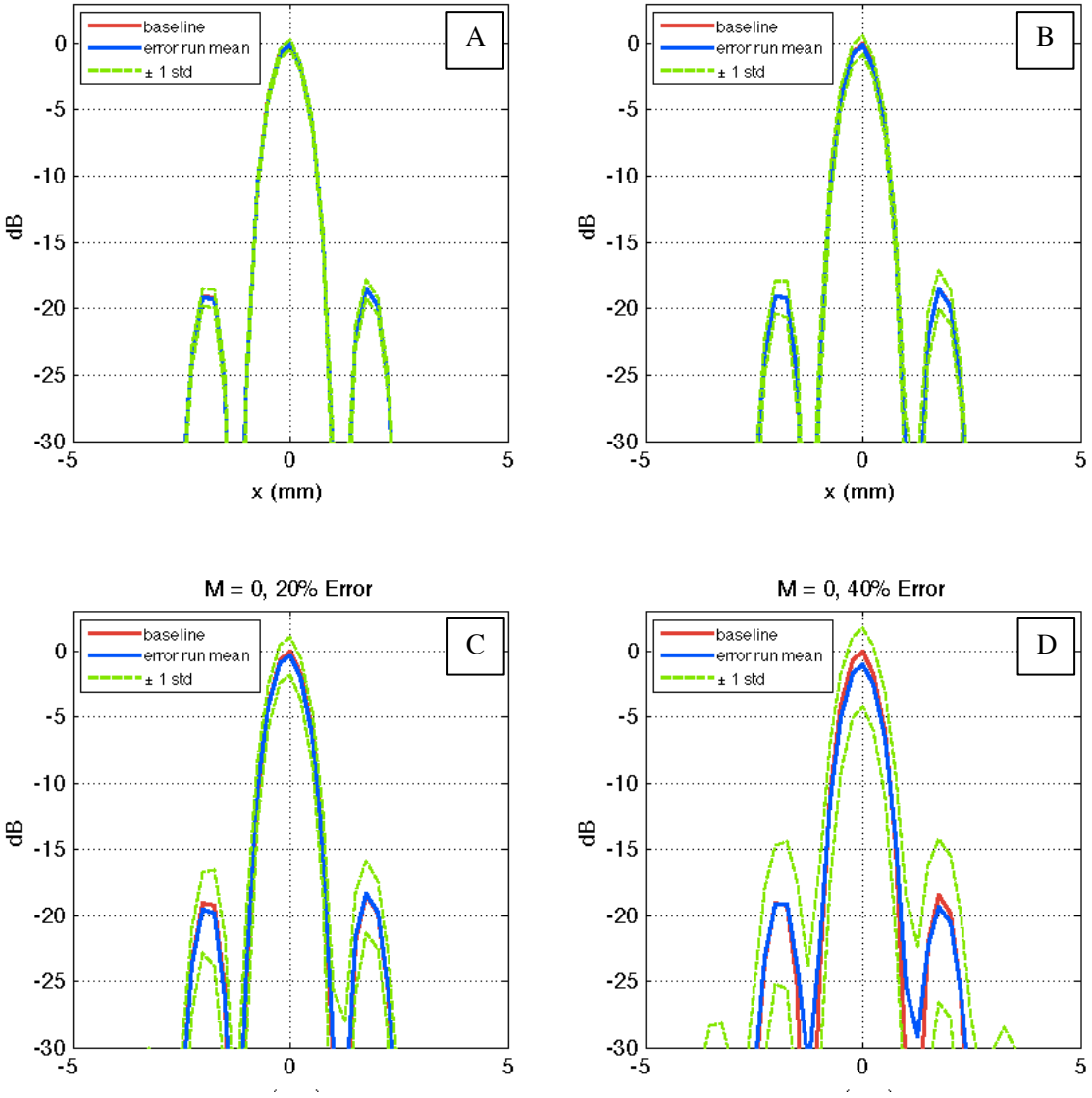

Figure 4.15. Simulated focal plane beam patterns at 825kHz, M=0, for RMS sector weight errors of 5, 10, 20 and 40 % (A-D, respectively).

The normalized M=3 focal plane intensity patterns at 825 kHz are shown in Figure 4.16 for four RMS sector weight levels. While the peripheral lobes behave similarly to the main lobe of the M=0 drive condition, the primary effect of random weight errors is to reduce the depth of the center null. This illustrates a potential vulnerability of the FT beamforming approach – nulls created through explicit subtraction of individual element contributions are more sensitive to errors than are lobes created by constructive interference.

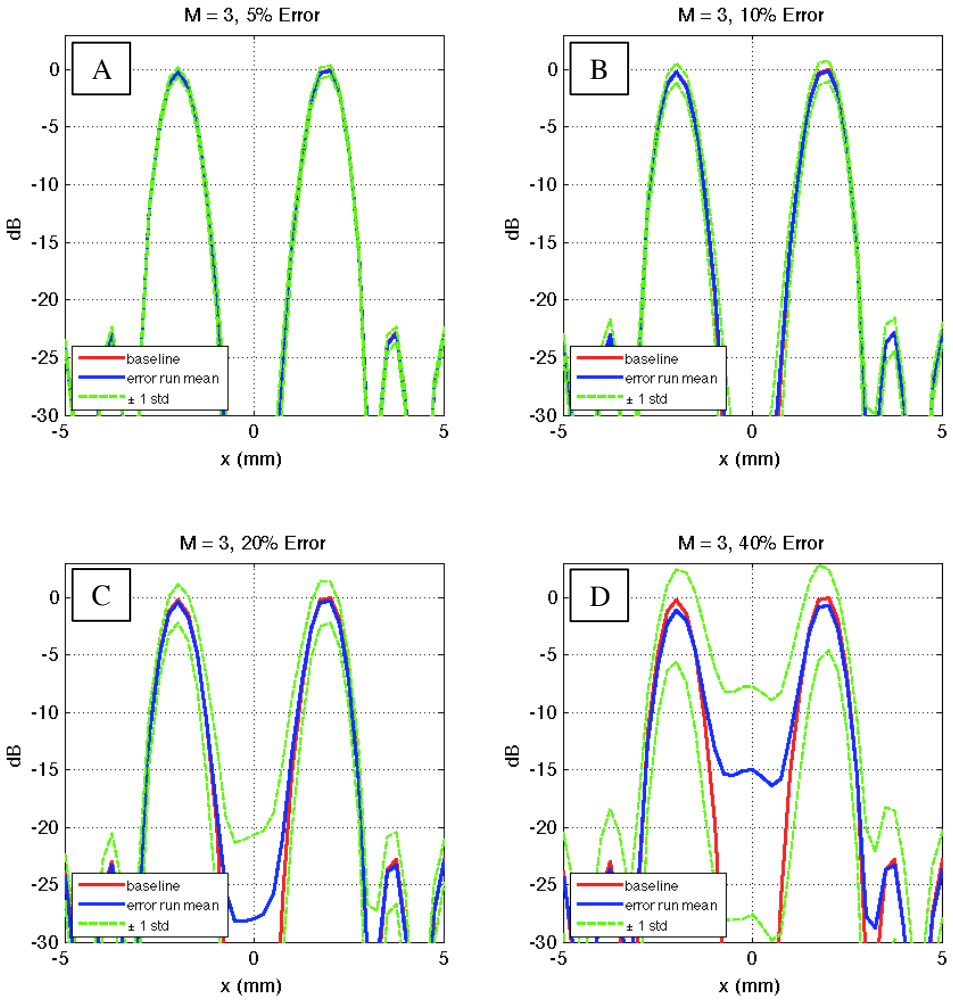

Figure 4.16. Simulated focal plane beam patterns at 825kHz, M=3, for RMS sector weight errors of 5, 10, 20 and 40 % (A-D, respectively).

A follow-up set of simulations was run to determine the impact of the sector weight errors on CFE shear estimation performance. For each random error ensemble, the ultrasonic intensity field was computed for carriers of 725 and 825 kHz, with the results used to calculate focal plane displacements using the viscoelastic model described in Chapter 2. The propagation medium was given a shear elasticity of 9.0 kPa and shear viscosity of 0.0 Pa•s. The relative phase of the displacements at the focal plane center was then fit to a two-parameter model ($G_{estimate} = \mu_1 + i\omega\mu_2$) which allowed non-zero values of shear viscosity.

The results of these simulations are displayed in Figure 4.17, where the cyan bars indicate ensemble mean value properties estimates, and the error bars span ± one standard deviation. At all error levels, the shear elasticity was estimated within 10% of the actual value. Shear viscosity shows a growing positive bias with increasing sector weight errors. This appears to be the result of contributions to the total displacement response from the displacements generated near the pattern center by elevated on-axis intensities (see Figure 4.15D). At the highest error level, displacements generated at the pattern center contaminate the total response most strongly at higher frequencies, where shear waves produced at the primary forcing lobe locations are more heavily attenuated by spreading losses in proportion to $\sqrt{k_s r}$. As center-generated displacements exceed those produced by the peripheral lobes, the relative phase response of the two carrier drives approaches zero. For the error cases studied here, the displacement phase response is "bent" upward with increasing frequency, deviating from a simple linear delay expected for elastic wave propagation. The shear fit model interprets the distorted phase as being

produced by a slightly stiffer material with a high viscosity, whose contributions to the shear modulus increase linearly with frequency.

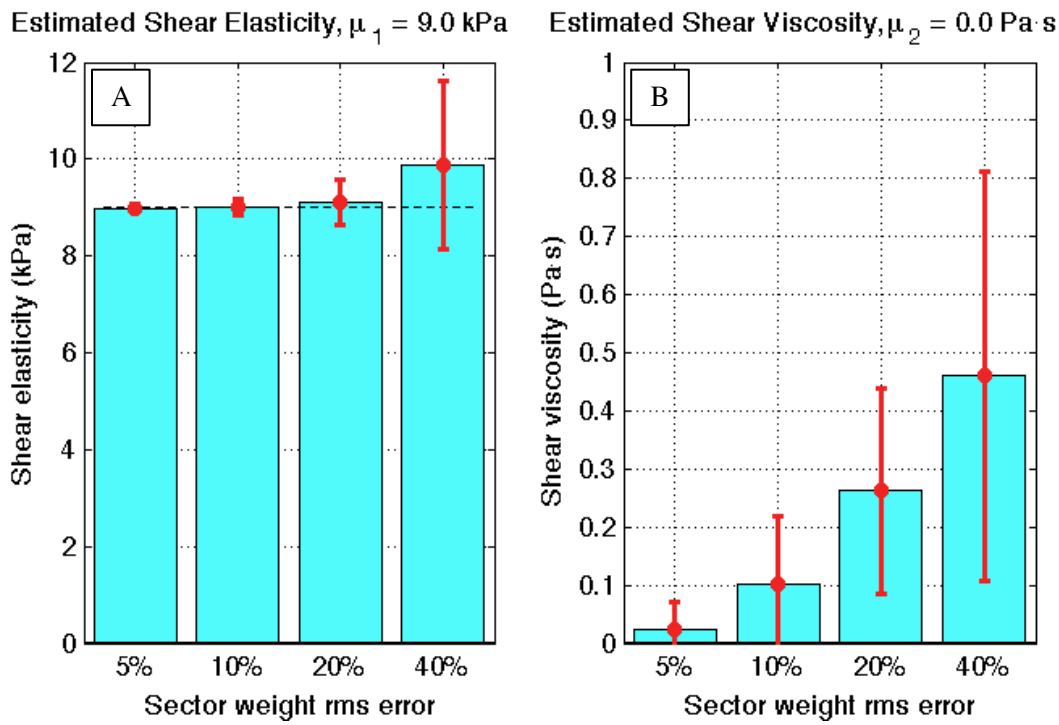

Figure 4.17. Sector weight error impact on shear elasticity (A) and viscosity (B) estimation.

In the current CFE prototype, FT sectors are driven in groups of three, and the measured output magnitude and phase differences between groups are in the range of 1-2%. Therefore, the system is run without intentional sector or group weight corrections. The simulations presented here demonstrate the effects of uncorrected drive or calibration errors on shear property estimation performance. The impacts of measurement noise and tissue complexity (in the form of bone transmission) are considered in Chapters 7 and 8, respectively.

4.8 Calibration Summary

The prototype CFE transducers were calibrated, and despite small deviations from their respective predicted behaviors, both transducers appeared suitable for testing of the CFE concept. Specifically, the slight radial condensation of the FT field patterns could be compensated for by a 10% downshift in drive frequency. The VT showed somewhat elevated sidelobe levels in the 2-4mm radial range, but the overall characteristics of the transducer appeared to be adequate. FT drive harmonic generation was investigated, and a method for defining harmonic suppression drive waveforms was demonstrated. Effects of uncompensated FT sector output variability were quantified, and it was found that shear viscosity estimation is sensitive to FT intensity pattern degradation.

CHAPTER 5

POINT TARGET TESTING

"Lasers make it look like you know what you are doing" – Peter Cameron, 2011

5.1 Objectives

Having calibrated the individual prototype CFE transducers, a sequence of experiments was designed with the goal of validating the force generation and vibration measurement procedures with a repeatable and independently verifiable apparatus. Specifically, the objectives were to:

- Demonstrate that motion generated by the force generation transducer (FT) could be accurately measured with the vibrometer transducer (VT);
- Validate vibrometer experiment results through independent measurement; and
- Investigate and mitigate any FT signal contamination of VT data that degrades processed results.

The vibrometer algorithm is discussed in section 5.2, followed by the methods and results for validation testing in sections 5.3 and 5.4, respectively.

5.2 Vibrometer Algorithm

Under a parallel effort, a vibrometry algorithm was developed (Martin, Rogers, & Gray, 2011) with the intention of providing the sensitivity of pure-tone doppler techniques and the range resolution of pulse-echo techniques. The algorithm thus

developed was an updated version of the non-invasive vibration amplitude measurement system (NIVAMS), which was originally developed for measuring motion of fish internal auditory structures (Cox & Rogers, 1987). NIVAMS originally employed continuous signals and achieved range specificity using separate transmitting and receiving transducers whose beams intersected in a spatially concentrated region in space. Subsequent efforts enabled determination of vibration phase within the transmit-receive beam crossing region (Finneran & Hastings, 2004). The refined processing approach used in the present work provided displacement as a function of time and distance along the vibrometer beam axis, and was renamed NIVMS because both amplitude and phase information are produced (Martin, Rogers, & Gray, 2011).

The NIVMS tonal/pulsed hybrid vibrometry method may be illustrated in terms of its transmission signals, shown in Figure 5.1. A sequence of N broadband pulses is emitted with pulse repetition period T. The ensemble of pulses has a spectrum with the bandwidth (BW) of a single pulse and the tonal resolution of the sequence of pulses ($1/(N \bullet T)$), as demonstrated through comparison with a true tonal signal with duration $N \bullet T$ (Figure 5.1E). Whether the transmission is pulsed or tonal, scattering objects with vibration components along the beam path will produce sidebands around each of the carrier tones. The use of a pulsed (broad band) transmission signal allows range mapping of these vibrations. The extraction of low frequency displacement data from the modulated carrier information presumes that the amplitude of these displacements is small compared to a carrier wavelength. For the present system, this restriction caps the displacement amplitudes below approximately 10 μm, which is much larger than the maximum predicted displacement with CFE at 12+ cm depth in any tissue-like material.

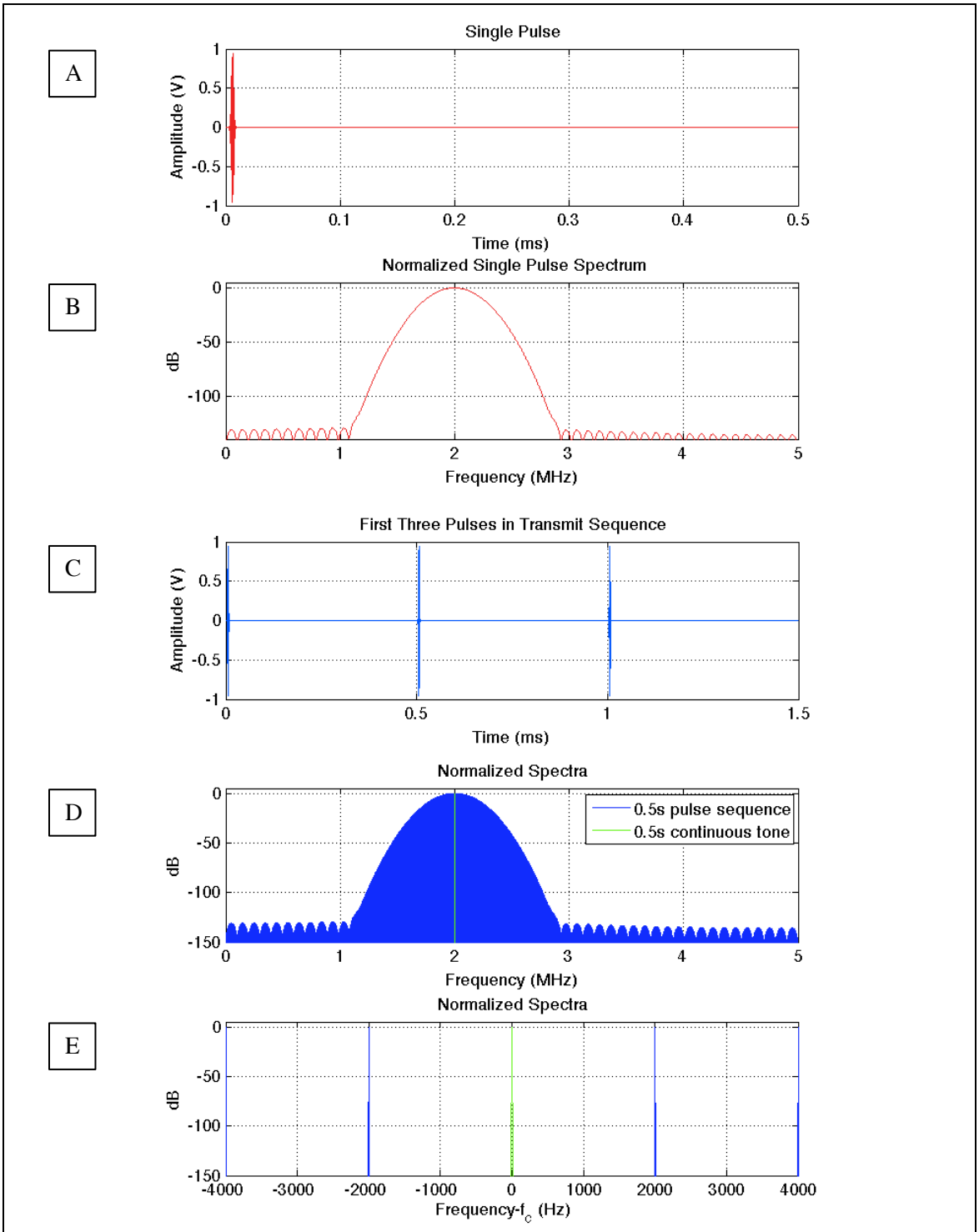

Figure 5.1. Single pulse vibrometer signal (A) and normalized spectrum (B). Example of multi-pulse sequence with T = 0.5 ms (C). Half-second duration multi-pulse sequence and tonal full band spectra (D) and carrier-centered spectra (E) zoomed +/-4kHz.

The pulse repetition period also defines the output sampling frequency ($1/T$), bandwidth ($1/2T$), and maximum reverberation time. In practice, this latter quantity limits the largest one-way distance ($cT/2$) from which a scattered signal can be received without wraparound into the subsequent pulse period. For example, with T = 500 μs, c = 1500 m/s, $N \bullet T$ = 0.5 s, and BW = 1.0 MHz, NIVMS may unambiguously resolve vibration from scatterers up to 37.5 cm from the vibrometer transducer, reporting vibration magnitude and phase up to 1kHz in 2 Hz bins. Axial resolution (Δz) is associated with the bandwidth of the individual pulses ($\Delta z \sim \frac{c}{2}\frac{1}{BW}$).

While operation on a sequence of pulses offers a degree of random noise suppression, further improvements in measurement signal to noise ratio (SNR) were made by increasing the interrogating signal energy. Such energetic increases may be achieved through increases in pulse amplitude, but these amplitudes are capped by ultrasound safety considerations. Moreover, when the data acquisition dynamic range is limited (as with the 12 bit analog to digital converter used in the present work), increasing pulse amplitude is only useful if dynamic range is optimized as a result.

By contrast, increases in pulse length (constrained to be less than T) can be used to augment incident energy regardless of digitizer dynamic range. When long transmission pulses were used, a compression process was used to recover the range resolution of a minimal duration transmission, subject to the condition that scatterer displacements are much smaller than the carrier wavelength (Martin, Rogers, & Gray, 2013). This condition was already assumed in the fundamental vibrometry algorithm, and was valid for laboratory CFE experiments, but the validity of compression processing during physiologic motion of live animals remains to be tested.

Vibrometer [‡‡] developments within the scope of this dissertation were in transducer design, drive signal design and processing of the raw vibrometer data to reduce contamination from force transducer output, as discussed in the remainder of this document.

5.3 Experiment Configuration

One class of validation approaches used in the elastography literature is the use of one or more small reflectors as targets. The origin of many of these methods was the sphere radiometer (Dunn, Averbuch, & O'Brien, 1977), wherein a solid sphere target was suspended at the end of a thin filament in order to form a simple pendulum. A steady beam of ultrasound emitted by a transducer exerted a radiation force on the sphere (as a result of scattering, not absorption), displacing it from its equilibrium position. Since the force on the sphere was proportional to incident acoustic intensity, measurement of static displacement could be used to calibrate the transducer. Dynamic radiation force measurement techniques based on the radiometer approach embedded the sphere target in gelatin (Chen, Fatemi, & Greenleaf, 2002) or fastened it to a thin membrane (Chen, et al., 2004). In both cases, constraining the sphere with an acoustically transparent material minimized static deflection and simplified measurement of dynamic motion with ultrasonic or laser vibrometers.

The membrane-suspension approach, shown in Figure 5.2, was chosen for its simplicity of implementation. A 0.74 mm diameter sphere made of 440 stainless steel

---

[‡‡] Development of the range-resolving vibrometer algorithm was led by James Martin, Georgia Institute of Technology.

(Bal-tec, Los Angeles, CA) was adhered to a 13um thick membrane of low-density polyethylene (CVS Pharmacy Inc., Woonsocket, RI) using silicone (Loctite, Avon, OH). The membrane was stretched over an 18.4 cm diameter circular PVC frame with just enough tension to remove visible wrinkles, and was held in place using a combination of adhesive and an O-ring. The membrane frame was attached to a two-axis positioner for use in aligning the sphere target with the transducers used in this experiment.

In all experiments, the FT was driven with all elements in phase (M = 0) and aligned with the sphere target on the basis of backscatter strength. Ultrasonic estimates of FT-induced sphere motion were made with the VT employing the NIVMS algorithm described in the section 5.2. A single waveform generator was used for FT and VT signal creation, with low pass filters used to reduce residual digital-to-analog conversion noise passed to the amplifiers. Power amplifier output levels were monitored with scope probes. A clock source (SRS CG635) provided a highly stable 10 MHz reference signal for the waveform generator and digitizer, reducing timing jitter and improving vibrometer performance. Ultrasonic data sets were processed off line in MATLAB to yield target displacement estimates.

Independent estimates of sphere motion were made using a laser Doppler vibrometer (LDV: Polytek PDV100, Tustin, CA). The analog output of the LDV is velocity, so the only additional processing was compensation for internal and external filter delays, and gain correction for the index of refraction. The latter was required because the LDV internal processor assumed operation in air, but the vibrations modulating the light beam occurred in water, where the index of refraction was 1.33 (Giancoli, 1984).

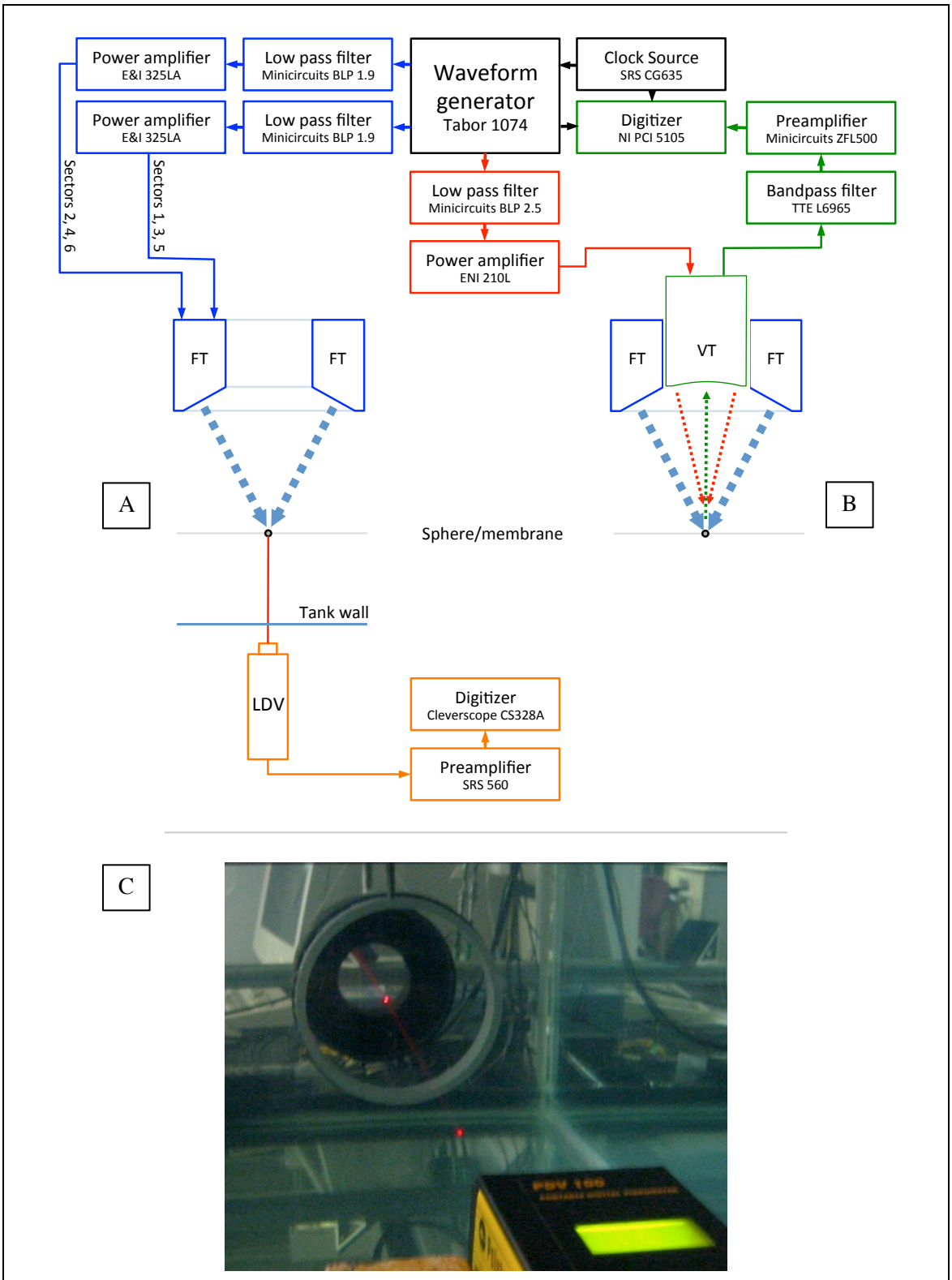

Figure 5.2. Sphere target experiment configuration illustrations with laser (A) and ultrasonic (B) vibrometers, and a photograph of the laser configuration (C).

The baseline VT drive waveform for these experiments, shown in Figure 5.3, was a 33 μs duration, 1.1MHz bandwidth chirp centered at 1.975MHz, with a repetition frequency of 2 kHz. The center frequency was between the harmonics of likely FT drive frequencies (fundamental 850kHz and 2nd harmonic of 1750 kHz), and the signal bandwidth spanned the range of best performance of the VT transducer. The baseline pulse rate of 2 kHz meant that vibrations at frequencies above 1 kHz would be aliased by the vibrometer, which had no inherent low pass filtering capability.

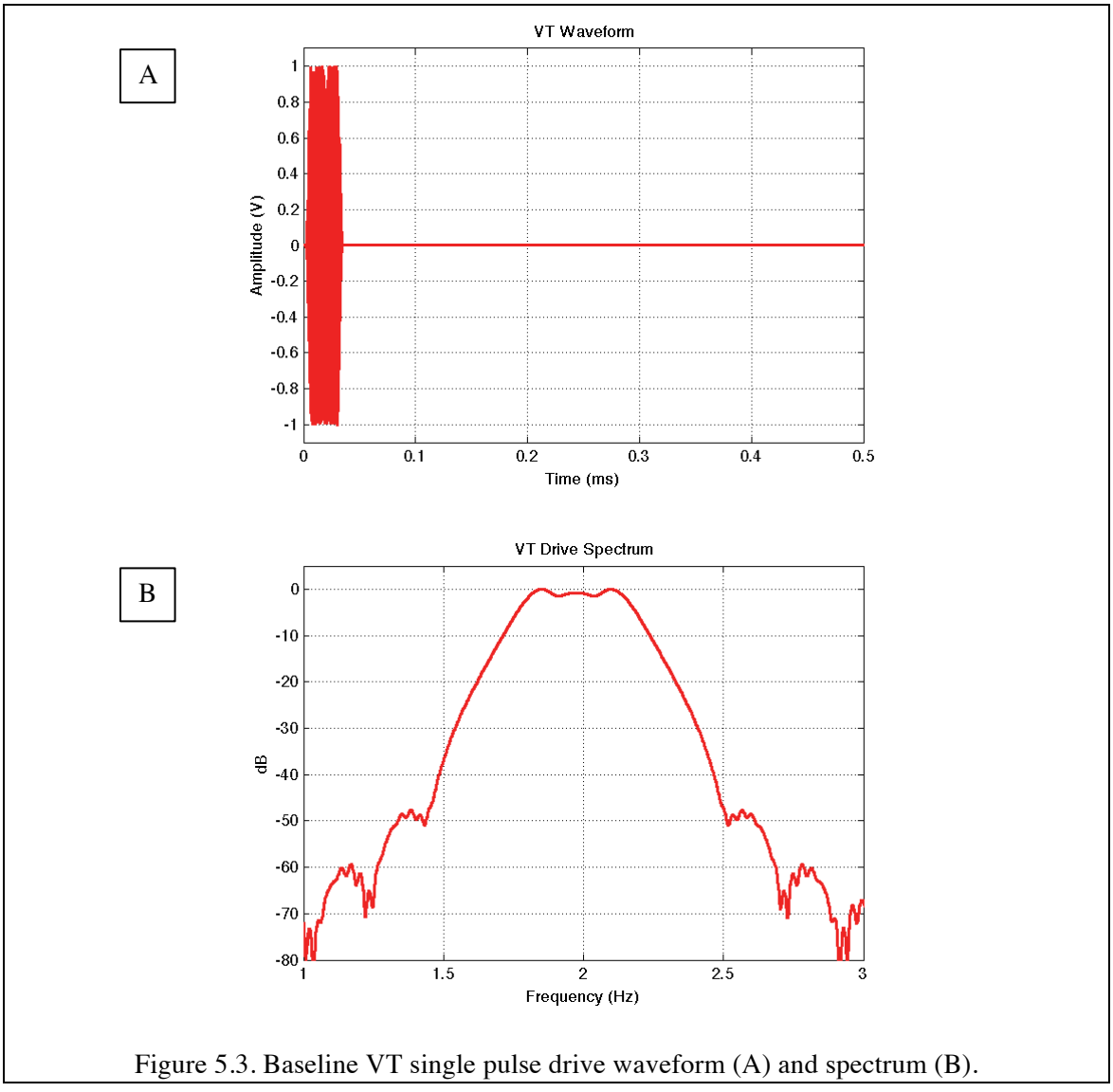

Figure 5.3. Baseline VT single pulse drive waveform (A) and spectrum (B).

The baseline FT drive signal was a 2920 μs Hanning-windowed 850 kHz tone pulse, with 64 Hz pulse repetition frequency. The use of pulsed signals was intended in part as a diagnostic measure, allowing time-separation of potential interactions between CFE transducers. The motivation for such diagnostics came from preliminary experiments that yielded no meaningful results when employing continuous FT drive signals. Pulsed drives also provided a convenient method for collecting vibration data at multiple frequencies per transmission (as result of pulse duration), and for signal filtering to avoid vibrometer aliasing. The force generated by the FT is proportional to the square of its drive voltage. As seen in Figure 5.4, the low frequency signal-squared spectrum behaved as a low pass filter, strongly suppressing frequencies above 1kHz.

When multiple pulses are processed together, they produce a comb spectrum, just as with the VT pulse sequence (Figure 5.1). For the specific choice of a 64 Hz FT pulse rate, the comb tones were integer multiples of 64 Hz (Figure 5.4B), with the property that drive-squared tones above 1kHz and below 7kHz would not alias onto driven tones below 1 kHz. For example, the highest two multi-pulse tones below 1kHz were 896 and 960 Hz, while the first two aliased components would wrap around to 2000 – (1024, 1088) = (976, 912).

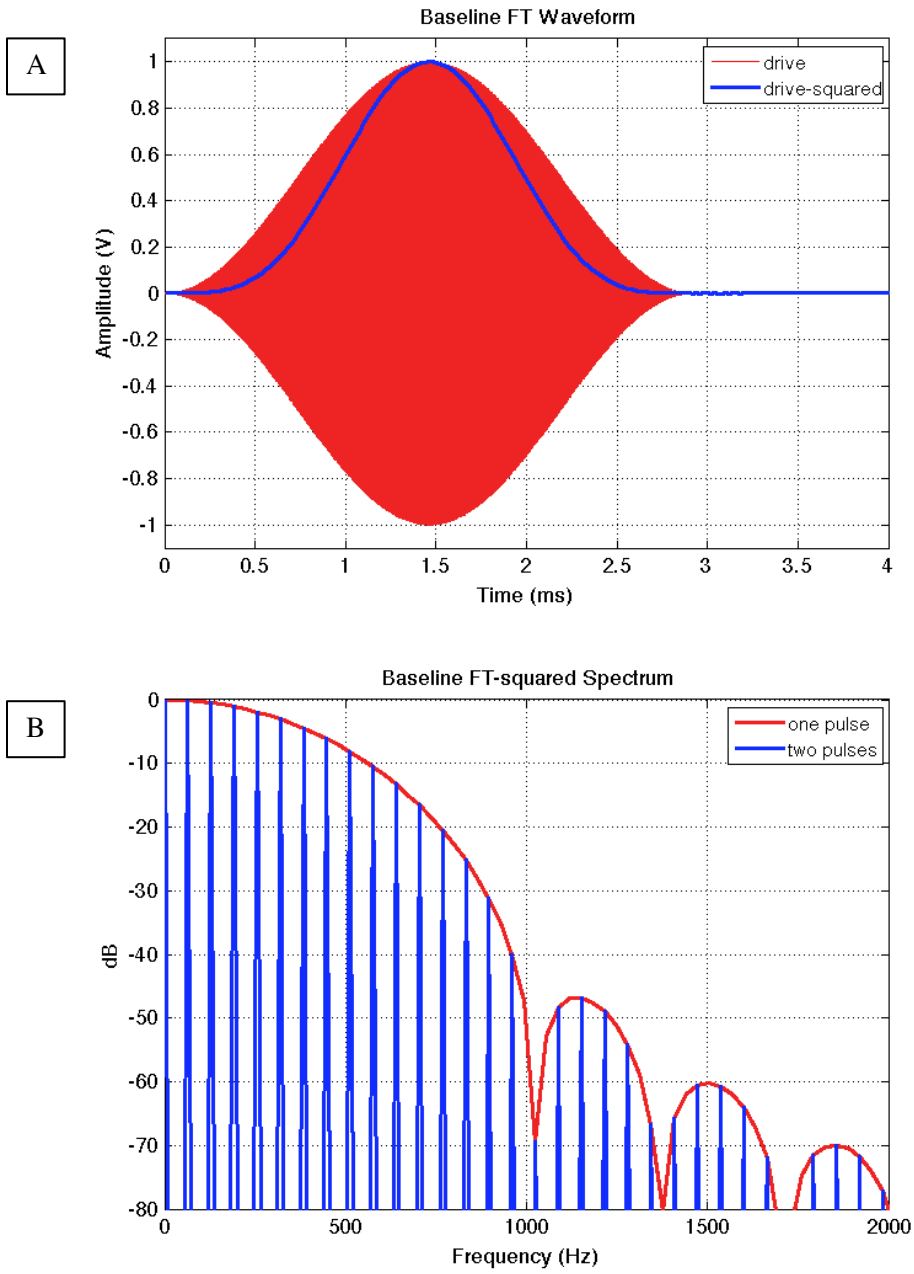

Figure 5.4. Baseline FT waveform (A) and drive-squared spectra for one and two pulses (B).

5.4 Results

5.4.1 Baseline waveform testing

Figure 5.5 shows the velocity of the sphere target during four FT drive cycles as measured by the VT and LDV, with the latter shown at its original sampling rate and downsampled to the NIVMS output rate of 2kHz. The VT signal was inverted in order to match the sign convention of the LDV measurement made on the opposite side of the target. In the time domain, the VT response varied significantly from pulse to pulse, with some apparent phase drift. The LDV results were consistent pulse-to-pulse, although when down-sampled to 2kHz, they showed modest variation in amplitude. This was a result of the FT pulse repetition frequency of 64 Hz not being an integer divisor of the 2kHz sampling rate, causing the waveform to be sampled differently depending on its position in the time record. This effect repeats in cycles of four FT pulse periods (4/64 seconds = 125 cycles at 2kHz).

The frequency response of the LDV in Figure 5.5B consisted primarily of 64 Hz multiples, as expected from the drive signal employed. The VT response was similar to the LDV at the expected frequencies, but it included an additional set of high amplitude tones offset from the expected frequencies by 32 Hz. Since the NIVMS algorithm and instrumentation had been validated using a non-ultrasonic vibration source (Martin, Rogers, & Gray, 2011), it was thought that in the present experiment, the RT radiation was contaminating the VT in some way.

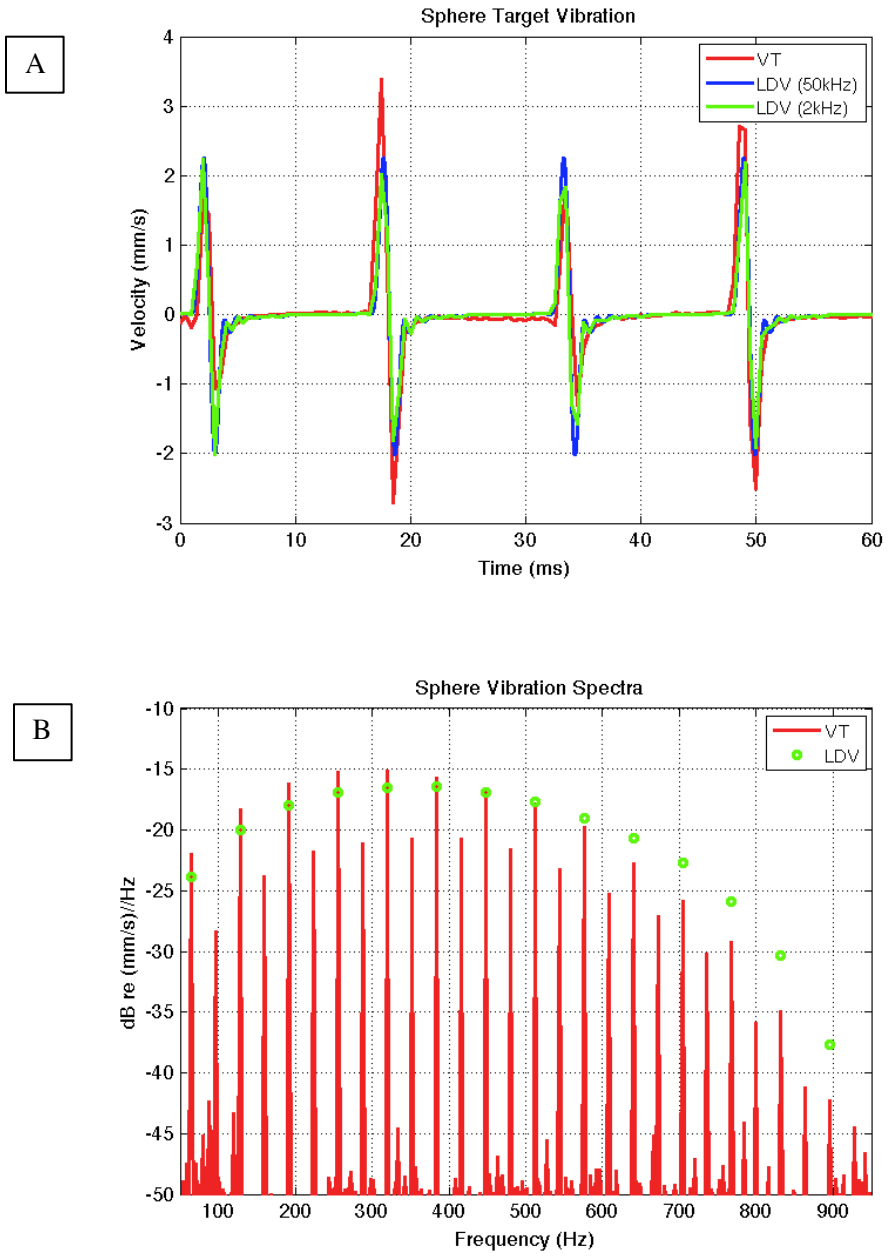

Figure 5.5. Sphere target vibration time series (A) and spectra (B).

Figure 5.6 shows the raw VT receiver data used to generate the processed results in Figure 5.5. The very first received pulse in the time record (~15mV amplitude) was cross-talk between the VT transmitting and receiving elements, and indicated the start of a VT period. The second pulse, approximately 70 mV in amplitude and delayed 186 μs

from the initial transmission, was the scattering from the sphere target. The third and smallest pulse was a reflection from absorbers at the back of the tank. This three-pulse receive cycle repeats at the VT pulse repetition rate of 2 kHz (1/0.5 ms). The first and last 0.5 ms periods in the time record shown are indicative of how the receiver behaved when the FT was not transmitting. At and around the center of the time record, the VT receiver showed a change in its response, corresponding in duration to the FT transmission. The timing appeared to correspond to scattering of the FT transmission by the sphere target, as indicated by the green line in Figure 5.6A, formed by delaying a scaled version of the FT drive-squared signal (blue line) by the two-way propagation time between transducers and the target.

Figure 5.6B shows windowed spectra both during and between FT transmissions. The "between" measurement was indicative of the VT response in the absence of any FT transmission. The "during" measurement showed strong contamination around the FT drive band (850kHz) and its harmonics at 1.7 and 2.55 MHz. This contamination distorted nearby NIVMS tones (2kHz spacing), and produced tones within the NIVMS processing band that could be falsely interpreted as target vibration-generated signals. There also appeared to be a mixing effect between FT and VT transmissions, producing a reduced-amplitude, frequency-shifted version of the VT output in the 2.5-3.2 MHz range. The data sets were originally processed with a 1.1 MHz compression pulse ("compulse"), indicated by the green line in Figure 5.6B. This compulse acts like a bandpass filter on the raw VT data, although as processed, contamination from the 2nd FT harmonic at 1.7 MHz may still have been significant.

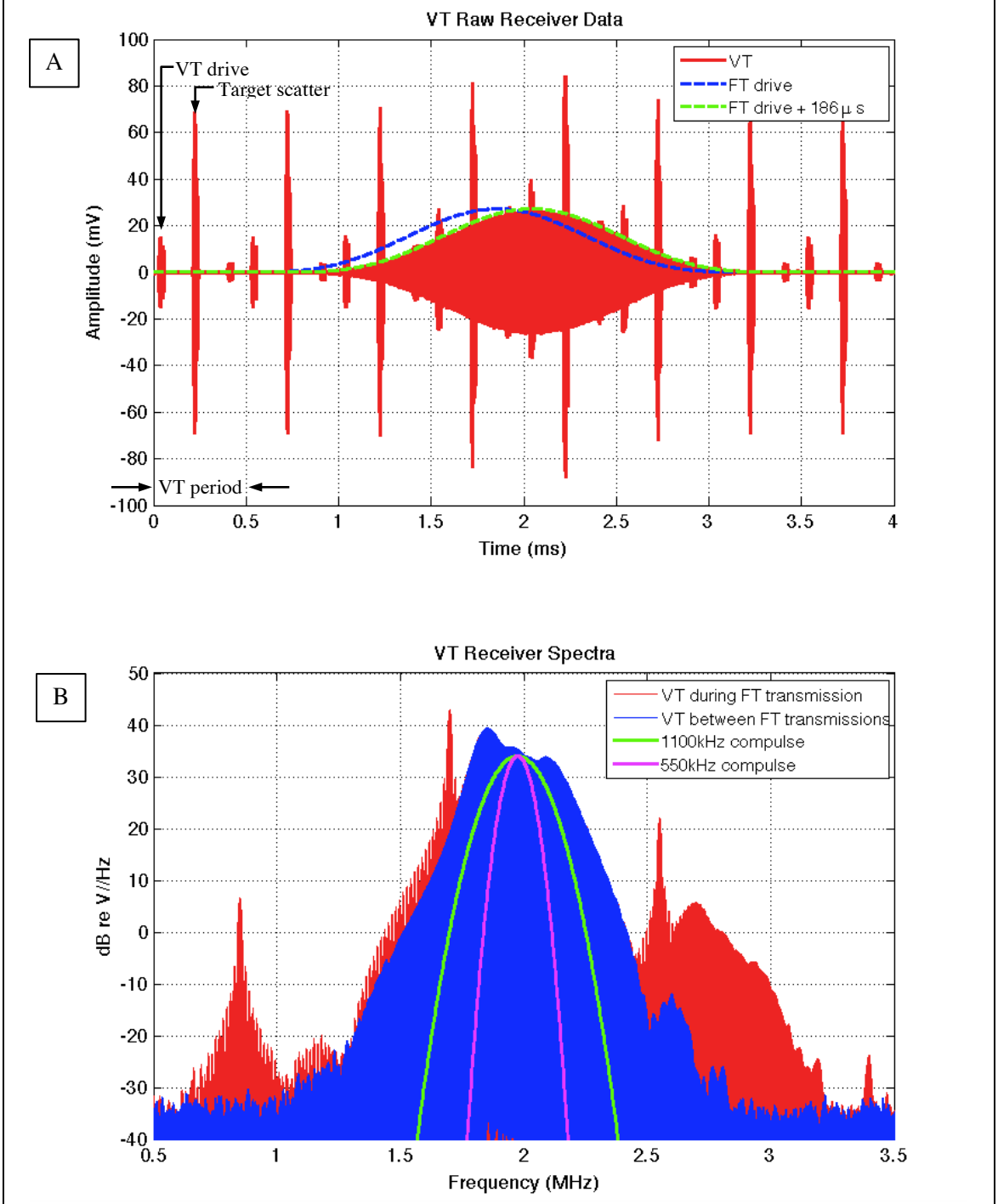

Figure 5.6. VT time series (A) and spectra (B) with baseline drive waveforms.

Target velocities calculated from a 550 kHz bandwidth compulse are shown in Figure 5.7, where the ultrasonic and laser methods are in agreement, and the primarily response frequencies are associated only with the FT pulse rate and its integer multiples.

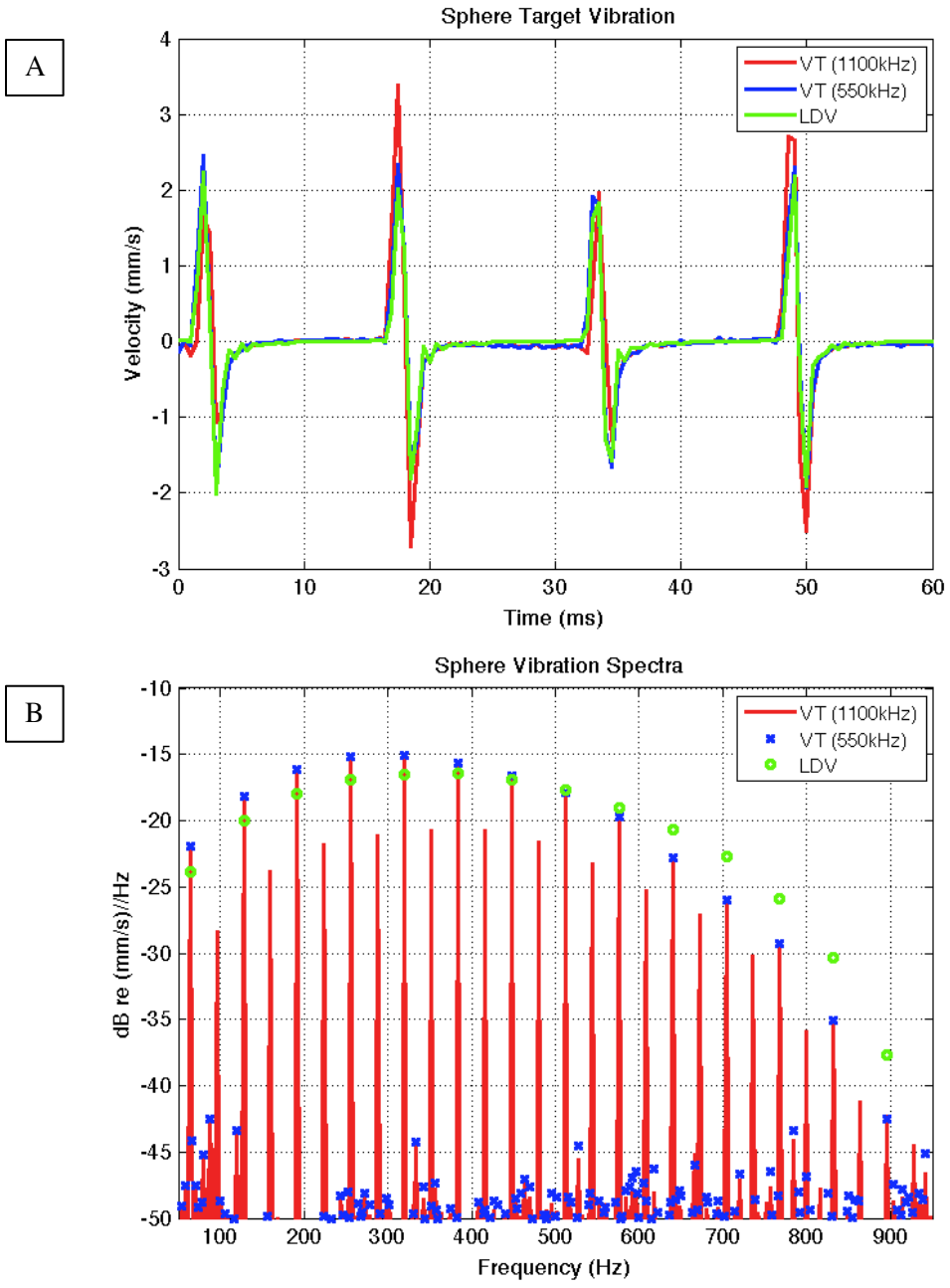

Figure 5.7. Sphere target vibration time series (A) and spectra (B) with reduced bandwidth vibrometer processing.

The residual spectral shape differences appeared to be a consequence of the membrane tension decreasing between initial LDV trials and subsequent VT trials, producing a downshift in sphere-membrane resonance frequency. There may also have been some degree of residual FT-VT contamination.

An adverse consequence of using a reduced bandwidth for vibrometry processing is a loss of axial spatial resolution. This is illustrated in Figure 5.8 with the normalized backscattered power from the sphere target. As processing bandwidth is reduced, the scattering from the 0.74 mm diameter target is spread over an increasingly large region in space. The legend entries show the half-power full-width scaling approximately with processing bandwidth, although the spreading effect is slightly attenuated by the low frequency roll-off of the VT element sensitivities and the target strength of the sphere.

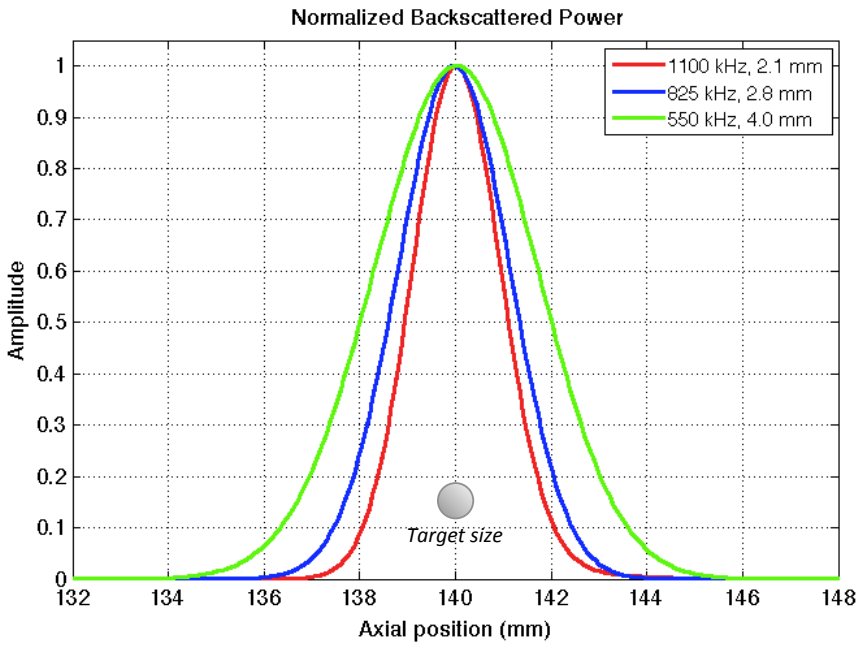

Figure 5.8. Sphere backscatter beamwidth as a function of processing bandwidth.

5.4.2 Coupling reference processing

An alternative FT-VT coupling mitigation strategy was formulated so that the vibrometer processing bandwidth would not be restricted. In addition to the normal measurements made with both the FT and VT running, a "coupling reference" measurement was made with only the FT transmitting. The coupling reference data collected on the VT receiver would be subtracted from the normal system measurement data prior to NIVMS processing. In principle, this process would remove several (but not all) of the potential system coupling mechanisms:

- Scattering of RT harmonics from the target;
- Direct path acoustic coupling between the FT and VT;
- Electronic coupling between the FT and VT;

All of the above mechanisms are linearly additive, and distinguishable by timing relative to FT transmission. VT contamination by FT target scattering was by far the dominant mechanism observed in the sphere target experiments.

Figure 5.9 shows examples of reference coupling subtraction results in the raw ultrasonic VT time series and spectra. The subtraction process was highly effective in suppressing the FT primary and second harmonic contributions to the VT response, but less so at the FT third harmonic. The spectral features between 2.5 – 3.2 MHz were essentially unchanged, consistent with the thinking that they had been caused by a mixing of the FT and VT beams, and therefore would not be captured in the reference measurement (with no VT transmission).

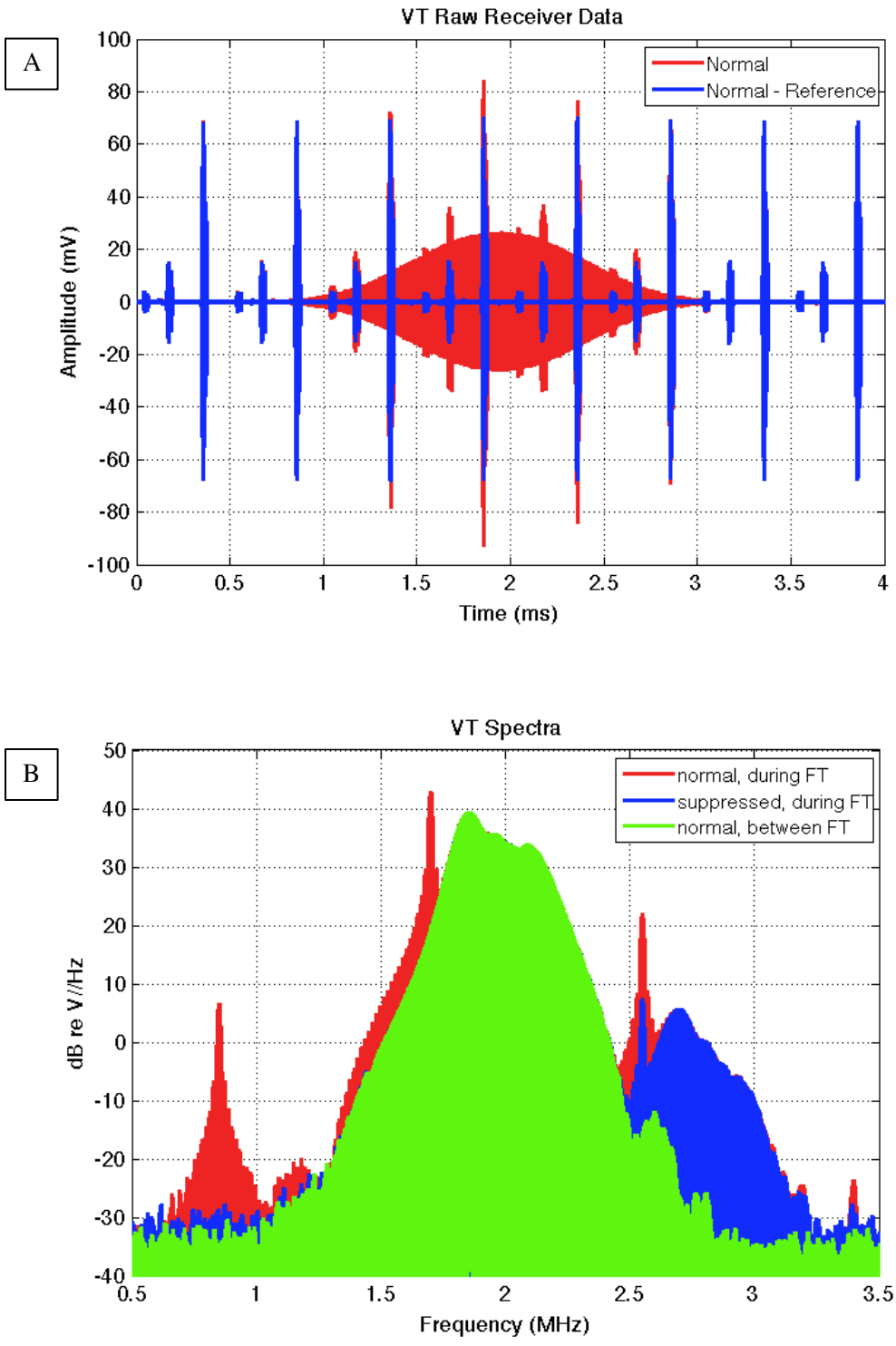

Figure 5.9. VT receiver time series (A) and spectra (B) illustrating FT coupling suppression by reference subtraction.

Figure 5.10 shows the target vibration time series and spectra derived from the data in Figure 5.9. The reference subtraction process used with 1.1MHz processing bandwidth provided nearly identical results to those obtained with 550kHz bandwidth without subtraction. So, by performing an additional reference measurement during a normal CFE experiment, FT-VT coupling can be significantly suppressed without sacrificing bandwidth and range resolution.

5.4.3 FT gap window waveforms

As described in the previous section, the reference subtraction process should be effective in removing additive coupling, but other forms may remain. One of these, FT-VT transmission mixing, was directly visible in the spectra of Figure 5.10. It was hypothesized that a modification to the FT drive waveforms could minimize additive and multiplicative (mixing) coupling effects, without the need for a separate measurement. Specifically, if the FT and VT transmissions do not overlap in time, transmission signal mixing should not occur, and FT harmonic scattering from the target would not occur at a time when VT scattering is being observed for calculation of target motion. The challenge in coordinating these transmissions was that the baseline FT signal was approximately six times longer than the VT repetition period, so that transmission overlap was inevitable (Figure 5.11A). Since the FT duration was chosen as an anti-aliasing measure, shortening it would be counterproductive. However, if the FT signal was composed of a sequence of shorter pulses, the anti-aliasing and transmission overlap objectives could both be met.

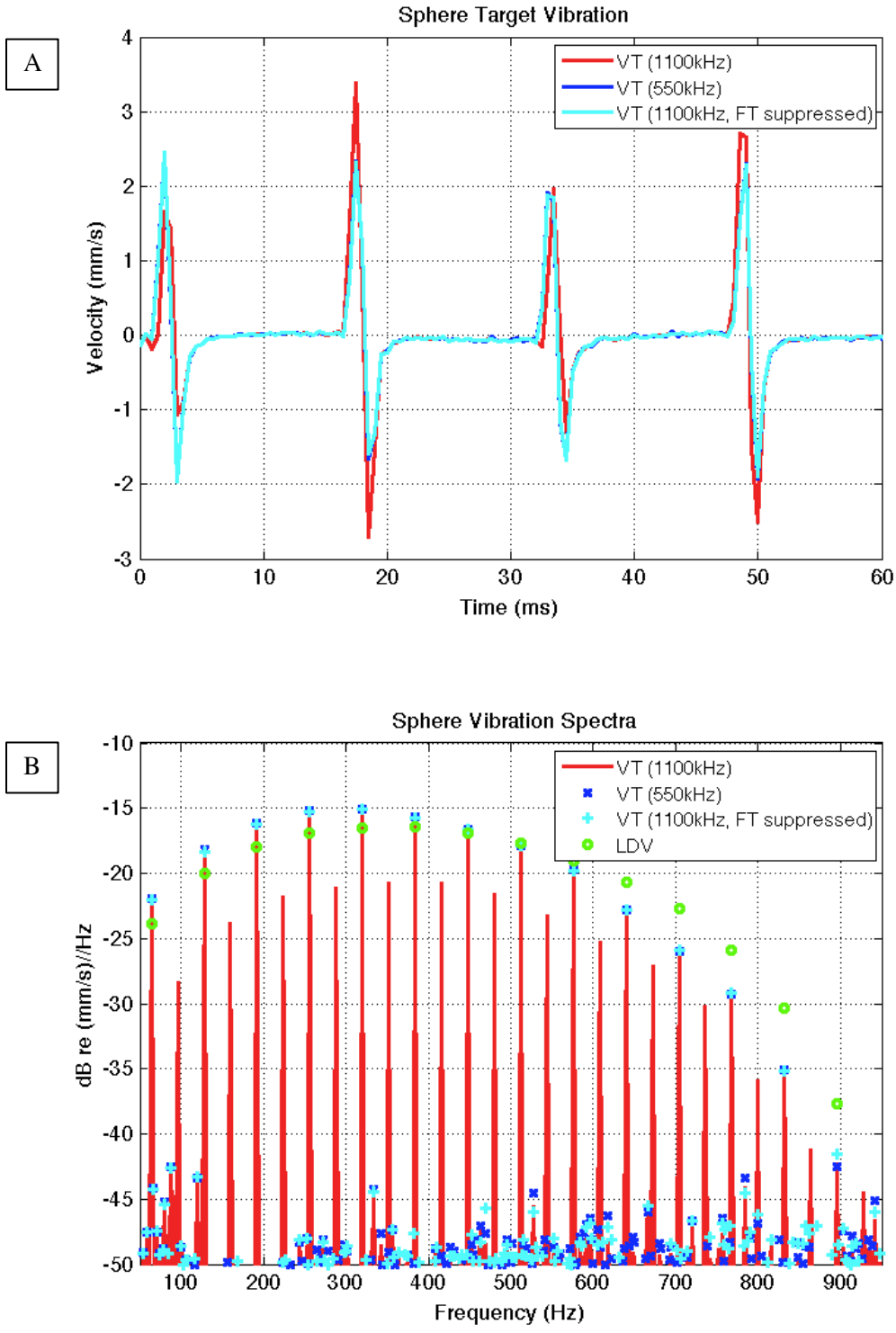

Figure 5.10. Sphere target vibration velocity time series (A) and spectra (B), illustrating FT coupling suppression by reference subtraction.

An example of one such waveform is illustrated in Figure 5.11B. The modified FT drive signal was composed of a 2920 μs sequence of 190 μs duration Hanning-windowed tone pulses separated by 60 μs gaps. This "gap windowed" FT drive waveform avoided temporal overlap with VT transmissions shorter than 60 μs.

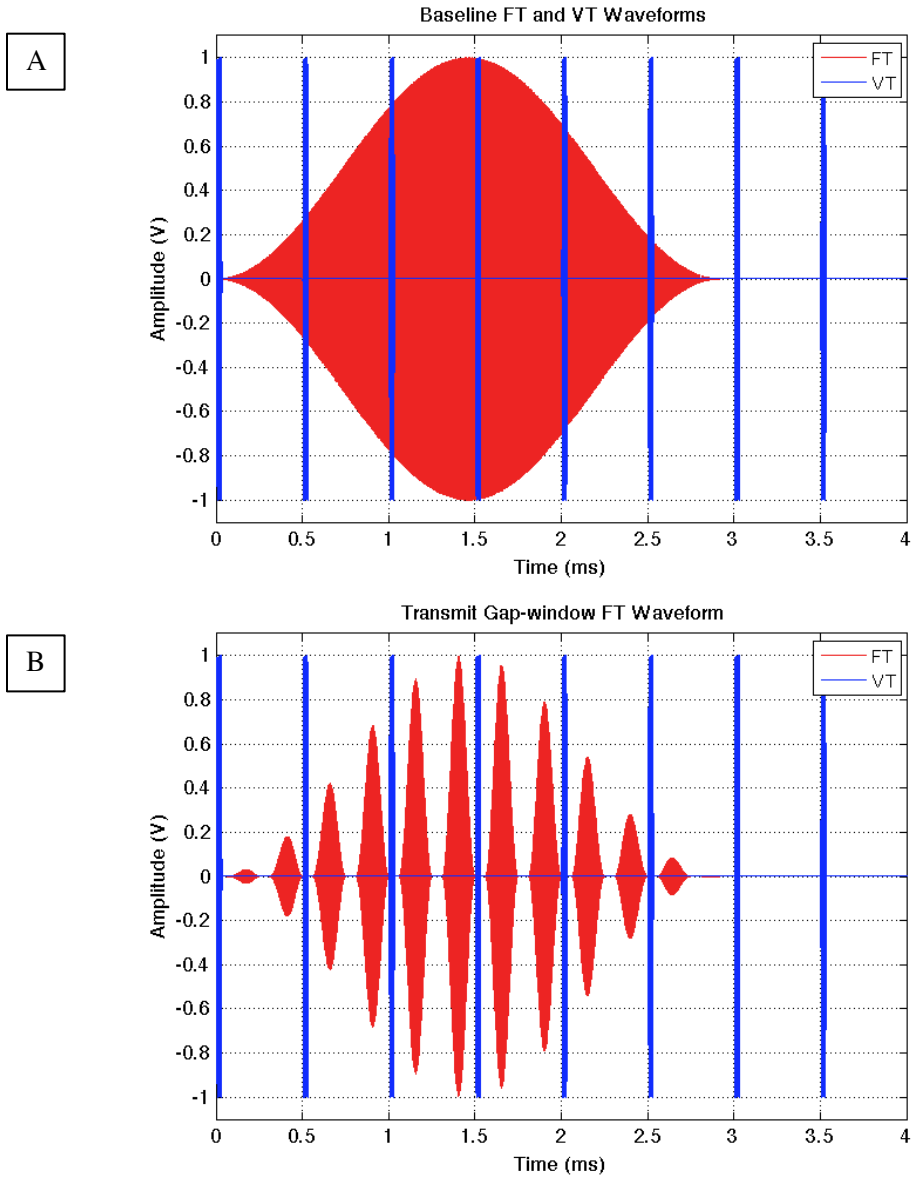

Figure 5.11. Baseline (A) and transmit gap-windowed (B) 2920us FT waveforms, overlaid with 33us duration VT waveforms.

In this example, a 33 us VT pulse is shown, with pulse timing such that scattering could be cleanly observed from the CFE focal plane and up to 1.8 cm beyond. This was done both to allow some flexibility in VT pulse length, and with an eye towards testing in phantoms and tissues, where scattering is spatially distributed.

Two effects of gap-window shaping on the low frequency signal-squared (forcing) spectrum are observed in Figure 5.12. First, the low frequency amplitude was attenuated relative to the baseline waveform. Second, the periodic spacing (250 μs) of intra-waveform pulses introduced large response lobes at 4kHz intervals. The reduced signal energy relative to the baseline waveform of identical peak amplitude could be compensated for by increasing the drive voltage to the transducer – in this case by a factor of 1.9. Ultimately this would not be necessary, as ultrasound exposure safety limits mandated a reduction of FT drive levels for this combination of waveform duration and repetition rate. The impact of the 4kHz-spaced lobes was expected to be minimal for the sphere target experiments. As described previously, the choice of FT and VT pulse rates at 64 and 2000 Hz, respectively, dictated that any vibrations between 1 and 7 kHz would not alias to the primary band tones. At these higher frequencies, the impedance of the sphere-membrane system was mass-controlled, so that aliased vibration near and above 4 kHz would be decreasingly small relative to the vibrations below 1kHz.

The particular values for gap width, intra-pulse duration, and intra-pulse windowing were chosen after assessment of associated tradeoffs. Broader gap widths allow longer VT transmissions and/or longer scattering windows without FT transmission interference. The former benefits vibrometer SNR, but at the expense of radiation force per unit drive voltage. Broader gaps also raise low frequency spectral sidelobe levels (as

with the 4kHz lobes in Figure 5.12). The intra-pulse window function (e.g. Tukey, Hanning) impacts signal energy and high frequency sidelobes, which may be important if residual coupling suppression is needed through reference subtraction. The present gap window design, while not formally optimal, appeared to provide an adequate means to evaluate the concept for waveform-based coupling suppression.

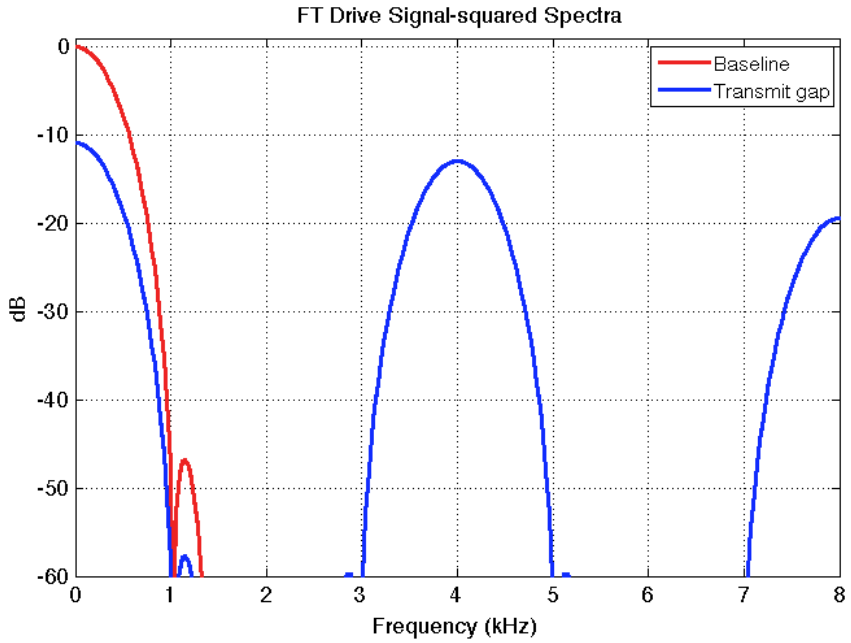

Figure 5.12. FT drive signal-squared low frequency spectra.

Figure 5.13 shows raw VT receiver time series and spectra obtained with the gap-windowed FT waveform shown in Figure 5.11. The disturbance to the VT signals is minimal during the target scattering period, as the FT scattering (outlined in blue) does not overlap with the VT scattering peaks. The spectra in Figure 5.13B show that in contrast to the baseline waveform, the gap windowed FT waveform produces negligible harmonic or mixing contamination. These transforms were computed in a 70us tapered window centered on the VT scattering peak between FT transmission maxima. The

presence of low level spectral content at the FT fundamental frequency appeared to be a result of processing window leakage. No FT harmonics were observed, since the window edge regions correspond to times where the FT drive amplitudes were small.

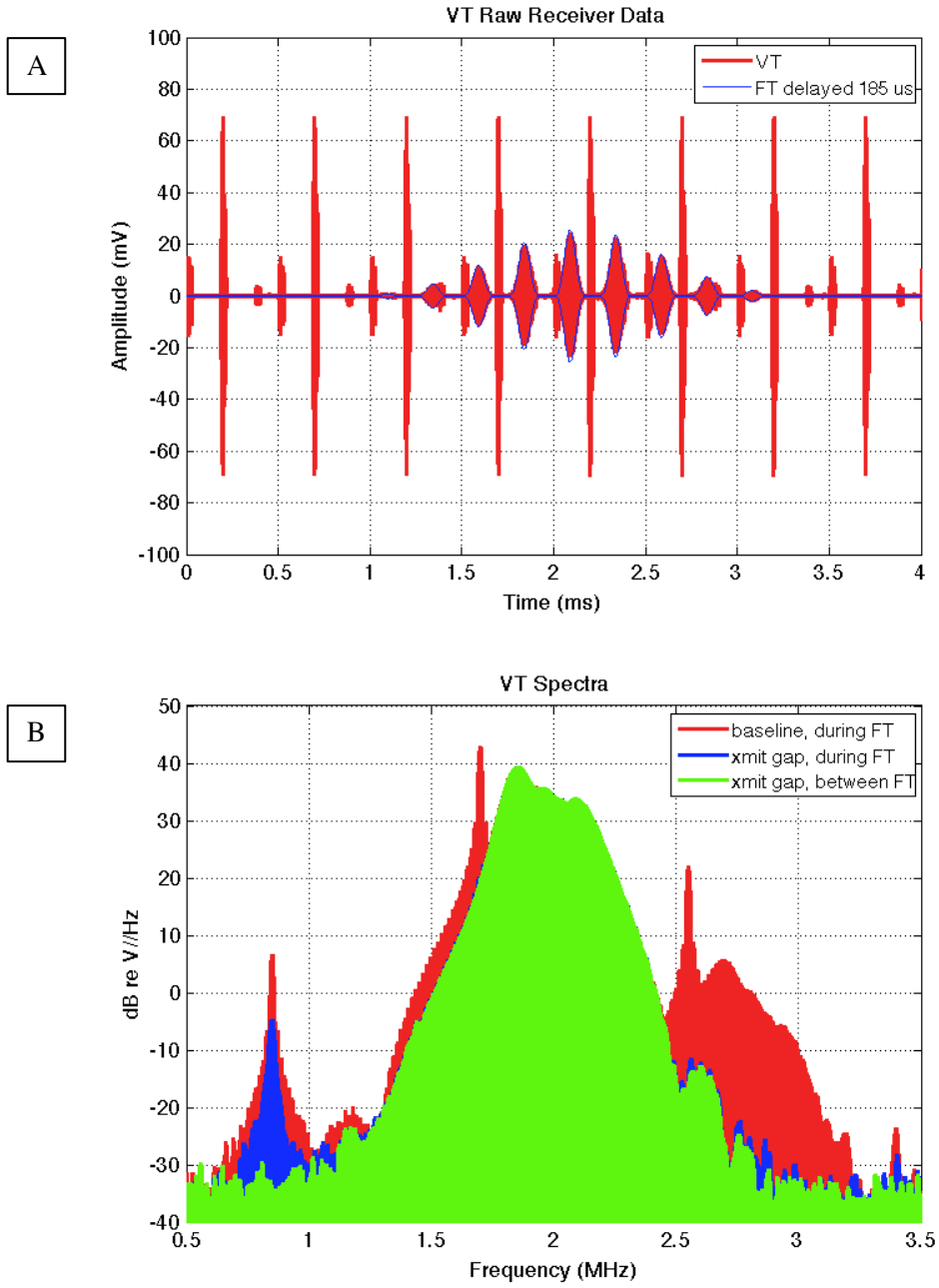

Figure 5.13. VT receiver time series (A) and spectra (B) demonstrating transmit gap-windowed FT waveform coupling reduction.

Figure 5.14 shows the target vibration time series and spectra derived from the data in Figure 5.13. All responses were calculated with a processing bandwidth of 1.1MHz. For display, the transmit gap-windowed data was scaled by the ratio of baseline and gap window drive signal powers (3.5), and averaged four times longer than with the baseline case. The reduced SNR in this measurement was still evident, but the overall results were consistent with those achieved using reference coupling subtraction with the baseline FT waveform. To that extent, the hypothesis that FT waveform design could by itself provide a significant degree of FT-VT coupling reduction was confirmed. Additional experiments showed that the above results held true when the baseline and gap windowed waveforms were transmitted at the same power.

An additional variant on the FT drive signal construction was investigated, where the intra-waveform Hanning pulse spacing and duration were arranged so that there was no temporal overlap between FT transmission and either VT transmission or focal plane scattering reception. Results were nearly identical to those for the transmit gap-window waveform design, with a slight additional penalty of reduced transmit power.

When the NIVMS concept was described in section 5.2, the pulse compression feature was described as a method for enhancing measurement SNR through the use of long-duration transmissions. In the sphere target tests, VT waveform durations were constrained between 33 and 56 μs, providing only modest SNR gain relative to the broadest bandwidth compression pulse (~ 14 μs). This particular partitioning of time between (non-overlapping) FT and VT transmissions was useful for exploring various coupling suppression techniques. This issue is revisited in Chapter 7 in the context of tissue phantom testing.

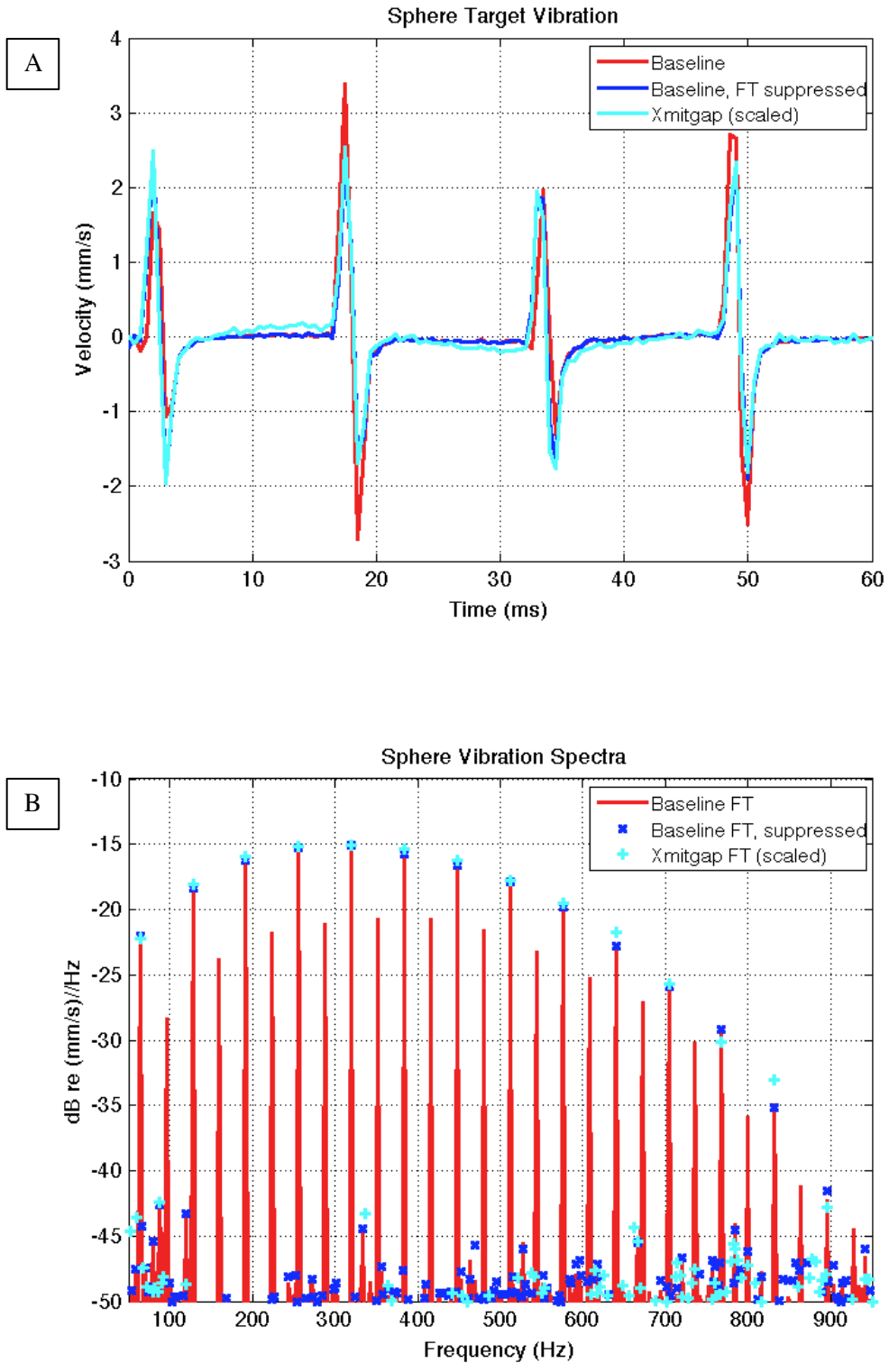

Figure 5.14. Sphere target vibration velocity time series (A) and spectra (B), illustrating FT coupling suppression by reference subtraction and gap window design.

5.5 Point Target Testing Summary

A simple discrete-target experimental model was developed for testing CFE operation, and in particular, for identifying and mitigating adverse interactions between the FT and VT subsystems. Three independent methods for FT-VT coupling suppression were identified, based on FT waveform design, VT pre-processing with a coupling reference measurement, and VT processing with reduced bandwidth. All methods seemed to address coupling arising from a common origin – that of temporal overlap of FT and VT transmissions. Avoiding this overlap through waveform design and sequencing appeared to yield valid ultrasonic vibrometry results without constraining processing bandwidth or performing additional measurements. That said, all three methods could be used together if deemed necessary.

The point-like target testing described in this chapter differed in several ways from planned testing with tissue-like materials. These materials were expected to scatter sound throughout the VT and FT beam paths, so gap windowing waveform designs may not be adequate for coupling suppression purposes. However, the expected frequency dependent path attenuation (soft tissue attenuation increases as f^n, with n usually greater than unity) may help reduce FT harmonic levels. Finally, the point target testing was conducted with the FT operating with all sectors in phase (M=0), which meant that the FT and VT beams had significant spatial overlap. Going forward, the FT would operate with M=3, so that there should be minimal FT-VT beam overlap, especially near the focal plane. As such, mixing effects may not be an issue for M=3 operation. These issues are all addressed in Chapter 7.

CHAPTER 6

TISSUE PHANTOM DEVELOPMENT

6.1 Objectives

After concluding the point target experiments, the next step in the evaluation of the CFE prototype system was to conduct experiments with tissue-mimicking materials, or "phantoms". It was of interest to perform these experiments using materials having ultrasonic and low frequency viscoelastic properties representative of cetacean living tissues. However, as was the case with viscoelastic properties, there were no values for *in vivo* cetacean soft tissue ultrasonic properties in the literature. The significance of this lack of information was that both the attenuation and intrinsic backscatter strength directly affect CFE performance. Force generation levels are impacted by attenuation, while vibrometer signal strength is influenced by both attenuation and backscatter strength. Therefore, in the absence of relevant properties information, prototype tests would be conducted with materials that may yield misleading results regarding the feasibility of working with the actual tissues of interest.

In order to make meaningful laboratory assessments of the CFE system, a set of experiments was carried out with the objective of measuring the ultrasonic properties of living cetacean tissues. These measured values would then be used to define properties for laboratory tissue phantoms. This chapter describes the live animal testing, data processing and properties estimation, and the phantoms created based on the test results.

6.2 Cetacean Testing

6.2.1 Subjects and Measurement Regions

Ultrasound data were collected on a total of three cetaceans housed at Georgia Aquarium facilities. The test subjects were two *Tursiops truncatus* (bottlenose dolphins): *TT1* (female, age 44, 160kg), *TT2* (male, age 2, 90kg), and one *Delphinapterus leucas* (beluga whale): *DL* (male, age 18, 773kg). All procedures followed a protocol approved by the Georgia Aquarium Conservation, Research and Animal Care Committee and the Institutional Animal Care and Use Committee at the Georgia Institute of Technology.

Backscatter data were collected with the transducer held on the skin over the proximal mandible and temporal regions, as illustrated in Fig. 6.1. For each of these regions of interest, data were collected at four sites by advancing the transducer rostrocaudally in steps of approximately 1 cm, which was much broader than the transducer beamwidth and therefore ensured the measurements were statistically independent. At each of the sites, four to eight sets of 128 backscatter pulses were acquired.

6.2.2 Measurement Hardware

The measurement system used for the cetacean tissue tests is shown in Figure 6.2. Ultrasonic backscatter data was collected using a transducer (Imasonic 6090A101) consisting of two concentric elements with 85 mm radius of curvature. The inner transducer element was driven with a pulser (Panametrics 5072PR) to produce a short tissue interrogation signal (–6 dB band: 1.6 - 3.7 MHz), which was found through in-water calibration to have a peak negative pressure, spatial peak time averaged intensity,

and both soft tissue and bone thermal indices that were well below the limits for diagnostic ultrasound in humans (US Dept. of Health and Human Services, 2008). Backscattered ultrasound from internal tissues was measured on the outer transducer element and preamplified by the receiver section of the pulser. Data was digitized at 50Msamples/second (Cleverscope CS328A) and stored on a laptop computer.

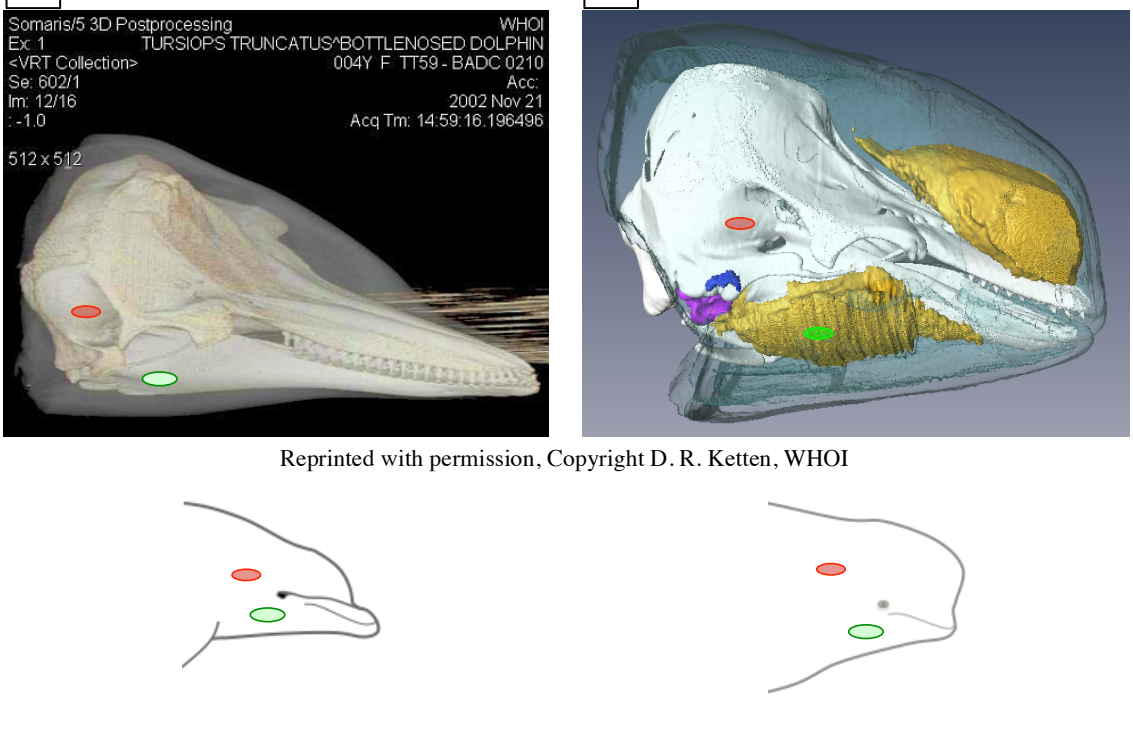

Figure 6.1. Measurement regions on a bottlenose dolphin (A) and beluga whale (B).

The transducer was fitted with a 40mm standoff collar filled with distilled, degassed water, and covered with latex. When testing fully submerged sites on the subjects, the collar was held directly on the skin. Otherwise, ultrasound gel (Parker Laboratories, Aquasonic Clear) was used to acoustically couple the latex collar cover to the skin. A thermocouple (Omega HSTC-TT), spring-mounted to the collar, was used to measure skin surface temperature through a companion reader (Omega HH603A).

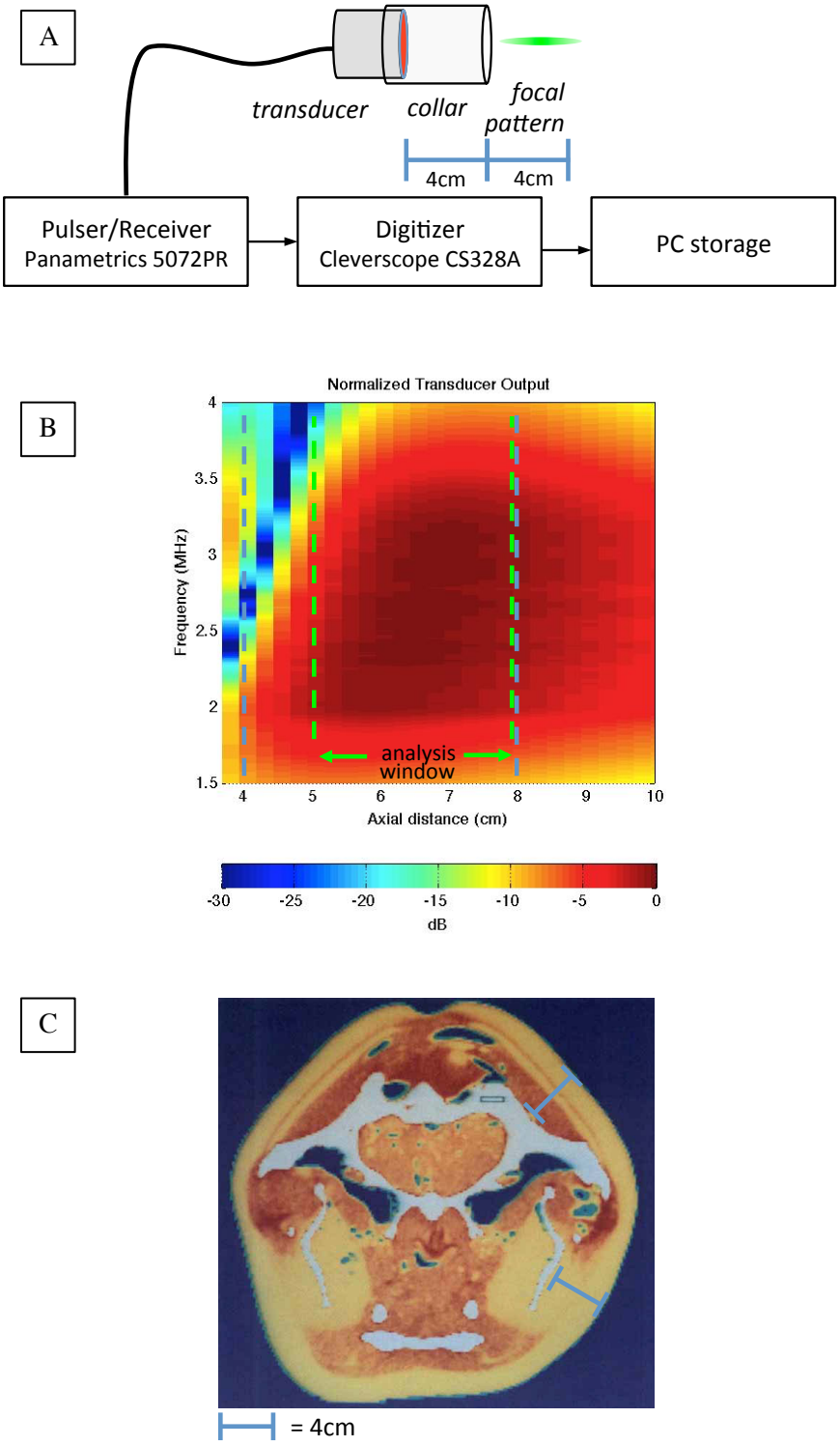

[C] from Cranford, Amundin & Norris (1996), Copyright 1996 Wiley-Liss Inc.

Figure 6.2. Experiment instrumentation (A), transducer axial output (B), and bottlenose dolphin anatomic reference (C).

As seen in Figure 6.2B, the standoff collar places a smoothly varying acoustic field inside the soft tissues of interest. The 3 cm analysis window samples primarily fatty tissues in the mandibular region, and a mixture of fatty, connective, and muscle tissue in the temporal region (Figure 6.2C), all of which were exterior to bone.

6.2.3 Data Processing and Results

The average ultrasonic attenuation (α_{est}) in each region of interest was calculated through comparison with a homogeneous reference material (Yao, Zagzebski, & Madsen, 1990) whose properties had been independently determined:

$$\alpha_{est}(f) = \alpha_{ref}(f) - \frac{ln\left(B(f,z_2)/B_{ref}(f,z_2)\right) - ln\left(B(f,z_1)/B_{ref}(f,z_1)\right)}{4(z_2 - z_1)}$$

where α_{ref} and B_{ref} are the attenuation and backscattered intensity in the reference material, B is the backscattered intensity in the tissue, and z is tissue depth. All backscatter measurements, whether for animal or phantom testing, were performed with identical instrumentation. The use of a reference material therefore captures the combined effects of transducer transmission and reception beam patterns, simplifying data processing. In calculating backscatter as a function of depth and frequency, data were processed in one-way windows of 4mm length, or 2.67μs duration, presuming a sound speed of 1500 m/s. The impact of this latter assumption will be discussed later.

Figure 6.3 shows examples of estimated *in vivo* ultrasonic attenuation, averaged over all sites in each region of interest, and over a 3 cm depth span. In each case, attenuation curves (in linear units of np/cm) are shown with +/-1 standard deviation error bars. A reference curve equivalent to 1.0 dB/cm/MHz, a "classic" soft tissue attenuation

rate, is shown for comparison. The lowest values were in the mandibular region, and smallest in the juvenile bottlenose dolphin (*TT1*). The temporal attenuations were higher, and quite similar between the adult bottlenose dolphin (*TT2*) and beluga whale (*DL*). The temporal region contains a higher proportion of connective and muscle tissues, which in mammals have been shown to have greater attenuations than fatty tissues (Goss, Johnston, & Dunn, 1980).

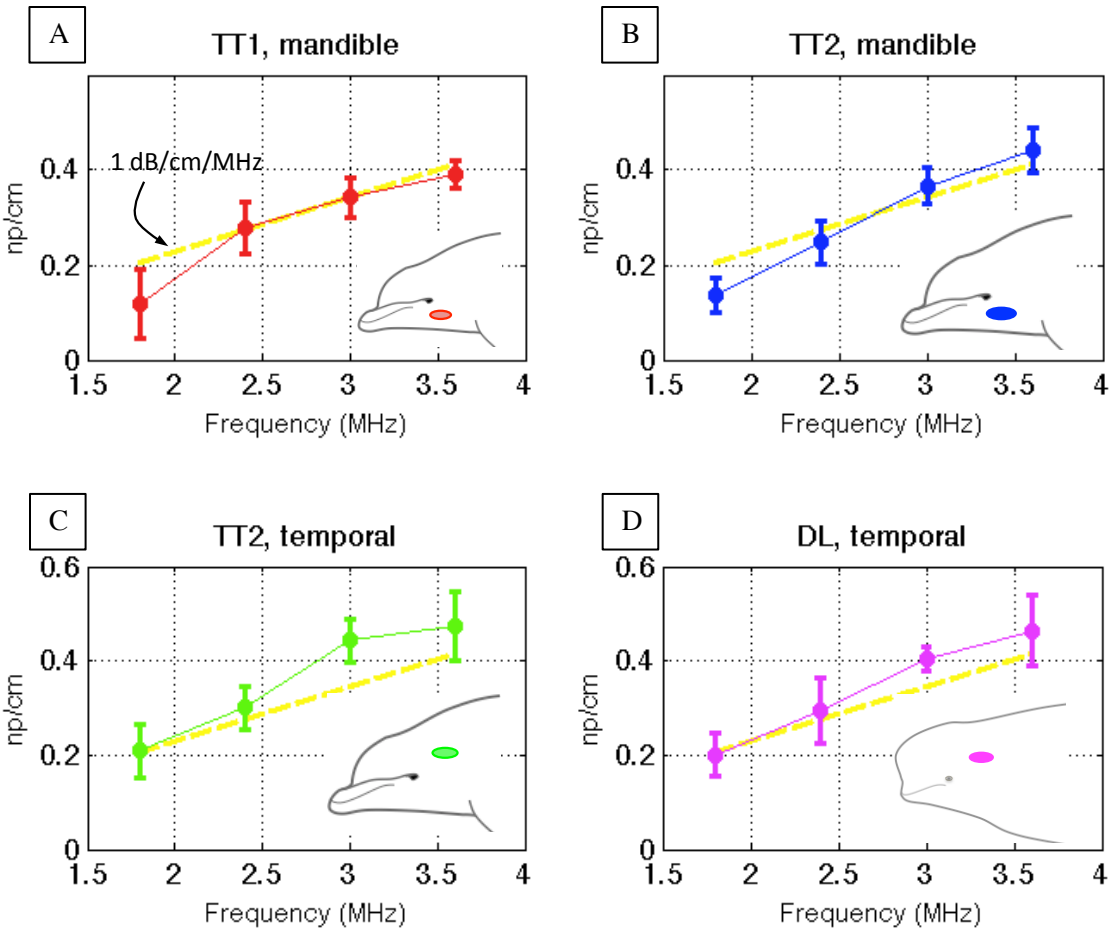

Figure 6.3. *In vivo* ultrasonic attenuation: TT1 mandible (A), TT2 mandible (B), TT2 temporal (C) and DL temporal (D).

Figure 6.4 contains a summary of the *in vivo* results (color symbols) shown along with values from other mammal studies (black symbols). The bovine fat results (Bamber, 1979) are shown to illustrate the problems with *in vitro* attenuation measurements - fatty tissues are particularly sensitive to temperature. In the case of a marine mammal, it is not clear what the *in vivo* temperature distribution would be, especially in hearing-specialized peripheral tissues; so even a well-controlled *in vitro* experiment may be limited in its utility. The lone marine mammal result in Figure 6.4 (Soldevilla et al., 2004) was for tissue harvested from a deceased neonate Cuvier's beaked whale that had been through a freeze-thaw cycle. In the frequency range where CFE was to be used (2.5 MHz and below), the data from the *in vivo* cetacean tests were lower than all values in the literature.

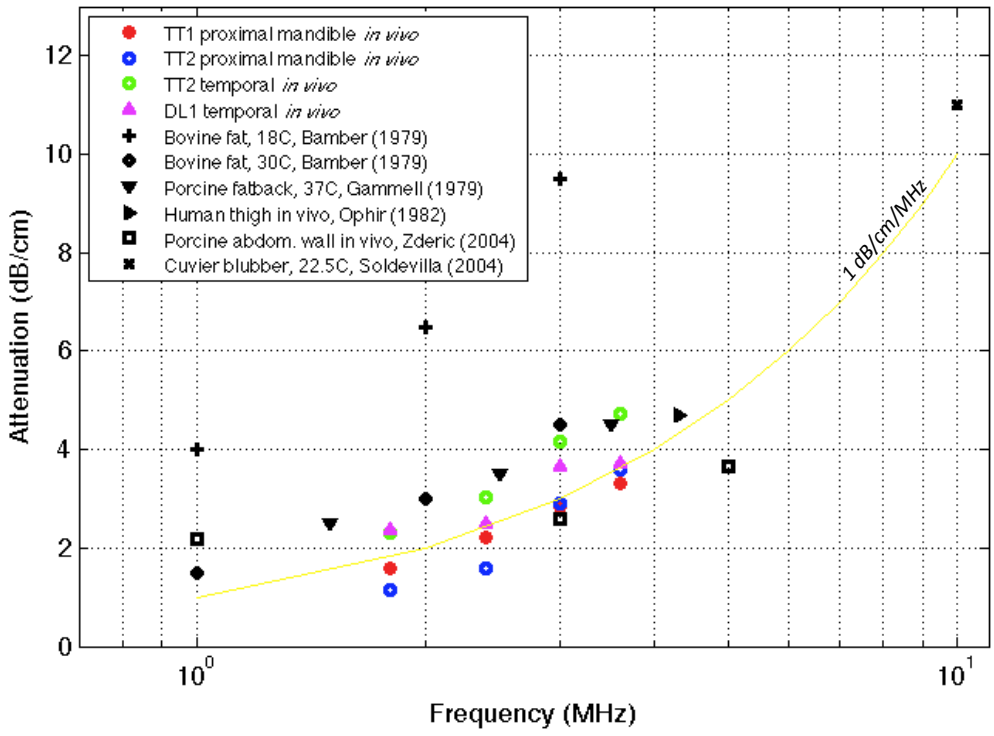

Figure 6.4. Ultrasonic attenuation summary.

While the reference phantom used for the attenuation calculations had spatially uniform properties (sound speed, density, attenuation, and backscatter strength), the interrogated tissues most likely did not. Estimation of the impact of sound speed uncertainty was assessed using simulations of backscatter from materials having different speeds than that of the reference phantom, but with uniform scattering strength. Synthetic data sets were then processed the same way as was the *in vivo* data, and the resulting attenuation estimation errors were determined. It was found that the error was no more than 8% for fatty tissue (1425 m/s), and no more than 20% for connective tissue (1650 m/s). These results correspond to sound speed uncertainties (relative to the assumed value) of 5 and 10%, respectively.

The attenuation data sets were processed assuming backscatter strength did not vary with tissue depth. One way to test this assumption was to remove the estimated depth-averaged attenuation ($e^{-4\alpha z}$) from the backscatter data, and look for abrupt transitions in the residual as a function of depth. Figure 6.5 shows examples of this process for two *in vivo* measurements, and the reference phantom material, all at 1.9 MHz. Over the depth range shown, the *in vivo* data closely follow the form of the phantom, with the vertical shift indicating relative backscatter strength. Since no sharp slope transitions were visible in the results, it appeared that the assumption of uniform backscatter strength with depth was acceptable. Had such variations been encountered, the attenuation results would be interpreted over shorter depth ranges, where the scattering properties appeared to be more uniform.

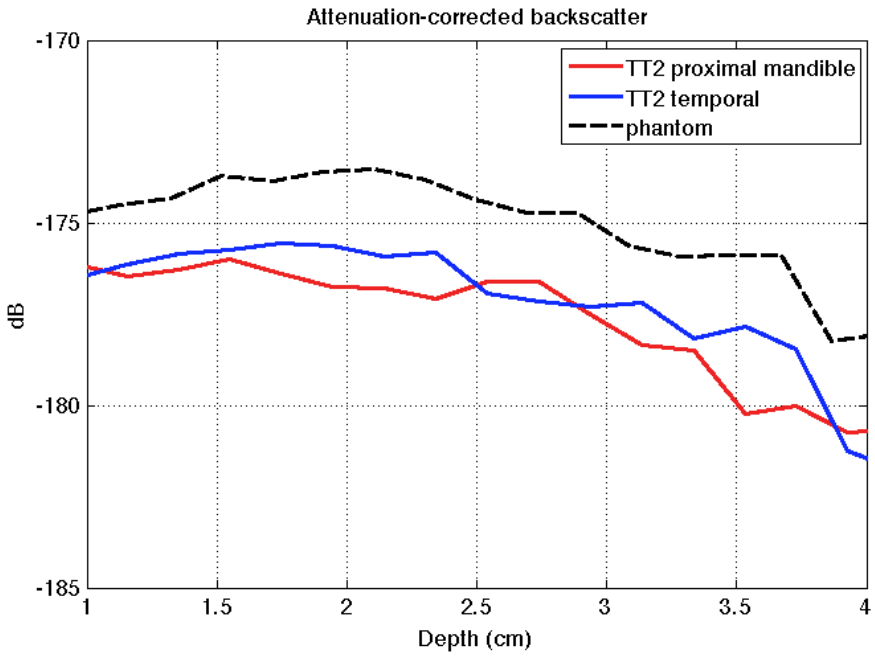

Figure 6.5. Attenuation-corrected backscatter strength.

6.3 Phantom Properties

The attenuation and backscatter strength results from the mandibular region of the adult bottlenose dolphin were used as target properties in the procurement of tissue phantoms for use in laboratory testing of the CFE prototype. The target range for sound speed was broadly set to 1350-1525 m/s, representative of odontocete jaw tissues (Prasad, 2003). Backscatter levels were not formally quantified, but were specified relative to baseline manufacturer-supplied material samples.

Two phantoms were procured – one each from two manufacturers. The first was a proprietary formulation produced by Blue Phantom Inc. to produce the desired ultrasonic properties, but without the ability to specify low frequency shear properties. The second phantom, produced by CIRS Inc. (Norfolk, CT), was intended to match the

desired ultrasonic properties while providing low frequency shear elasticity in the range of published values for *in vivo* human brain (1.7-3.4kPa in Green, Bilston, & and Sinkus, 2008). This phantom was constructed of Zerdine, a proprietary hydrogel.

Upon receipt, ultrasonic sound speed and attenuation were determined using through-transmission measurements (Bamber, et al., 1977), while backscatter was determined using the same instrumentation and procedures used for *in vivo* data collection. All tests were conducted at temperatures between 21 and 23 °C. A summary of the sound speed, attenuation, and spatially-averaged backscatter is presented in Table 6.1. Both phantom attenuations were slightly low, and their attenuation-corrected backscatter levels were slightly high compared to the respective goals. The significance of this relative to the CFE system would be a modest increase in the SNR. Both phantoms showed an attenuation frequency exponent greater than unity, which is consistent with results obtained with these types of materials in other labs (Browne et al., 2003; Zell et al., 2007). Extensive ultrasonic scans of both phantoms were conducted in order to look for voids. None were detected, although the BP3G phantom was found to have a highly non-uniform scattering distribution.

Table 6.1. Phantom Ultrasonic Properties

Material	**c (m/s)**	**α (np/cm)**	**B_{avg} (dB), 2 MHz**
TT2 (goal)	1350-1525	0.075 at 2 MHz	-177
BP "3G"	1451	0.069 at 2 MHz $\alpha_{fit} = 0.055 f^{1.29}$	-173
CIRS "E2315"	1532	0.064 at 2 MHz $\alpha_{fit} = 0.045 f^{1.39}$	-174

The low frequency shear properties of the BP3G material were estimated using the configuration shown in Figure 6.6. The surface of the phantom was vibrated using a shaker, and the resulting surface motions were measured using a laser vibrometer (LDV). The LDV measurements of normal surface velocity were made over a span of 40mm along a radial line extending from the surface drive point, proceeding in 1mm increments. The shaker (and therefore its motion axis) was inclined approximately 20 degrees off the phantom surface normal in order to allow the drive point and starting LDV beam position to be as close as possible, thus maximizing measurement SNR.

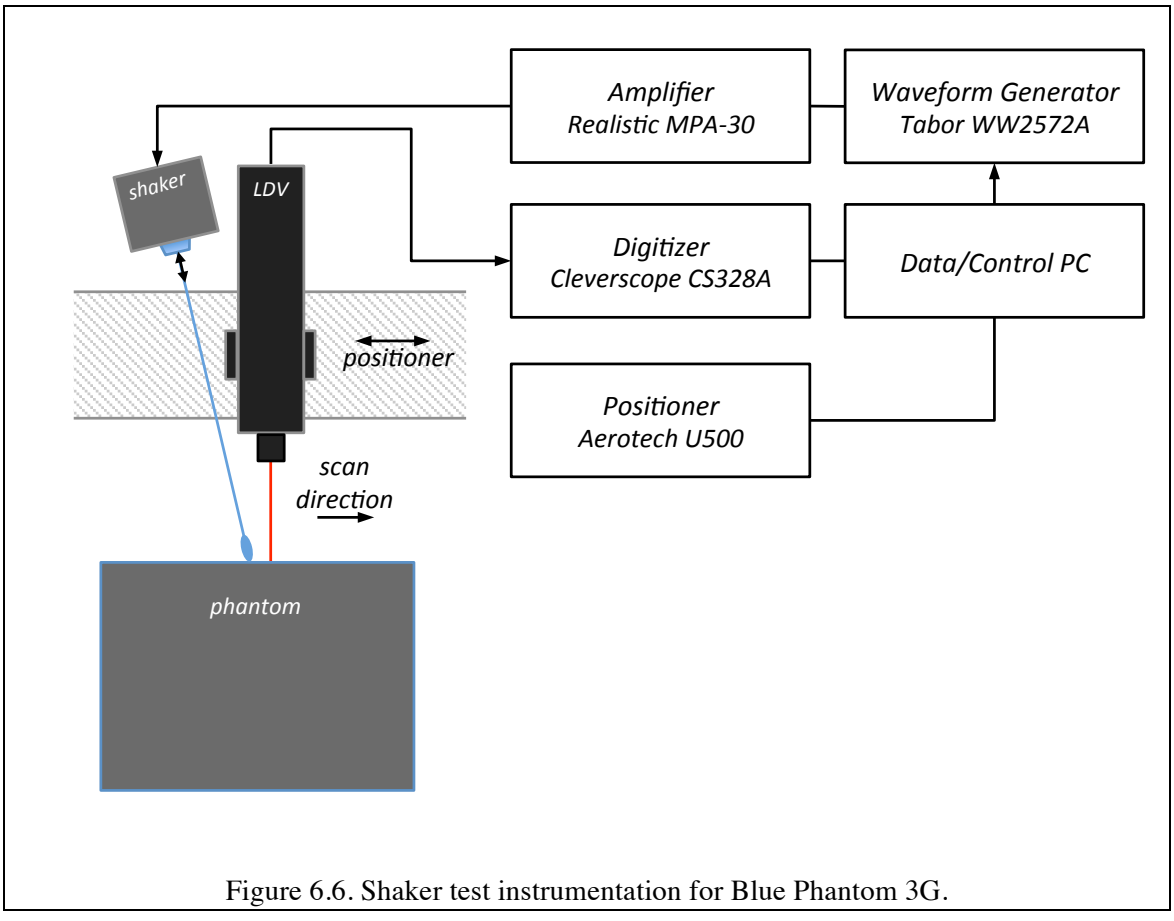

Figure 6.6. Shaker test instrumentation for Blue Phantom 3G.

For a point-like surface load, compressional, shear and Rayleigh (surface) waves are generated. However, as a consequence of their relatively high speeds, the compressional waves would induce no meaningful phase changes over the scan distances used. When the material is nearly incompressible (Poisson ratio~0.5), the shear wave speed is related to the surface wave speed by $c_{shear} \sim 1.047\ c_{surf}$ (Achenbach, 1984). Given the close relative speeds and short measurement scan distances, there was no basis to distinguish the two wave contributions. For the purposes of this estimate, it was assumed that the measured surface response phase was determined by the average of the shear and surface wave speeds.

Shear speed was estimated using the following steps:

- Time domain velocity data were Fourier-transformed to give a velocity spectrum as a function of distance: $V(f,x)$;
- At each frequency, the real part of the shear wavenumber $k_s(f)$ was estimated from a linear fit to the phase of $V(f,x)$;
- The shear wavenumber was converted to shear speed: $real(c_s) = \frac{2\pi f}{k_s(f)}$;
- Shear modulus G was modeled as having an elasticity μ_1 and viscosity μ_2: $G_{est} = \mu_1 + i\omega\mu_2$ (Oestreicher, 1951), and these two component parameters were fit to the measured shear speeds, minimizing the error between $real(c_s)$ and $real\left(\sqrt{G_{est}/\rho}\right)$, where ρ is the density.

The face of the CIRS phantom was covered in a skin-like membrane in order to prevent desiccation. The presence of this membrane invalidates surface wave testing (as

used with the Blue Phantom material) in very low shear materials. Therefore, low frequency shear properties of the CIRS material were found using an alternative approach, applied to quality assurance (QA) sample as shown in Figure 6.7. The QA sample had been poured into a 25 mm long, 51 mm inner diameter PVC pipe section covered in a thin membrane on both flat ends. For shear testing, small wedges of syntactic foam ($\rho \sim 380$ kg/m^3) were glued to each membrane. One wedge was driven with a shaker so as to apply a tangential force to the phantom material. Motion parallel to the drive plane was measured with an LDV. Peaks in the response spectra corresponding to half-wavelength shear resonances were identified and related to the shear speed (c_s) from: $f_n = {}^{nc_s}/_{2L}$, where L is the sample thickness, and $n = 1, 2, 3\ldots$. The frequency dependent shear speed derived from the above was then fit to a complex shear modulus in the same way as done for the BP3G tests.

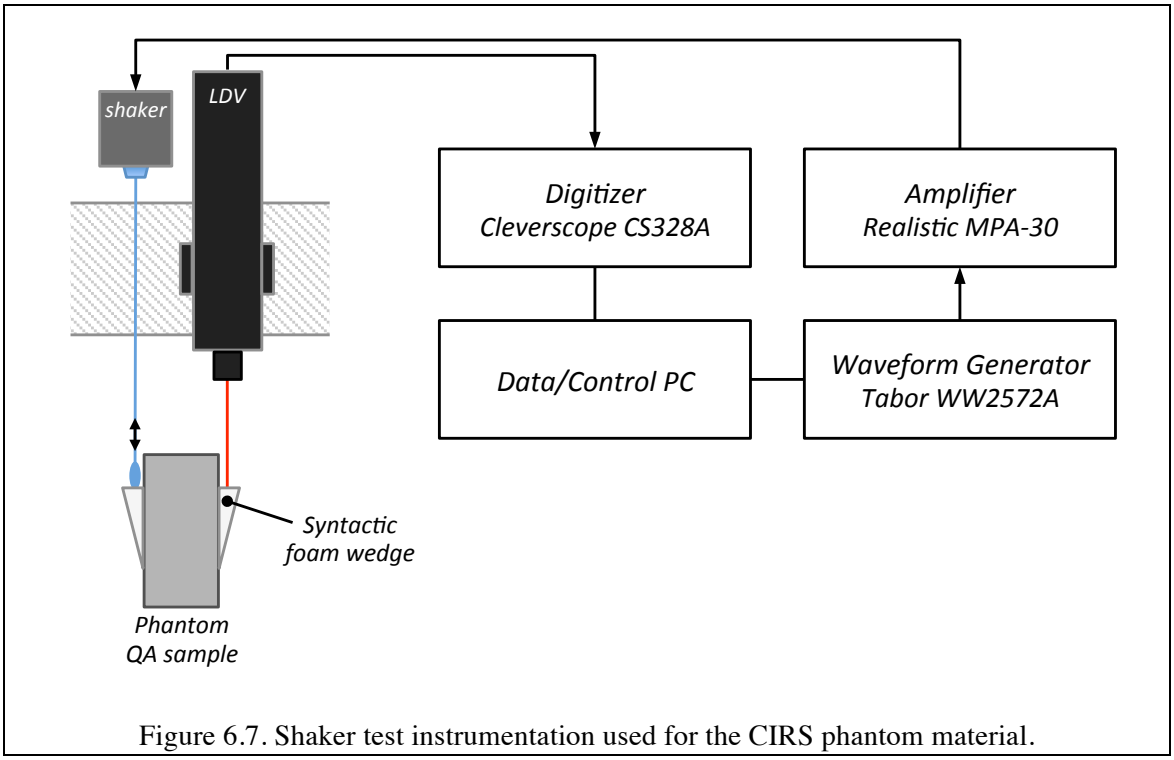

Figure 6.7. Shaker test instrumentation used for the CIRS phantom material.

The low frequency shear test results are summarized in Table 6.2, along with data from other studies. The two-parameter fit error for both phantom materials was less than 6%. The BP3G material, whose shear properties were not specified or controlled by the manufacturer, was in the reported range of *in vitro* bovine muscle and *in vivo* porcine myocardium. The CIRS material shear elasticity of 2.2 kPa was slightly lower than the manufacturer's measurement (2.3 kPa, based on 6.9 kPa static Young's modulus and assuming an incompressible material), but was in the reported range of *in vivo* human brain tissue, as intended. The shear viscosity was low, but for some perspective, the imaginary part of the shear modulus ($2\pi f\mu_2$) would be equal in magnitude to the real part at approximately 500 Hz. Under other circumstances, this would be considered to be an extremely lossy material, but in the context of biological tissue evaluations, the CIRS phantom material will exhibit uncommonly low shear propagation losses.

Table 6.2. Phantom and Soft Tissue Shear Properties

Phantom/Study	**Shear Elasticity** μ_1 (kPa)	**Shear Viscosity** μ_2 (Pa•s)	**Description**
Blue Phantom 3G	19.0	6.5	Tissue phantom, 23.2 C; 140 – 360 Hz
CIRS E-2315	2.2	0.7	Tissue phantom, 23.1 C; 50 - 150 Hz
Chen et al., 2009	29	9.9	*In vitro* bovine muscle: along fiber, 100-400Hz
	12	5.7	*In vitro* bovine muscle: across fiber,
	2.2	2.0	*In vivo* porcine liver
Green et al., 2008	3.1	4.4	*In vivo* human brain (white matter, 90Hz)
	2.7	4.4	*In vivo* human brain (grey matter, 90 Hz)
Sack et al., 2008	1.17	3.1	*In vivo* human brain, 25 Hz
	1.56	3.4	*In vivo* human brain, 50 Hz
Urban et al., 2013	~2	~3	*In vivo* porcine myocardium, diastole, 50-350Hz
	~20	~2	*In vivo* porcine myocardium, systole
Weaver et al., 2005	8.7-9.7	-	*In vivo* human heel fat pad, low stress

Both measurement procedures had a common error source – the regions of material sampled for shear estimation were different than the regions to be directly interrogated by the CFE system. The BP3G shear data was representative of material near the mechanically driven surface (within a few wavelengths ~ 1-2 cm), and may behave differently than the internal bulk material due to curing or mixing issues during production. The CIRS QA sample was poured from the same production batch as the bulk phantom, but its moisture content may have been altered relative to the bulk phantom after weeks in a different container and sealed with a different material. Options are few for non-intrusive evaluation of the internal bulk phantom material properties independent of the CFE system – this is why new elastography methods are sought. One established method would be magnetic resonance elastography (Sack et al., 2008, for example), but the required facilities were not available.

6.4 Phantom Summary

A set of measurements was carried out in order to determine typical ultrasonic properties of living odontocete head tissues. Results from these measurements, along with values from the literature on shear and additional ultrasonic properties, were used to define specifications for tissue phantoms. Lab testing of two phantom materials showed some degree of deficiency - BP3G with highly non-uniform scatterer distribution, and CIRS with low shear viscosity. However, they appear to bracket ranges of relevant biological tissue properties, and therefore were considered acceptable for CFE prototype evaluation.

CHAPTER 7

TISSUE PHANTOM TESTING

"Real things shake funny" – David Trivett, 1994

7.1 Objectives

Building upon the lessons learned from point target testing (Chapter 5), the objective of the tissue phantom testing was to demonstrate the CFE concept in biologically representative materials at depths of up to 12 cm. More specifically, the experiments were designed to assess:

a) the ability to estimate the frequency dependent shear properties using ultrasonic levels within diagnostic exposure safety limits; and
b) the factors that limit system performance, including noise, and speckle scattering;

Section 7.2 describes pre-test simulations that were carried out in support of experiment planning and waveform design. Section 7.3 describes the configuration and instrumentation for the tissue phantom experiments, followed by experiment data processing in section 7.4, experiment results in sections 7.5 and 7.6, and ultrasonic exposure safety in section 7.7.

7.2 Tissue Phantom Simulations

Frequency dependent shear wave magnitude and phase responses were calculated using the simulation approach described in Chapter 2. The forcing field was defined by the forcing transducer (FT) ultrasonic intensity patterns, whose measurements were described in Chapter 4. The measured shear and bulk properties of the two tissue phantoms described in Chapter 6 were used as input material properties.

Prior to predicting displacements for specific FT drive waveforms, the response of the two phantom materials as a function of frequency was calculated. Figure 7.1A shows the magnitude of these responses calculated using the intensity pattern for the FT transducer at a carrier frequency of 800 kHz. Responses were evaluated at the center of the focal plane and normalized by their respective DC values. Both materials exhibited strong attenuation with increasing frequency, in part from the innate responses of the materials, and in part from higher frequency spatial integration effects where the forcing beam size was comparable to greater than a shear half-wavelength.

These results suggested that the waveform design developed in Chapter 5 to mitigate possible vibrometer aliasing effects would not be required for tissue phantom testing. This is illustrated in Figure 7.1B, showing the displacement spectrum obtained with the 2920μs gap windowed FT drive signal. The convolution of the drive-squared waveform spectrum with the forced response of the two phantom media further suppressed high frequencies to extremely small values. Aliasing with respect to the baseline vibrometer Nyquist rate of 1kHz would produce errors no larger than -20dB in the baseband at approximately 950 and 900 Hz for the CIRS and BP3G materials, respectively.

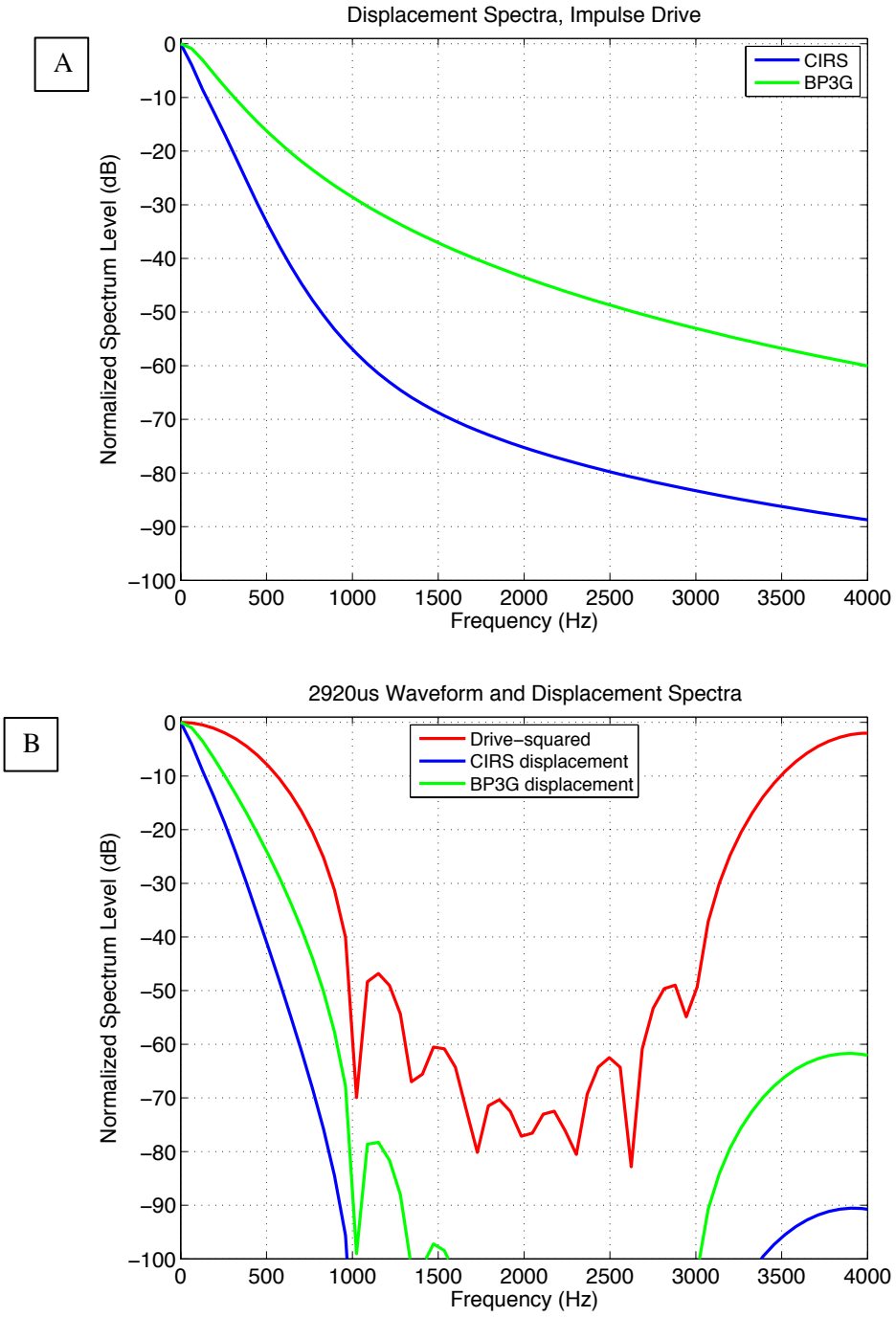

Figure 7.1. Displacement frequency response at the focal plane center (A) and as modified by the 2920us gap window drive waveform (B).

Figure 7.2 shows simulated time domain displacements for the two phantom materials, again using the 800kHz FT intensity/forcing pattern and the 2920μs gap window drive waveform. All curves were normalized by their respective maximum amplitudes, and were calculated with a 16 kHz sampling rate (8x higher than normal) to emphasize the drive signal features. A potential complication with the long duration drive signal is evident – despite the slow propagation of shear waves from drive locations to the central observation point, the material's response may be visible before the drive signal has ceased. If there were any residual FT-VT interactions, they may blend with and be difficult to discern from the initial portion of the true displacement response. The overlap appeared to be minimal for brain-like tissue (after which the CIRS material was modeled), but was significant for the BP3G material (similar to muscle tissue).

Given that the anti-aliasing function provided by the extended FT drive signal duration was not needed for the tissue phantom work, and out of concern for potential overlap between residual coupling and true displacement, an alternative drive waveform sequence was developed. The principle was simply to apply all forcing signal energy between two consecutive VT transmissions (comprising a NIVMS sample period), so that at worst, FT harmonic scattering could contaminate only one vibrometer cycle. This approach upheld the primary lesson of the sphere target testing (FT and VT drive signals should not overlap in time or space). A degree of low frequency drive bandwidth control was still of interest, however, since high frequency (above 1kHz) forced vibration of the phantom materials was not predicted to produce a significant signal. Alternately, a drive waveform with a slower high frequency roll-off than was provided by the baseline 2920us would enhance mid-band response levels.

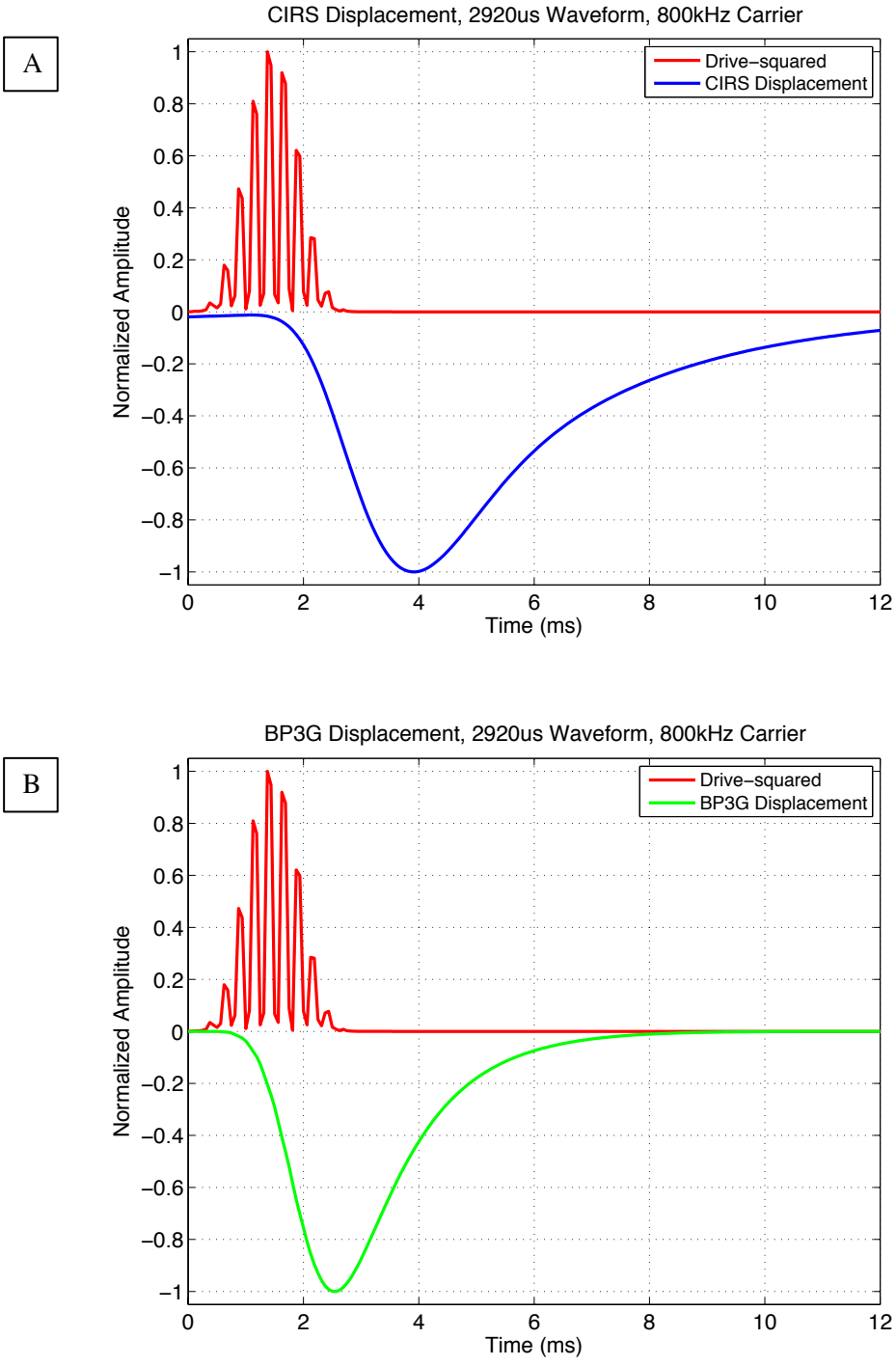

Figure 7.2. Normalized drive-squared and simulated displacement time series for the CIRS (A) and BP3G (B) phantoms.

From the above considerations, the VT and FT sequence was modified as shown in Figure 7.3. The VT pulse repetition rate was slowed from 2.0 to 1.6 kHz, allowing more time between pulses for the FT transmission, which became a simple windowed tone pulse 574 μs in duration. The VT pulse duration was set to 41 μs, with the FT pulse equally spaced between VT pulses, with a 5 μs buffer ("quiet period") on either end.

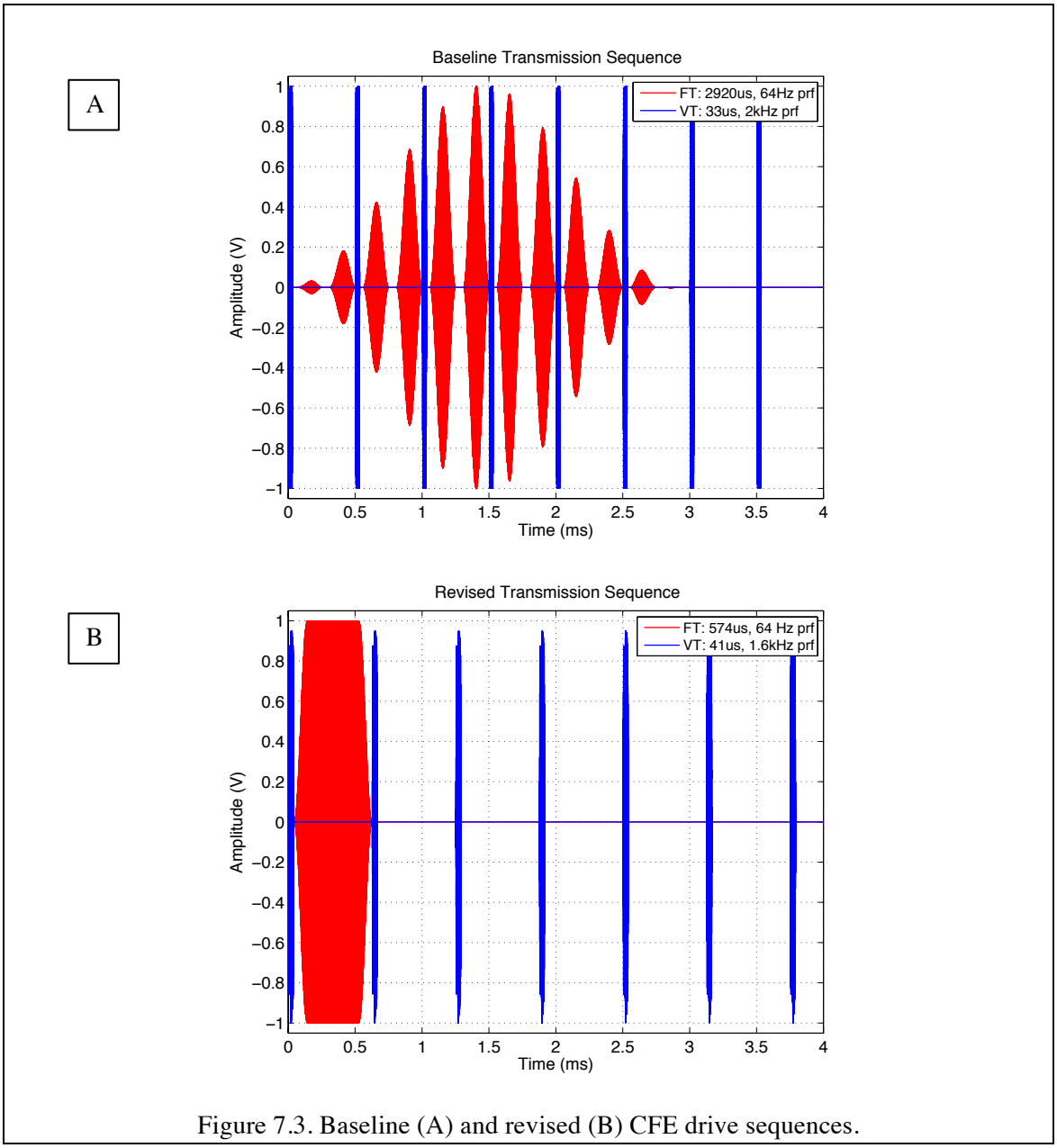

Figure 7.3. Baseline (A) and revised (B) CFE drive sequences.

A side benefit of slowing the VT pulse rate (f_{vt}) was that it extended the one-way range over which displacements could be resolved without wraparound ambiguity. Specifically, the unambiguous range (= cf_{vt}) was extended from 37.5 to 46.9 cm, assuming a sound speed of 1500 m/s. The practical benefit of increased distances is an increased tolerance for working in reverberant environments such as in a hard wall-terminated phantom (CIRS) or in the head of a cetacean.

Figure 7.4 shows predicted displacement spectra obtained with the revised FT drive signal applied to both tissue phantoms. Comparing with 7.1B, the drive-squared signal is much flatter, leading to elevated mid and upper band displacement levels. Aliasing tones relative to the revised vibrometer Nyquist rate of 800 Hz indicate that aliasing errors would be no greater than 10% at approximately 600 and 450 Hz for the CIRS and BP3G materials, respectively.

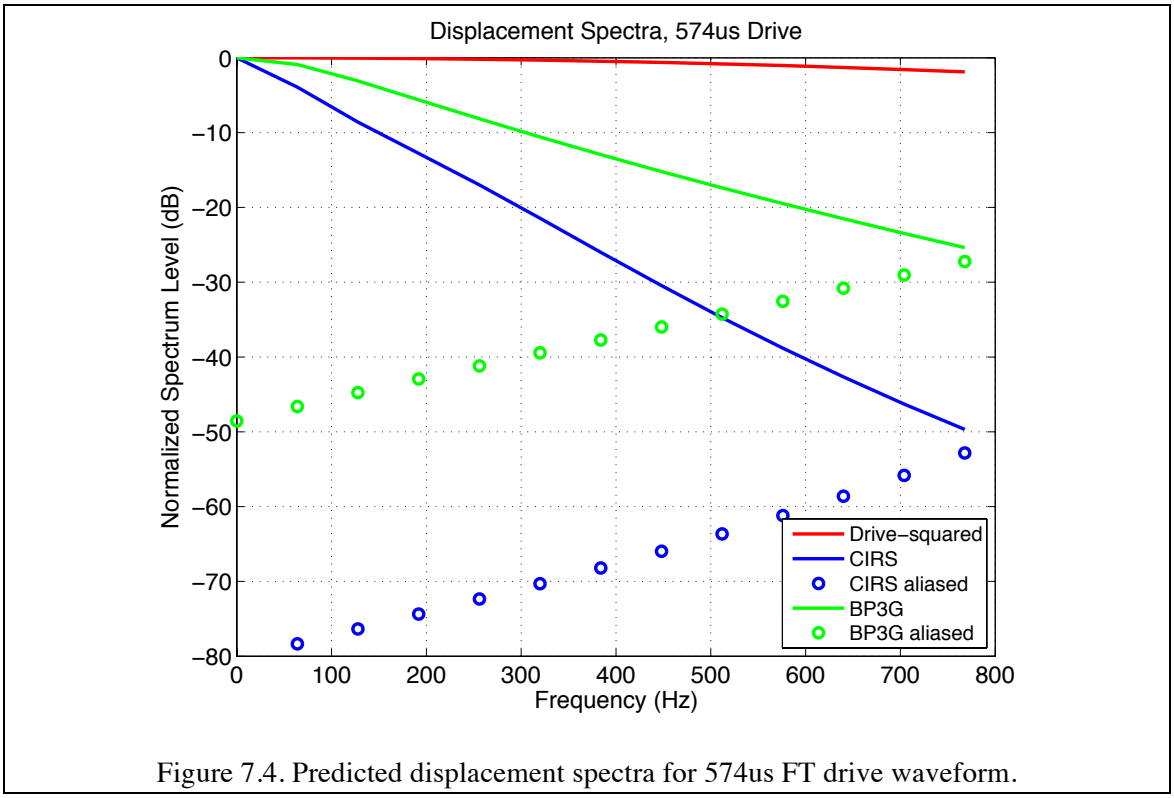

Figure 7.4. Predicted displacement spectra for 574us FT drive waveform.

The significance of the aliasing-induced bandwidth limit is offset to some degree by the diminishing signal sizes at higher frequencies. For a flat noise spectrum (as is the case with the electronic noise limited vibrometry system), the displacement measurement signal to noise ratio (SNR) is expected to decrease rapidly with increasing frequency. The impact on measurement bandwidth and properties estimation will be revisited throughout this chapter.

Figure 7.5 shows the time domain FT drive-squared (forcing) signal and corresponding displacement predictions for the CIRS (A) and BP3G (B) phantom materials. All waveforms are shown with a 16 kHz output sampling rate. Relative to the baseline 2920 μs duration FT drive waveform, the new 574 μs waveform provides improved time separation between drive and displacement response, as expected.

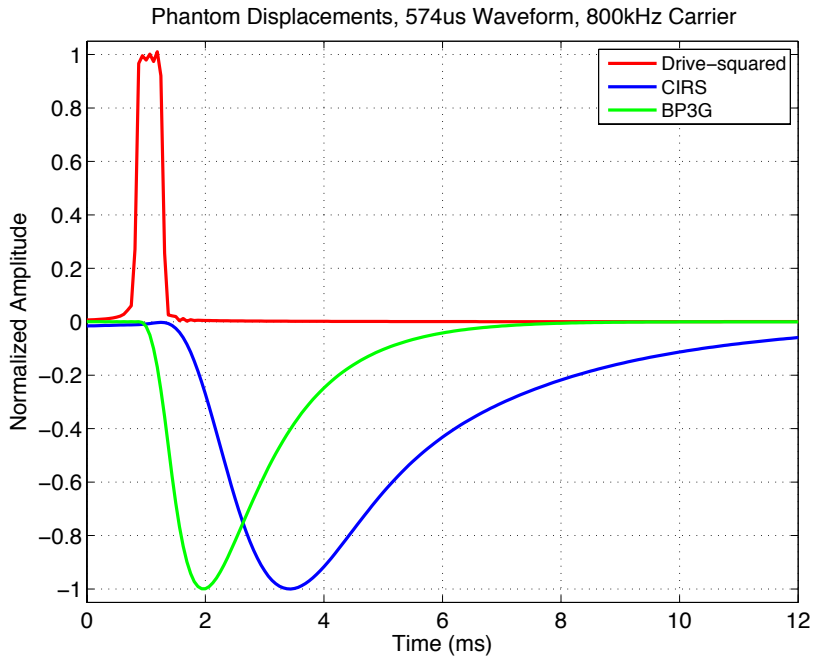

Figure 7.5. Normalized drive-squared and simulated phantom displacement time series.

An additional set of simulations was carried out in order to examine the effect of displacement signal to noise (SNR) level on CFE shear estimation performance. Noise-free displacements were calculated in the transducer focal plane for a material with the shear elasticity (μ_1 = 2.3kPa) of the CIRS phantom, and two different shear viscosity (μ_2 = 0.0, 0.5 Pa•s) values. These reference displacements were normalized to have a root mean square (RMS) value of unity. Zero-mean noise with a specified RMS value was added to the baseline displacement signals, and the relative phase of the noisy signals was used to estimate shear properties (see Section 7.4.4 for details). This process was conducted for RMS SNRs of 60 to 10 dB in steps of 10 dB, with the shear estimation calculations run for one hundred noise realizations at each RMS SNR.

Figure 7.6 shows examples of the displacement spectrum magnitude (upper row) and relative phase (lower row) for a 10 dB RMS SNR. Looking first at the noise-free signals with zero shear viscosity, the displacement magnitude and phase both fall rapidly, with further roll-off at high frequencies as a consequence of the FT beam size relative to the shear wavelength. The effect of elevated viscosity is to increase the rate of signal attenuation and slow the rate of phase change with increasing frequency. The latter effect is caused by the increasing contribution of the viscous component to the total shear modulus with increasing frequency ($G = \mu_1 + i\omega\mu_2$): the material is stiffer at higher frequencies, so the shear speed increases, and the phase deviates from simple linear monotonic behavior.

When noise is added to the baseline signals, the frequency bandwidth over which the phase (or magnitude) data can be used for shear estimation processing decreases.

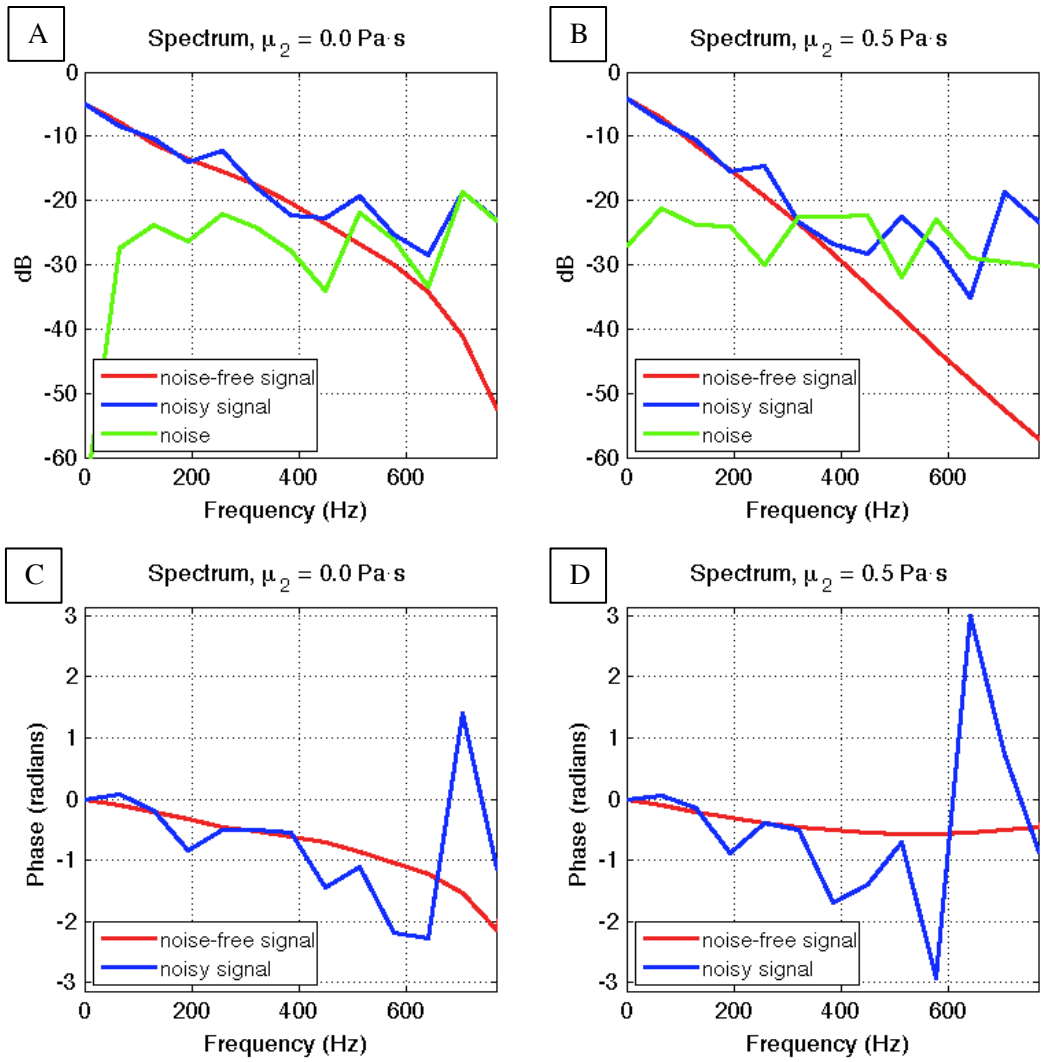

Figure 7.6. Simulated displacement spectra with -10dB RMS added noise: magnitudes (A and B) and relative phases (C and D) for two values of shear viscosity.

The foregoing illustrates the challenge in shear viscosity estimation – viscosity effects are better observed at higher frequencies, where SNR is typically a minimum. Figure 7.7 quantifies the bandwidth reduction effects of noise, showing the highest individual frequency with at least 20 dB SNR. The error bars indicate the span of ±1 standard deviation. In both materials, bandwidth falls as RMS SNR decreases, with the viscous material's bandwidth less tolerant of additive noise.

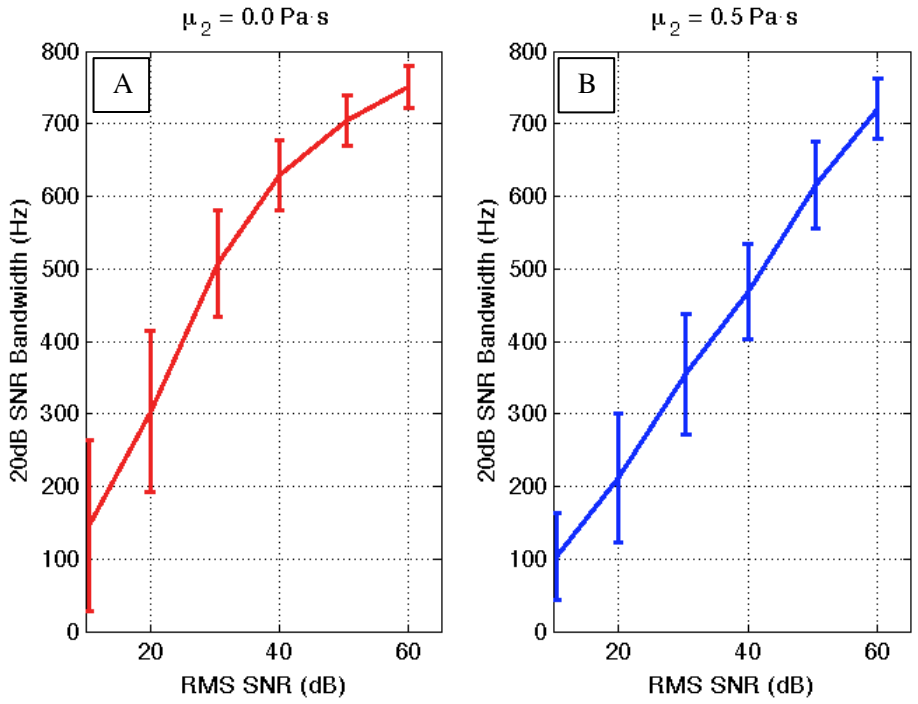

Figure 7.7. Impact of displacement noise level on high SNR bandwidth in an inviscid (A) and viscous (B) material.

The shear properties estimation errors induced by added noise are shown in Figure 7.8, with the low and high viscosity cases in the upper and lower rows, respectively. The shear elasticity and viscosity estimates were calculated using the 20 dB bandwidth determined for each noise realization. The error bars indicate one standard deviation, and the connected values are the noise ensemble mean values. The shear estimates are made with a finite bandwidth, so that the presence of noise simply reduces the amount of information available for the estimation processing. Even with 60 dB RMS SNR, the viscous material shows some degree of variability in the estimated moduli because its spectral level falls rapidly with increasing frequency, and the highest frequencies are most easily contaminated by noise. The mean value trends for shear

elasticity are weakly dependent on noise, while the estimated shear viscosity tends to increase considerably with increasing noise. The viscosity bias error comes from the fact that phase of the noise tends to oscillate around zero, exhibiting no broadband delay trend. A higher estimated viscosity mimics this noise trend by "flattening" the phase.

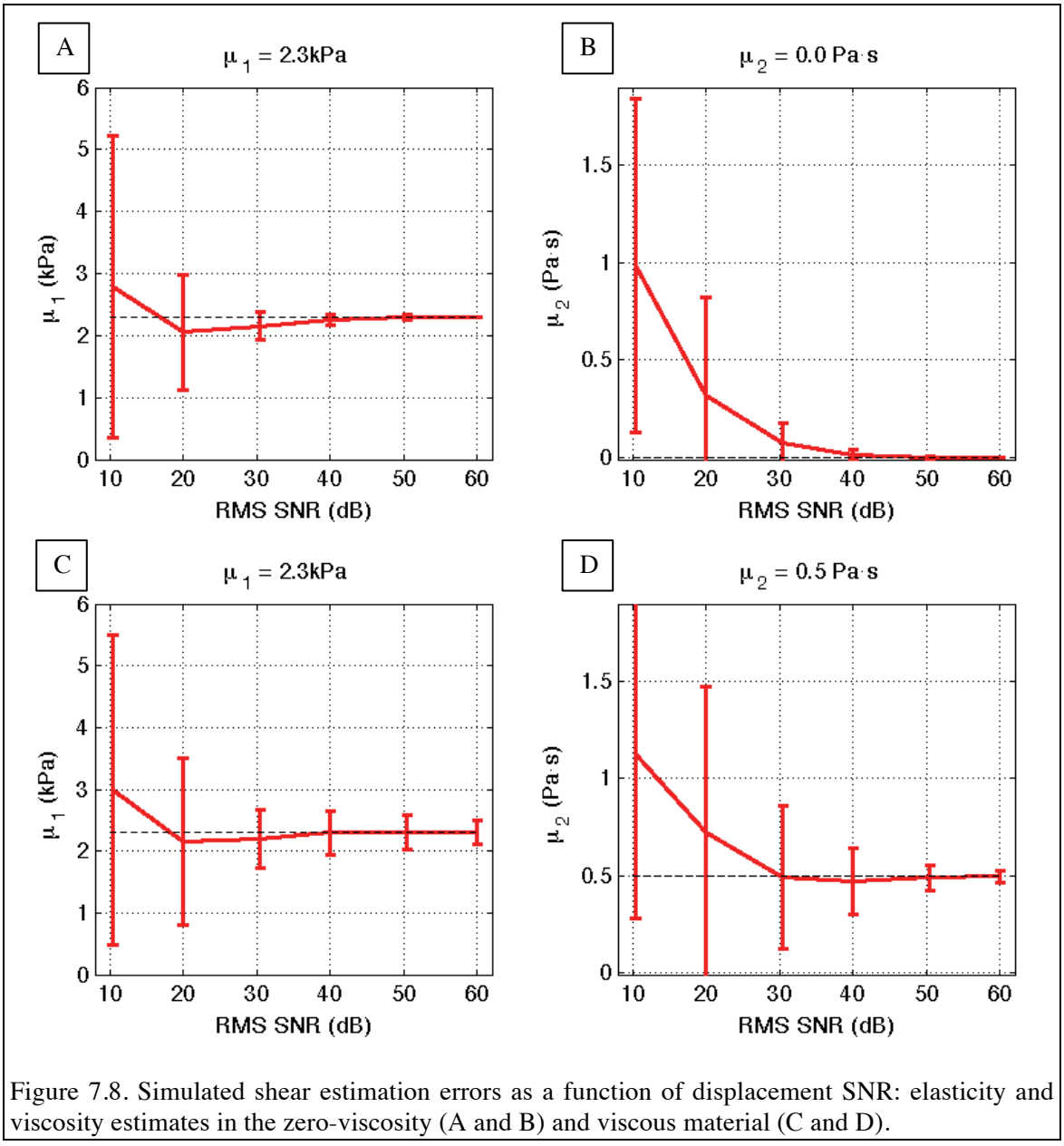

Figure 7.8. Simulated shear estimation errors as a function of displacement SNR: elasticity and viscosity estimates in the zero-viscosity (A and B) and viscous material (C and D).

7.3 Tissue Phantom Testing Instrumentation

The instrumentation for phantom testing is shown in Figure 7.9, and is similar to the configuration used for point target testing described in Chapter 5. The active faces of the CFE transducers were coupled to the face of the phantom with distilled water filling a reservoir that was mounted to the cylindrical phantom body. The nested CFE transducers were suspended from a two-axis positioner, used primarily for careful submergence and retrieval from the test well. The use of distilled water and the partial submergence configuration were intended to preserve the prototype transducers, which had proven to be rather fragile by this point in the experimental effort.

All drive signals originated from a common waveform generator, after which they were filtered to remove residual digital-to-analog conversion noise and passed through variable attenuators for amplitude tuning prior to power amplification. The low pass output filters on the FT power amplifiers were intended to reduce drive harmonic frequencies, while the filters in the VT receiver signal path were intended to minimize FT contamination of the vibrometer data, and to provide improved high frequency anti-aliasing performance. For these tests, the VT preamplifier was changed from the Minicircuits unit used for point target testing to the LeCroy unit because of its greater compression-free output range. When the input to a fixed-gain preamplifier is such that the device exceeds its output compression threshold, the preamplifier gain will not be constant, resulting in signal distortion.

The waveform generator and digitizer shared a common 10MHz clock in order to minimize timing jitter errors and improve NIVMS algorithm performance. Half-second time records of raw vibrometer data, along with copies of VT and FT drive signals, were

digitized at 10MHz and stored on the host computer for offline processing. All drive signals, as well as the VT raw receiver signal, were monitored during data collection using digital oscilloscopes. The temperature of the FT transducer active face was monitored using an internal thermocouple and an external reader (Omega HH603A). Once submerged, the transducer temperature matched that of the phantom-water interface (as measured with a separate thermocouple) within a few tenths of a degree Celsius. The transducer temperature was not observed to vary more than 0.1-0.3 °C during system testing unless the lab air handling system was running.

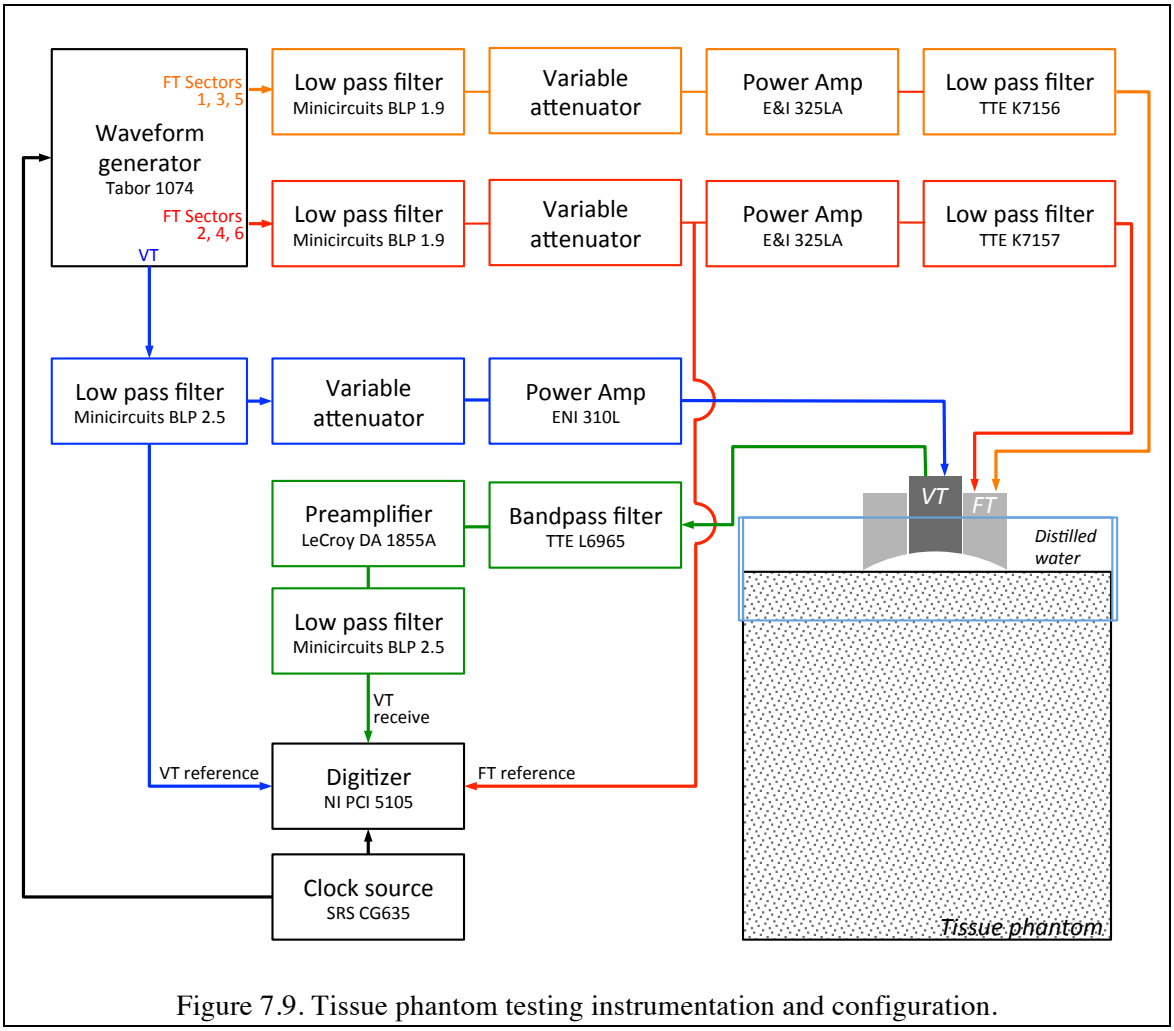

Figure 7.9. Tissue phantom testing instrumentation and configuration.

The final form of the FT drive signal used in the tissue phantom experiments consisted of a sequence pulses whose carrier frequencies alternated between two values, thereby applying forces at two alternating radii. For example, a sequence alternating between pulses with 725 and 825 kHz carrier frequencies would produce forcing radii that alternate between approximately 3.2 and 2.8 mm, respectively. This approach provided all data required to estimate shear speed as a function of frequency within a single measurement.

7.4 Experiment Data Processing

This section describes the processing of raw ultrasonic data to yield shear estimates. Raw digitized data were processed with the NIVMS algorithm (Martin, Rogers & Gray, 2011) implemented in Matlab, outputting band-averaged backscattered power $B(z)$ and the time history of axial displacement $d(t, z)$, both as a function of range (z) along the FT beam.

7.4.1 Coupling Reference Processing

If review of the displacement time series data revealed evidence of FT contamination in the form of false signals appearing before a shear wave could have arrived, the raw displacement data was be reprocessed using the coupling reference subtraction method described in section 5.4.2.

7.4.2 Ensemble Averaging

If multiple measurements were made under identical test conditions, the power and displacement results were coherently averaged over all available ensembles to improve signal to noise ratio (SNR). The data acquisition system was not triggered, so

prior to averaging, separately acquired data sets were temporally aligned using recorded FT drive signals.

7.4.3 Spatial Averaging

The NIVMS processing code produced displacement data in axial range increments of Δz=75 μm, which is the one-way distance associated a single data set sample period at the acquisition rate of 10MHz. This degree of range granularity was not indicative of the true axial resolution of the vibrometer, which was seen in Chapter 5 to be on the order of 2-4 mm depending on VT signal and processing bandwidth.

A second factor relative to range-related effects is that the non-electronic noise level at a point along the vibrometer beam is inversely proportional to the ultrasonic backscattered power at that point. If a region in space being analyzed for vibration has low backscatter, then the ultrasonic estimate of vibration will be noisier than a high backscatter region vibrating with the same amplitude. Backscatter in soft tissue phantoms is modeled to resemble "speckle" in biological tissues caused by ultrasonically small, randomly distributed variations in compressibility and density (Kuttruff, 1992). The random scatterer distribution produces a rapidly varying interference pattern, illustrated in Figure 7.10 for measurements taken 2.0 mm apart in the CIRS phantom.

To mitigate the effects of low-scattering regions on displacement SNR, a backscatter-weighted spatial averaging process was implemented: $d_{avg}(t, z_n) = \sum(d(t, h_n) * B(h_n)) \Big/ \sum B(h_n)$, where h_n is an array of range points centered at z_n. In forming the spatially averaged displacement d_{avg}, this process deemphasized the adverse

noise impact of low-scattering range points. The axial extent of h_n was typically chosen to be no less than the axial resolution expected from the transmitted VT signal.

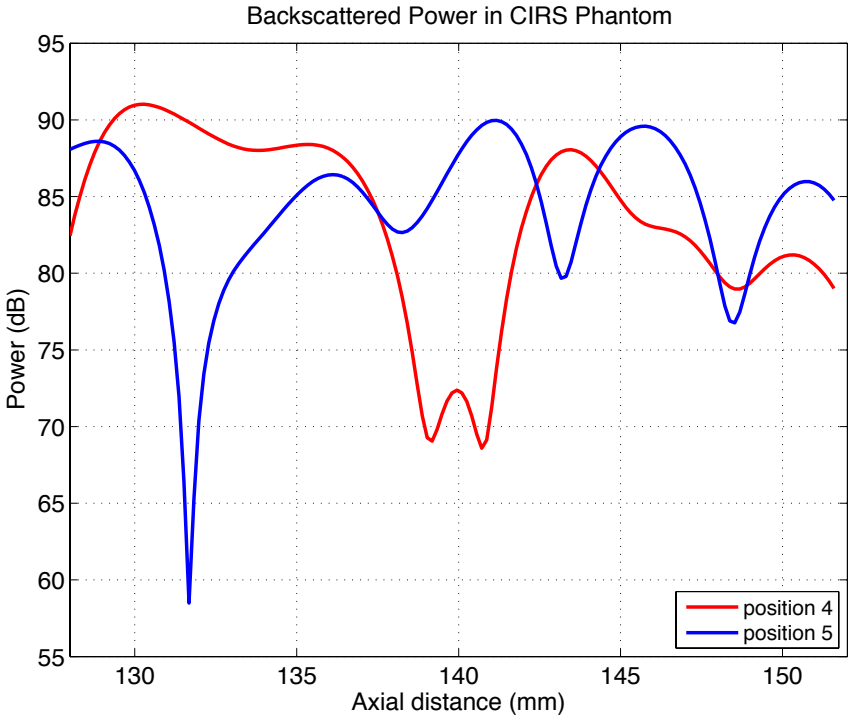

Figure 7.10. CIRS phantom scattering along two parallel scan lines separated by 2mm.

7.4.4 Final Time Series and Spectra

Displacement time series were condensed from the baseline full record length of 0.5 seconds to a length of ($T=2/f_{FTprf}$) by averaging successive segments. For example, for a FT pulse frequency f_{FTprf} of 64 Hz, sixteen successive data segments of duration 2/64 = 31.2ms were coherently averaged. The condensed displacement data consisted of a segment containing the response to the first FT carrier ($d_{1,avg}(t)$: $0 \le t \le 1/f_{FTprf}$) followed by a segment containing the response to the second FT carrier ($d_{2,avg}(t)$: $1/f_{FTprf} \le t \le 2/f_{FTprf}$). The two segments were individually windowed and Fourier-transformed to yield corresponding displacement spectra $D_1(\omega, z)$ *and* $D_2(\omega, z)$. Finally, the relative

displacement phase of the displacement (φ), indicative of change in shear wave propagation distance induced by the FT carrier change, was found from: $\varphi(\omega, z) = atan(imag(R_{12}(\omega, z))/real(R_{12}(\omega, z))$, where $R_{12}(\omega, z) = D_1(\omega, z)/D_2(\omega, z)$.

7.4.5 Shear Modulus Estimation

Two methods were pursued for shear speed and modulus estimation. In the first, a constant force radius shift $\Delta r$was presumed, and forcing beam width changes with carrier frequency were ignored. The real part of the shear speed was estimated from the relative displacement phase: $real(c_s(\omega, z)) = \frac{\omega \Delta r}{\varphi(\omega, z)}$. Shear modulus G, expressed in terms of elastic (μ_1) and viscous (μ_2) terms ($G = \mu_1 + i\omega\mu_2$), was then fit to the shear speed data using a Voigt model of the tissue (Oestreicher, 1951):

$c_s = \left(\frac{2(\mu_1^2 + \omega^2 \mu_2^2)}{\rho\left(\mu_1 + \sqrt{\mu_1^2 + \omega^2 \mu_2^2}\right)} \right)^{1/2}$, where ρ is the material density. This approach has been used by several ultrasonic elastography researchers (Yamakoshi, Sato, & Sato, 1990; Chen, et al., 2009) studying both phantoms and living systems. The given expression of shear modulus in terms of elastic and viscous terms arises from the Voigt model, which treats tissue as a spring and damping element in parallel. There are several other soft tissue models that may be used (Chen, Yao, Zheng, Lin, & Zheng, 2012), the relative merits of which can be investigated once the displacement data are available.

The second method for shear estimation directly fits the displacement phase data with the analytical model described in Chapter 2. In this method, a series of predictions of the shear field and differential displacement phases are calculated using measured transducer intensity data and a matrix of shear elasticity and viscoelastic constants.

While a nonlinear optimization would work well for this problem, evaluation of the model for all the shear constants was rapid (on a laptop computer). Final material fit parameters were chosen which gave the minimum least squares error fit to the experiment data. This method has the advantage of directly accounting for the carrier dependence of FT beam size, in addition to beam radius. A prediction of the frequency response of the displacement magnitudes is also available from this method, allowing further refinement of the data fit. However, it was found that the magnitudes were less sensitive to shear properties than were the phases.

7.5 CIRS Phantom Results

7.5.1 Axial Averaging

As described in the previous section, axial spatial averaging was used to mitigate backscatter variability. Figure 7.11 shows the backscattered power from within the CIRS phantom as a function of depth for four interrogation lines (indicated by different colors), with varying degrees of spatial averaging implemented for each. Averaging over successively wider windows (2-4mm) reduced the depths of the scattering nulls. The variations in level and spatial distribution amongst the traces were also well mitigated by axial averaging. The broader trend of decreasing backscatter with increasing depth was indicative of the ultrasonic attenuation of the medium.

The relationship between backscattered power and low frequency displacement noise is shown in Figure 7.12. The scattering data is displayed in red, while the root-mean-square displacement noise in the 128-512 Hz band is displayed in blue. The displacement noise is from a single data acquisition consisting of 100 coherent averages,

and very clearly trends with the inverse of the backscatter. Regardless of degree of spatial averaging, the attenuating backscatter strength with increasing depth led to commensurate elevation in displacement noise.

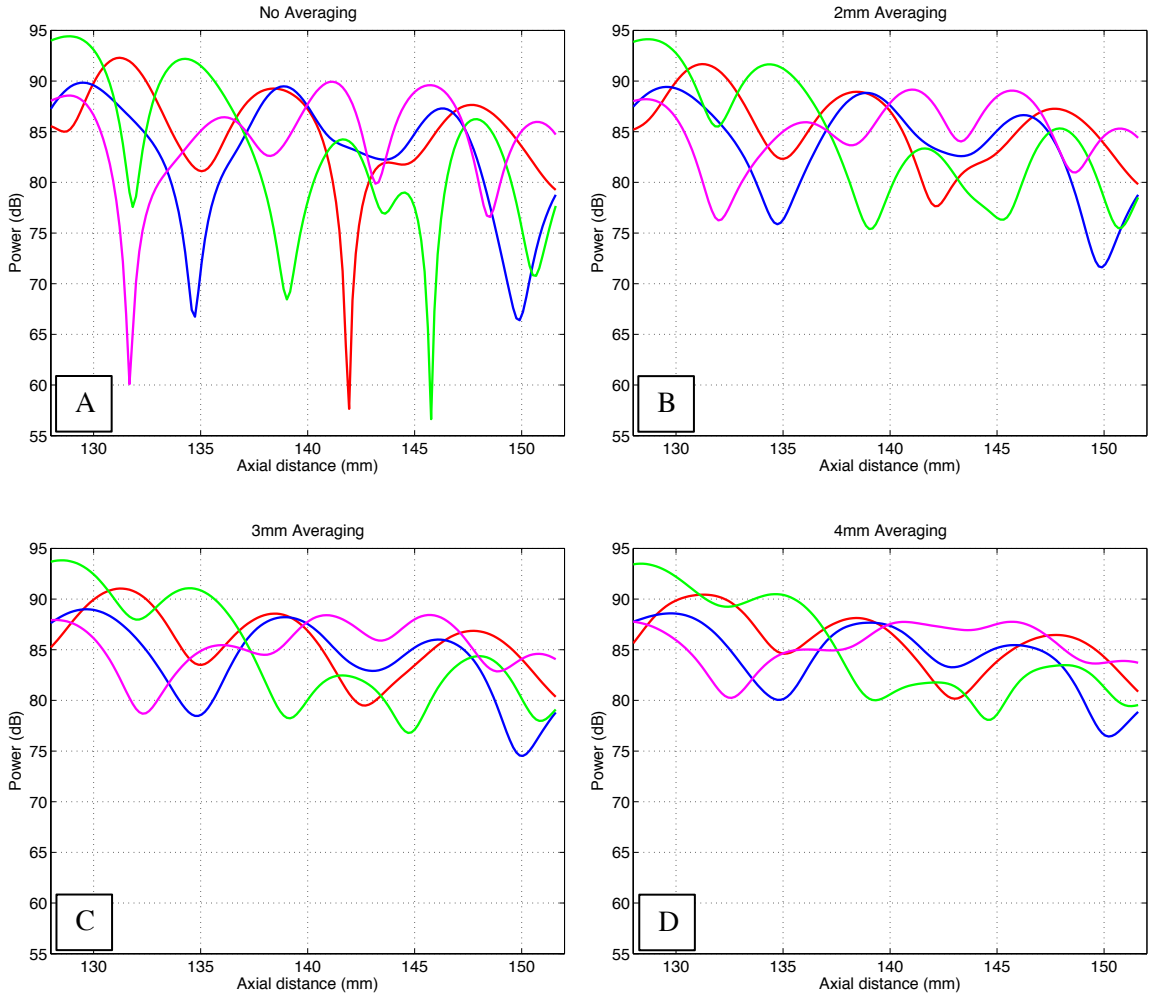

Figure 7.11. CIRS phantom backscattered power from four different locations, with no spatial averaging (A), 2mm averaging (B), 3mm averaging (C) and 4mm averaging (D).

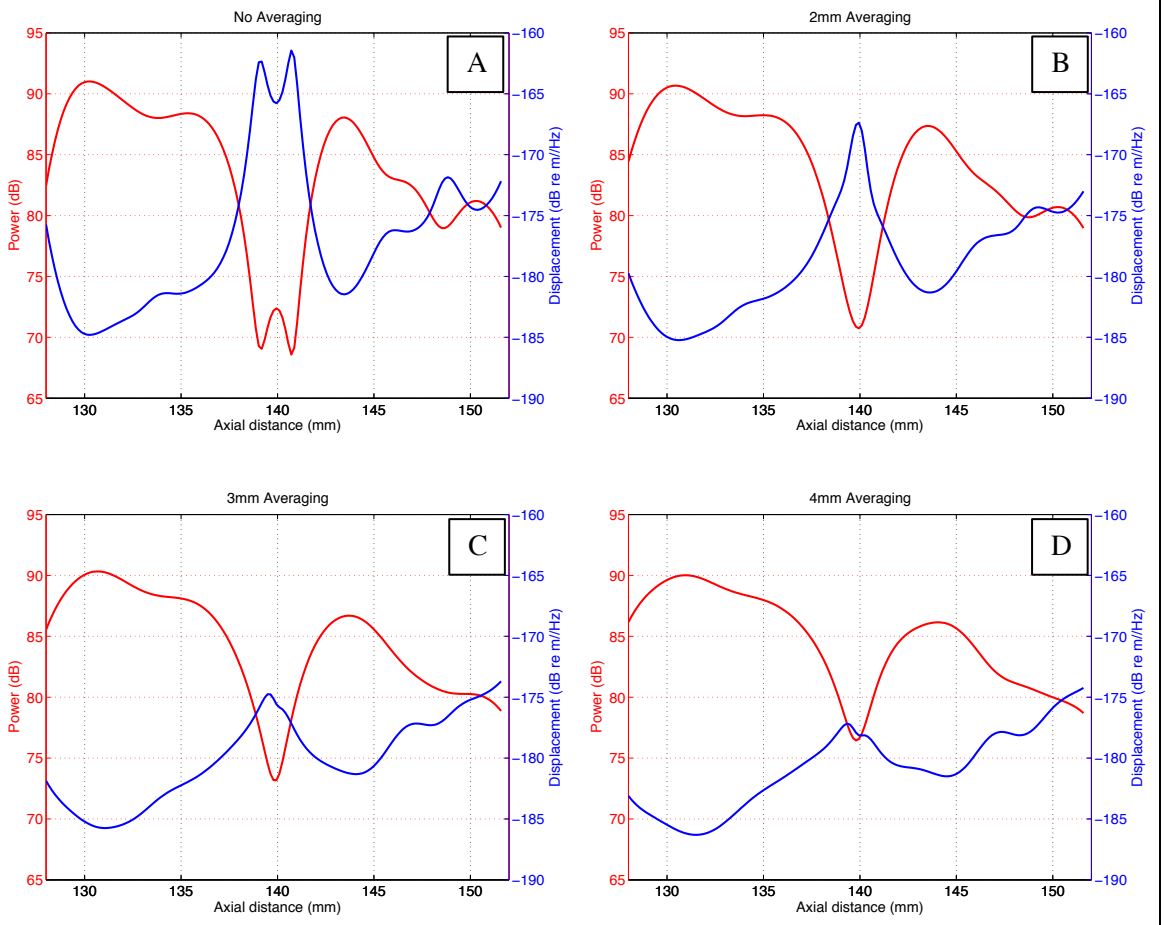

Figure 7.12. Backscattered power and 128-512 Hz RMS displacement noise, with no spatial averaging (A), 2mm averaging (B), 3mm averaging (C) and 4mm averaging (D).

7.5.2 Shear Displacements

Figure 7.13 shows examples of displacements in the CFE focal plane (z=140mm) for the two FT carrier pairs tested with the CFE phantom: 825/725 kHz, and 850/700 kHz. Since higher FT carrier frequencies produce force patterns with smaller mean radii, shear waves generated from higher frequency carriers should arrive before those generated by lower frequency carriers, as seen in both plots. The wider frequency spread

in the 700/850 kHz carrier pair produced a larger relative delay between shear wave arrivals, as expected.

Figure 7.14 shows the displacement spectrum measured in the focal plane, using the 825 kHz carrier FT drive waveform, processed with 4mm axial averaging. The blue error bars indicate the full data range of five independent data records. The spectral amplitudes fell off rapidly with increasing frequency, at a rate similar to that which was predicted in section 7.1. The noise in this measurement was relatively flat with frequency – a result seen throughout this work. The noise floor was previously shown to be dominated by the high frequency digitizer that records vibrometer data (Martin, Rogers & Gray, 2013), and was recently demonstrated by simultaneously recording duplicate copies of vibrometer data on three input channels of the digitizer. When coherently averaged and processed to yield displacements, low frequency displacement noise floor of the individual traces dropped by approximately $\sqrt{3}$, which could only occur if the high frequency (NIVMS processing band) noise was different on each of the three recording channels.

Based on the observed displacement measurement SNR, an upper frequency limit of 384 Hz was chosen for phase-based shear speed estimation.

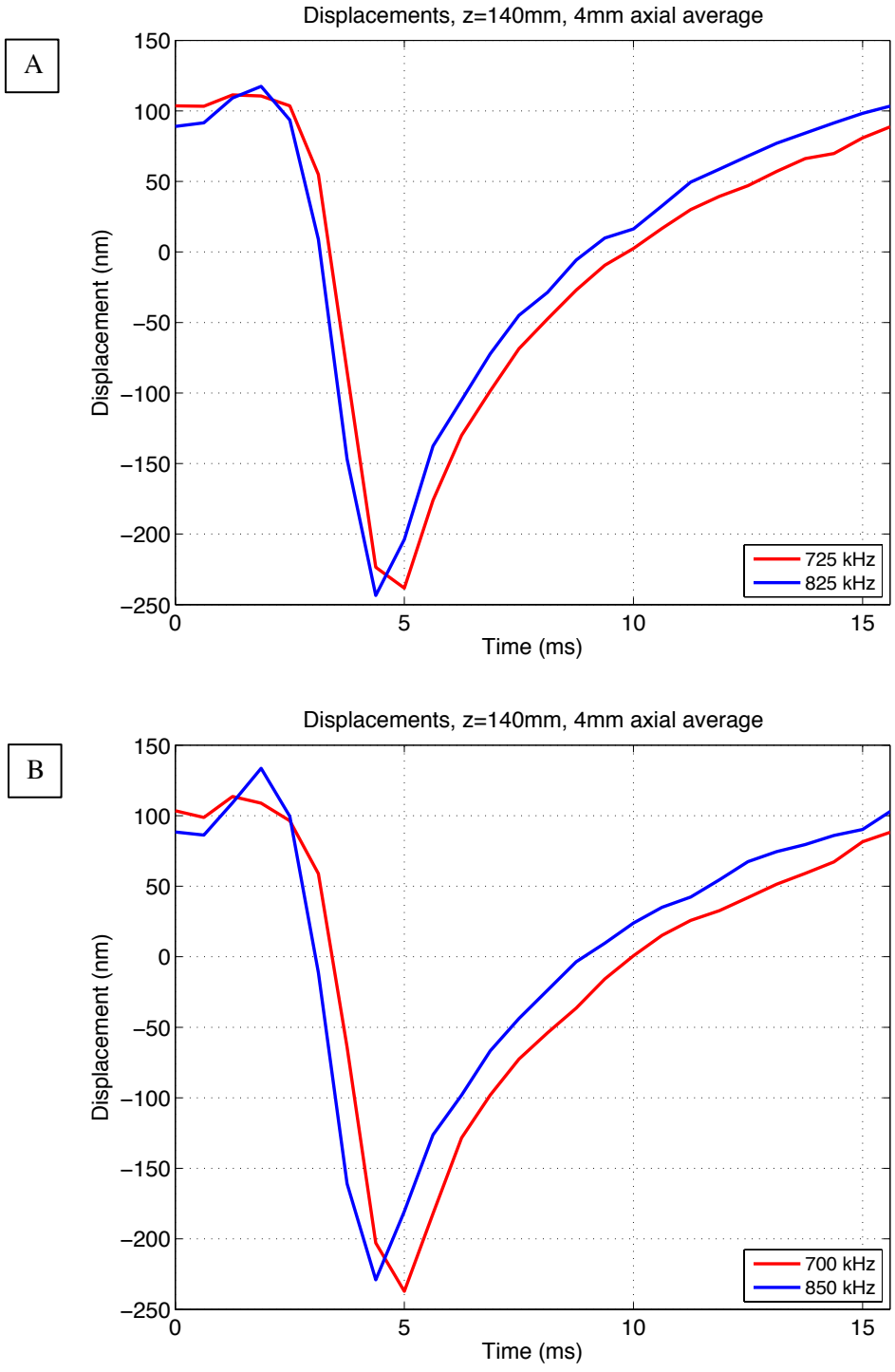

Figure 7.13. Examples of focal plane displacements obtained with 725/825 kHz (A) and 700/850 kHz carrier pairs (B).

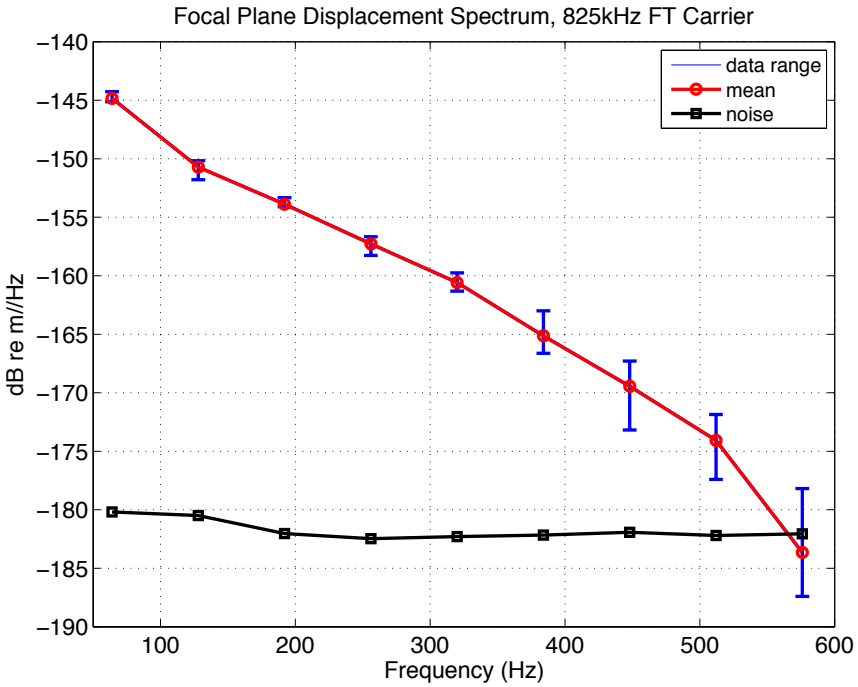

Figure 7.14. Displacement spectrum and background noise examples in the CIRS phantom.

Figure 7.15A shows the axial distribution of displacements in the time domain for the 825 kHz FT drive carrier. The peak displacements occur short of the focal plane (z=140mm), presumably because of modest attenuation of the FT beam by the phantom material. The timing of the displacement signals exhibits an increased delay on either side of the focal plane, correlating with the modestly curved shape of the FT intensity patterns (Chapter 4). This is illustrated in Figure 7.15B with radial intensity centroids at each axial distance, for each of the four FT carriers used for the CIRS tests. As displayed, there appears to be considerable tilt to the intensity patterns, but over most of the axial range the tilt angle is no more than two degrees off vertical. The 825kHz centroid curve was normalized by estimated shear speed and displayed as a dashed black line onto 7.15A, showing qualitative agreement with shear wave arrival time.

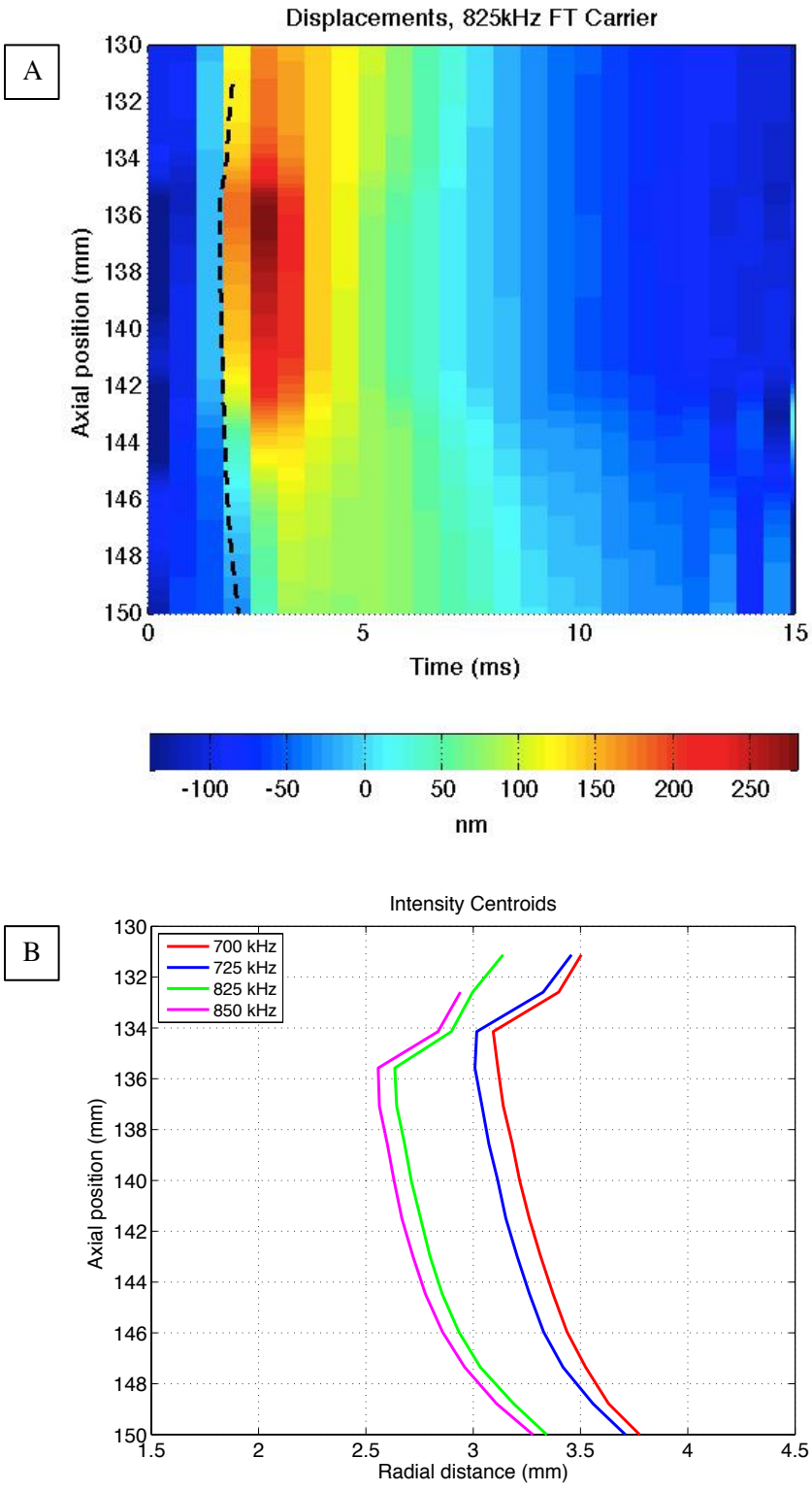

Figure 7.15. Axial displacement distribution (A) and FT intensity pattern centroids (B).

The radial centroid shifts with respect to carrier frequency were approximately constant for 136 < z <146, allowing a single radial shift to be used for an initial estimate of shear speed using the Voigt model fit method (Chen et al., 2009) in section 7.4.5.

7.5.3 Shear Modulus Estimation

Figure 7.16 shows the shear speed and modulus estimates for CIRS phantom, using the 725/825 carriers (~0.39mm force radius change) and the 700/850 kHz carriers (~0.58mm force radius change) in subplots A and B, respectively. The red curves indicate the real part of the shear wave speed computed directly from the carrier-related force radius shift and measured displacement phase change. The error bars indicate the full data range for four different interrogation lines (positions over the face of the phantom). The blue curves show a fit to the wave speeds using shear elasticity (μ_1) and viscosity (μ_2) as the fit parameters, as was done in with the mechanical testing data in Chapter 6. The fit errors were 6.9 and 13.0% for the 725/825 and 700/850 carrier pairs, respectively. The green curves show the data fits for the CIRS QA sample described in Chapter 6. The average temperatures during the QA and full phantom experiments were 23.1 and 21.9 C, respectively.

The mean values of the phase-estimate shear speeds (red curves) were quite similar for the two carrier-pair cases, although they exhibited weak and opposite dispersion trends. As such, the fitted shear elasticities were in close agreement with each other, the QA sample fit, and the manufacturer's static modulus of 2.3 kPa (estimated from their measurement of Young's modulus and presuming the phantom material to be incompressible).

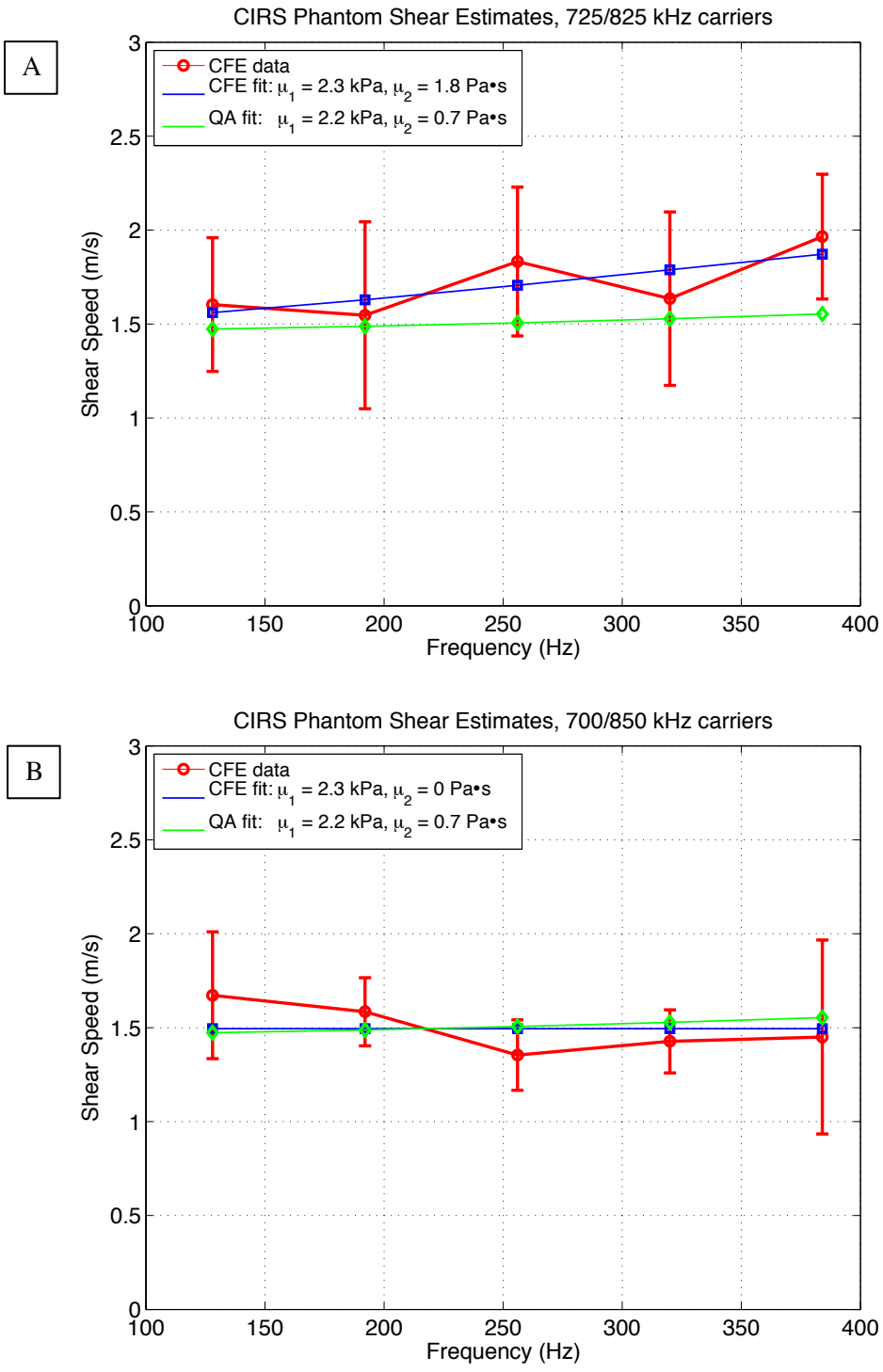

Figure 7.16. CIRS phantom shear speed and modulus estimates.

The shear viscosities varied between 1.8 and 0.0 Pa•s for the 725/825 and 700/850 kHz carrier pair experiments, bounding the QA sample estimate of 0.7 Pa•s. The zero viscosity result arose from the constraint that the shear modulus should have a non-negative imaginary part. Since the broader carrier separation produces a larger force radius shift, the 700/850 kHz pair result was expected to yield a more accurate result. It may be that the differences in beam width accompanying the greater radial shift introduce additional discrepancies, especially as the forcing beam width becomes wider with respect to a shear wavelength at higher frequencies.

The influence of the full forcing field on shear estimation was investigated using the model-based fit method described in section 7.4.4. No single carrier-induced radial force shift is presumed, but instead, the in-water measured intensities of the FT beams were used to specify the 3-D forcing function in the phantom material. The values of shear elasticity and viscosity that fit the relative measured phase response data are shown in Figure 7.17. The fit errors were 11.6% and 9.3% for the 725/825 and 750/850 kHz carrier pair measurements, respectively. With the model-based approach, the two carrier pair results were in closer agreement with each other regarding the shear viscosity.

Table 7.1 summarizes the estimated shear properties of the CIRS phantom determined from the fixed radial shift and full model methods described above. All measurements are in close agreement for shear elasticity. The variation seen in the shear viscosity is indicative of the difficulty in estimating loss factor in a low-loss material and with limited data bandwidth. A material with shear elasticity and viscosity of 2.2 kPa and 0.1 Pa•s, respectively, would have a shear speed loss tangent of approximately only 0.05 at 384 Hz – the highest frequency used in the data analysis. The impact of such a

small loss factor on the real part of the shear speed – the quantity that determines differential propagation phase used in the analyses – is difficult to measure unless some combination of bandwidth or SNR is increased. The CIRS phantom was therefore an interesting if unplanned opportunity to determine how well CFE can measure lack of loss.

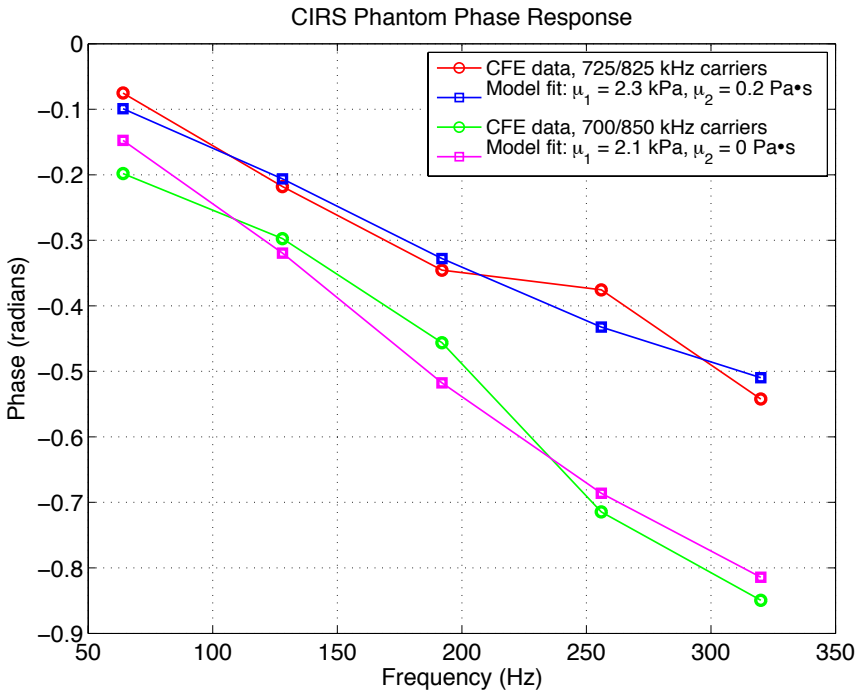

Figure 7.17. Measured and model-fit displacement phase responses.

Table 7.1. Summary of CIRS Phantom Material Properties

Method	μ_1 **(kPa)**	μ_2 **(Pa•s)**	**Data fit error (%)**
QA Sample static modulus	2.3	-	-
QA Sample shaker test	2.2	0.7	-
Phantom CFE 725/825 kHz, fixed Δr	2.3	1.8	6.9
Phantom CFE 700/850 kHz, fixed Δr	2.3	0.0	13.0
Phantom CFE 725/825 kHz, field model	2.3	0.2	11.6
Phantom CFE 700/850 kHz, field model	2.1	0.0	9.3

The model-based shear properties estimation method has the advantage of providing phase and magnitude information for comparison with the measured displacements. An example is shown in Figure 7.18 with the spectral magnitudes obtained for the 825kHz FT carrier. The measured and modeled spectra were normalized by their respective 256 Hz levels for ease of comparison. Agreement was within 1 dB over the analyzed frequency range.

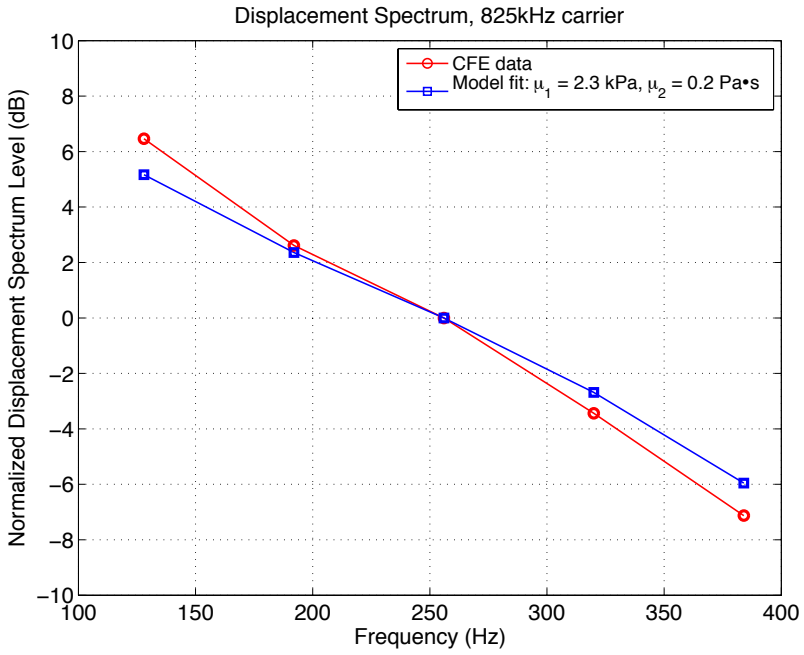

Figure 7.18. Displacement spectra normalized at 256 Hz.

7.5.4 CIRS Test Summary

To summarize, the experiments conducted with the CIRS phantom demonstrated the ability of the prototype CFE system to estimate shear properties 12 cm into a homogenous phantom tissue-like ultrasonic and low frequency shear properties. Two methods for data interpretation were tested and found to give very similar results.

7.6 Contrast Inclusion Phantom Testing

7.6.1 Objective and Approach

After completing tests with a homogeneous phantom material, it was of interest to determine if the prototype CFE system could differentiate localized stiffness discontinuities from an otherwise uniform elastic background. One such model system was available in the form of an "elastography phantom" procured from CIRS Inc. prior to the live animal testing that was used to define the material used for the experiments described in the previous section. The CIRS elastography phantom ("CE"), illustrated in Figure 7.19, featured 20mm diameter spherical inclusions having static Young's moduli of 15 and 50 kPa in a background material of 30 kPa, all as determined by the manufacturer. These equate to static shear elasticities of 5, 16.7 and 10 kPa, respectively – all higher than the 2.3 kPa value for the CIRS phantom material described in Section 7.5. The attenuation (1 dB/cm/MHz), sound speed (1550 m/s), and backscatter strength were specified to be uniform within all phantom components, so that in principle the inclusions could not be detected by conventional ultrasound.

As manufactured, the rectangular cross section of the CE phantom enclosure was approximately 20mm larger than expected in all dimensions, and there was no record of where the contrast inclusions were placed within the enlarged container. X-ray images[§§] revealed no evidence of inclusions. Consequently, CFE testing with the CE phantom was somewhat more of a "blind" exercise than expected.

[§§] Imaging courtesy of Georgia Tech Health Services

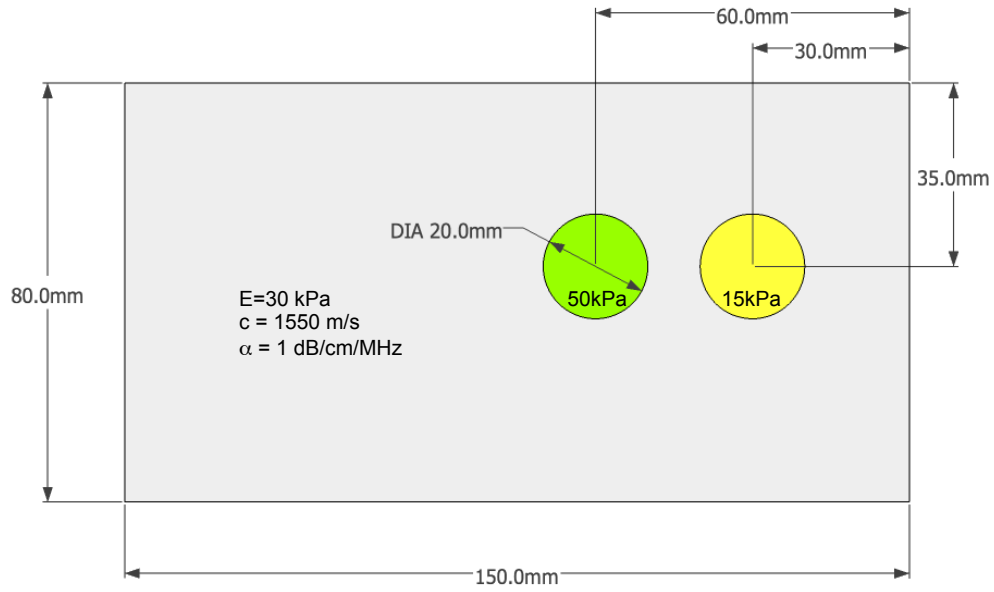

Figure 7.19. Side view of the CIRS elasticity phantom as designed.

The use of the CE phantom presented several challenges beyond those encountered with the homogeneous phantom. First, all constituent materials, including the softest of the inclusions, were stiffer than the homogeneous phantom. Stiffer materials decrease measurement SNR and decrease the relative phase of the displacements induced by a CFE carrier shift, resulting in a considerable increase in noise sensitivity. Second, the ultrasonic backscatter properties were quite different than the homogeneous phantom (and therefore, different than the live cetacean tissues previously tested): the backscatter strength was low by a factor of three and the attenuation was high by approximately 0.5 dB/cm/MHz. This was compensated to a degree by the necessity to offset the CFE transducers from the phantom so that the focal plane would intercept the inclusion centers. However, doing so also produced a large water-phantom interface

reflection that set the upper limit of the digitizer dynamic range and required that the NIVMS interrogation signal be decreased by approximately a factor of three.

An additional challenge with the CE phantom was with regard to axial resolution. Figure 7.20 shows a single inclusion and a CFE FT beam pattern shown on the same geometric scale. The 20 mm inclusion spans the majority of the forcing pattern, including the ±4mm region centered at 140mm where a carrier shift produces a nearly uniform radial pattern shift. At the extremes of the FT pattern, the shift is a function of axial position. The significance of the above is twofold: the FT beam will likely introduce considerable spatial integration beyond what accompanies the vibrometer processing, and it is unclear how CFE processing could be used to interpret data well outside the focal plane, where the displacement fields integrate a range of pattern shifts.

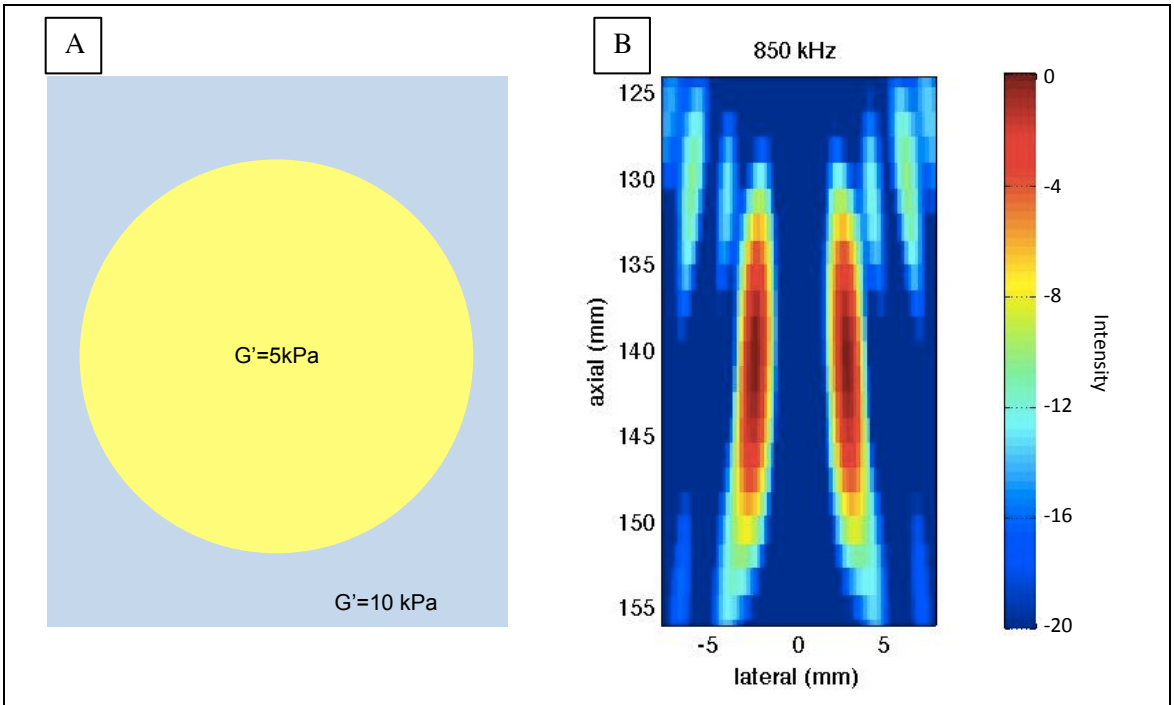

Figure 7.20. CE inclusion (A) and FT lateral-axial beam pattern (B).

7.6.2 Instrumentation

The electronics used for the CE phantom experiments were the same as used for the homogeneous CIRS phantom. The CE phantom case was fitted with a water bath, wherein the CFE transducers were suspended so that the focal plane was 35 mm into the phantom. This configuration resembled that which might occur if the CFE prototype was being used to determine shear properties of exterior jaw fats or shallow extracranial tissues. The large standoff from the phantom surface produced a large surface reflection because of its proximity to the focal plane, requiring that the VT transducer drive level be dropped by approximately a factor of three to avoid clipping the digitizer channel recording the VT receiver. The only other limitation on CFE testing with this configuration was that the ability to interrogate material near the corners of the phantom was impeded by scattering from the phantom case edges and the floor of the water bath installed around the case perimeter.

7.6.3 Results

Figure 7.21 shows the normalized backscatter (A) and root-mean-squared axial displacement (B) measured over the notional scan volume (C). In the latter, the "E" values are static Young's moduli specified by the manufacturer. The displacements were normalized by the lateral average of the results obtained in the "background region", corresponding to the scan range of 0-10mm. Relative to the background region, the displacement field clearly shows enhanced levels in a circular region approximately the size of the soft inclusion, and shows diminished levels approximately where the stiff inclusion was expected to be.

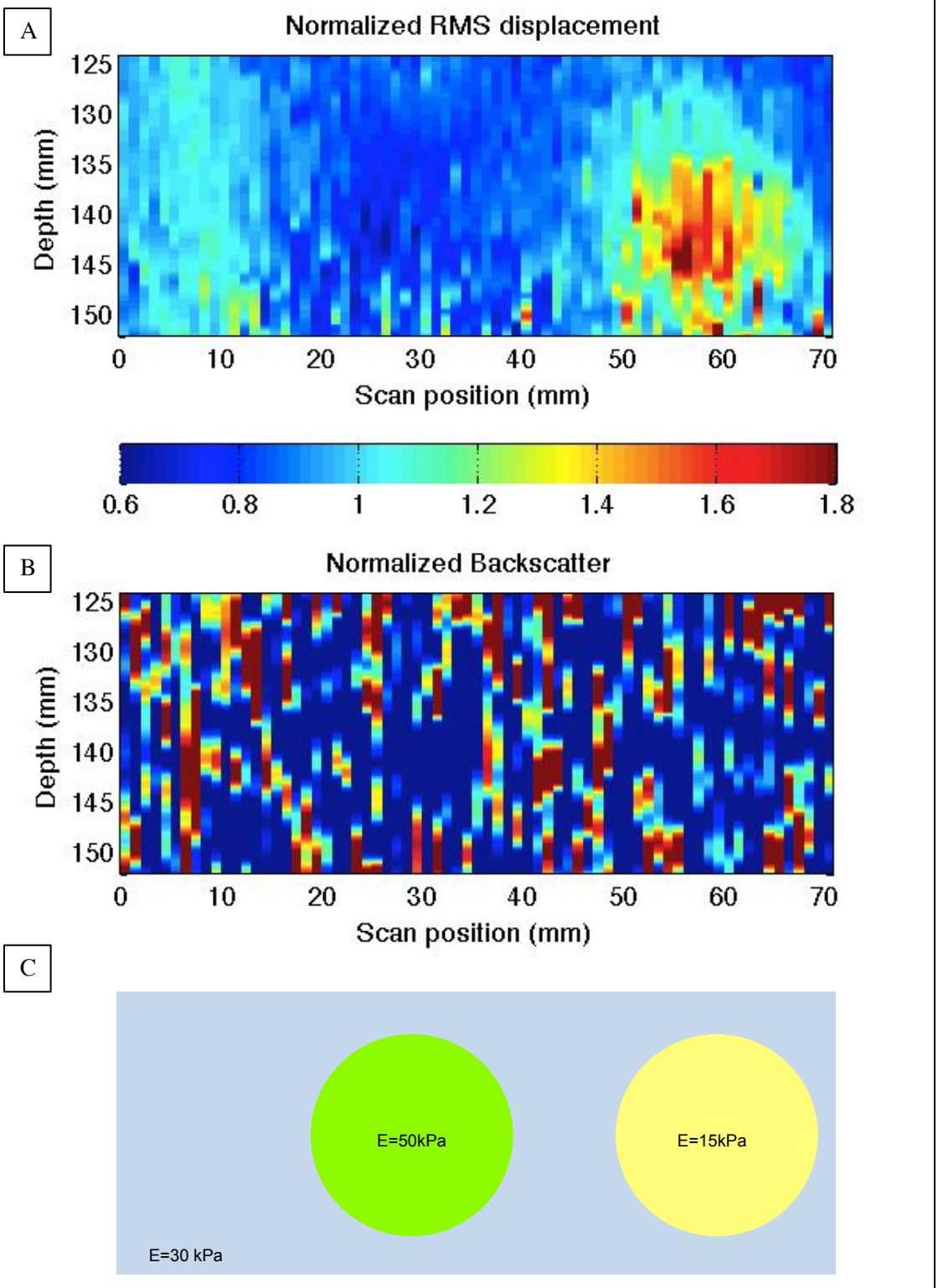

Figure 7.21. Normalized backscatter (A) and root-mean-squared axial displacement (B) measured over the notional scan volume (C).

The backscatter scan data in Figure 7.21B was normalized in the same way as the displacements, and plotted with the same factor-of-three dynamic range. Despite the inclusion phantoms being advertised to have no backscatter or attenuation contrast with the background medium, it appears that the scattering levels were in fact reduced in the inclusion regions (where displacements were seen to vary significantly relative to the background). Overall, the backscatter data also showed considerable spatial variability, which reinforces the difficulties that may be encountered by any ultrasound elastography system. When backscatter is low, either because of attenuation or low scattering contrast, received ultrasonic signals will be small, and the vibrometer noise floor will be elevated.

Proceeding with shear speed estimation using methods described in Section 7.6, it was found that the relative phase data generated from comparison of displacements generated with 850 and 700kHz FT carriers did not look like any data previously encountered. Figure 7.22 shows examples of relative phase in the CFE focal plane depth for data recorded in the background and "soft" inclusion regions. Both phase data sets are shown with predictions based on the manufacturer's elasticity specifications. The background material result exhibits a fairly simple delay characteristic, while the "inclusion" result shows an anomalous phase response. When trying to fit the measured phase data as part of the standard shear estimation processing, it was found that the regions with elevated or depressed displacement levels also had especially high fit errors (7.22C).

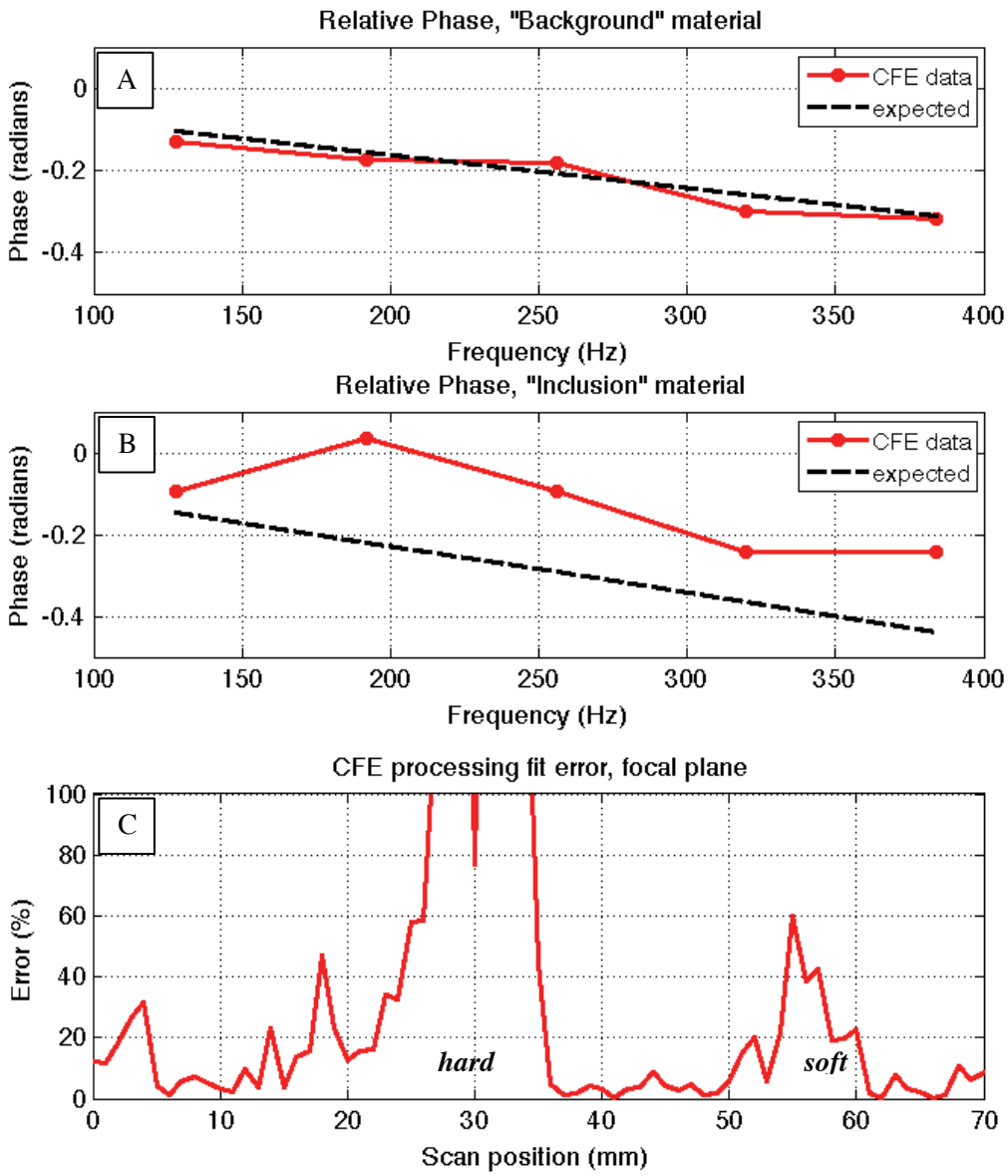

Figure 7.22. Displacement relative phase data from the (A) background and (B) soft inclusion regions, and the shear elasticity fit error in the focal plane (C).

The above results may be explained in terms of shear reverberation inside the inclusions. Whether soft or hard relative to the background material, shear waves inside an inclusion would reflect at the inclusion-background boundary, and a spherical inclusion would geometrically focus these reflections. This effect becomes resonant

when the inclusion diameter is at least on shear wavelength. For example, if the "soft" inclusion has a shear elasticity of 5kPa, the radius of the inclusion would be equal to a half shear wavelength at 110 Hz – well within the present measurement range. As seen by the vibrometer beam at the center of the forcing pattern, the direct shear wave arrival would be followed by a series of later arrivals from the inclusion boundaries, with their timing depending on where the forcing beams were inside the inclusion. The differential phase induced by an FT carrier shift could be contaminated if reverberant effects were strong, as suspected inside a spherical reflecting shape. The significance of reflected fields both inside and outside elastic contrast inclusions has been studied by several groups developing elastography techniques (Deffieux et al., 2011; Rouze et al., 2012), and led to testing of a method using resonant modes for detection and classification of contrast inclusions (Henni, Schmitt, Trop, & Cloutier, 2012). De-reverberation signal processing techniques have been developed based on various forms of wavenumber filtering, requiring that two or three dimensional displacement field data be available for each force application. Such data is not available in the CFE prototype.

An initial attempt to reduce reverberation effects in the data was made by applying a short, tapered time window prior to calculating displacement Fourier transforms. While increasing tapers started "flattening" the phase, it did so at the expense of discarding much of the energy of the direct signal. Therefore, an alternative approach at processing the CE phantom data was pursued. First, the shear properties of the "background" material were found using the full model fit process previously demonstrated with the homogeneous phantom. Next, the relative delays in the displacement signal start times between the background and inclusion scan regions were

computed by cross correlation. Given the shape of the displacement waveforms, this process emphasized the timing of the direct arrival from the CFE forcing regions. For example, if the displacement waveform at a particular location is found to arrive later than observed in the background material, the shear speed in the vicinity of that location must be lower than that of the background material. Formally, the delays calculated from the cross correlation process would be associated with shear group velocity, not phase velocity. However, in a weakly dispersive (low loss) material, the group and phase velocities are approximately equal. The background material shear modulus fit gave $G_{background} = 10.8e3 + 3.8i\omega$ Pa (fit error = 16.4%). With these values, shear viscosity contributes no more than 10% to the real part of the shear speed at the highest analysis frequency of 448 Hz. As such, the correlation technique may yield a reasonable broad-band estimate if the inclusion materials have similar loss tangents to that of the background material.

Correlation delays were estimated from the displacement data as a function of depth after windowing and up-sampling from the base rate of 1.6 kHz to 32 kHz. All delays $\Delta t(z)$ were computed relative to an average "background" scan line, from which a local shear speed $c_{est}(z)$ was found from: $c_{est} = \left(\frac{\Delta t}{r} + \frac{1}{c_{s,background}}\right)^{-1}$, where r is the FT beam intensity pattern radius. The shear elasticity was then found from $G_{est} = \rho c_{est}^2$, where ρ is the material density, in this case provided by the manufacturer. An added benefit of this method is that it allows estimation of the properties of all material in the scan area, thereby extending the useful axial extent of measurements made with the prototype system.

Figure 7.23 shows the estimated shear modulus within the scan region, along with the displacement image repeated from 7.21. The high displacement region (scan 50-70mm) clearly transforms to a low shear region, with tapering at the region edges indicative of the spatial averaging in both the physical arrangement of CFE beams and in the signal processing. While the low displacement region (scan 20-40mm) shows elevated moduli estimates, the values have a noisy distribution. The background region (scan 0-15 mm) is also variable but somewhat less noisy.

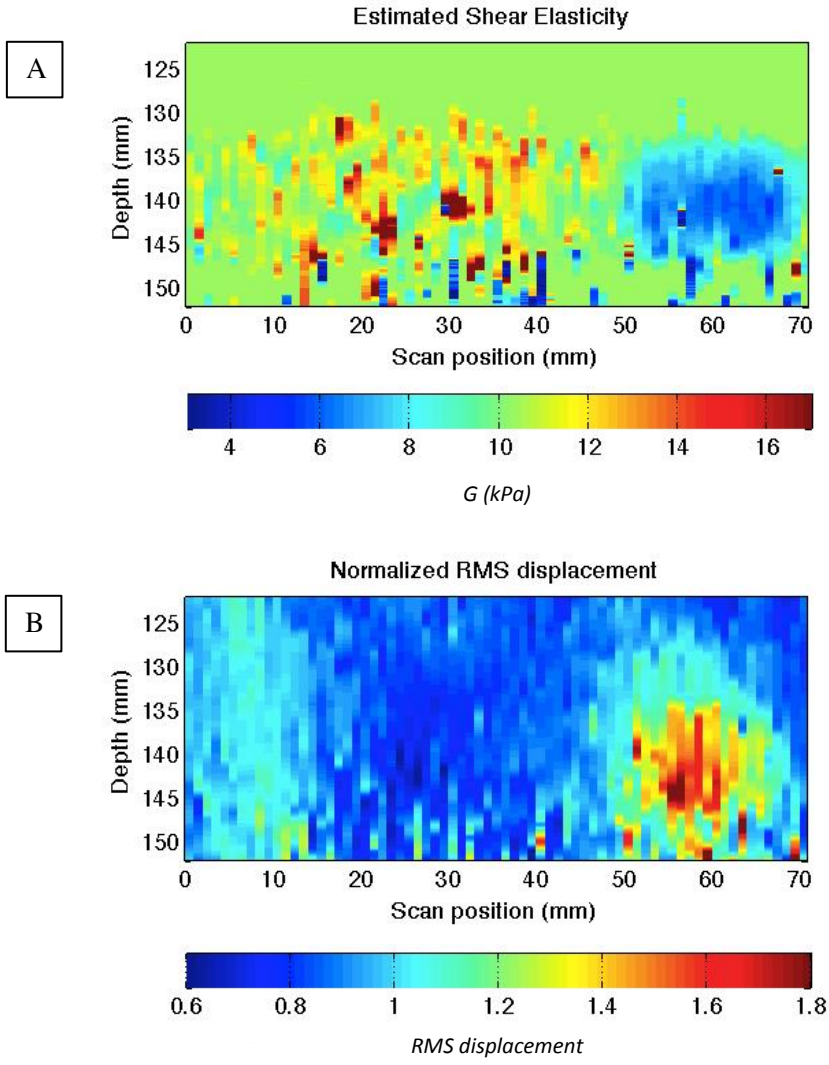

Figure 7.23. Estimated shear elasticity (A) and rms displacement (B) in the CE phantom.

These results are all consistent with the backscatter trends in Figure 7.21. The backscatter is highest as the shallowest depths, and the shear estimates are nearly uniformly at the background elasticity level, as would be expected from the phantom design. Near the focal plane (140mm) the least noisy results are seen with the soft inclusion region, which had nearly twice the displacement level as the background. At larger depths, all regions exhibit more variability in the shear estimates, as might be expected when backscatter is minimal.

One curious aspect of the scan images in Figure 7.23 was the apparent shape mismatch between the displacement and elasticity maps in the vicinity of the soft inclusion. Specifically, the displacement image was nearly circular, while the elasticity image appeared vertically truncated. A set of diagnostic measurements was conducted to verify scan alignment, and based on displacement magnitudes, it appeared that the original scan line was offset from the inclusion centerline by approximately 5 mm. A second scan of the CE phantom was taken to assess the impact of the apparent alignment error. These results are compiled in Figure 7.24. The displacement contrasts for both the hard and soft inclusion regions (left and right columns, respectively) were more readily visible in the second scan, which led to the notion that the second scan was better aligned with the inclusion centers. In the shear elasticity maps, the hard region appeared to be better defined in the second scan, but the soft region was largely unchanged. The CFE prototype spatially integrates both laterally and axially. Laterally, the FT beams encircle the VT scan line. Axially, the FT beams span over 20 cm, and the VT output resolution further integrates on the scale of ~ 3-4 mm in large part to mitigate noise due to backscatter irregularity. This suggests that the system would show much greater

integration / averaging in the vertical direction, but it does not explain why the two inclusion types would exhibit seemingly different vertical extents in their shear maps.

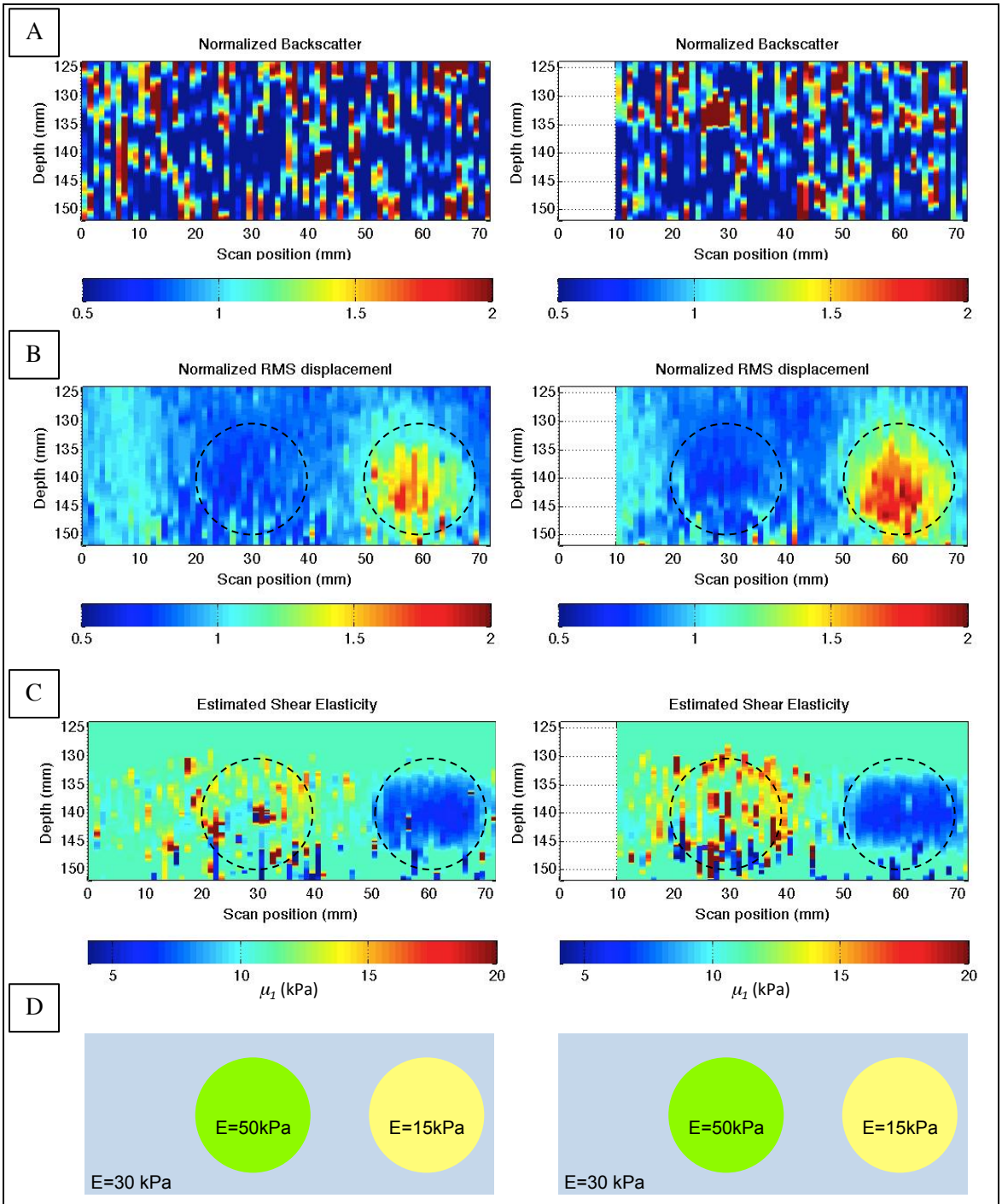

Figure 7.24. Summary results for the misaligned first (left column) and second (right column) scans of the CE phantom: normalized backscatter (row A), normalized RMS displacement (row B), estimated shear elasticity (row C), and notional phantom layout (row D).

Figure 7.25 summarizes the shear properties in the CE phantom as a function of scan, processing type, and material type. For each material, Figure 7.25 shows the mean and +1 standard deviation of the shear elasticity estimated within an eight by eight millimeter square region of interest (ROI) axially centered in the focal plane of the CFE transducers. The two processing types were the full model "CFE" and background delay "correlation" methods. The green dashed lines indicate elasticity values determined using the shaker test methods in Chapter 6 after removing the protective membrane from the phantom. Specifically, the background material properties were determined using surface excitation of the intact phantom, while the inclusion properties were determined by directly exciting the excised inclusions on the shaker.

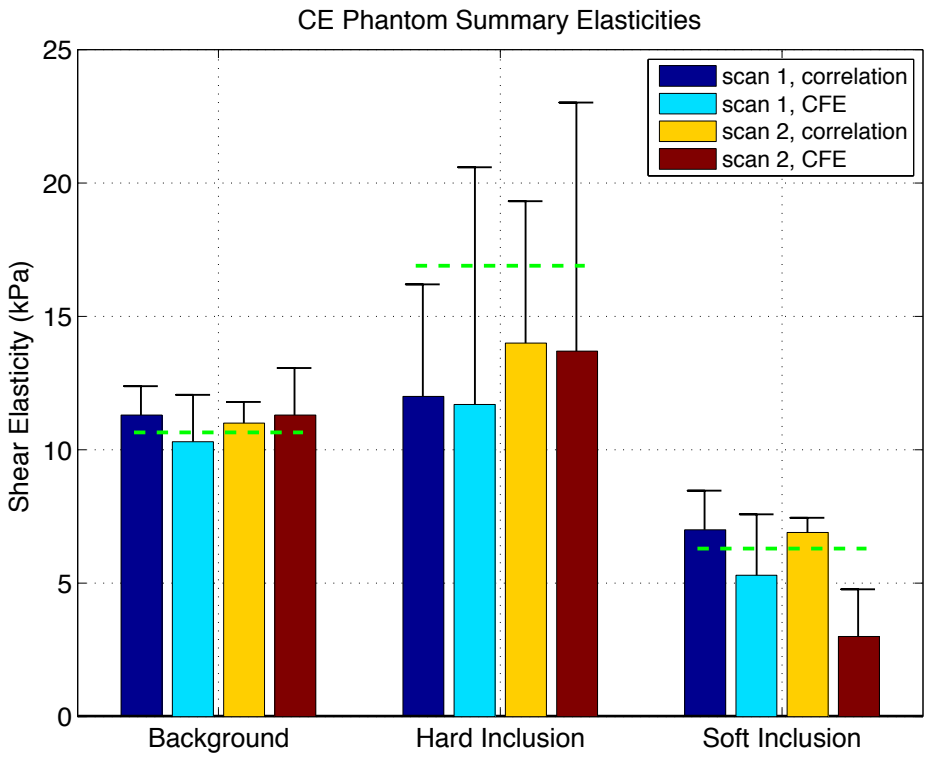

Figure 7.25. Summary statistics for the CE phantom scans.

The results for the background material were fairly uniform with respect to method and scan, and within 10% of the shaker test value. The results for the hard inclusion trended low relative to the expected value, with large variations within the data sets. The results for the soft inclusion bounded the expected value, with varying degrees of deviation. For both inclusion types, the standard deviations for the correlation (arrival time) method were lower than for the CFE processing method, reiterating the difficulty of interpreting complex wave fields with the system as implemented.

7.6.4 Inclusion Testing Summary

CFE testing with a phantom with shear contrast inclusions provided several challenges relative to the homogeneous phantom material tests in the previous section. The baseline methods for estimating shear speed from carrier-induced displacement phase shifts did not appear to work as effectively inside regions believed to contain local shear variations relative to the background material. It was hypothesized that aberrant phase responses were caused by reverberation within the spherical inclusion, and an alternative method for estimating depth-dependent shear elasticity was proposed. The method allowed quantification of shear discontinuities, with results generally consistent with the expected inclusion geometry. This method would not be valid in highly dispersive (high shear viscosity) media, but such media would be also suppress longer propagation paths and with them, any significant reverberation effects.

A considerable body of work has been reported using relative displacement or strain imaging (Doherty, Trahey, Nightingale, & Palmeri, 2013; Gao, Parker, Lerner, & Levinson, 1996). Although relatively immune to the processing noise issues encountered

with modulus estimation, quantitative diagnostic use of displacement images can be challenging because the displacement magnitudes depend on the applied force (impacted by high frequency material properties, especially attenuation), and the desired low frequency material properties. All of these quantities are unknown *a priori*, but this is not necessarily a critical restriction. Ultrasound backscatter by itself is quite commonly used for diagnostic, if non-quantitative purposes, despite a lack of high frequency properties information. However, *in vivo* ultrasound attenuation can be estimated using methods such as that which was used in Chapter 5, or with more sophisticated methods (Bigelow, 2010). If the CFE ultrasonic data was first processed to quantify and then offset gross variations in attenuation, it may be possible to use measured displacement as either a standalone metric or as a compliment to shear modulus estimation.

In the present study, the contrast between inclusion materials was fairly small (within a factor of two) compared to some order of magnitude cases found in nature (Skovoroda, et al., 1995). However, both the displacement and elasticity maps provided superior contrast to conventional ultrasound.

7.7 Ultrasound Safety

The ultrasonic exposure safety of the transmissions used in the foregoing experiments was assessed relative to prescribed limits for diagnostic systems (US Dept. of Health and Human Services, 2008), using the expressions in Chapter 1.7. The FT transmissions were calculated to be:

- 48% of the maximum allowable mechanical index (*MI*), which quantifies the risk of tissue damage due to cavitation during negative pressure phases; and

- 87% of the maximum allowed spatial peak time averaged intensity (I_{spta}) of 7200 W/m^2, which quantifies risk of tissue damage due to heating.

The VT transmissions had *MI* and I_{spta} values that were 4% and 7% of the maximum allowable values, respectively. Therefore, as intended, full CFE system operated within prescribed safety limits.

An additional step was taken to quantify the temperature rise in the tissue phantom as a function of time, applying acoustic properties of the phantom and thermal properties of human brain (NCRP, 1992) to the simulation method described in Chapter 2.4. Figure 7.26 shows the estimated temperature rise in the focal plane of the CFE system as produced by the FT transducer driven as in the CIRS experiments, but with the carrier fixed at 850kHz - the highest value tested. This was done because higher frequencies were expected to produce the largest heating effects as a result of ultrasonic absorption increasing with frequency. The limiting case for these calculations was with no convective heat transfer out of the ensonified region from blood flow (no perfusion).

In Figure 7.26, the temperature distribution is shown along a radial line centered on one of the six incident intensity lobes, shown in black for reference. After one second of exposure, there was a peak temperature rise of less than 0.01C corresponding in space to the location of maximum ultrasonic intensity. After 500 seconds, corresponding to ten typical data collection ensembles, the temperature rise elevated to less than 0.25 °C, with the spatial distribution leveling off at small radii. This indicates longer-term diffusion of the heat generated by the individual lobes of the ultrasound pattern. All values were well below the safety limit of 6 °C.

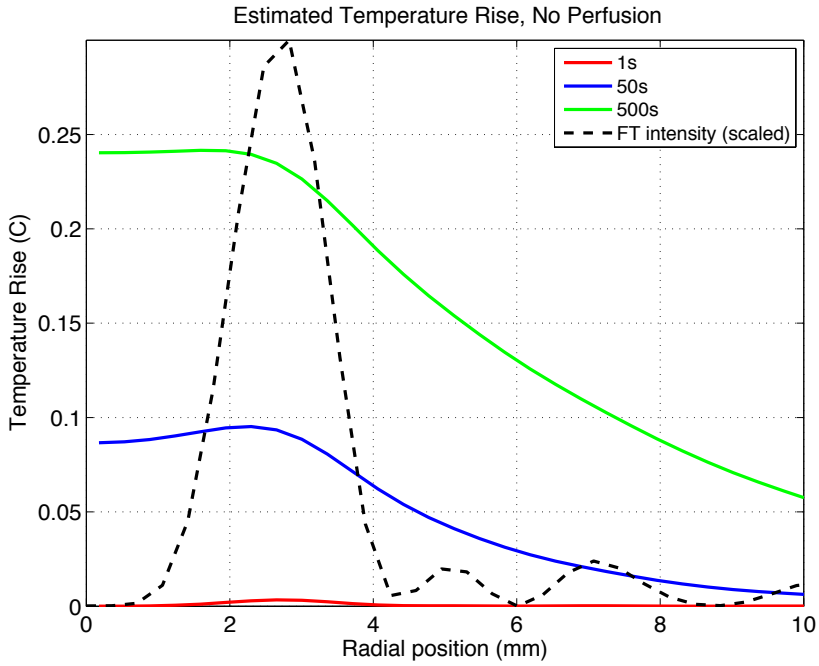

Figure 7.26. Estimated temperature rise in the CFE focal plane, using the drive conditions employed during CIRS phantom testing.

This finding was generally consistent with other studies done in support of ultrasonic elastography systems (Palmeri & Nightingale, 2004), where it was argued that significantly elevated incident intensities would be safe on the basis of quantified thermal effects, rather than those inferred from a single intensity metric.

The specific combination of FT signal amplitude, duration and pulse rate used in the phantom tests was chosen as a tradeoff between maximizing low frequency signal content (via drive duration) and minimizing harmonic generation (via drive amplitude). Pulse rate was used to control time-averaged intensity once duration and amplitude targets were established. A further amplitude-related issue was discovered during testing, where the FT power amplifiers were found to behave somewhat unreliably when peak

output voltages exceeded approximately 17 V. Although the manufacturer stated that the amplifiers could produce up to 50V peak (into 50 Ohms) in pulsed mode, the threshold for internal compression was at approximately 20V. Conceivably, a combination of higher capacity amplifiers and improved impedance matching would enable higher drive amplitude levels, with the pulse rate slowed to keep the time averaged intensity within safety limits.

For example, if the FT drive signal was doubled, the pulse intensity (as well as force and resulting tissue displacement) would quadruple, requiring the pulse rate to be slowed by a factor of four to maintain exposure safety with respect to time-averaged intensity. On a per-pulse basis, SNR would double, but because there are fewer pulses, over a one-second data collection period the integrated SNR obtained with the baseline and double amplitude, quarter pulse rate drive signals would be the same. However, if the two displacement data sets were windowed for a common duration of time (e.g. $1/64^{th}$ of a second following each drive pulse, regardless of pulse rate), the double amplitude, quarter rate data set would have a net 6 dB SNR benefit. This would reduce the data collection/averaging time required to meet a given SNR goal by a factor of four, translating to shorter test/examination times with no loss in safety margin.

7.8 Tissue Phantom Summary

The CFE system was tested with tissue-mimicking phantoms having uniform properties and with shear (but no other intended) contrast inclusions. All tests were done with waveforms and drive levels designed to operate the CFE system within diagnostic ultrasound safety limits. The homogeneous phantom, which had a shear elasticity in the

range of published values for human brain, yielded results that were in close agreement with separate mechanical tests and manufacturer static modulus values.

The shear contrast inclusion experiments revealed several technical challenges for the CFE prototype which, as presently implemented with a single vibrometer scan line, was not well equipped to deal with both direct and reflected shear waves. An alternative method for estimating local shear speed was tested and found to provide a credible description of the shear properties distribution. This was an example of how, in the absence of useable relative phase data, a "calibrated" response of the system could be used to estimate properties. A more general challenge was encountered as a result of the constituent materials all being much stiffer than the homogeneous phantom. When combined with elevated ultrasonic attenuation and reduced scattering, noise-limitations on the shear-estimation performance of the CFE prototype were revealed. Design modifications to address the above problems are discussed in Chapter 9.

CHAPTER 8

CETACEAN BONE TRANSMISSION

8.1 Objectives

In cetaceans, many of the tissue measurement targets of interest, such as brain and specialized jaw fats, are obscured by bone. While the CFE prototype was designed to have the axial extent to reach these tissues in an adult bottlenose dolphin, it was not known what effects the intervening bone may have on the beam patterns and signal strengths. The primary objective of the experiments in this chapter was to investigate the transmission of CFE signals through representative samples of bottlenose dolphin skull and mandibular bone in order to assess cumulative attenuation, refraction, and diffraction effects and their impact on elastography measurements. A secondary objective was to quantify bone surface temperature rise as a direct measure of thermal exposure safety.

8.2 Methods

Dry, flensed bottlenose dolphin bone samples were received from a marine mammal stranding network office in South Carolina. The decision to use samples without adjoining soft tissues was made in the interest of first understanding bone transmission in the absence of any other complicating factors. The significance for in situ experimentation is discussed at the end of this chapter. The skull specimen (MMES-2004-003-SC) and jaw specimen (MMES-2004-160-SC) were photographed and examined for surface curvature and roughness, thickness. The skull specimen was cut

along the mid-sagittal plane for access to the interior. Additional photographs were taken with the interior sample surfaces illuminated with a white light in order to visualize regions of relative transmission (Figures 8.1 and 8.2). Efforts were made to center the light within the skull in order to minimize position-related biases. While quantitative assessment of light transmission would have required greater experimental precision, it was qualitatively found through subsequent caliper measurements that regions with highest light transmission corresponded with low bone thickness and surface roughness.

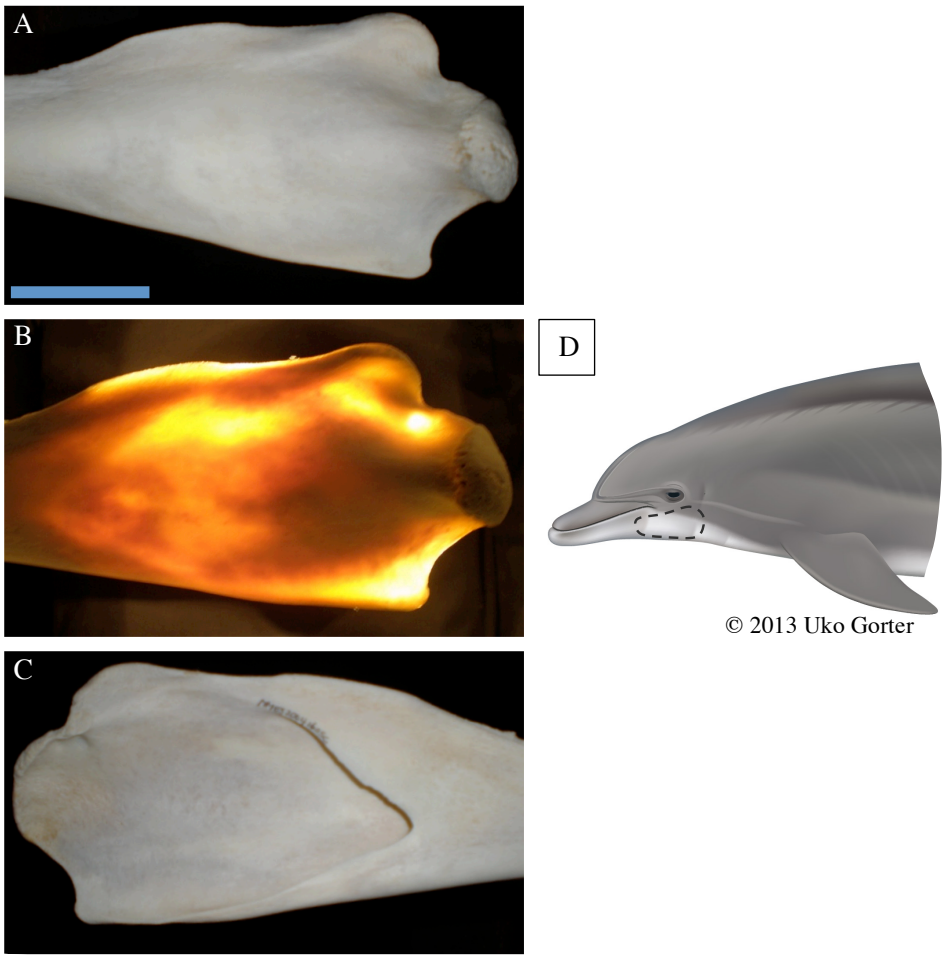

Figure 8.1. Bottlenose dolphin mandible exterior illuminated with room light (A) and back light (B), interior (C), and illustration of location within an intact animal (D). 5mm scale bar.

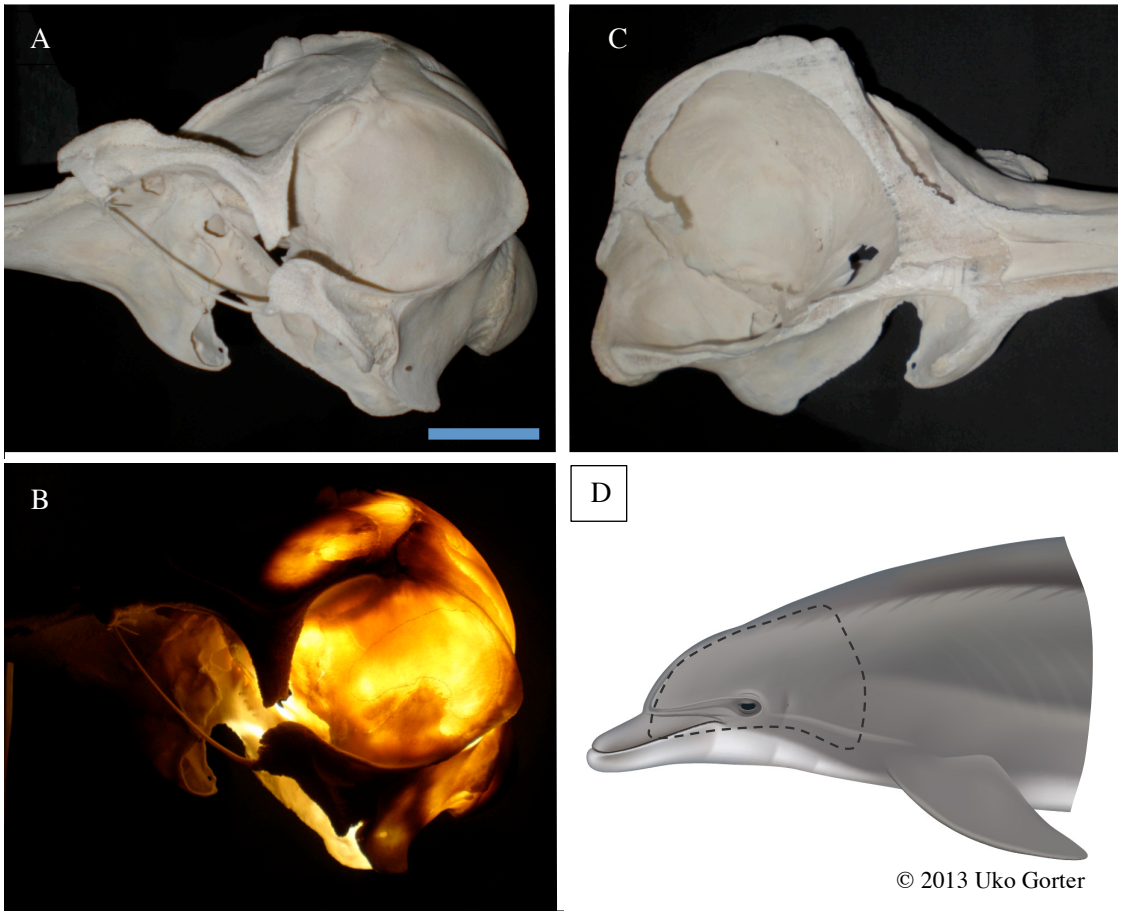

Figure 8.2. Bottlenose dolphin skull exterior illuminated with room light (A) and back light (B), interior (C), and illustration of location within an intact animal (D). 5cm scale bar.

Favorable light transmission does not guarantee favorable ultrasound transmission, but there does appear to be a correlation dating back to the notion of the jaw as an acoustic window (Norris, 1968) based on initial optical observations.

A set of points within the high light transmission regions on the mandible and skull, indicated in Figure 8.3, were defined for acoustic testing. The selection process was intended to support a limited acoustic survey of regions where absorption, refraction and scattering effects would be least likely to adversely affect the CFE beam patterns and levels. Two distinct regions were selected on the skull: the temporal fossa, identified as a

likely high transmission window (Chapter 1), and the supraoccipital bone, which showed a relatively large surface area of high light transmission, low surface roughness, and absence of ridges or sutures (where adjoining bone segments interlock). Other regions, including the interparietal skull bone, were seen to have some areas with superficially favorable characteristics, but either had small spatial extent (< 4cm^2), adjoined bony projections that would make them difficult to locate in an *in vivo* application, or were characterized by complex curvature that could cause excessive beam refraction.

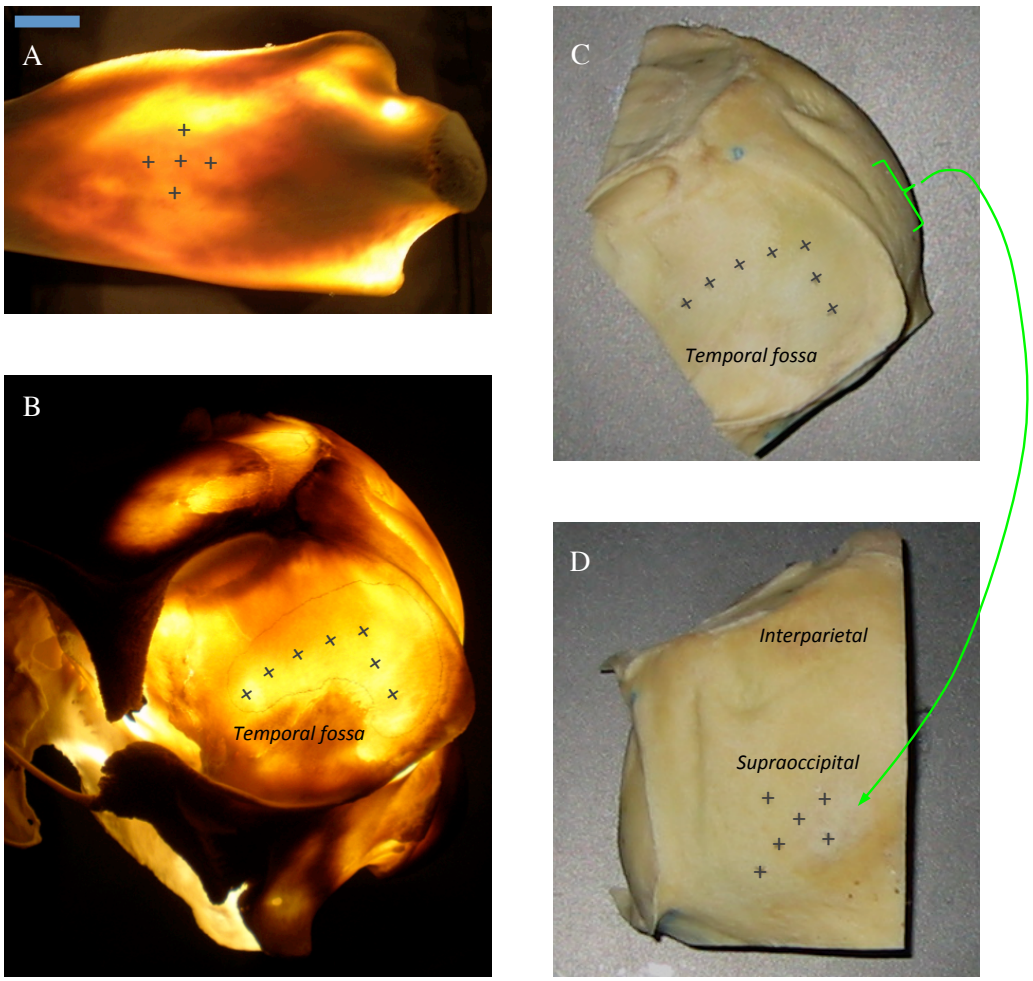

Figure 8.3. Bottlenose dolphin bone samples with markings indicating locations on which acoustic tests were centered. (A) Back-illuminated mandible with 2cm scale bar, (B) back-illuminated skull, (C) front-illuminated temporal fossa, and supraoccipital bone (D).

Bone thicknesses at each marked location were measured using digital outside calipers with a display resolution of 0.1 mm. Calibration of the calipers against reference gages (Starrett Webber grade 2) revealed an accuracy bias of -0.2 mm, as averaged from eight measurements on gages of two different thicknesses.

Dry bone samples were re-hydrated in distilled water salinized with Instant Ocean (Spectrum Brands, Inc.). The immersed samples were first held under vacuum for 12 hours, and then pressurized at 30 psi. This pressure cycling was conducted three times. For acoustic testing, samples were transported submerged to the water tank in which acoustic testing was conducted.

The instrumentation for the bone transmission experiments was the same as used for CFE transducer calibrations (Chapter 4). Bone samples were held between the transducers and a needle hydrophone using common chemistry lab equipment, and suspended from a manual two-axis positioner for fine-tuning. The ultrasonically illuminated bone surface was held 118-122 mm (confirmed by acoustic reflection measurement) from the CFE transducers, equivalent to 18-22 mm above the hydrophone. Horizontal plane scans were conducted with both the FT and VT transducers driven, using the same amplitudes as used during CFE system operation during tissue phantom experiments. Alignment of a selected bone interrogation location with the CFE beam axes and hydrophone scan center point was achieved using a red light laser cross hair arrangement, shown in Figure 8.4.

Separately, each of the regions tested with the CFE system was ultrasonically scanned in order to quantify bone curvature, as in Figure 8.5. Two opposing 20 MHz focused transducers (Olympus Panametrics V317) were driven with a pulser-receiver

(Panametrics 5072PR), with echoes from the interior and exterior bone surfaces recorded on a high-speed digitizer (Cleverscope 328A). Flight times were converted to distance estimates using an expression for the temperature dependence of sound speed (Chen & Millero, 1976) and thermocouple measurements of water temperature at the beginning and end of each scan.

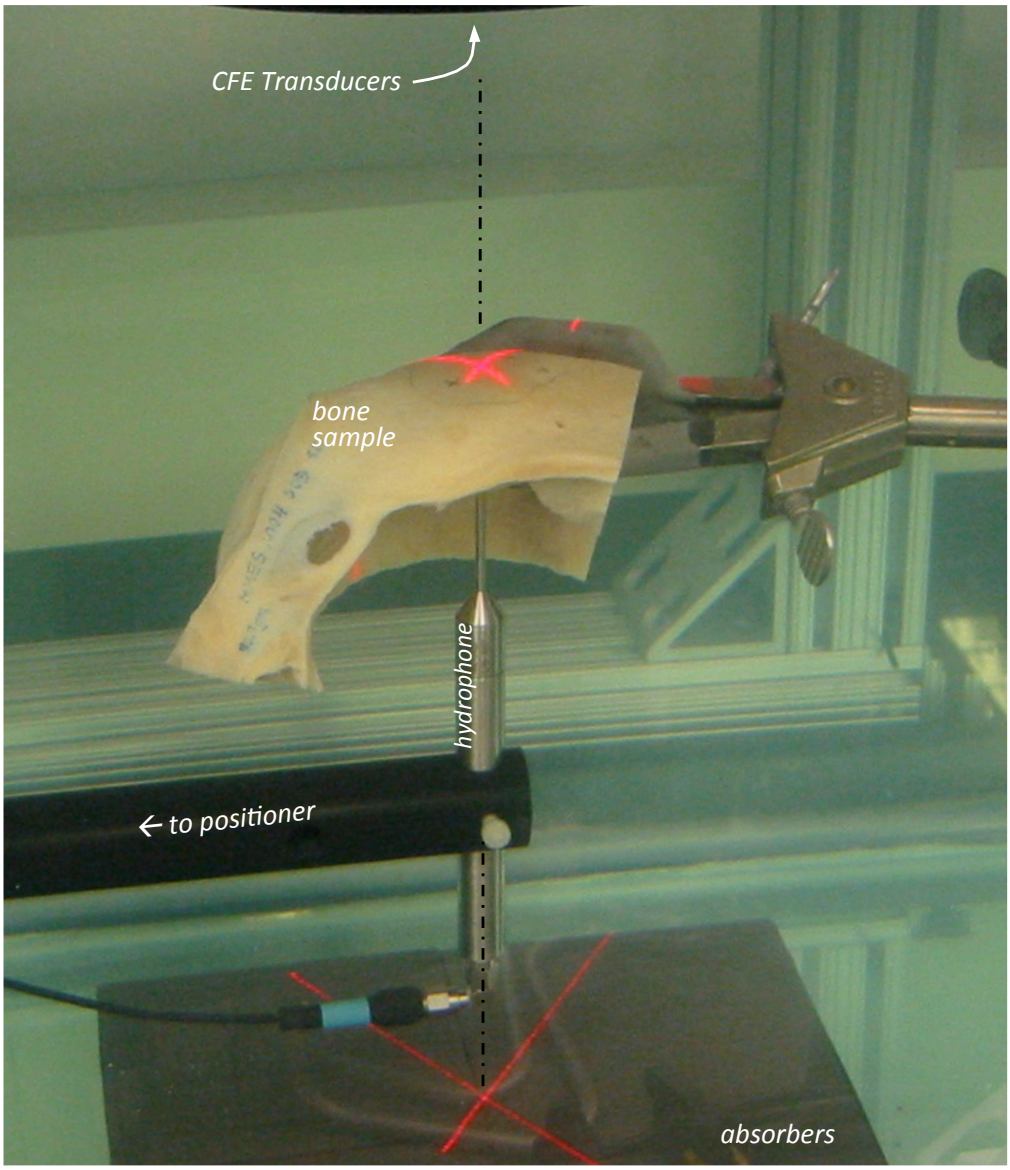

Figure 8.4. Ultrasonic bone transmission experiment configuration.

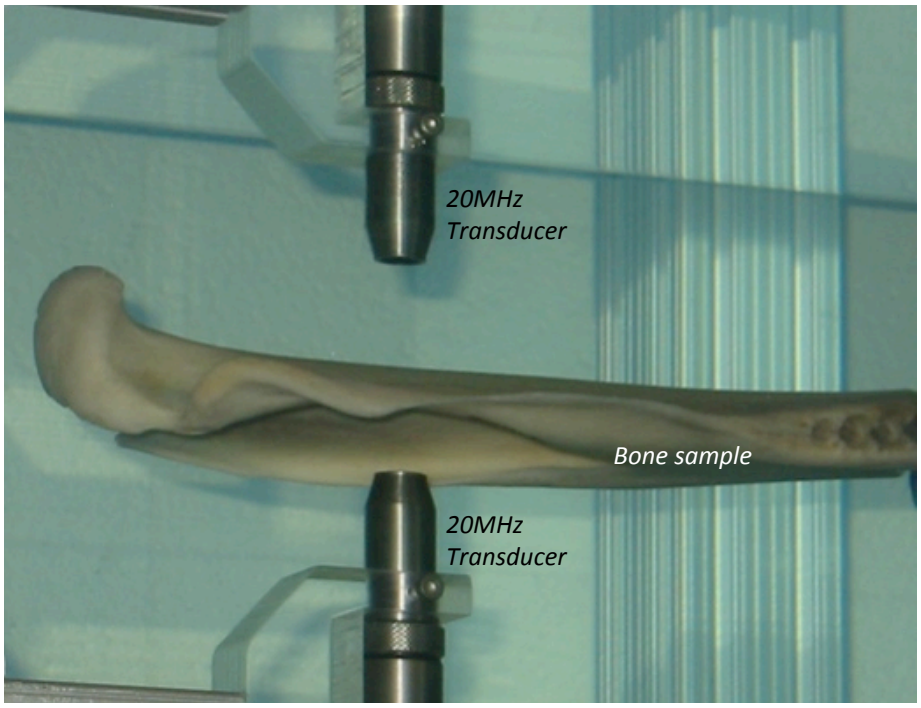

Figure 8.5. Ultrasonic bone curvature mapping experiment configuration.

Finally, a set of thermal impact measurements was conducted by placing the exposed tip of a type-K thermocouple on the ultrasonically interrogated bone. Temperature readings were noted as a function of time after turning the transducers on using a digital thermometer with 0.1 °C display increments. Three measurements were made at each interrogated site, each time slightly changing the location of the thermocouple but staying close to the center of the ~6mm characteristic diameter of the FT beam pattern. Additional readings were taken in the absence of bone in order to calibrate any temperature rise in the thermocouple itself.

8.3 Results

8.3.1 Vibrometer Transducer Response

The focal plane beam patterns of the vibrometer transducer (VT) are shown in Figure 8.7 for the reference case (no bone) and examples from each of the three bone regions tested (Figure 8.6). The data were frequency-weighted and summed over the 1.5 - 2.5 MHz band in a manner approximately equivalent to the transmissions used for prototype CFE testing. All pressures were normalized by the reference pattern's peak amplitude. Qualitatively, the dominant effect of transmission through these bone samples was signal attenuation. Bulk refraction (whole-beam shifting) effects were minimal, and the patterns appeared to retain their general forms, but with greater sidelobe variability.

This is seen in more detail in Figure 8.8, showing beam pattern cross-sections for the proximal mandible. The coronal plane patterns (along the length of the mandible) showed a modest degree of beam width expansion and sidelobe reduction. The dorsoventral (vertical) plane patterns more closely matched the reference beam shape.

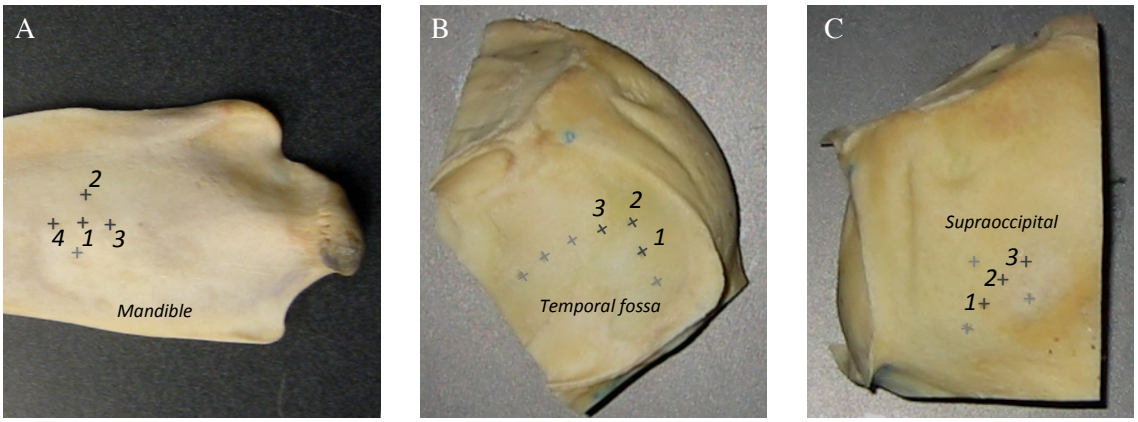

Figure 8.6. Enumerated locations of scan data: (A) Proximal mandible, (B) Temporal fossa, (C) Supraoccipital.

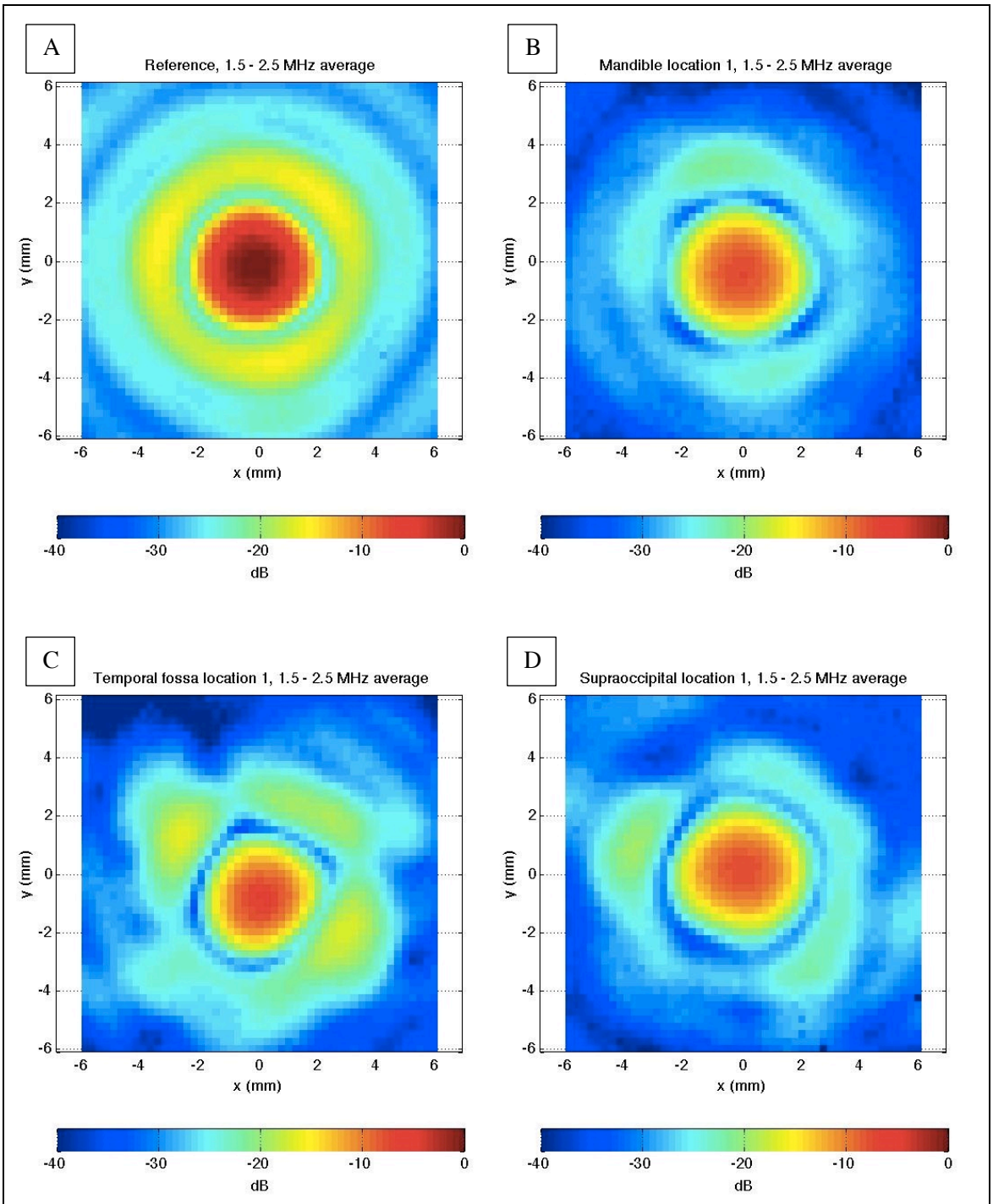

Figure 8.7. VT normalized, frequency-averaged focal plane beam patterns: (A) reference, (B) Mandible location 1, (C) Temporal fossa location 1, and (D) Supraoccipital location 1. The "x" and "y" directions are coronal and dorsoventral, respectively.

A

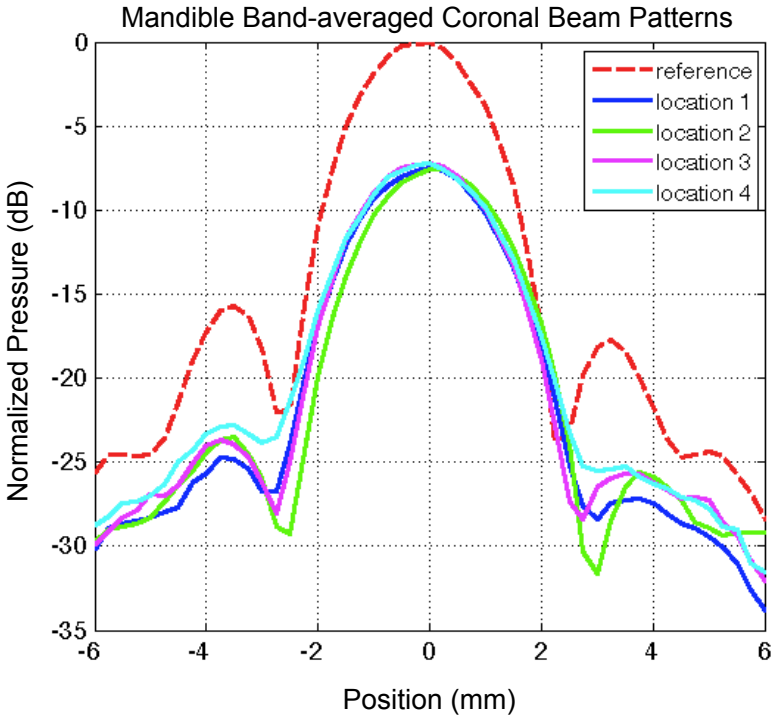

B

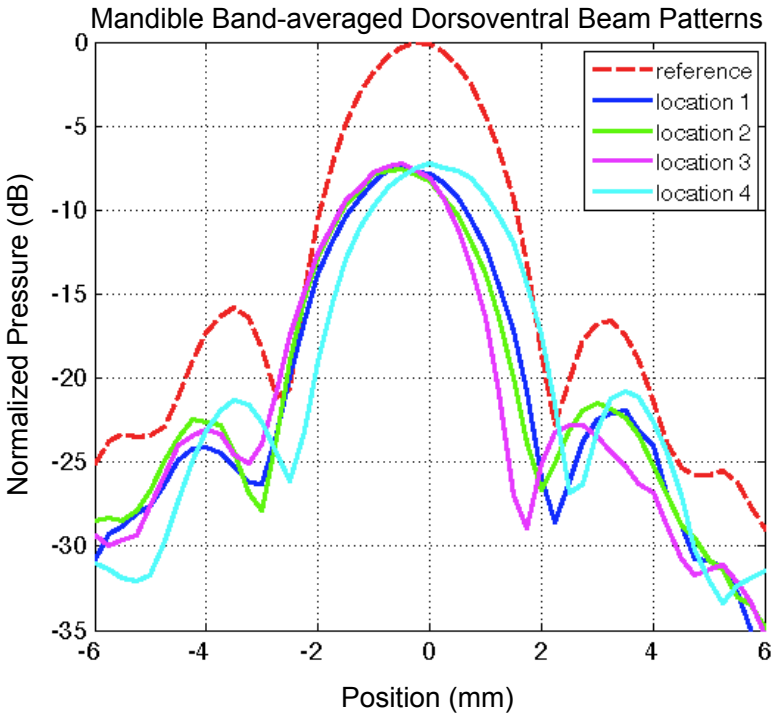

Figure 8.8. Proximal mandible coronal (A) and dorsoventral (B) VT beam patterns.

Figure 8.9 shows VT beam patterns transmitted through the temporal fossa and supraoccipital bones. The former superficially appeared to have nearly spherical local curvature, while the latter appeared elliptical – somewhat of an intermediate case between mandible and temporal fossa. In many but not all cases, the coronal and dorsoventral trends for beam sidelobe shape and size were similar.

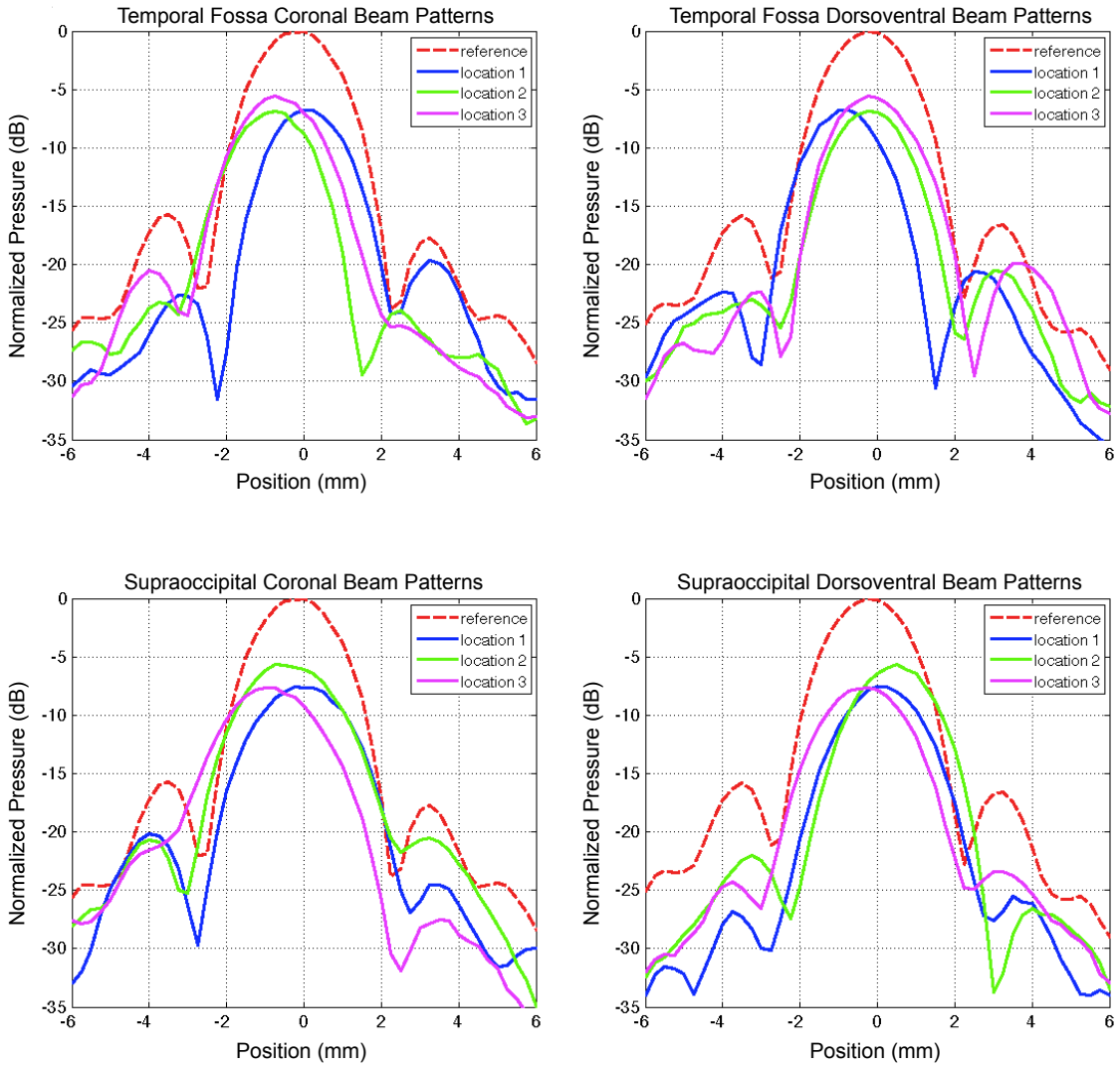

Figure 8.9. Temporal fossa (upper row) and supraoccipital (lower row) coronal (left column) and dorsoventral (right column) VT beam patterns.

The insertion loss of the VT beam pattern main lobe, calculated as the ratio of received pressure without and with bone present, is shown in Figure 8.10 for each of the bone types tested, with bone thicknesses noted for each location. Interestingly, the general trends did not correlate with bone thickness. The mean mandible thickness, while in the range of previously reported values (Nummela et al., 2004), was nearly twice that of the temporal fossa. However, the insertion loss trends were quite similar for the two bone regions, suggesting surface reflection was the dominant effect over absorption within the bone. One aspect of the curves that appeared to relate to thickness was the 1-2 dB amplitude oscillation in the frequency responses. These oscillations suggested the existence of boundary reflections within the bone that interfere with direct path propagation. The sum of the direct and internally reflected waves leads to a normal incidence intensity transmission function (Pierce, 1989) that, assuming parallel layer faces, oscillates in relation to the thickness h and propagation speed c_b:

$$T = \left(1 + \frac{1}{4}\left[\frac{(\rho c)_b}{(\rho c)_{water}} - \frac{(\rho c)_{water}}{(\rho c)_b}\right]^2 sin^2\left(\frac{2\pi f}{c_b} h\right)\right)^{-1}$$

For a fixed c_b, the oscillation period decreases with increasing h, with the frequency spacing between two maxima (or two minima) of the transmitted intensity $\Delta f = \frac{nc_b}{2h}$, where n is an integer. This expression has been used to estimate the propagation speed in bone, presuming that compressional waves were preferentially excited over shear waves at and near normal incidence (White, Clement, & Hynynen, 2006). Compressional speeds were estimated from those amongst the present data sets showing clear oscillatory transmission functions, yielding mean values of 3.0, 2.5, and 3.0 km/s for mandible, temporal fossa, and supraoccipital bones, respectively. The precision of the estimates

was limited by the sample thickness measurements and the bandwidth of the insertion loss data, translating to the observable number of thickness-related oscillations.

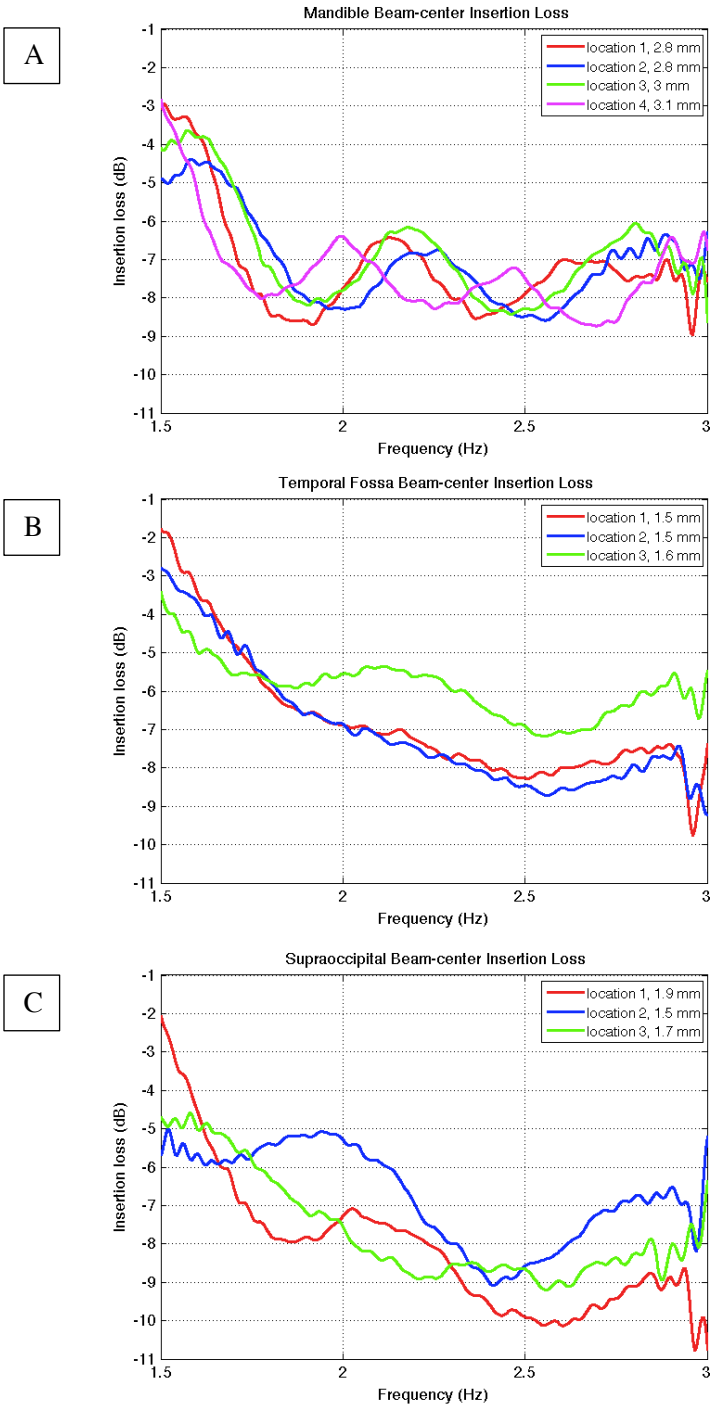

Figure 8.10. VT main lobe insertion loss through mandible (A), temporal fossa (B) and supraoccipital bone (C).

The compressional speed and thickness estimates and were used to analytically examine refraction effects in the bone samples using ray acoustics methods (Pierce, 1989), simplified by considering the bone to only support compressional waves. Figure 8.11 shows examples of rays connecting half the aperture of the VT transducer to its focal point. The left plot shows the ray paths in water (all identical), and the right plot shows the paths with a 3mm thick planar layer with compressional speed c_b = 3km/s. The red segments indicate paths in the layer, which itself is indicated with black dashed lines. For the limited angular span of the VT (≤10.5°), refraction effects are minimal. With the layer in place, the calculated spread in arrival times at the focus was approximately 34 nanoseconds, which when integrated over the transducer face yielded a focal pressure level degradation relative to the un-obscured case of only 3.3% at 2.0 MHz. These results are consistent with the high degree of measured VT beam preservation.

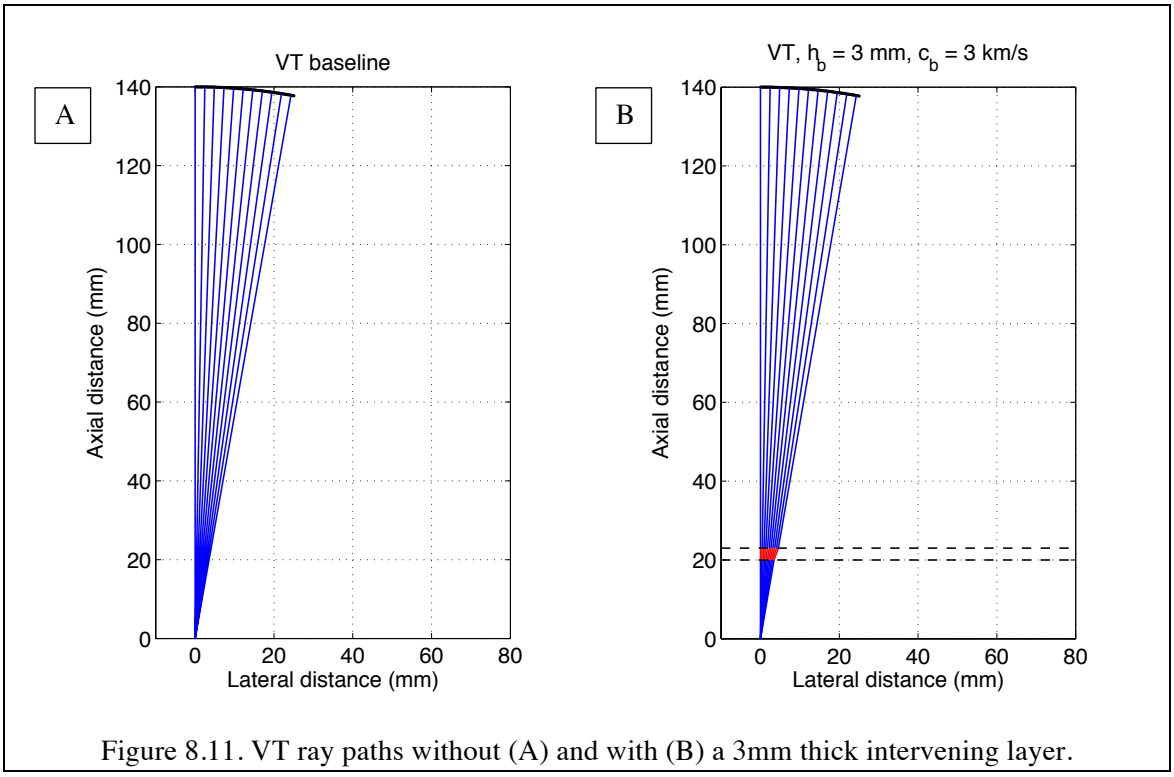

Figure 8.11. VT ray paths without (A) and with (B) a 3mm thick intervening layer.

Overall the pattern distortion effects on the VT transducer were minor. The primary impacts of the presence of bone on the functioning of the CFE system were observed to be signal loss and bone backscattering. In the 1.5-2.5 MHz frequency range currently used for the CFE vibrometer, the average VT insertion loss through bone was approximately 7 dB. Assuming that the receiver element signals would be attenuated by the same amount, the net loss in signal strength would be 14 dB, which is equivalent to adding 35 - 70 mm of soft tissue in the propagation path. This degree of signal loss could be partially offset by using longer VT transmissions (if the pulse rate is slowed from 1600 to 1400 Hz, for example), and potentially by shifting to lower frequencies. The latter is not an option for the current CFE prototype, as the VT transducer sensitivity falls off rapidly below 1.5 MHz. According to analysis presented in Chapter 2, vibrometer sensitivity and soft tissue scattering tradeoffs are small for a 300-500 kHz downshift in VT operating band. Total bandwidth reduction may, however, be an issue.

The scattered levels from the bone surface were quite large compared to all other signals encountered with the system. In the experiments described in this Chapter, the bone surface scattering had an amplitude of 8-10 volts, approximately twenty times larger than the maximum signal recorded without bone present. The presence of bone in the propagation path therefore places broader requirements for the dynamic range of the system electronics. Currently, with a 12-bit digitizer, system measurements are limited by digitizer noise. To maintain the current (and non-ideal) noise-limited situation while accommodating bone scattering, the digitizer would need to be upgraded to at least 14 bits after accounting for soft tissue path losses that would be present. This is achievable

with commercially available hardware. High speed preamplifier gating or other front-end circuitry may also mitigate bone scattering levels, independent of digitizer capability.

8.3.2 Force Generation Transducer Response

Transmitted force generation transducer (FT) pressures are shown in Figure 8.12 for the reference case (no bone) and examples from each of the three bone regions tested, all for a carrier frequency of 800 kHz. The temporal fossa had the best-preserved pattern, while the mandible showed the greatest distortion. Although only one example from each region is shown, they are representative of the quality of the transmitted patterns for each bone type.

Figure 8.13 shows estimated FT ray paths using the same layer model as in Figure 8.11. With the larger span of FT incidence angles (15.5° – 32.5°), the rays between the transducer surface and the focal point form shallower angles in the water, and steeper angles within the layer. The rays that travel to the focal region illuminate a broad area of the bone/layer, making the propagation problem more susceptible to errors due to variations in properties or geometry. For the on-axis case (8.13 A, B), the range of arrival times at the focus was 0.51 μs, which when integrated over the transducer face leads to an estimated focal degradation of approximately 2.4 dB. This minor degree of temporal decorrelation is consistent with the FT pattern results, which all show a region of minimum intensity (of varying width) at the pattern center. For the offset case (8.13C, D) corresponding to a pair of sectors transmitting to a force lobe location, the refraction effects in the bone layer are seen to be asymmetric.

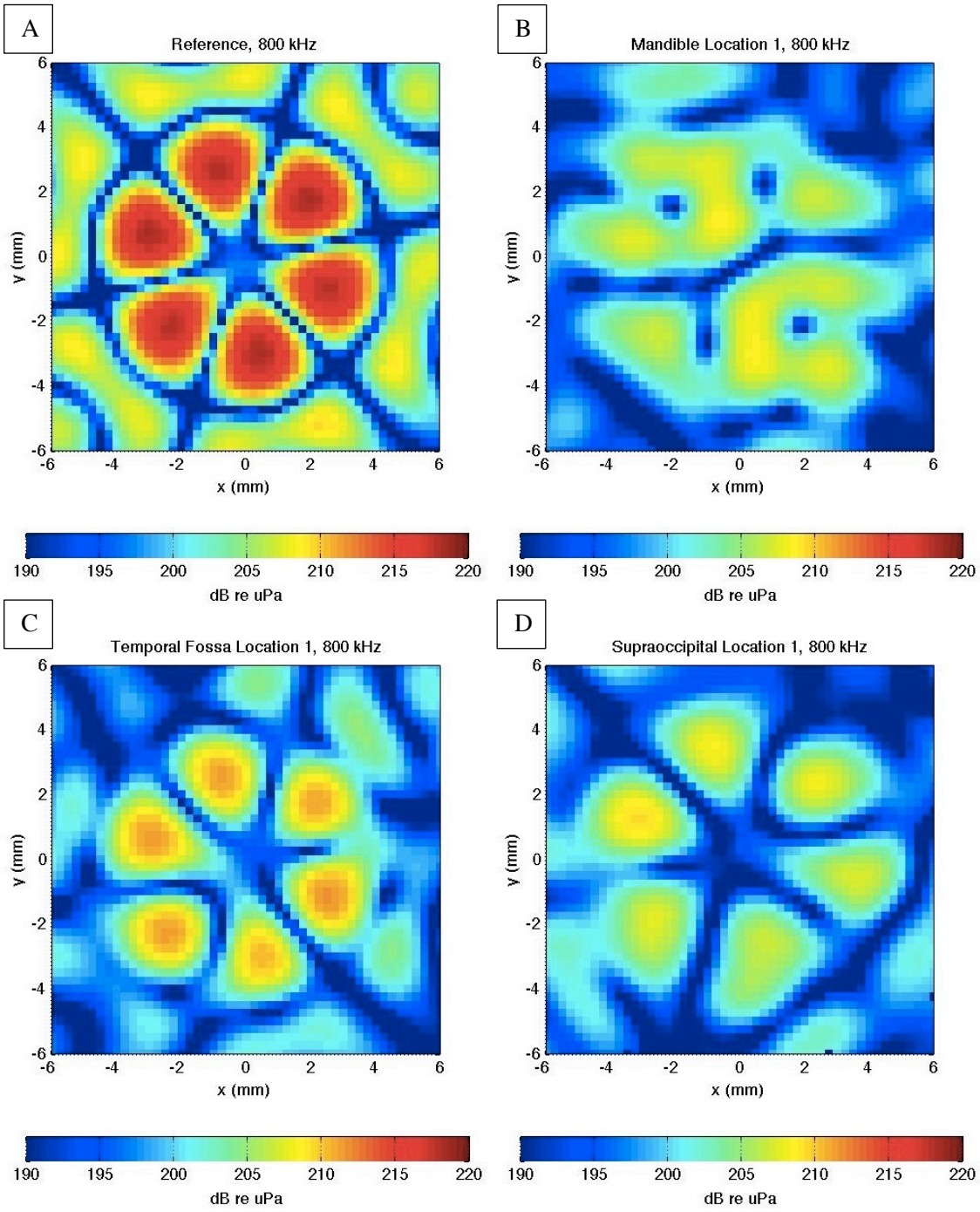

Figure 8.12. FT focal plane pressure beam patterns for 800 kHz carrier: (A) reference, (B) mandible location 1, (C) temporal fossa location 1, and (D) supraoccipital location 1. The "x" and "y" directions are coronal and dorsoventral, respectively.

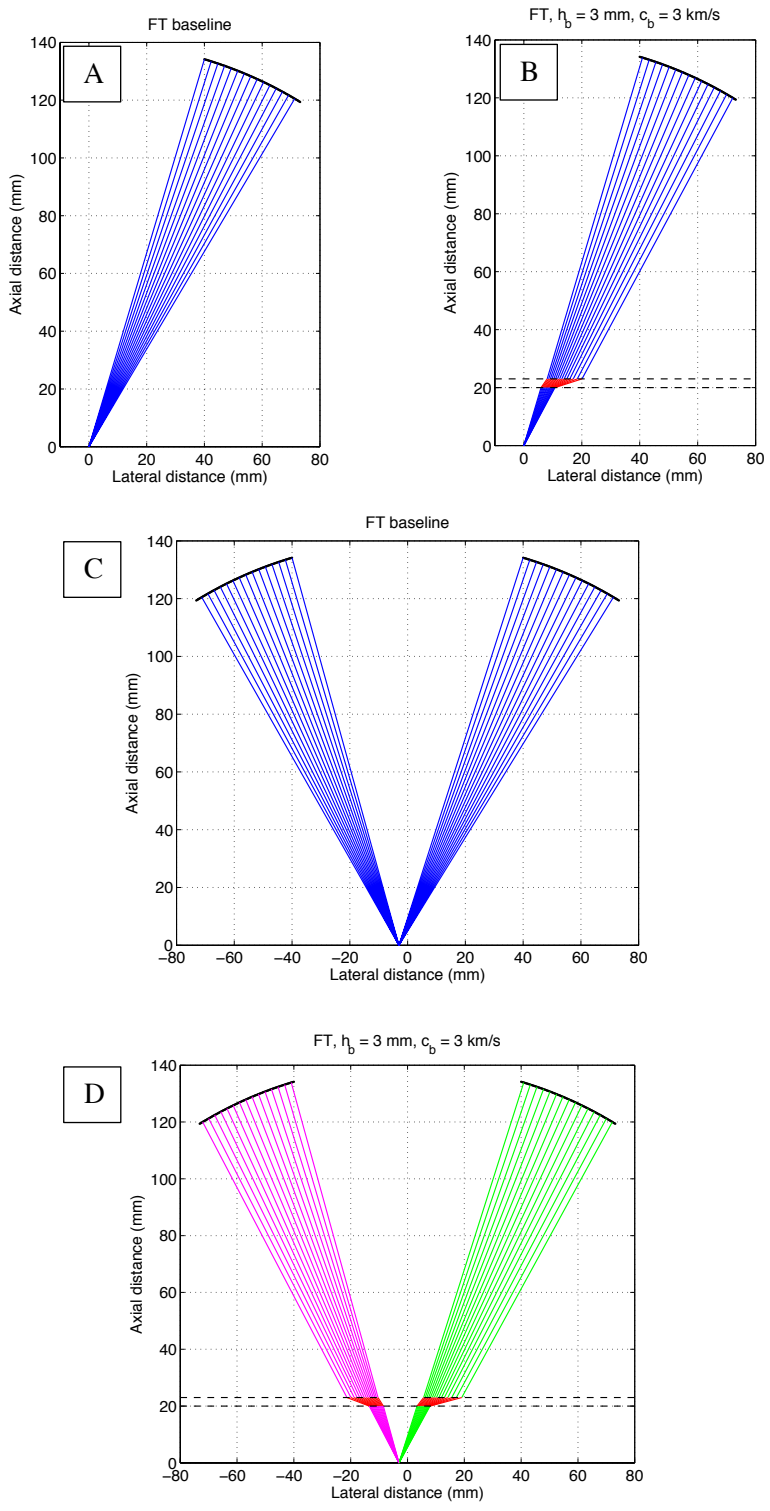

Figure 8.13. FT rays to an on-axis point in the focal plane without (A) and with (B) a bone layer, and rays to point 3mm off-axis without (C) and with (D) a bone layer.

Non-normally incident rays of sound refract away from the beam axis and have an elongated path through the bone layer. Wider incident angles lead to longer layer propagation paths, in turn producing a layer attenuation function with a strong angular dependence. The significance of these refraction effects is illustrated in Figure 8.14A, which shows the ray path lengths in the simulated bone layer. The three curves correspond by color to the path sets shown in 8.13 C and D. Path lengths range from 3-4 times the thickness of the layer, which raises the question of layer attenuation effects. Figure 8.14B shows estimates of bone-absorbed power, using a value of 8.6 np/cm at 800 kHz determined from the average of 35 human temporal bone samples (Hueter, 1952). Taken by itself, the attenuation would effectively radially "shade" (or gradually turn off) the FT radiating aperture, causing a general decreasing in focal plane focusing. A lower layer compressional speed or thickness (as in the temporal fossa) would decrease path elongation and attenuation effects.

An additional effect is observed through consideration of the intensity transmission through the bone layer (White, Clement, & Hynynen, 2006). This computation is shown in Figure 8.14C for two carrier frequencies used in CFE testing, without any layer absorption. The rays incident at larger angles upon the layer are weakly transmitted, but perhaps more importantly, the transmission curves (i.e. their maxima) are strongly frequency dependent. With the layer re-shaping the transmitted field in this way, the ability to control force lobe position with carrier frequency may be significantly degraded.

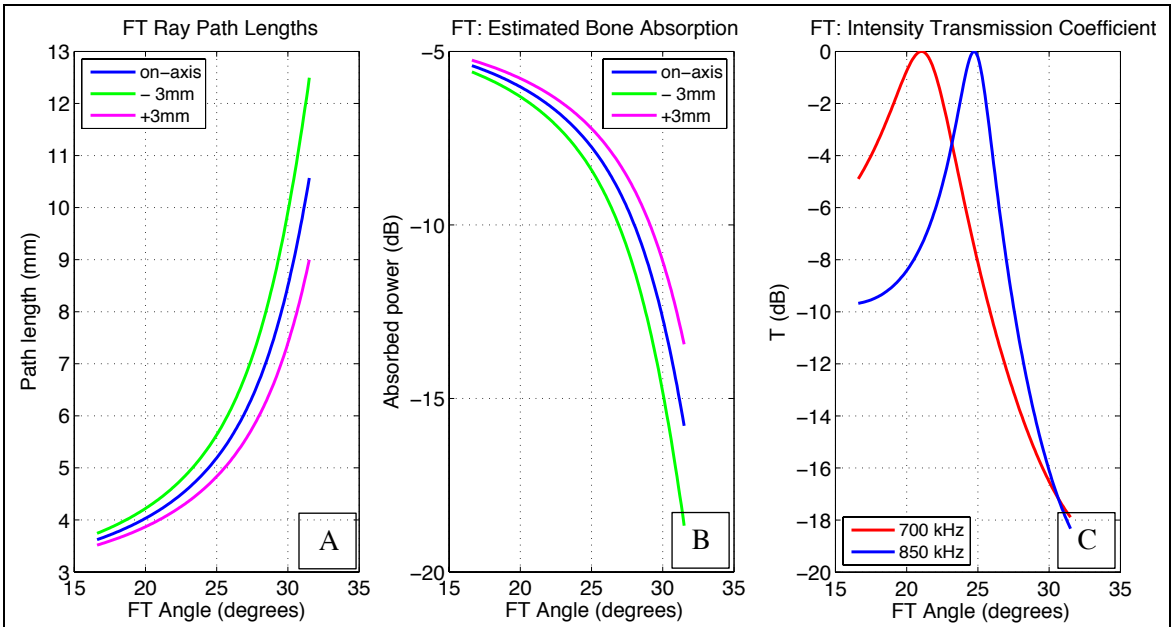

Figure 8.14. Bone layer ray path lengths (A), absorption (B), and intensity transmission (C).

The foregoing discussion all applies to propagation through a flat layer, which appears to be an extreme case in terms of the impact of angle-dependent signal loss and distortion. If, however, the bone has convex curvature, the effective range of incident angles can be significantly reduced, as are the perturbations of path length and propagation time. This is illustrated in Figure 8.15. The degree of beam pattern preservation through curved bone would depend on the radius of curvature, the extent to which it is axisymmetric and of uniform thickness and sound speed, and how well the transducer beam axis (symmetry axis) is aligned with the bone surface normal. In the present experiments, the bone sample was manipulated in order to maximize backscatter, which was previously found to maximize bone transmission and minimize pattern refraction (Gray, Martin, & Rogers, 2006; Ammi, et al., 2008). This procedure was rapid

and seemingly effective, but has the disadvantage of raising system dynamic range requirements, as described previously.

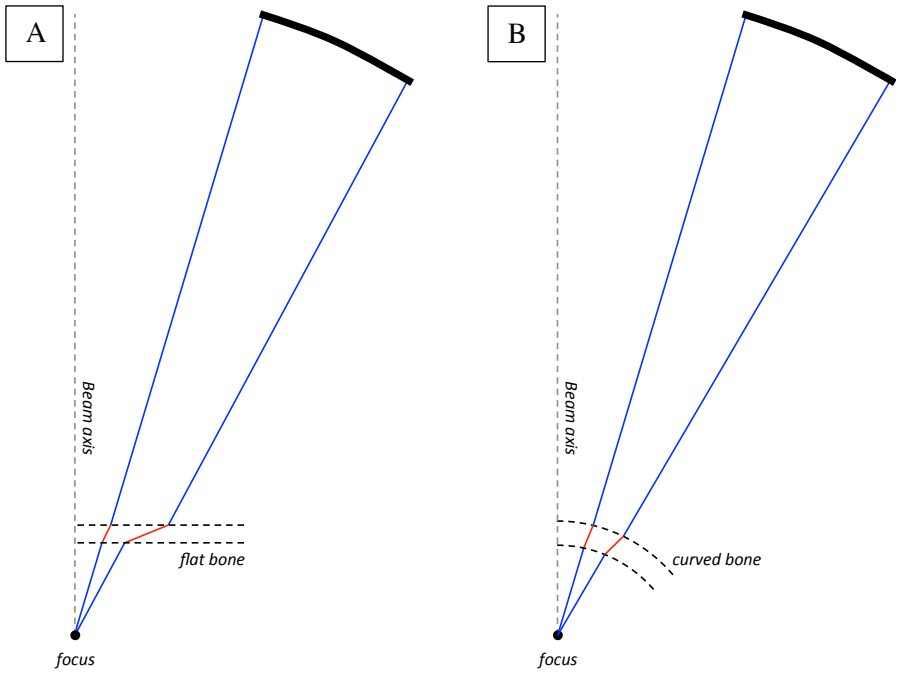

Figure 8.15. Effect of bone morphology on extreme ray paths: flat (A) and curved (B) layers.

Figure 8.16 shows examples of ultrasonically determined bone curvature for each of the bone regions tested. The legends of each plot contain estimated radii of curvature in the coronal and transverse planes. As expected from visual inspection, the mandible appeared to be approximately cylindrical, being essentially flat in the coronal plane. The temporal fossa and supraoccipital regions exhibited modest curvature in both the coronal and transverse planes. The temporal fossa results showed the most similar curvature radii in the two planes. Since this bone region also showed the best FT transmission characteristics, the significance of bone curvature is substantiated.

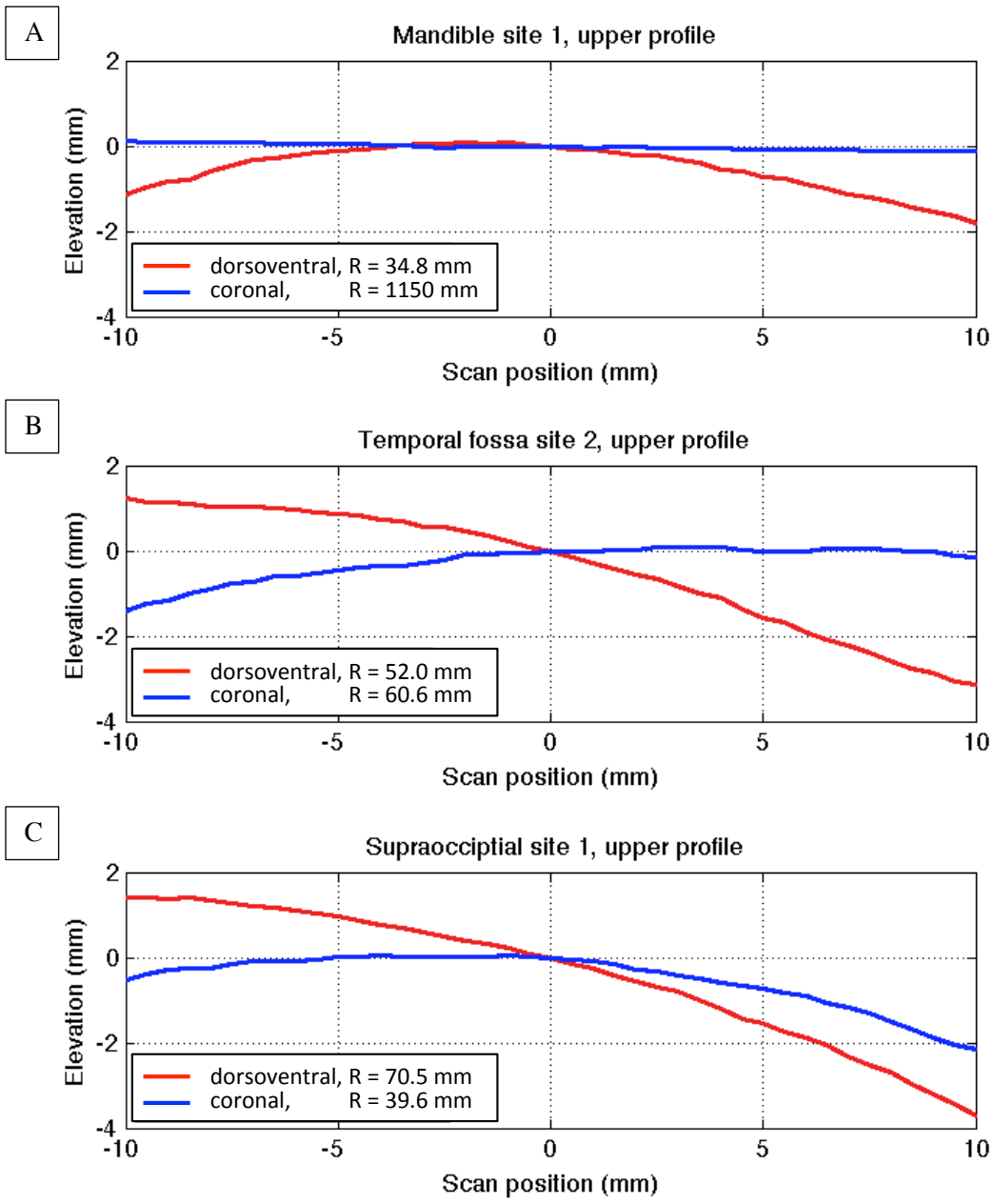

Figure 8.16. Measured exterior bone curvature for mandible (A), temporal fossa (B) and supraoccipital (C) regions.

The estimated mean radius of curvature in the temporal fossa (54.3 mm) was larger than the offset between the bone and nominal focal plane (20.4 mm) during the CFE transmission experiments. The implication is that in this specific measurement

configuration, the focus quality was likely better at greater depths than those that were measured. More generally, the quality of system beam transmission will be best when the transducer and bone radii of curvature are concentric (origin of the bone curvature is at the nominal focus of the transducers).

To summarize the foregoing, bone curvature, thickness and propagation speed all appear relevant to CFE beam insertion loss and distortion. The VT beam, with relatively shallow incident angles, was not strongly distorted by passage through the bone samples tested. The FT beam was distorted by varying degrees, with an apparent correlation to bone curvature and sound speed. One aspect of the problem not considered was coupling of incident fluid waves to shear waves in the bone, particularly at angles beyond the compressional critical angle. Shear mode coupling has been seen in human skull studies (Clement, White, & Hynynen, 2004) to partially offset wide angle transmission losses associated purely with compressional waves. A more complete picture of cetacean bone transmission could be found from a detailed study of angle-dependent transmission.

8.3.3 CFE Simulations

With some of the bone transmission results showing a modest degree of FT pattern preservation, it was of interest to see whether the carrier-induced beam shifting approach used for CFE was maintained. Figure 8.17 shows examples of -3dB pressure contours from each of the bone regions, along with a calibration reference, all with FT carriers of 725 and 825 kHz. The vibrometer beam is also shown for alignment reference. As might be anticipated from the foregoing analyses, the mandible FT contours were most distorted, and showed an unusually large pattern shift with increasing

frequency. The temporal fossa results are the closest to the reference in terms of FT carrier-induced lobe shifting. In all cases, the enclosed area of the VT lobe did not vary significantly, although its placement did drift within the FT pattern.

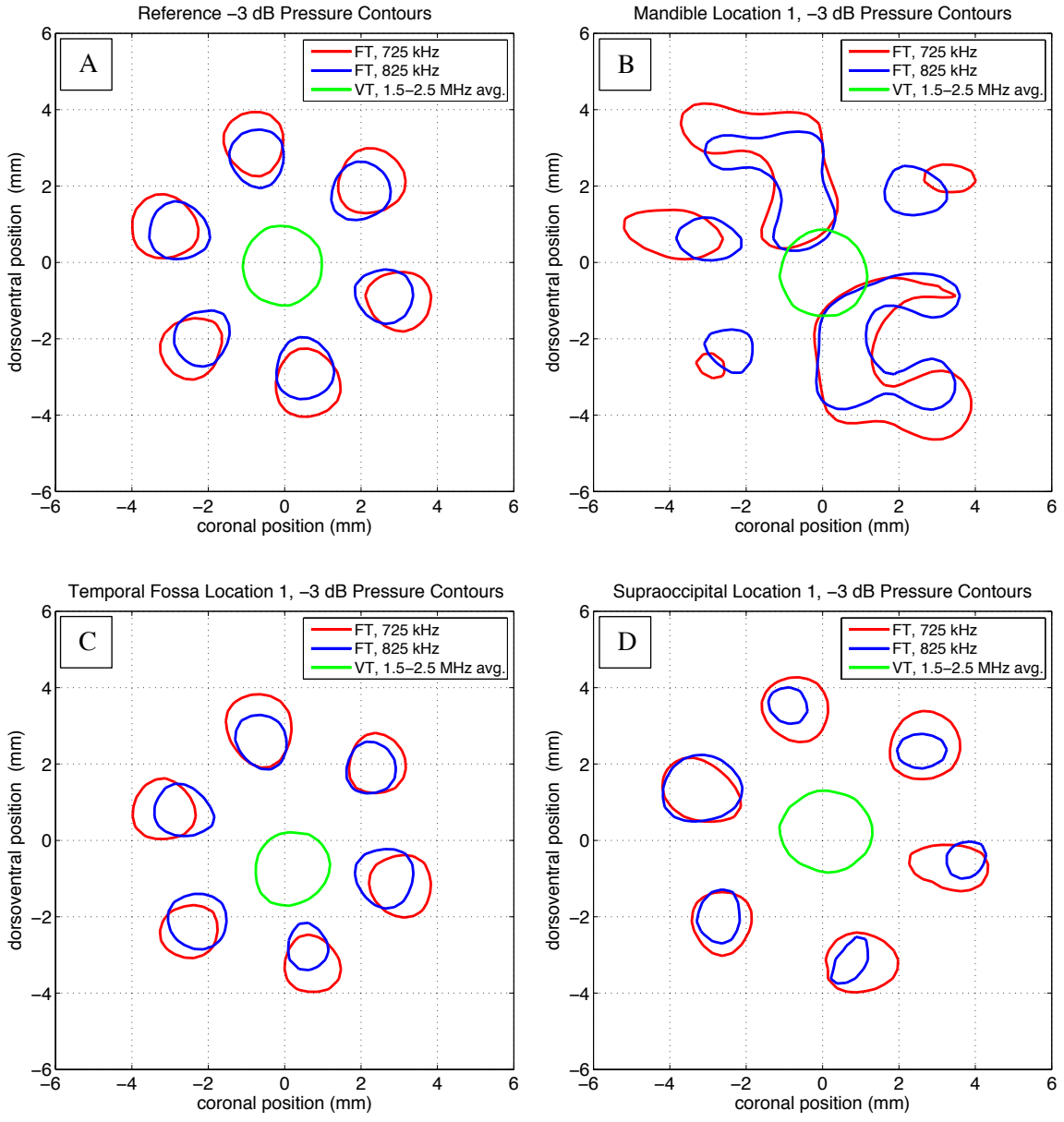

Figure 8.17. -3dB pressure contours for the reference (A), and through locations on the mandible (B), temporal fossa (C), and supraoccipital (D) bone regions.

To quantify the cumulative effects of the bone transmission on CFE performance, the shear wave fields generated by the measured FT beams were predicted using the analytical model described in Chapter 2. The displacements observed at the measured vibrometer beam locations were calculated and relative phases used to estimate shear speed. The properties of the CIRS phantom were used for these simulations.

The shear elasticities estimated from the simulations are shown in Figure 8.18. In the absence of any transmission-related distortion, all results would be equal to the expected value of 2.3 kPa. The mandible results all returned a low elasticity as a consequence of exaggerated beam shifts seen in Figure 8.17. The supraoccipital results showed no distinct trends. The temporal fossa results had a standard deviation of 24% with respect to the expected value (11% in shear speed). This shows that cumulatively, the properties of the temporal fossa region induced a minimal disruption to the CFE system as currently implemented.

As it was with the vibrometer transmission loss, the impact of FT beam attenuation through bone was highly detrimental to system SNR. For the samples tested, displacement amplitudes were predicted to fall 12-20 dB relative to their un-obscured levels. This, combined with the VT signal losses, considerably offset the SNR gains made by the prototype design in order to make elastography measurements possible in soft tissues in the absence of bone. As described in Chapter 7, it is possible to use larger amplitude FT transmissions. The use of a denser or continuous forcing ring pattern would also elevate generated displacement levels. In addition to signal level enhancement, noise floor reduction through the use of higher quality electronics may also restore measurement SNR to a significant extent.

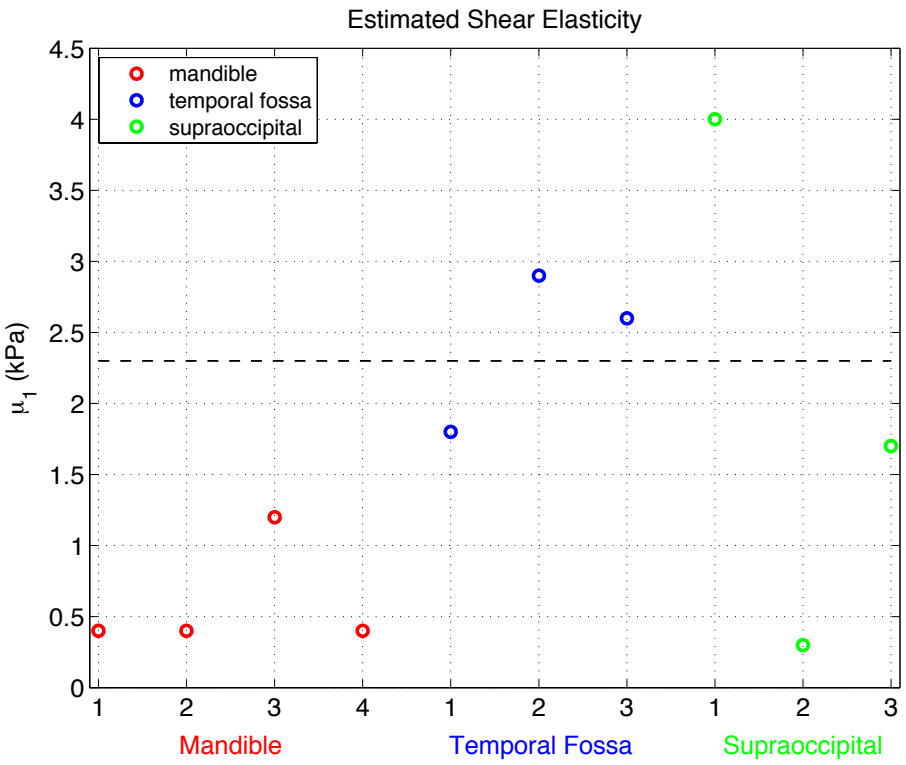

Figure 8.18. Simulated CFE performance through bottlenose dolphin bone.

8.3.4 Thermal Response

Measurements of temperature rise at the ultrasonically illuminated side of three bone samples are shown in Figure 8.19. In all cases, the full system was turned on at t=1 minute. At a later time, the system was shut off, and the cooling rate was observed. The curves show error bars spanning the full data range from three trials.

The temperature rise in all cases was less than 1.0 °C – much lower than the thermal safety limit of 6 °C for diagnostic ultrasound. With no attenuating soft tissue between the transducers and bone, the test conditions represented an upper bound in bone heat generation as a consequence of elevated incident ultrasound levels.

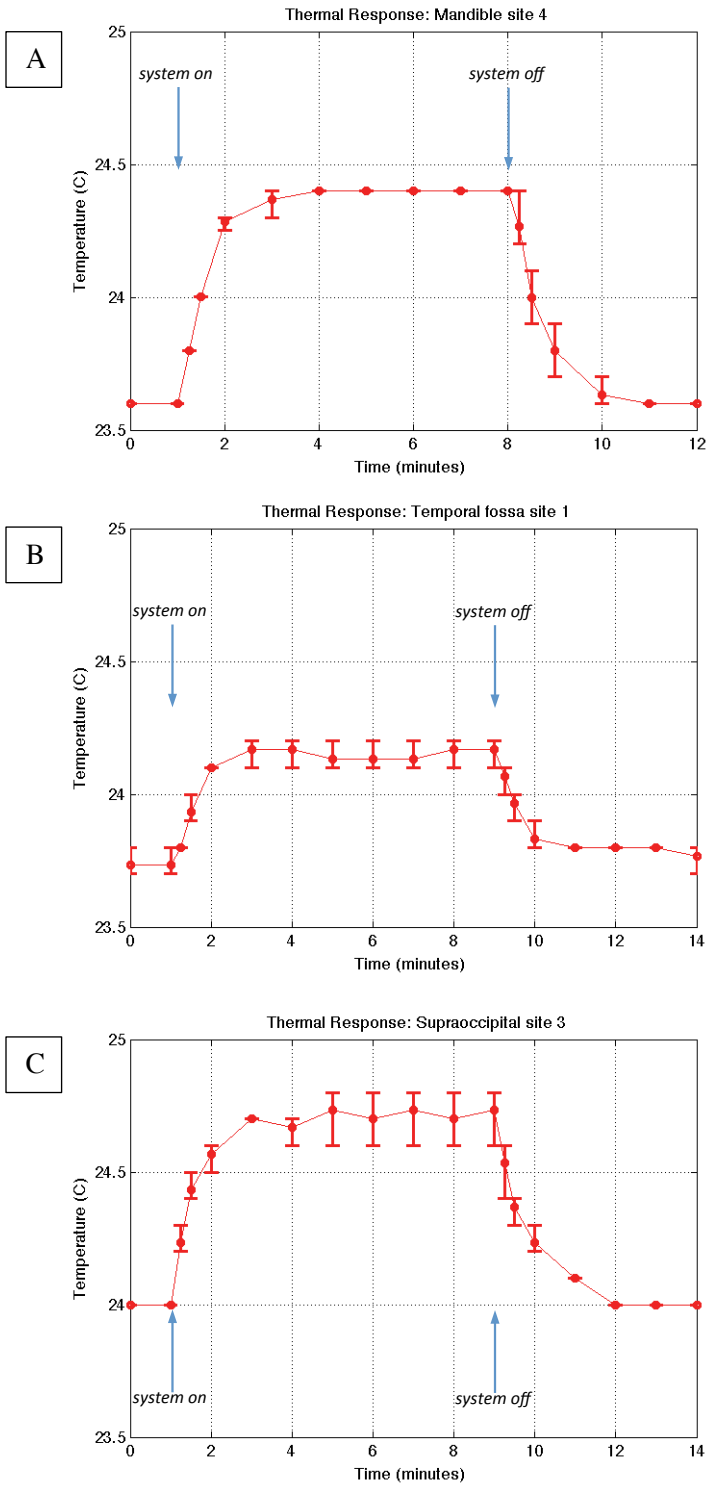

Figure 8.19. Bottlenose dolphin bone temperature rise during CFE exposure for proximal mandible (A), temporal fossa (B) and supraoccipital (C) bone samples.

Recalling that heat generation is proportional to incident intensity, the present test cases generated approximately 2.4 times more heat than if soft tissue had been present in the beam path. This estimate is based on the attenuation in the CIRS phantom material, and would be nearly a factor of ten if the intervening tissue had a "classic" soft tissue attenuation of 1 dB/cm/MHz. It is more difficult to say whether the resulting temperature rise was high or low relative to a living system. In the experiment, heat transfer away from the ultrasonically ensonified bone occurred through conduction in the bone and surrounding water. Free convection also could have enhanced heat transfer on the upper surface, but at the lower surface, warmed water likely accumulated. In a living cetacean, tissues surrounding cranial bone (e.g. brain case) are likely to be well-perfused, and heat transfer rates may be enhanced by blood flow. For mandibles, which are surrounded by fatty tissues, insulation effects may be more important.

Overall, it appears that bone heating from CFE ultrasound exposure is not a major technical issue.

8.4 Summary

Tests conducted on bottlenose dolphin mandible and skull samples revealed several technical issues to be addressed for performing elastography measurements through bone. The cumulative reflection and attenuation of VT and FT beams led to a signal loss on the order of 24-30 dB, while also requiring an increase in VT system dynamic range to account for bone backscattering. The results of this limited study suggested a combination of bone curvature, sound speed and thickness as controlling mechanisms for beam pattern preservation. FT beam distortion manifested both in

alteration of the forcing lobe pattern and uncertainties in carrier-induced force lobe shifts. Still, simulations performed using measured signals transmitted through cranial bone yielded shear speed estimates with a standard deviation of 11% with respect to the true value. Thermal effects, as observed with bone samples exposed under conditions corresponding to an upper bound on heat generation rate, do not appear to be a significant issue.

The results presented here were generated from a small data set collected on re-hydrated bone samples without any adjoining tissues. Studies of trabecular bone have indicated sensitivity of elasticity to hydration (Wolfram, Wilke, & Zysset, 2010; Lievers, Poljsak, Waldman, & Pilkey, 2010). However, these studies have not specifically addressed re-hydration effects in compact bone (which was exclusively tested in the present work), where there appears to be limited potential for water absorption and swelling of the constituent fibers.

The decision to use flensed samples was made in the interest of directly studying the multiple types of acoustic and thermal interactions with the bone tissues themselves. Quantification of bone thickness and curvature, for example, would not have been possible if the full suite of soft tissues was present. Attenuation in these soft tissues was necessarily missing from the bone experiments, but the effects are easily accounted for using measured or presumed ultrasonic attenuation rates.

The dominant limiting factor in this study was likely the sample size – one skull and one jaw were examined. The present data set allowed quantification of transmission losses for a range of bone thicknesses, curvatures, and propagation speeds, all of which helped to build a physical picture of the problem and technical challenges faced.

However, any design effort toward building the next generation CFE system would greatly benefit from additional data sets demonstrating bone geometry and elasticity variation by species, gender, and age.

Finally, it is noted that the limited number and size of seemingly "favorable" transcranial propagation windows restricts the intracranial volume of tissue that may be examined. These limits will likely vary by animal species, gender and age, but may be alleviated to some degree with array-based enhancements of the CFE technique as discussed in Chapter 9.

CHAPTER 9

SUMMARY AND RECOMMENDATIONS

"It is what it is" – Bill Belichick

9.1 Summary

The convergent field elastography (CFE) concept for "deep tissue" ultrasonic elastography was developed and demonstrated. This concept extended the depth of ultrasound-based shear viscoelastic property assessment to over 12 cm – well beyond the capability of existing systems. The depth extension was primarily enabled by three design features: (1) a novel multi-beam force generation scheme that enhanced shear wave amplitudes while maintaining compliance with diagnostic ultrasound exposure safety limits, (2) lowering the operating frequencies to enhance signal levels, and (3) utilizing vibrometer signal processing techniques to lower the measurement noise floor.

The study began with the development of a simulation capability enabling ultrasonic field calculations for notional transducers, and using the results to predict in situ shear displacement fields. System simulations were used to design prototype transducers for proof-of-concept testing. To support more realistic laboratory assessments, ultrasonic properties of living cetaceans were measured and used to guide development of tissue mimicking phantoms with nominally homogeneous composition and isotropic ultrasonic bulk and low frequency shear properties. The prototype CFE system was demonstrated at depths of 12 ± 1 cm into these tissue phantoms. This range

is approximately equivalent to mid-brain in an adult bottlenose dolphin, which was the design target for the study.

The CFE system was subsequently tested on a phantom with spherical inclusions contrasting from the surrounding background material only in their low frequency elastic properties. This set of tests presented several challenges and revealed limitations of the CFE prototype, particularly regarding self-noise, axial resolution and interpretation of shear reflections inside the inclusions. Nonetheless, the CFE system was shown to be effective at distinguishing materials based on displacement magnitude, and the low shear material was clearly imaged on the basis of its elasticity. Low signal levels and potentially elevated reverberation limited performance with the high-shear inclusion. A modified imaging technique was used to expand the axial range over which shear speed could be estimated.

A set of tests was performed to quantify CFE signal loss and beam distortion when propagating through re-hydrated samples of bottlenose dolphin skull and mandibular bone. Transmission losses seemed only weakly correlated with bone thickness. Instead, bone curvature appeared to be a critical parameter in preservation of transducer beam patterns, particularly the force generation transducer, which illuminated a broader surface and from wider incident angles than the vibrometer transducer. The combined bone-induced transmission losses and scattering levels significantly reduced system signal to noise ratio. While the current CFE prototype would not support through-bone elastography, simulations performed with the measured transmitted beam patterns indicated that shear property estimation may be possible if sufficient engineering upgrades were made. Such upgrades are discussed in the next section.

Although initially motivated by needs for cetacean studies, applications for the CFE technique may extend to a wide range of diagnostic targets, including the bodies of large or obese humans. Examples are shown in Figure 9.1, where the blue bars indicate the reach of existing systems[***][†††][‡‡‡], and the green bars indicate a 12 cm reach as demonstrated with the current CFE prototype. In these examples, the increased operating depth extends the useful range beyond peripheral fat and into internal organs or to deep muscle. In the absence of obscuring bone, applications for CFE may include non-invasive assessments of tissue state following therapy, surgery, or injury. In all cases, the system is anticipated to have the cost and portability on the scale of existing diagnostic ultrasound systems, as opposed to MRI systems.

Extension of the CFE techniques to human brain diagnostics or therapeutics would appear to require similar if not greater means for signal loss compensation and beam distortion than what would be required based on the bottlenose dolphin data in the present study. This assessment is based on the relative complexity of the human skull, where for example the temporal region contains a layer of trabecular tissue between cortical boundaries that are frequently not parallel (Ammi, et al., 2008). Non-invasive methods for focusing through human skull bone have included CT-based correction (Aubry et al., 2003; Clement & Hynynen, 2002) and implemented arrays of over one thousand individually controlled elements to optimize transmitted beams broadcast in the low 100s of kHz (Song et al., 2012; McDannold et al., 2010). It would appear likely that

[***] http://usa.healthcare.siemens.com/ultrasound/arfi-elastography
[†††] http://www.healthcare.philips.com/main/products/ultrasound/technologies/elastography.wpd
[‡‡‡] http://www.supersonicimagine.com/Aixplorer-R/Presentation

a CFE system intended specifically for human transcranial application would need to incorporate the lessons learned from these preceding studies.

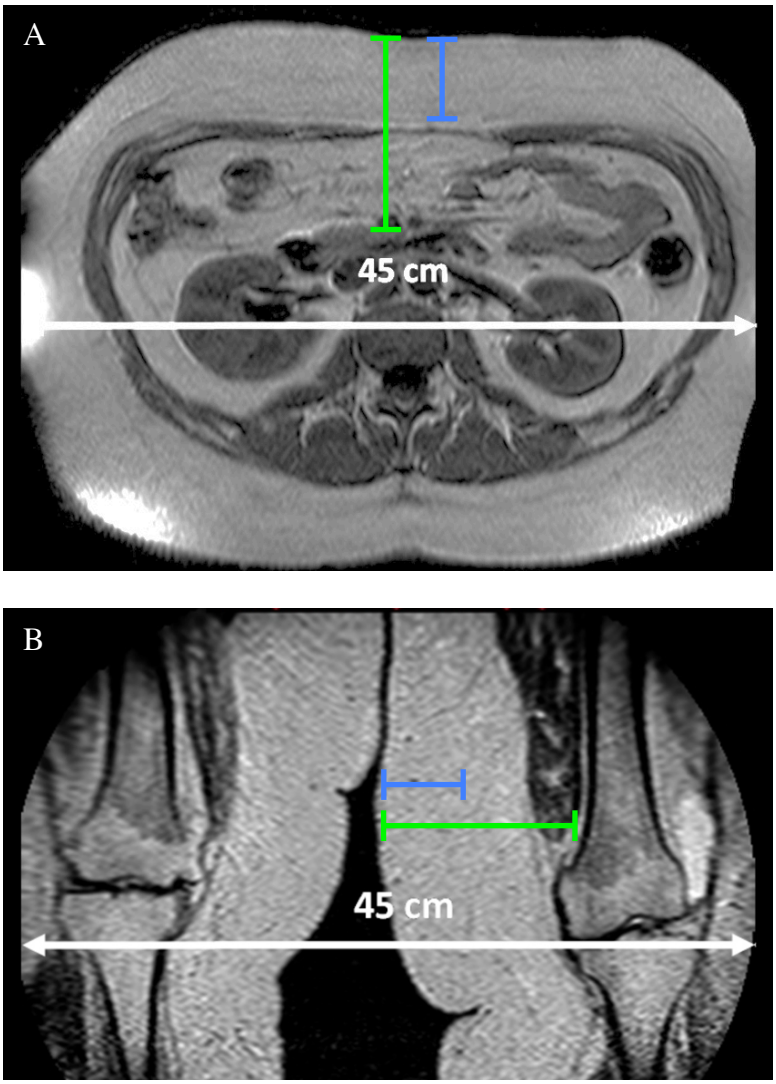

(De Bucourt, 2010) *Images used with permission, Copyright 2010 Springer*

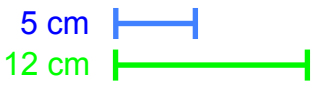

Figure 9.1. MR images of an obese human (A) torso and (B) legs.

If transcranial imaging challenges can be mitigated, traumatic brain injury (TBI) is an intriguing diagnostic application for CFE. Gross pathologies associated with TBI, including brain tissue swelling and associated intracranial pressure elevation (ICP) (Colgan et al., 2010), are not necessarily well-characterized with a CFE-like system. However, there is evidence of decreased brain tissue shear stiffness in close proximity to brain trauma (Boulet, Kelso, & Othman, 2013). It may also be possible to assess ICP effects by examining the low frequency forced responses of ventricular tissues, taking advantage of the radiation pressure generated by reflection (and therefore momentum change) at the interface of cerebrospinal fluid / tissue interfaces. Such an approach may also be applicable to diagnosis of certain types of hydrocephalus, where elevated ICP compresses brain tissue (Rigamonti, 2014).

9.2 Technology Development Recommendations

As tested, the prototype CFE system was valuable for proof-of-concept testing, but translation to a field- or clinic-ready system will require substantial development to overcome the current system's limitations.

i. Spatial coverage. Chief among the limitations of the prototype was the use of fixed-focus ultrasound transducers that yielded shear data over a limited axial range near the focal plane. Examination of tissues at other axial or lateral locations required physically translating the transducers.

ii. Anisotropy assessment. The tube-like forcing pattern produced by the FT transducer led to a circumferentially averaged shear estimate. Assessment of

anisotropy, as has been noted in muscle tissue (for example, Chen, et al., 2009), was not possible.

iii. Reverberation. The prototype system employed a single fixed beam for measuring vibration at the center of the forcing pattern. This appeared to work well except in the shear contrast inclusion experiments, where direct and reflected shear waves were present. The ability to separate shear wave arrivals in reverberant environments would be valuable in more realistic biological scenarios.

iv. Self-noise. The noise floor of the system was limited by electronic noise in the digitizer used to collect vibrometer data. Ensemble averaging was used to mitigate electronic noise, but this is not a preferred approach in light of the associated increase in testing time.

v. Beam correction. The prototype transducers had a relatively small number of elements and associated input controls, limiting the ability to correct or optimize ultrasonic beam shapes transmitted through complex tissues, especially those containing bone.

vi. Physical configuration. The prototype transducers were surprisingly fragile, requiring multiple repairs for leaks and related problems. Even if they had been more robust, the concave transducer face geometry would be difficult to couple to the test subject if not submerged.

A planar array configuration, illustrated in Figure 9.2, is proposed to address the above limitations for the next generation of CFE. The transducer is shown as consisting

of a central grid of rectangular elements for the vibrometer, surrounded by an array of ring segments for force generation. The number of drive and receive elements would be compatible with current commercially available array electronics[§§§], as well as some clinical ultrasound systems. The multi-lobe force generation intensity pattern could be produced by driving the array elements in sectors of alternating polarity. The forcing radius could be changed through a combination of carrier frequency and modal content, providing larger radial forcing shifts, which should in turn produce larger differential phases for improved shear estimates.

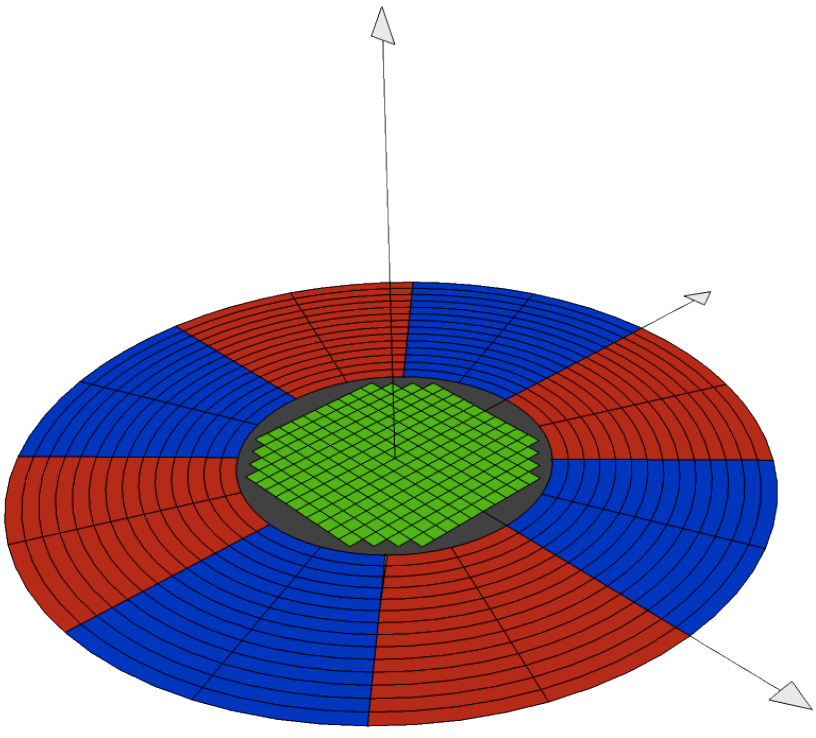

Figure 9.2. Planar array implementation of CFE. Force generation elements are shown in red and blue, indicating opposite polarity. Vibrometer elements are shown in green.

[§§§] for example: http://www.verasonics.com/7

This array configuration could also be used to produce continuous ring forcing patterns by using radial rather than circumferential weighting distributions. Production of a continuous ring field should increase the size of the generated shear displacements in proportion to the total power delivered to the tissue. Axial steering of the forcing and vibrometry beams would enable continuous shear properties estimation as a function of depth from near-surface to maximum depth.

Implementation of the vibrometer in a multi-element array form would allow lateral scanning of the vibration tissue, with the resulting data used to estimate properties over a wider region (perhaps $25mm^2$ or more, depending on tissue properties) for single force application. Data describing the lateral distribution of shear displacements could also be used to interpret reverberant shear field using conventional wavenumber transforms. For example, a set of displacement measurements over a single horizontal line can be wavenumber-transformed as a function of time to indicate the evolution of the wave fields generated by CFE and any reflections from mechanical boundaries present in the tissue. Such an approach may also aid in the assessment of anisotropy, through interpretation of shear wave arrivals along different axis. The use of multiple receiving elements should also be valuable in reducing electronic noise when the element signals are coherently summed.

The reduction in noise floor should also extend the low frequency measurement bandwidth, leading to improved estimates of shear viscosity. Extended bandwidth estimates are of particular interest for the study of mid-frequency sonar interactions with marine mammals. If the viscosity (μ_2) is established from limited bandwidth

measurements of soft tissue shear response, extension to higher frequencies using a modulus of the form $G= \mu_1+i\omega\mu_2$ will be possible.

A more direct way to investigate anisotropy may be to modify the forcing beams so that they resemble lines or arcs, instead of full rings. This may be done by modifying the modal content of the beamforming weights, or by avoiding circumferential modal weights altogether. Line or short arc beam shapes may be formed by conventional additive beamforming of a subset of adjoining array sectors, and may therefore be more robust than modal (differential) beamforming in terms of maintaining beam shape when transmitting through complex tissues. Relative to a ring-like approach, there would likely be a disadvantage in terms of generated shear wave displacement size because of the reduced forcing perimeter (scaling total forcing volume).

The use of phased arrays may greatly improve beam pattern preservation through bone by allowing modifications to the beamforming weights. For example, if the transducer is positioned over a bony region of interest, a geometric image scan could be performed prior to CFE, wherein the curvature of the bone is interpreted through conventional backscatter ultrasound. This data could be used to adjust transducer beamforming weights to "reshape" the array to match the bone curvature. Further adjustments may also be made based on known or assumed bone sound speeds and thicknesses, although more sophisticated methods based on coupled CT (Aubry et al., 2003) or invasive reference measurements (Tanter, Thomas, & Fink, 1998) are not of practical interest for a system taken to the field.

As with any hand-held imaging system, errors may be introduced due to relative motion of the transducers and a specific region of interest within the imaging subject.

Image registration errors (uncertainty in the location of the interrogated tissue) induced by inadvertent tilting of the transducers will increase linearly with imaging depth. Approaches to mitigating such errors in the context of clinical applications have included robotic control of the transducer position (Schlosser, Salisbury, & Hristov, 2010) and optical tracking of the transducer within a fixed coordinate frame (Bouchet et al., 2001). Even if the transducer location and orientation is tracked, motion of the imaging subject may introduce residual registration errors and degrade elastography estimates. The latter can be especially problematic in the case of respiratory motion (Bell et al., 2012), but such effects should be much smaller when imaging head tissues, which are supported and constrained by the skull. Voluntary or involuntary motion of the imaging subject could produce displacements of sufficient size to invalidate the assumptions used in the NIVMS process or degrade temporally averaged raw data sets. The impact of such errors may be decreased by collecting a larger number of short duration data acquisition sequences, as an alternative to the baseline approach of a small number of long duration sequences.

This section concludes with a few comments on physical configuration. The use of a planar array transducer should make patient coupling considerably simpler than the fixed focus transducers used for the proof of concept experiments. The size of the planar array may limit application in some cases, as the array size scales with the maximum depth at which the system would be used and the accompanying frequency range, presuming preservation of some set of nominal beamwidth characteristics. Several laptop-based ultrasound systems are currently available, all of which drive planar array transducers. It is not currently known whether these systems would be readily adaptable to CFE implementation – including power requirements for force generation. A survey

of ultrasonic array technologies should be performed in order to determine whether CFE or some modified version of it could be implemented with an existing transducer/electronics/processing system.

REFERENCES

Abbott, J. (1999). Rationale and derivation of MI and TI - a review. *Ultrasound in Med. & Biol. , 25* (3), 431-441.

Achenbach, J. (1984). *Wave propagation in elastic solids*. Amsterdam: Elsevier Science.

Alexander, R. (1961). Visco-elastic properties of the tunica externa of the swimbladder in cyprinidae. *J. Exp. Biol. , 38*, 747-757.

Ammi, A., Mast, T., Huang, I., Abruzzo, T., Coussios, C., Shaw, G., et al. (2008). Characterization of ultrasound propagation through ex vivo human temporal bone. *Ultrasound in Med. & Biol. , 34* (10), 1578-1589.

Aroyan, J. (2001). Three-dimensional modeling of hearing in Delphinus delphis. *J. Acoust. Soc. Am. , 110* (6), 3305-3318.

Au, W. (2000). Hearing in whales and dolphins: an overview. In W. P. Au (Ed.), *Hearing by whales and dolphins* (pp. 1-42). New York: Springer-Verlag.

Aubry, J., Tanter, M., Gerber, J., Thomas, J., & Fink, M. (2001). Optimal focusing by spatio-temporal inverse filter II. Experiments. Application to focusing through absorbing and reverberating media. *J. Acoust. Soc. Am. , 110* (1), 48-58.

Aubry, J., Tanter, M., Pernot, M., Thomas, J.-L., & Fink, M. (2003). Experimental demonstration of noninvasive transskull adaptive focusing based on prior computed tomography scans. *J. Acoust. Soc., Am. , 113* (1), 84-93.

Ballance, L. (2009). Cetacean Ecology. In W. Perrin, B. Wursig, & J. Thewissen, *Encyclopedia of Marine Mammals, 2nd Edition* (pp. 196-201). Burlington, MA: Academic Press.

Bamber, J., Fry, M., Hill, C., & Dunn, F. (1977). Ultrasonic attenuation and backscattering by mammalian organs as a function of time after excision. *Ultrasound in Med. & Biol. , 3*, 15-20.

Barannik, E., Girnyk, S., Tovstiak, V., Marusenko, A., Volokhov, V., Sarvazyan, A., et al. (2004). The influence of viscosity on the shear strain remotely induced by focused ultrasound in viscoelastic media. *J. Acoust. Soc. Am. , 115* (5), 2358-2364.

Baryshnikova, L. (1986). Acoustic mode conversion at an interface between biological media. *Sov. Phys. Acoust. , 32* (2), 142-144.

Bell, M., Byram, B., Harris, E., Evans, P., & Bamber, J. (2012). In vivo liver tracking with a high volume rate 4D ultrasound scanner and a 2D matrix array probe. *Phys. Med. Biol. , 57*, 1359-1374.

Bercoff, J., Tanter, M., & Fink, M. (2004). Supersonic shear imaging: a new technique for soft tissue elasticity mapping. *IEEE Trans. on Ultrasonics, Ferroelectrics, and Freq. Control. , 51* (4), 396-409.

Bercoff, J., Tanter, M., Muller, M., & Fink, M. (2004). The role of viscosity in the impulse diffraction field of elastic waves induced by the acoustic radiation force. *IEEE Trans. on Ultrasonics, Ferroelectrics, and Freq. Control , 51* (11), 1523-1536.

Besharse, J. (1971). Maturity and sexual dimorphism in the skull, mandible, and teeth of the beaked whale mesoplodon densirostris. *J. Mammalogy , 52* (2), 297-315.

Bigelow, T. (2010). Estimating the total ultrasound attenuation along the propagation path by applying multiple filters to backscattered echoes from a single spherically focused source. *IEEE Trans. Ultrasonics, Ferroelectrics, and Freq. Control , 57* (4), 900-907.

Bigelow, T., Church, C., Sandstrom, K., Abbott, J., Ziskin, M., Edmonds, P., et al. (2001). The thermal index: its strengths, weaknessess and proposed improvements. *J. Ultrasound Med. , 30*, 714-734.

Blomberg, J., & Jensen, B. (1976). Ultrasonic studies on the head oil of the north atlantic pilot whale (globicephala melaena melaena). *J. Acoust. Soc. Am. , 60* (3), 755-758.

Bouchet, L., Meeks, S., Goodchild, G., Bova, F., Buatti, J., & Friedman, W. (2001). Calibration of three-dimensional ultrasound images for image-guided radiation therapy. *Physics in Medicine and Biology , 46*, 559-577.

Boulet, T., Kelso, M., & Othman, S. (2013). Long-term in vivo imaging of viscoelastic properties of the mouse brain after controlled cortical impact. *Journal of Neurotrauma , 30*, 1512-1520.

Calle, S., Remenieras, J., & Matar, O. (2005). Temporal analysis of tissue displacement induced by a transient ultrasound radiation force. *J. Acoust. Soc. Am. , 118* (5), 2829-2840.

Campbell, J., & Waag, R. (1984). Measurements of calf liver ultrasonic differential and total scattering cross sections. *J. Acoust. Soc. Am. , 75* (2), 603-609.

Carstensen, E., Child, S., Norton, S., & Nyborg, W. (1990). Ultrasonic heating of the skull. *J. Acoust. Soc. Amer. , 87* (3), 1310-1307.

Chatelin, S., Constaninesco, A., & Willinger, R. (2010). Fifty years of brain tissue mechanical testing: from in vitro to in vivo investigations. *Biorheology , 47*, 255-276.

Chen, C., & Millero, F. (1976). Re-evaluation of Wilson's sound-speed measurements for pure water. *J. Acoust. Soc. Am. , 60* (6), 1270-1273.

Chen, K., Yao, A., Zheng, E., Lin, J., & Zheng, Y. (2012). Shear wave dispersion ultrasound vibrometry based on a different mechanical model for soft tissue characterization. *J. Ultrasound Med , 31*, 2001-2011.

Chen, S., Fatemi, M., & Greenleaf, J. (2004). Quantifying elasticity and viscosity from measurement of shear wave dispersion. *J. Acoust. Soc. Am. , 115* (6).

Chen, S., Fatemi, M., Kinnick, R., & Greenleaf, J. (2004). Comparison of stress field forming methods for vibroacoustography. *IEEE Trans. on Ultrasonics, Ferroelectrics, and Freq. Control , 51* (3), 313-321.

Chen, S., Urban, M., Pislaru, C., Kinnick, R., Zheng, Y., Yao, A., et al. (2009). Shear wave dispersion ultrasound vibrometry (SDUV) for measuring tissue elasticity and viscosity. *IEEE Trans. Ultrasonics, Ferroelectrics and Freq. Control , 56* (1), 55-62.

Chu, B., & Apfel, R. (1982). Acoustic radiation pressure produced by a beam of sound. *J. Acoust. Soc. Am. , 72* (6), 1673-1687.

Clement, G., & Hynynen, K. (2002). A non-invasive method for focusing ulrasound through the human skull. *Phys. Bed. Biol. , 47*, 1219-1236.

Clement, G., & Hynynen, K. (2002). Correlation of ultrasound phase with physical skull properties. *Ultrasound in Med. & Biol. , 28* (5), 617-624.

Clement, G., Sun, J., & Hynynen, K. (2001). The role of internal reflection in transskull phase distortion. *Ultrasonics , 39* (2), 109-113.

Clement, G., White, P., & Hynynen, K. (2004). Enhanced ultrasound transmission through the human skull using shear mode conversion. *J. Acoust. Soc. Am. , 115* (3), 1356-1364.

Colgan, N., Cronin, M., Gobbo, O., O'Mara, S., O'Connor, W., & Gilchrist, M. (2010). Quantitative MRI analysis of brain volume changes due to controlled cortical impact. *Journal of Neurotrauma , 27*, 1265-1274.

Coulouvrat, F. (1993). Continuous field radiated by a geometrically focused transducer: numerical investigation and comparison with an approximate model. *J. Acoust. Soc. Am. , 94* (3), 1663-1675.

Cox, M. (1987). *An experimental investigation of the mechanics of the peripheral auditory system in goldfish*. Georgia Institute of Technology.

Cox, M., & Rogers, P. (1987). Automated non-invasive motion measurement of auditory organs in fish using ultrasound. *J. Vibration, Stress, and Reliability in Design , 109*, 55-59.

Cox, T., Ragen, T., Read, A., Vos, E., Baird, R., Balcomb, K., et al. (2006). Understanding the impacts of anthropogenic sound on beaked whales. *J. Cetacean Res. Manage. , 7* (3), 177-187.

Cranford, T., McKenna, M., Soldevilla, M., Wiggins, S., Goldbogen, J., Shadwick, R., et al. (2008). Anatomic geometry of sound transmission and reception in Cuvier's beaked whale (Ziphius cavirostris). *The Anatomical Record , 291*, 353-378.

De Bucourt, M. (2010). Obese patients in an open MRI at 1.0 tesla: image quality, diagnostic impact and feasibility. *European Radiology , 21* (5), 1004-1015.

Deffieux, T., Gennisson, J., Bercoff, J., & Tanter, M. (2011). On the effects of reflected waves in transient shear wave elastography. *IEEE Transactions on Ultraosnics, Ferroelectrics, and Frequency Control , 58* (10), 2032-2035.

Doherty, J., Trahey, G., Nightingale, K., & Palmeri, M. (2013). Acoustic radiation force elasticity methods in diagnostic ultrasound. *IEEE Transactions on Ultrasonics, Ferroelectrics, and Frequency Control , 60* (4), 685-701.

Duck, F. (1999). Acoustic saturation and output regulation. *Ultrasound in Med. & Biol. , 25* (6), 1009-1018.

Duck, F. (2002). Nonlinear acoustics in diagnostic ultrasound. *Ultrasound in Med. & Biol. , 28* (1), 1-18.

Dunkin, R. (2004). *Ontogenetic changes in the thermal and buoyant properties of atlantic bottlenose dolphin (Tursiops truncatus) blubber*. MS Thesis, Department of Biological Sciences, University of North Carolina at Wilmington.

Dunn, F., Averbuch, A., & O'Brien, W. (1977). A primary method of the determination of ultrasonic intensity with the elastic sphere radiometer. *Acoustica , 38*, 58-61.

Evans, D., & England, G. (2001). *Joint interim report: Bahamas marine mammal stranding event of 15-16 March, 2000*. United States Department of Commerce and United States Navy.

Fatemi, M., & Greenleaf, J. (2000). Probing the dynamics of tissue at low frequencies with the radiation force of ultrasound. *Phys. Med. Biol. , 45*, 1449-1464.

Fatemi, M., & Greenleaf, J. (1999). Vibro-acoustography: an imaging modality based on ultrasound-stimulated acoustic emission. *Proc. Natl. Acad. Sci. , 96*, 6603-6608.

Filipczynski, L. (1986). Absorption of longitudinal and shear waves and generation of heat in soft tissues. *Ultrasound in Med. & Biol. , 12* (3), 223-228.

Finneran, J., & Hastings, M. (2004). A continuous-wave ultrasound system for displacement amplitude and phase measurement. *J. Acoust. Soc. Am. , 115* (6), 3202-3209.

Fitzgerald, E. (1975). Dynamic mechanical measurements during the life to death transition in animal tissues. *Biorheology , 12*, 397-408.

Fitzgerald, E., & Fitzgerald, J. (1995). Blubber and compliant coatings for drag reduction in water. 1. Viscoelastic properties of blubber and compliant coating materials. *Materials science & engineering C-biomimetic materials sensors and systems , 2* (4), 510-522.

Fitzgerald, E., Ackerman, E., & Fitzgerald, J. (1957). Preliminary measurements on the viscoelastic properties of animal tissues at audio frequencies. *J. Acoust. Soc. Am. , 29* (1), 61-64.

Fjield, T., & Hynynen, K. (1996). Experimental verification of the sectored annular phased array for MRI guided ultrasound surgery. *IEEE Ultrasonics Symposium* , 1273-1276.

Fjield, T., & Hynynen, K. (1997). The combined concentric-ring and sector-vortex phased array for MRI guided ultrasound surgery. *IEEE Trans. on Ultrasonics, Ferroelectrics, and Freq. Control , 44* (5), 1157-1167.

Fjield, T., Fan, X., & Hynynen, K. (1996). A parametric study of the concentric-ring transducer design for MRI guided ultrasound surgery. *J. Acoust. Soc. Am. , 100* (2), 1220-1230.

Frizzell, L., & Carstensen, E. (1976). Shear properties of mammalian tissues at low megahertz frequencies. *J. Acoust. Soc. Am. , 60* (6), 1409-1411.

Fry, F. B. (1978). Acoustical properties of the human skull. *J. Acoust. Soc. Am. , 63* (5), 1576-1590.

Garo, A., Hrapko, M., van Dommelen, J., & Peters, G. (2007). Towards a reliable characterization of the mechanical behavior of brain tissue: the effects of post-mortem time and sample preparation. *Biorheology , 44*, 51-58.

Gefen, A., & Margulies, S. (2004). Are in vivo and in situ brain tissues mechanically similar? *J. Biomech. , 37*, 1339-1352.

Giancoli, D. (1984). *General Physics*. Englewood Cliffs: Prentice-Hall.

Goss, S., Frizzell, L., & Dunn, F. (1980). Dependence of the ultrasonic properties of biological tissue on constituent proteins. *J. Acoust. Soc. Am. , 63* (3), 1041-1044.

Goss, S., Johnston, R., & Dunn, F. (1980). Compilation of empirical ultrasonic properties of mammalian tissues II. *J. Acoust. Soc. Am. , 68* (1), 93-108.

Graff, K. (1991). *Wave Motion in Elastic Solids*. New York: Dover.

Gray, M., Martin, J., & Rogers, P. (2006). *Transmission of ultrasound through bottlenose dolphin tursiops truncatus jaw andskull bone*. J. Acoust. Soc. Am. Honolulu, HI: 4th Joint Meeting of Acoustical Society of America and the Acoustical Society of Japan.

Green, M., Bilston, L., & and Sinkus, R. (2008). In vivo brain viscoelastic properties measured by magnetic resonance elastography. *NMR Biomed , 21*, 755-764.

Guenther, D., & Walker, W. (2007). Optimal apodization design for medical ultrasound using constrained least squares part II: simulation results. *IEEE Trans. Ultrasonics, Ferroelectrics, and Freq. Control , 54* (2).

Guillot, F., & Rogers, P. (2006). Photographs of cetacean skulls from the collection of the Smithsonian Institution. *unpublished* .

Henni, A., Schmitt, C., Trop, I., & Cloutier, G. (2012). Shear wave induced resonance elastography of spherical masses with polarized torsional waves. *Applied Physics Letters , 100*, 133702-1-5.

Hertz, V., & Mende, H. (1939). Der Schallstrahlungsdruck in Flussigkeiten. *Z. Phys. , 114*, 354-367.

Houser, D., Finneran, J., Carder, D., Van Bonn, W., Smith, C., Hoh, C., et al. (2004). Structural and functional imaging of bottlenose dolphin (tursiops truncatus) cranial anatomy. *J. Exp. Biol. , 207*, 3657-3665.

Hrapko, M., van Dommelen, J., Peters, G., & and Wismans, J. (2008). The influence of conditions on characterization of the mechanical properties of brain tissue. *J. Biomech. Eng. , 130*, 1-10.

Hueter, T. (1952). Messung der ultraschallabsorption im menschlichen schadelknochen und ihre abhangigkeit von der frequenz. *Naturwissenschaften , 39*, 21-22.

Hydrocephalus Association. (2015). *About hydrocephalus - a book for famlies*. Bethesda: Hydrocephalus Association.

Hynynen, K., Clement, G., McDannold, N., Vykhodtevea, N., King, R., White, P., et al. (2004). 500-element ultrasound phased array system for noninvasive focal surgery of the brain: a preliminary rabbit study with ex vivo human skulls. *Mag. Res. in Med. , 52*, 100-107.

Jensen, J., & Svendsen, N. (1992). Calculation of pressure fields from arbitrarily shaped, apodized, and excited ultrasound transducers. *IEEE Trans. on Ultrasonics, Ferroelectrics and Freq. Control , 39* (2), 262-267.

Jepson, P., Arbelo, M., Deaville, R., Patterson, I., Castro, P., Baker, J., et al. (2003). Gas-bubble lesions in stranded cetaceans. *Nature , 425*, 575-576.

Ketten, D. (2000). Cetacean ears. In W. Au, A. Popper, & R. Fay, *Hearing by whales and dolphins* (pp. 43-108). New York: Springer.

Ketten, D. R. (2005). *Beaked whale necropsy finding for stranding in the Bahamas, Puerto Rico and Madeira, 1999-2002*. Woods Hole Oceanographic Institution. Technical Report WHOI-2005-09.

Konofagou, E., & Hynynen, K. (2003). Localized harmonic motion imaging: theory, simulations and experiments. *Ultrasound in Med. & Biol. , 29* (10), 1405-1413.

Koopman, H., Budge, S., Ketten, D., & Iverson, S. (2006). Topographical distribution of lipids inside the mandibular fat bodies of odontocetes: remarkable complexity and consistency. *IEEE J. Oceanic Eng. , 31* (1), 95-106.

Kremkau, F., Barnes, R., & McGraw, C. (1981). Ultrasonic attenuation and propagation speed in normal human brain. *J. Acoust. Soc. Am. , 70* (1), 29-38.

Krishnan, S., Hamilton, J., & O'Donnell, M. (1998). Suppression of propagating second harmnic in ultrasound contrast imaging. *IEEE Trans. on Ultrasonics, Ferroelectrics, and Freq. Control , 45* (3), 704-711.

Krouskop, T., Dougherty, D., & Levinson, S. (1987). A pulsed Doppler ultrasonic system for making noninvasive measurements of the mechanical properties of soft tissues. *J. Rehabil. Res. Biol. , 24*, 1-8.

Krouskop, T., Wheeler, T., Kallel, F., Garra, B., & Hall, T. (1999). Elastic moduli of breast and prostate tissues under compression. *Ultrasonic Imaging , 20*, 260-274.

Krysl, P., Cranford, T., Wiggins, S., & and Hildebrand, J. (2006). Simulating the effect of high-intensity sound on cetaceans: modeling approach and a case study for Cuvier's beaked whale (siphius cavirostris). *J. Acoust. Soc. Am. , 120* (4), 2328-2339.

Kuttruff, H. (1992). Physcial ultrasound phenomena in tissues. In P. Altmeyer, S. el-Gammal, & K. Hoffman, *Ultrasound in Dermatology* (pp. 3-11). Berlin: Springer-Verlag.

Lebedeva, L. (1965). Measurement of the dynamic complex shear modulus of animal tissues. *Soviet Physics-Acoustics , 11* (2), 163-165.

Lerner, R., Huang, S., & Parker, K. (1990). "Sonoelasticity" images derived from ultrasound signals in mechanically vibrated tissues. *Ultrasound in Med. & Biol. , 16* (3), 231-239.

Lerner, R., Parker, K., Holen., J., Gramiak, R., & Waag, R. (1988). Sono-elasticity: medical elasticity images derived from ultrasound signals in mechanically vibrated targets. *Acoustical Imaging , 16*, 317-327.

Levinson, S., Shinagawa, M., & Sata, T. (1995). Sonoelastic determination of human skeletal muscle elasticity. *J. Biomechanics , 28* (10), 1145-1154.

Lievers, B., Poljsak, A., Waldman, S., & Pilkey, A. (2010). Effects of dehydration-induced structural and material changes on the apparent modulus of cancellous bone. *Medical Engineering & Physics , 32*, 921-925.

Litchfield, C., Greenberg, A., Caldwell, D., Caldwell, M., Sipos, J., & Ackman, R. (1975). Comparative lipid patterns in acoustical and nonacoustical fatty tissues of dolphins porpoises and toothed whales. *Comp. Biochem. Physiol. , 50*, 591-597.

Litchfield, C., Karol, R., Mullen, M., Dilger, J., & Luthi, B. (1979). Physical factors influencing refraction of the echolative sound beam in delphinid cetaceans. *Marine Biology , 52*, 285-290.

Liu, D., & and Waag, R. (1994). Correction of ultrasonic wavefront distortion using backpropagation and a reference waveform method for time-shift compensation. *J. Acoust. Soc. Am. , 96* (2), 649-660.

Lubinski, M., Emelianov, S., & O'Donnell, M. (1999). Speckle tracking methods for ultrasonic elasticity imaging using short-time correlation. *IEEE Trans. Ultrasonics, Ferroelectrics and Freq. Control , 46* (1), 82-96.

Lupsor, M., Badea, R., Stefanescu, H., Sparchez, Z., Branda, H., Serban, A., et al. (2009). Performance of a new elastographic method (ARFI technology) compared to unidimensional transient elastography in the noninvasive assessment of chronic hepatitis c. Preliminary results. *J. Gastrointestin Liver Dis. , 18* (3), 303-310.

Mace, E., Cohen, I., Montaldo, G., Miles, R., M., F., & Tanter, M. (2011). In vivo mapping of brain elasticity in small animals using shear wave imaging. *IEEE Trans. on Med. Imag. , 30* (3), 550-558.

Madigosky, W., Lee, G., Haun, J., Borkat, F., & and Kataoka, R. (1986). Acoustic surface wave measurements on live bottlenose dolphins. *J. Acoust Soc Am , 79* (1), 153-159.

Madsen, E., Frank, G., Hobson, M., Lin-Gibson, S., Hall, T., Jiang, J., et al. (2008). Instrument for determining the complex shear modulus of soft-tissue-like-materials from 100-300Hz. *Phys. Med. Biol. , 53*, 5313-5342.

Madsen, E., Sathoff, H., & Zagzebski, J. (1983). Ultrasonic shear wave properties of soft tissues and tissuelike materials. *J. Acoust. Soc. Am. , 74* (5), 1346-1355.

Maleke, C., Pernot, M., & Konofagou, E. (2006). Single-element focused ultrasound transducer method for harmonic motion imaging. *Ultrasonic Imaging , 28*, 144-158.

Manduca, A., Oliphant, T., Dresner, M., Mahowald, J., Kruse, S., Amomin, E., et al. (2001). Magnetic resonance elastography: non-invaasive mappling of tissue elasticity. *Medical Image Analysis , 5*, 237-254.

Marino, L., Murphy, T., Deweerd, A., Morris, J., Fobbs, A., Humblot, N., et al. (2001). Anatomy and three-dimensional reconstructions of the brain of the white whale (Delphinapterus leucas) from magnetic resonance images. *The Anatomical Record , 262*, 429-439.

Martin, J., Rogers, P., & Gray, M. (2013). Pulse compression in a time variant system with application to ultrasonic vibrometry. *J. Acoust. Soc. Am. , 133* (3), 1503-1514.

Martin, J., Rogers, P., & Gray, M. (2011). Range discrimination in ultrasonic vibrometry: theory and experiment. *J. Acoust. Soc. Amer. , 130* (3), 1735-1747.

McAleavey, S., Collins, E., Kelly, J., Elegbe, E., & Menon, M. (2009). Validation of SMURF estimation of shear modulus in hydrogels. *Ultrasonic Imaging , 31*, 131-150.

McAleavey, S., Menon, M., & Orszulak, J. (2007). Shear-modulus estimation by application of spatially-modulated impulsive acoustic radiation force. *Ultrasonic Imaging , 29*, 87-104.

McAleavey, S., Nightingale, K., Stutz, D., Hsu, S., & Trahey, G. (2003). Image reconstruction with acoustic radiation force induced shear waves. *Proceedings of SPIE, Medical Imaging: Ultrasonic imaging and signal processing , 5035*, 223-234.

McCall, G. (1994). Brute force and ignorance methods in engineering. *personal communication*.

McDannold, N., Park, E., Mei, C., Zadicario, E., & Jolesz, F. (2010). Evaluation of three-dimensional temperature distributions produced by a low-frequency transcranial focused ultrasound system within ex vivo human skulls. *IEEE Transactions on Ultrasonics, Ferroelectrics and Frequency Control , 57* (9), 1967-1976.

McKenna, M., Goldbogen, J., Leger, J., Hildebrand, J., & Cranford, T. (2007). Evaluation of postmortem changes in tissue structure in the bottlenose dolphin (tursiops truncatus). *Anatomical record-advances in integrative anatomy and evolutionary biology , 290* (8), 1023-1032.

Mead, J., & Fordyce, R. (2009). The therian skull: a lexicon with emphasis on the odontocetes. *Smithsonian Contributions to Zoology , 627*, 1-261.

Melodelima, D., Bamber, J., Duck, F., & Shipley, J. (2007). Transient elastography using impulsive ultrasound radiation force: a preliminary comparison with surface palpation elastography. *Ultrasound in Med. & Biol. , 33* (6), 959-969.

Mohl, B., Au, W., Pawloski, J., & Nachtigall, P. (1999). Dolphin hearing: relative sensitivity as a function of point of application of a contact sound source in the jaw and head region. *J. Acoust. Soc. Am. , 105* (6), 3421-3424.

Montie, E., Manire, C., & Mann, D. (2011). Live CT imaging of sound reception anatomy and hearing measurements in the pygmy killer whale, feresa attenuata. *J. Exp. Biol. , 214*, 945-955.

Muthupillai, R., Rossman, P., Lomas, D., Greenleaf, J., Riederer, S., & Ehman, R. (1996). Magnetic resonance imaging of transverse acoustic strain waves. *Magnetic Resonance in Medicine , 36*, 266-274.

NCRP. (1992). *Report No. 113: Exposure criteria for medical diagnostic ultrasoundL I. Criteria based on thermal mechanisms*. National Council on Thermal Protection and Measurements, Bethesda.

Nicolle, S., Lounis, M., Willinger, R., & Palierne, J. (2005). Shear linear behavior of brain tissue over a large frequency range. *Biorheology , 42*, 209-223.

Nightingale, K., McAleavey, S., & Trahey, G. (2003). Shear-wave generation using acoustic radiation force: in vivo and ex vivo results. *Ultrasound in Med. & Biol. , 29* (12), 1715-1723.

Nightingale, K., Palmeri, M., Nightingale, R., & Trahey, G. (2001). On the feasibility of remote palpation using acoustic radiation force. *J. Acoust. Soc. Am. , 110* (1), 625-634.

Nightingale, K., Soo, M., Nightingale, R., & Trahey, G. (2002). Acoustic radiation force impulse imaging: in vivo demonstration of clinical feasibility. *Ultrasound in Med. & Biol. , 28* (2).

Norris, K. (1968). The evolution of acoustic mechanisms in odontocete cetaceans. In E. Drake (Ed.), *Evolution and Environment. A symposium pressented on the occasion of the one hundredth anniversary of the foundation of peabody museum of natural history at Yale university*. New Haven: Yale University Press.

Norris, K., & Harvey, G. (1974). Sound transmission in the porpoise head. *J. Acoust. Soc. Am. , 56* (2), 659-664.

Nummela, S., Kosove, J., Lancaster, T., & Thewissen, J. (2004). Lateral mandibular wall thickness in tursiops truncatus: variation due to sex and age. *Marine Mammal Science , 20* (3), 491-497.

Nyborg, W. (1988). Solutions of the bio-heat transfer equation. *Phys. Med. Biol. , 33*, 785-792.

Oelschlager, H. (1990). Evolutionary morphology and acoustics in the dolphin skull. In J. a. Thomas, *Sensory abilities of cetaceans. Laboratory and field evidence* (pp. 137-162). New York: Plenum Press.

Oestreicher, H. (1951). Field and impedance of an oscillating sphere in a viscoelastic medium with an application to biophysics. *J. Acoust. Soc. Am. , 23*, 707-714.

Ophir, J., Cespedes, I., Ponnekanti, H., Yazdi, Y., & Li, X. (1991). Elastography: a quantitative method for imaging the elasticity of biological tissues. *Ultrasonic Imaging , 13*, 111-134.

Orescanin, M., & Insana, M. (2010). Shear modulus estimation with vibrating needle stimulation. *IEEE Trans. Ultrasonics, Ferroelectrics and Freq. Control , 57* (6), 1358-1367.

Palmeri, M., & Nightingale, K. (2004). On the thermal effects associated with radiation force imaging of soft tissue. *IEEE Trans. on Ultrasonics, Ferroelectrics and Freq. Control , 51* (5), 551-565.

Palmeri, M., Wang, M., Dahl, J., Frinkley, K., & Nightingale, K. (2007). Quantifying hepatic shear modulus in vivo using acoustic radiation force. *Ultrasound in Med. & Biol. , 34* (4), 546-558.

Parker, K. (1983). Ultrasonic attenuation and absorption in liver tissue. *Ultrasound in Med. & Biol. , 9* (4), 363-369.

Pennes, H. (1948). Analysis of tissue and arterial blood termperatures in the resting human forearm. *J. Appl. Phys. , 1*, 93-122.

Penttinen, A., & Luukkala, M. (1976). The impulse response and pressure nearfield of a cuved ultrasonic radiator. *J. Phys. D: Appl. Phys. , 9*, 1547-1557.

Pernot, M., Aubry, J.-F., Tanter, M., Thomas, J., & Fink, M. (2001). Experimental validation of 3D finite differences simulations of ultrasonic wave propagation through the skull. *IEEE Ultrasonics Symposium* , 1547 -1550.

Pichardo, S., Sin, V., & Hynynen, K. (2011). Multi-frequency characterization of the speed of sound and attenuation coefficient for longitudinal transmission of freshly excised human skulls. *Phys. Med. Biol. , 56*, 219-250.

Pierce, A. (1989). *Acoustics, an introduction to its physical principles and applications*. Woodbury, NY: Acoustical Society of America.

Pinton, G., Aubry, J., Fink, M., & Tanter, M. (2011). Effects of nonlinear ultrasound propagation on high intensity brain therapy. *Med. Phys. , 38* (3), 1207-1216.

Pinton, G., Dahl, J., & Trahey, G. (2006). Rapid tracking of small displacements with ultrasound. *IEEE Transactions on ultrasonics, ferroelectrics and frequency control , 53* (6), 1103-1117.

Prasad, K. (2003). *Sound speed investigation of dolphin tissue (Master's Thesis)*. University of Massachusetts Dartmouth.

Rahman, M. (1995). Some fundamental axisymmetrical singular solutions of elastodynamics. *Quarterly Journal of Mechanics and Applied Mathematics , 48*, 329-342.

Raju, B., & Srinivasan, M. (2001). High-frequency ultrasonic attenuation and backscatter coefficients of in vivo normal human dermis and subcutaneous fat. *Ultrasound in Med. & Biol. , 26* (11), 1543-1556.

Reynolds, J., Odell, D., & Rommel, S. (1999). Marine Mammals of the World. In J. a. Reynolds (Ed.), *Biology of Marine Mammals* (pp. 1-14). Washington: Smithsonian Institution Press.

Ridgway, S. (1999). An illustration of Norris' acoustic window. *Marine Mammal Science , 15* (4), 926-930.

Rigamonti, D. (. (2014). *Adult Hydrocephalus*. Cambridge: Cambridge University Press.

Robert, B., Sinkus, R., Larrat, B., Tanter, M., & Fink, M. (2006). A new rheological model based on fractional derivatives for biological tissues. *IEEE Ultrasonics Symposium* , 1033-1036.

Rommel, S., Costidis, A., Fernandez, A., Jepson, P., Pabst, D., McLellan, W., et al. (2006). Elements of beaked whale anatomy and diving physiology and some hypothetical causes of sonar-related stranding. *J. Cetacean Res. Manage. , 7* (3), 189-209.

Rommel, S., Pabst, D., & McLellan, W. (2009). Skull Anatomy. In W. W. Perrin, *Encyclopedia of Marine Mammals, 2nd Edition* (pp. 1033-1047). Amsterdam: Academic Press.

Rouze, N., Wang, M., Palmeri, M., & Nightingale, K. (2012). Parameters affecting the resolution and accuracy of 2-D quantitative shear wave images. *IEEE Transactions on Ultrasonics, Ferroelectrics, and Frequency Control , 59* (8), 1729-1740.

Sack, I., Beierback, B., Hamhaber, U., Klatt, D., & Braun, J. (2008). Non-invasive measurement of brain viscoelasticity using magnetic resonance elastography. *NMR in Biomedicine , 21*, 265-271.

Sarvazyan, A., Rudenko, O., & Nyborg, W. (2010). Biomedical applications of radiation force ultrasound: historical roots and physical basis. *Ultrasound in Bed. & Biol. , 36* (9), 1379-1394.

Sarvazyan, A., Rudenko, O., Swanson, S., Fowlkes, J., & Emelianov, S. (1998). Shear wave elasticity imaging: a new ultrasonic technology of medical diagnostics. *Ultrasound in Med. & Biol. , 24* (9), 1419-1435.

Schlosser, J., Salisbury, K., & Hristov, D. (2010). Telerobotic system concept for real-time soft-tissue imaging during radiotherapy beam delivery. *Medical Physics , 37* (12), 6357-6368.

Skovoroda, A., Klishko, A., Gukasyan, D., Maevskii, E., Ermiloa, V., Oranskaya, G., et al. (1995). Quantitative analysis of the mechanical charateristics of pathologically latered soft biological tissues. *Biofizika , 40* (6), 1335-1340.

Skurczynski, M., Duck, F., Shipley, J., Bamber, J., & Melodelima, D. (2009). Evalutation of experimental methods for assessing safety for ultrasound radiation force elastography. *British Journal of Radiology , 82*, 666-674.

Smithsonian National Museum of Natural History Marine Mammal Program. (2007). *Mesoplodon Densirostris Skull Morphology*. Retrieved January 2012, from Beaked Whale Identification Guide: http://vertebrates.si.edu/mammals/beaked_whales/pages/mde/mde_ost_pg4.htm

Soldevilla, M., McKenna, M., Wiggins, S. M., Shadwick, R., Cranford, T., & Hildebrand, J. (2005). Cuvier's beaked whale (ziphius cavirostris) head tissues: physical properties and CT imaging. *J. Exp. Biol. , 208*, 2319-2332.

Song, J., & Hynynen, K. (2010). Feasibility of using lateral mode coupling method for a large scale ultrasound phased array for noninvasive transcranial therapy. *IEEE Transactions on Biomedical Engineering , 57* (1), 124-133.

Song, J., Pulkkinen, A., Huang, Y., & Hynynen, K. (2012). Investigation of standing-wave formation in a human skull for a clinical prototype of a large-aperture, transcranial MR-guided focused ultrasound (MRgFUS) phased array: an experimental and simulation study. *Transactions on Biomedical Engineering , 59* (2), 435-444.

Starritt, H., Duck, F., & Humphrey, V. (1991). Forces acting in the direction of propagation in pulsed ultrasound fields. *Phys. Med. Biol. , 36* (11), 1465-1474.

Strowitzki, M., Brand, S., & Jenderka, K. (2007). Ultrasonic radio-frequency spectrum analysis of normal brain tissue. *Ultrasound in Med. & Biol , 33* (4), 522-529.

Sugimoto, T., Ueha, S., & Itoh, K. (1990). Tissue hardness measurement using the radiation force of focused ultrasound. *IEEE Ultrasonics Symposium* , 1377-1380.

Sun, J., & Hynynen, K. (1999). The potential of transskull ultrasound therapy and surgery using the maximum available skull surface area. *J. Acoust. Soc. Am. , 105* (4), 2519-2527.

Tanter, M., Bercoff, J., Athanasiou, A., Deffieux, T., Gennisson, J., Montaldo, G., et al. (2007). Quantitative assessment of breast lesion viscoelasticity: initial clinical results using supersonic shear imaging. *Ultrasound in Med. & Biol. , 34* (9), 1373-1386.

Tanter, M., Thomas, J., & Fink, M. (1998). Focusing and steering through absorbing and abberating layers: application to ultrasonic propagation through the skull. *J. Acoust. Soc. Am. , 103* (5), 2403-2410.

Taylor, J. (1995). *Introduction to ultra-wideband radar systems*. Boca Raton: CRC Press.

Tubelli, A., Zosuls, A., Ketten, D., & Mountain, D. (2014). Elastic modulus of cetacean auditory ossicles. *The Anatomical Record , 297*, 892-900.

Tubelli, A., Zosuls, A., Ketten, D., Yamato, M., & Mountain, D. (2012). A prediction of the minke whale (Balaenoptera acutorostrata) middle-ear transfer function. *J. Acoust. Soc. Am. , 132* (5), 3263-3272.

Umemura, S., & Cain, C. (1989). The sector-vortex phased array: acoustic field synthesis for hyperthermia. *IEEE Transactions on Ultrasonics, Ferroelectrics, and Freq. Control , 36* (2), 249-257.

US Dept. of Health and Human Services, F. C. (2008). Information for manufacturers seeking marketing clearance of diagnostic ultrasound systems and transducers.

Van der Steen, A., Cuypers, M., Thijssen, J., & de Wilde, P. (1991). Influence of histochemical preparation on acoustic parameters of liver tissue: a 5 MHz study. *Ultrasound in Med. & Biol. , 17* (9), 879-891.

Vappou, J., Breton, E., Choquet, P., Willinger, R., & Constantinesco, A. (2008). Assessment of in vivo and post mortem mechanical behavior of brain tissue using magnetic resonance elastography. *J. Biomechanics , 41*, 2954-2959.

Varanasi, U., & Malins, D. (1972). Triacylglycerols characteristics of porpoise acoustic tissues. *Science , 176*, 926-928.

Vignon, F., de Rosny, J., Aubry, J., & Fink, M. (2007). Optimal adaptive focusing through heterogeneous media with the minimally invasive inverse filter. *J. Acoust. Soc. Am. , 122* (5), 2715-2724.

Viola, F., & Walker, W. (2003). Radiation force imaging of viscoelastic properties with reduced artifacts. *IEEE Transactions on Ultrasonics Ferroelectrics and Frequency Control , 50* (6), 736-742.

Viola, F., Kramer, M., Lawrence, M., Oberhauser, J., & and Walker, W. (2004). Sonorheometry: a noncontact method for the dynamic assessment of thrombosis. *Annals of Biomedical Engineering , 32* (5), 696-705.

Walker, W., Fernandez, F., & Negron, L. (2000). A method of imaging viscoelastic parameters with acoustic radiation force. *Phys. Med. Biol. , 45*, 1437-1447.

White, P., Clement, G., & Hynynen, K. (2006). Longitudinal and shear mode ultrasound propagation in human skull bone. *Ultrasound in Med. & Biol. , 32* (7), 1085-1096.

Wolfram, U., Wilke, H., & Zysset, P. (2010). Rehydration of vertebral tarbecular bone: influences on its anisotropy, its stiffness, and the indentation work with a view to age, gender and vertebral level. *Bone , 46*, 348-354.

Wu, Z., Rubens, D., & Parker, K. (2006). Sonoelastographic imaging of interference patterns for estimation of shear velocity distribution in biomaterials. *J. Acoust. Soc. Am. , 120* (1), 535-545.

Wunenburger, R., Mujica, N., & Fauve, S. (2004). Experimental study of the Doppler shift generated by a vibrating scatterer. *J. Acoust. Soc. Am. , 115* (2).

Yamakoshi, Y., Sato, J., & Sato, T. (1990). Ultrasonic imaging of internal vibration of soft tissue under forced vibration. *IEEE Trans. Ultrasonics Ferroelectrics and Freq. Control , 37* (2), 45-53.

Yang, M., Baldwin, S., Marutyan, K., & Wallace, K. (2006). Elastic stiffness coefficients (c11, c33, and c13) for freshly excised and formalin-fixed myocardium from ultrasonic velocity measurements. *J. Acoust. Soc. Am. , 119* (3), 1880-1887.

Yao, L., Zagzebski, J., & Madsen, E. (1990). Backscatter coefficient measurements using a reference phantom to extract depth-dependent instrumentation factors. *Ultrasonic Imaging , 12*, 58-70.

Zahorodny-Duggan, Z., Koopman, H., & Budge, S. (2009). Distribution and development of the highly specialized lipids in the sound reception systems of dolphins. *J. Comp. Physiol. B , 179*, 783-798.

Zhang, J., Yoganandan, N., Pintar, F., Guan, Y., Shender, B., Paskoff, G., et al. (2011). Effects of tissue preservation temperature on high strain-rate material properties of brain. *J. Biomechanics , 44*, 391-396.

Zhao, H., Song, P., Urban, M., Greenleaf, J., & Chen, S. (2012). Shear wave speed measurement using and unfocused ultrasound beam. *Ultrasound in Med. & Biol. , 38* (9), 1646-1655.

Zucca, P., Di Guardo, G., Pozzi-Mucelli, R., Scaravelli, D., & Francese, M. (2004). Use of computer tomography for imaging of crassicauda grampicola in a risso's dolphin (grampus griseus). *Journal of Zoo and Wildlife Medicine , 35* (3), 391-394.